Contributions to Acoustic Emission-based Structural Health Monitoring and Process Monitoring

Von der Fakultät für Ingenieurwissenschaften,
Abteilung Maschinenbau und Verfahrenstechnik der
Universität Duisburg-Essen
zur Erlangung des akademischen Grades
eines
Doktors der Ingenieurwissenschaften
Dr.-Ing.

genehmigte Dissertation

von

Sebastian Felix Wirtz
aus
Oberhausen

Gutachter:

Univ.-Prof. Dr.-Ing. Dirk Söffker
Univ.-Prof. Dr.-Ing. Claus-Peter Fritzen

Tag der mündlichen Prüfung: 16.06.2020

Danksagung

Diese Dissertation entstand in der Zeit von 2015 bis 2020 während meiner Tätigkeit als wissenschaftlicher Mitarbeiter am Lehrstuhl für Steuerung, Regelung, und Systemdynamik (SRS) an der Universität Duisburg-Essen. Mein besonderer Dank gilt Herrn Univ.-Prof. Dr.-Ing. Dirk Söffker für die fachliche Führung und Diskussionen, die meine Arbeit geprägt und mich stets motiviert haben. Dies gilt insbesondere für die Ermöglichung zahlreicher Tagungsbesuche, welche mir Gelegenheit boten, meine Perspektive auf Structural Health Monitoring und angrenzende Forschungsgebiete zu erweitern. Weiterhin möchte ich mich herzlich bei Univ.-Prof. Dr.-Ing. Claus-Peter Fritzen dafür bedanken, dass er sich bereit erklärt hat, als Zweitgutachter zu fungieren.

Außerdem möchte ich meinen Kolleginnen und Kollegen am Lehrstuhl SRS danken. Hier wurde ich bereits 2013 als studentische Hilfskraft offen und herzlich im Team aufgenommen. Unsere Zusammenarbeit war stets durch Hilfsbereitschaft und gegenseitige Wertschätzung geprägt. Darüber hinaus danke ich den Kolleginnen und Kollegen des Lehrstuhls für Industrie- und Fahrzeugantriebstechnik an der Ruhr-Universität Bochum sowie des Lehrstuhls für Technische Chemie I an der Universität Duisburg-Essen und der Arbeitsgruppe für Mess- und Regelungstechnik – Mechatronik an der Universität Siegen für die freundliche Kooperation. Mein herzlicher Dank gilt auch den Studierenden, die in dieser Zeit durch Ihre Abschlussarbeit oder als wissenschaftliche Hilfskraft am Erfolg mitgewirkt haben.

Schließlich möchte ich auch meiner Familie danken – insbesondere meinen Eltern dafür, dass sie mich viele Jahre gefördert und ermutigt haben, Herausforderungen anzunehmen. Nicht zuletzt danke ich meiner Frau für ihre Geduld und Unterstützung. Ich freue mich auf unsere gemeinsame Zeit, die vor uns liegt.

Mülheim an der Ruhr, Juli 2020 Sebastian Felix Wirtz

Abstract

Accurate in-situ measurements and suitable signal processing are important for reliable monitoring and control of modern industrial equipment. However, measuring relevant variables may be difficult due to physical and technological limitations. Acoustic Emission (AE), which refers to passively recorded mechanical stress waves using highly sensitive equipment, is frequently suggested to obtain in-situ measurements. For instance, AE can be detected due to the release of elastic energy in a material under load due to damage. Sources of AE are manifold and different source mechanisms can be distinguished using suitable signal processing. Furthermore, advantages such as high sensitivity to incipient damages, detectability of damages in a distance from the source, and characterization and localization of source mechanisms, are inherent to the measurement principle. Hence, AE can be identified as promising in-situ measurement technology.

The two main research areas (i) Structural Health Monitoring (SHM) and (ii) process monitoring and control are considered in this thesis. From a methodological point of view, both fields are related in that similar methods are used for analysis and interpretation of AE. Several research questions, which address key topics in AE-based monitoring, are established. In particular, suitable sensor mounting is crucial for successful detection of AE. However, some mounting techniques, which were successfully used in the laboratory, may be difficult to realize in practice. Therefore, the question raises if there are alternative mounting strategies, which are suitable to simplify the application of AE. Regarding the use of machine learning for analysis of AE it remains as an open question, how the reliability of an individual classification result depends on environmental and operational factors. Furthermore, characterizing the effect of variable operational and environmental conditions on AE signatures is a difficult topic. Regarding the use of AE for process monitoring and control, it can be stated as an open question, how AE can be processed effectively to characterize the productivity or quality of a process. Furthermore, the choice of a suitable hardware platform to implement AE-based monitoring and to realize control actions online is an important element of AE-based process control.

Accordingly, new results of AE for SHM and for process monitoring and control are presented in this thesis. However, the development of a complete AE-based SHM system is not within the scope. For data-acquisition and fast signal processing, a novel hardware architecture is suggested as low cost solution for AE measurements and control. Regarding the use of AE for SHM, the focus is placed on the use of data-driven approaches. The related applications include composite material and spur gears. The reliability of AE classification schemes is discussed at the example of damage classification in composites. Finally, the influence of external factors (i.e. load) and limitations due to signal attenuation are discussed. Furthermore, new results regarding the use of AE in process monitoring and control are presented. It is shown that AE can be used to characterize the lubrication condition during thread forming. As proof of concept, the online use of AE in process control is demonstrated at the example of nanoparticle synthesis using laser ablation.

Kurzfassung

Für die zuverlässige Überwachung und Steuerung moderner Industrieanlagen sind päzise in-situ Messtechnik und geeignete Signalverarbeitung von besonderer Bedeutung. Dabei kann die Erfassung relevanter Größen aufgrund physikalischer und technologischer Einschränkungen schwierig zu realisieren sein. Zur Durchführung von in-situ Messungen wird häufig Acoustic Emission (AE) vorgeschlagen. Dies bezeichnet elastische Wellen, die mit hochempfindlichem Equipment passiv gemessen werden können. Beispielsweise kann AE infolge der Freisetzung elastischer Energie in einem belasteten Prüfkörper aufgrund von Materialversagen gemessen werden. Im Allgemeinen sind AE-Quellen vielfältig und verschiedene Quellenmechanismen können durch geeignete Signalverarbeitung unterschieden werden. Darüber hinaus weist das Messprinzip verschiedene Vorteile wie eine hohe Empfindlichkeit zur frühzeitigen Detektion beginnender Schäden, die Erkennbarkeit von Schäden in einiger Entfernung von der Quelle sowie die Möglichkeit zur Charakterisierung und Lokalisierung von Quellenmechanismen mittels geeigneter Signalverarbeitung auf. Daher lässt sich AE als vielversprechende in-situ Messtechnik identifizieren.

In dieser Arbeit werden die beiden Hauptforschungsbereiche (i) Structural Health Monitoring (SHM) und (ii) Prozessüberwachung behandelt. Aus methodischer Sicht sind beide Bereiche insofern verwandt, als dass zur Analyse und Interpretation von AE ähnliche Methoden angewendet werden. Es werden verschiedene Forschungsfragen entwickelt, die sich mit Schlüsselthemen der AE-basierten Überwachung befassen. Konkret ist insbesondere eine geeignete Sensormontage bei der Durchführung von AE Messungen entscheidend. Jedoch sind einige Ansätze, die erfolgreich im Labor getestet wurden, in der Praxis möglicherweise schwierig zu realisieren. Daher stellt sich die Frage, ob es alternative Ansätze zur Sensormontage gibt, die geeignet sind, um die Durchführung von AE Messungen zu erleichtern. Bezüglich der Verwendung von maschinellen Lernverfahren zur Analyse von AE bleibt die Abhängigkeit der Zuverlässigkeit eines individuellen Klassifikationsergebnisses von Umgebungs- und Betriebsfaktoren offen. Darüber hinaus ist es schwierig, den Einfluss variabler Umgebungs- und Betriebsbedingungen auf AE-Signaturen zu charakterisieren. Bezüglich der Verwendung von AE zur Prozessüberwachung und -regelung kann als offene Frage angegeben werden, wie AE effektiv verarbeitet werden kann, um die Produktivität oder Qualität eines Prozesses zu charakterisieren. Darüber hinaus ist die Wahl einer geeigneten Hardware Plattform zur Implementierung AE-basierter Überwachung und zur Online-Realisierung von Steuereingaben ein wichtiges Element AE-basierter Prozessregelung.

Vor diesem Hintergrund werden in dieser Arbeit neue Ergebnisse hinsichtlich AE für SHM sowie zur Prozessüberwachung und -regelung vorgestellt. Dabei ist die Entwicklung eines vollständigen AE-basierten SHM-Systems nicht Bestandteil dieser Arbeit. Zur Messwerterfassung und zur schnellen Signalverarbeitung wird eine innovative Hardwarearchitektur als kostengünstige Lösung für AE-Messungen und zur Regelung vorgeschlagen. In Bezug auf die Verwendung von AE für SHM wird der Schwerpunkt auf die Verwendung datengetriebener Verfahren gelegt. Gegenstand der Untersuchungen sind Faserverbundwerkstoffe und Stirnradgetriebe. Die Zuverlässigkeit von Methoden zur Klassifikation von AE Signalen wird am

Beispiel der Fehlerklassifikation in Verbundwerkstoffen erörtert. Abschließend werden der Einfluss externer Faktoren (z. B. Last) und Einschränkungen aufgrund der Signaldämpfung dargestellt und diskutiert. Darüber hinaus werden neue Ergebnisse zum Einsatz von AE zur Prozessüberwachung vorgestellt. Es kann gezeigt werden, dass AE geeignet ist um den Schmierzustand während des Einbringens eines Gewindes durch Gewindeformen zu charakterisieren. Als Proof of Concept wird der Online-Einsatz von AE in der Prozessüberwachung am Beispiel der Nanopartikelsynthese mittels Laserablation demonstriert.

Contents

List of Figures

List of Tables

Abbreviations

AE	Acoustic Emission
AIC	Akaike Information Criterion
AUC	Area Under Curve
BASt	Federal Highway Institute
BUE	Build Up Edge
BVID	Barely Visible Impact Damage
CBD	Cityblock Distance
CBM	Condition Based Maintenance
CFRP	Carbon Fiber-Reinforced Polymer
CHD	Chebyshev Distance
CM	Condition Monitoring
CWT	Continuous Wavelet Transform
DTW	Dynamic Time Warping
DWT	Discrete Wavelet Transform
ED	Euclidean Distance
EMD	Empirical Mode Decomposition
EMI	Electromagnetic Interference
FCM	Fuzzy C-Means
FFT	Fast Fourier Transform
FIR	Finite Impulse Response
FPGA	Field Programmable Gate Array
FZG	Forschungsstelle für Zahnräder und Getriebebau
GFRP	Glass Fiber-Reinforced Polymer
HHT	Hilbert-Huang Transform
KNN	K-Nearest Neighbors
LS	Load Stage
MAR	Measured Amplitude Ratio
MWF	Metal Working Fluid
NDT	Non-Destructive Testing
PCA	Principal Component Analysis
PL	Programmable Logic
PLAL	Pulsed Laser Ablation in Liquids
PLB	Pencil Lead Break
POD	Probability of Detection
PS	Processing System
PWAS	Piezoelectric Wafer Active Sensor
PZT	Lead Zirconate Titanate
QMF	Quadrature Mirror Filter
RBF	Radial Basis Function
RMS	Root Mean Square

ROC	Receiver Operator Curve
SHM	Structural Health Monitoring
SK	Spectral Kurtosis
SNR	Signal-to-Noise Ratio
SoC	System On Chip
SOM	Self Organizing Map
SPR	Statistical Pattern Recognition
STA/LTA	Short Term Average/Long Term Average
STFT	Short-Time Fourier Transform
SVM	Support Vector Machine
TCM	Tool Condition Monitoring
UV/VIS	Ultraviolet/Visible
WD	Working Distance
WPT	Wavelet Packet Transform

1 Introduction

Due to the complexity of modern industrial equipment and processes, reliable fault detection and diagnosis is difficult. Therefore, data-driven approaches, which do not require detailed a-priori knowledge, are of particular practical relevance [51]. Empirical models are derived from monitoring data using statistical methods or machine learning. For successful diagnosis, suitable signal processing and data interpretation is of key importance to obtain damage information.

In this context, Structural Health Monitoring (SHM) is one of the most active research fields. According to Farrar and Worden, SHM is defined as "the process of implementing a damage identification strategy for aerospace, civil and mechanical engineering infrastructure" [84]. Following the Statistical Pattern Recognition (SPR) paradigm [84], this process can be divided into four successive steps: (i) operational evaluation, (ii) data acquisition, normalization, and cleansing, (iii) feature extraction and information condensation, and (iv) statistical model development. It is important to note that SHM includes integration or permanent installation of sensors for continuous or periodic inspection and the development of advanced signal processing algorithms for automated data analysis [50].

An extensive review of SHM literature is provided by Sohn et al. [227]. Prominent applications, which are frequently mentioned in the current literature, are related to aerospace structures, civil infrastructure, wind turbines, and rotating machinery. Typically, intensive manual inspection is required in context of safety critical systems or high value assets. Therefore, automated inspection has potentially a strong economic impact. In aerospace applications, SHM systems are attractive because maintenance costs represent a high share of the total operating cost. In particular, health monitoring of composite materials was studied intensively because, despite good mechanical properties, their use is currently limited by a lack of ductility and different micro-mechanical damage mechanisms. Therefore, the use of SHM was suggested to reduce maintenance cost and to increase reliability and safety of aerospace structures [70]. Furthermore, many public infrastructure administrations are facing high investments due to the progressive aging of civil infrastructure. According to the condition score published by Federal Highway Institute (BASt), short-term or immediate repair of many highway bridges in Germany was necessary in 2018. The corresponding condition assessment is based on periodic visual inspection according to DIN 1076, which is time consuming, labor intensive, and expensive. Reliable SHM can help to reduce effort for inspection, schedule maintenance due to timely detection of damage, and to extend the service life [171]. In context of wind turbines [30, 161], high availability is necessary for wind energy to be competitive with conventional energy sources. However, both efficient energy harvesting and maintenance are not possible at all time due to environment conditions. Therefore optimal scheduling of maintenance actions is difficult. Moreover, diagnosis of rotating machinery, which is also referred to as Condition Monitoring (CM), comprises a wide range of applications such as bearings, gears, pumps, or engines. Historically, CM can be considered as an independent research field and is relatively mature [50].

Similarly, data-driven approaches for diagnosis are developed in context of manufactur-

ing and chemical industry. According to Stavropoulos et al. "monitoring and control of manufacturing processes is becoming nowadays a driver for development and sustainability of manufacturing industry" [231]. A review of Tool Condition Monitoring (TCM) to detect fracture and wear of the tool in cutting processes such as drilling or turning is given by Sick [225]. Furthermore, due to increasing complexity of chemical processes, detailed a-priori knowledge is limited and direct measurements may be difficult to obtain. Therefore, reliable detection of faults such as catalyst deactivation, valve blockage, or compressor failure, can be useful to improve productivity and safety in process plants [165]. Another closely related research field is Condition Based Maintenance (CBM), which is focused to the implementation of an efficient maintenance program based on the current state of a system using diagnostic information [118].

1.1 Motivation and research questions

The possibilities to integrate different technologies (i.e. sensors, data acquisition hardware, and software for data analysis and interpretation) for SHM are manifold. However, the choice of suitable equipment is dependent on several factors including the system or structure to be monitored, different damage types to be detected, environmental and operational factors, and implementation cost. Thus, according to the SPR paradigm, the development of SHM systems starts with operational evaluation, which includes the definition of relevant physical variables and the choice of suitable measurement equipment [84].

Acoustic Emission (AE) is a phenomenon, which can be observed in materials under load. High-frequency elastic waves emerge from local sources as stress is released, e.g. due to damage. In SHM, AE measurements can be used for passive, in-situ monitoring. In context of SHM, AE is attractive because high sensitivity to incipient damages can be achieved using suitable sensors and data analysis.

Recently, AE received significant attention for SHM in a wide range of applications. These include for instance diagnosis of composite material used e.g. in aerospace structures [69] and wind turbine blades [262], bearings [217], gear boxes [152], pipelines [192] and rails [107], and concrete structures [33]. Depending on the application, damages on a sub-millimeter scale can typically be detected. For instance, detection of a 0.3 mm leak in a pipeline with accuracy of 97 % was reported in [192] with sensors mounted in a distance of approximately 1 m from the leak location. In case of composite materials, fracture of individual fibers, which is a damage mechanism that extends on a micrometer scale, can be detected [19]. Also, diagnosis of large-scale gear boxes (e.g. wind turbines) is difficult using conventional vibration monitoring. Early detection of faults can be improved using AE [152]. Furthermore, different damages can be localized using e.g. time-of-flight measurements.

Advantages of AE were summarized as follows [98]. Auxiliary energy to interrogate a structure or system is not needed because AE can be detected passively. Due to propagation of the stress waves, damages in different locations can be detected without the use of scanning techniques. Hence, relatively few sensors, which are mounted in a fixed position, are usually sufficient. If the sensors can be placed at a suitable location, access to the whole system is not required and AE can be measured without disassembly of the structure or system. Therefore, SHM can be implemented in-situ using AE, i.e. during normal operation. Furthermore, monitoring of AE activity is particularly well suited for continuous monitoring.

Despite promising results, widespread industrial application of AE is currently limited. Subsequently, the main research questions, which are discussed in this thesis, are established. The current challenges in diagnosis and monitoring of bearings and gear boxes, composite materials, and process monitoring, which are addressed subsequently can be summarized as follows. Regarding the use of AE for diagnosis of bearings and gears, it has to be noted that the sensitivity of AE depends on the propagation path between source and sensor [226]. Therefore, suitable placement of sensors is crucial. Most frequently, sensors were mounted on moving parts of bearings or gear boxes to achieve highest sensitivity. However, it was also mentioned that such a strategy may not be a suitable solution in practice [86]. Therefore, the question raises if there are alternative mounting strategies, which are suitable to simplify the application of AE in practice.

Furthermore, the attenuation of AE due to propagation is considered as major limiting factor [155]. As a solution, different approaches were suggested in literature [2, 155]. However, labor intensive and time consuming experiments are necessary, which may be prohibitive in some practical applications. Moreover, the dependence of AE attenuation on different operational and environmental factors could be relevant for diagnosis. Also, the performance evaluation of data-driven approaches is usually based on a test dataset, which provides an estimate of the performance on average, whereas the reliability of individual classification results is usually not considered. This leads to the question, how the reliability of an individual classification result depends on environmental and operational factors. Furthermore, characterizing the effect of variable operational and environmental conditions on AE signatures is a difficult topic.

Recently, the use of AE for monitoring and control of chemical engineering [62, 248, 271] and manufacturing processes [147, 154, 261] received attention in literature. It was suggested that control schemes, which use AE measurements to maintain efficient operation, may lead to improved productivity and optimal product quality [147, 248]. However, it remains as an open question how AE can be processed effectively to characterize the productivity or quality of a process. Furthermore, the choice of a hardware platform, which is suitable to implement AE monitoring such that control actions can be realized online, is an important element of AE-based process control.

1.2 Aims and scope

According to current research, there is a potentially high benefit associated with the use of AE to obtain in-situ measurements for SHM and process monitoring. However, despite promising results, challenges arise due to the specific requirements regarding automated data analysis and fast signal processing for online use of the analysis results. The aim of the present thesis is to address several key issues using new hardware solutions and data-driven approaches to advance towards the AE in SHM and process monitoring. The development of a complete AE-based SHM system is not within the scope. The objectives of this thesis can be summarized as follows:

- Exploration of new hardware solutions for fast processing of AE measurements
- Application of data-driven approaches to AE data analyses for SHM and process monitoring

- Discussion of the reliability of data-driven approaches in the light of variable operating and environment conditions as well as effects of wave propagation
- Demonstration of a proof of concept regarding the online use of an advanced AE signal processing algorithm for process control

1.3 Thesis outline

In this thesis, different contributions to AE-based SHM and process monitoring are presented. These are based on previously published journal papers [252, 254] and conference papers [255–258]. This thesis is structured as follows. In Chapter 1, the motivation for the use of AE in SHM and process monitoring is given and the main research questions, which are addressed in this thesis, are established. Furthermore, the aims and scope of this thesis are pointed out.

In Chapter 2, a summary of the relevant background is presented. This includes a general introduction to AE for SHM comprising a description of the AE phenomenon, related measurement technology, data analysis, and propagation of AE in solid materials. Furthermore, advanced signal processing and machine learning techniques are reviewed. Finally, the state-of-the-art in different applications (bearings and gear boxes, composite material, and process monitoring) is presented.

Chapter 3 covers the development of an AE measurement system. A low-cost System On Chip (SoC) is chosen as a hardware platform. It comprises a dual-core ARM architecture running a Linux operating system and Field Programmable Gate Array (FPGA) fabric, thus allowing software and hardware programmability. Due to small form factor and low power consumption, this device is well suited for field deployment. For fast processing of AE measurements, an FPGA-based implementation of the Discrete Wavelet Transform (DWT) is realized.

Chapter 4 is devoted to new results regarding AE for fault detection. This includes a method-oriented but practical methodology to detect AE waveforms. Using a data-driven approach to estimate signal probability, a parametric model is established based on preliminary measurements. Thus, a suitable detection threshold can be defined implicitly and is adjusted automatically according to the provided data. Furthermore, an experimental study regarding AE-based diagnosis using sensors mounted outside the housing is presented. Damage related signatures of different wear states are identified. Regarding the classification of AE, different shape-based similarity measures are compared using hierarchical clustering. The key idea is to distinguish between different source mechanisms by evaluating the similarity of local patterns in the AE waveform data. Additionally, the effect of different loading conditions on the reliability of data-driven classification is investigated. A Support Vector Machine (SVM)-based classification scheme for different damage mechanisms in composite material using frequency domain features is chosen as an example. Finally, the effect of signal attenuation on AE measurements due to wave propagation is investigated.

In Chapter 5, the focus is placed on the use of AE in context of process monitoring. First, an experimental study regarding the relationship between AE and wear at the example of thread forming is presented. In particular, interaction of tool and workpiece surfaces, which are in lubricated sliding friction contact, is considered. Based on AE signatures, different Metal Working Fluid (MWF) are distinguished using a clustering technique. Moreover,

AE measurements are used to characterize the productivity of Pulsed Laser Ablation in Liquids (PLAL). This is a process for synthesis of nanoparticles from different materials using high energy laser pulses. To show the correlation between AE measurements and PLAL productivity, comparison to spectroscopic measurements is provided. Finally, AE is used for automated adjustment of the working distance, which is a critical parameter for PLAL productivity.

Finally, this thesis is summarized in Chapter 6 and outlook on future work is given.

2 Background and literature review

Subsequently, the relevant theoretical background and state-of-the-art are presented. This chapter is structured as follows. First, an introduction to AE is given by summarizing different source mechanisms, which give rise to the AE phenomenon, and presenting the related measurement technology as well as data analysis techniques. Furthermore, the topic of wave propagation is addressed briefly. Subsequently, advanced signal processing techniques, which are used in context of AE-based SHM, are explained. Hereafter, different machine learning techniques, which are used for pattern recognition in this work, are described. Finally, a summary of the state-of-the-art of AE monitoring in different applications is presented.

2.1 Introduction to Acoustic Emission

The use of AE for damage detection emerged as a passive, in-situ inspection technique. The working principle of AE is illustrated in Figure 2.1. Using highly sensitive sensors, small surface displacements caused by ultrasound stress waves, which are related to the release of elastic energy in a material under load due to damage, can be recorded passively. In general, different source mechanisms can be distinguished using suitable data analysis and interpretation. For SHM, AE measurements are of particular practical relevance because it enables the detection, localization [180], and classification [164] of local damage. Similarly, AE can be used for monitoring and control of manufacturing processes [231].

Advantages of AE measurements for SHM include the ability to monitor large structures due to propagation of AE, in-situ detection of damage, and high sensitivity [220]. However, it has to be noted that in contrast to other methods e.g. acousto-ultroasonics, only active source mechanisms can be detected. Furthermore, detectability of AE depends on the source mechanism itself and can not be enhanced because the related stress waves are recorded passively [220].

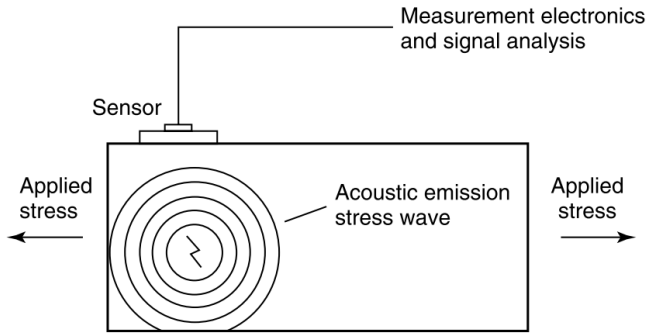

Figure 2.1: Working principle of AE [249].

2.1.1 Acoustic Emission phenomenon

According to standard terminology for nondestructive evaluations defined by ASTM International (E1316), AE denotes "the class of phenomena whereby transient elastic waves are generated by the rapid release of energy from localized sources within a material, ..." [15]. In general, AE source mechanisms are manifold. A summary of different source mechanisms by process type is presented in Table 2.1. Depending on the source mechanism, elastic waves in a frequency range between 10 kHz and 1 MHz are observed.

Table 2.1: Summary of AE source events organized by process [220].

Materials degradation	Defect growth, Crack advance, Plastic deformation, Inclusion or precipitate fracture, Surface degradation
Reversible Process	Crystallographic phase-transformation, Melting or solidification, Thermoelastic effects, Ferromagnetic and ferroelectric domain wall motion, Friction between surfaces
Fabrication process	Welding noise, Rolling, Forging, Machining, Drilling, Mixing, Grinding, Valve sequencing
Leak and flow	Flow of single- and two phase fluids and particles, Leaks, Gas evolution, Boiling

Furthermore, the terms burst and continuous emission are frequently used to characterize signals obtained from AE measurements qualitatively [15]. A burst signal denotes a wave packet of short duration that is localized at fixed points in time and, hence, can be associated to a discrete event. In contrast, continuous emission describes the case that multiple AE events cannot be distinguished. For instance, continuous emission is typically observed in AE recordings that were acquired during grinding processes [220]. Examples of burst and continuous AE signals are presented in Figure 2.2.

Typical damage related AE sources, which can be observed in metallic materials, are e.g. crack advance or plastic deformation. However, it has to be noted that possible AE source mechanisms are not limited to damage. For instance, crystallographic phase-transformations, such as martensitic transformation in metallic material [220], or – in case of ferromagnetic materials – the growth of magnetic domains might generate AE events as well. In particular, the Pencil Lead Break (PLB) test – also known as Hsu-Nielsen source – is widely accepted for testing purposes of AE equipment. A burst type signal that can be easily detected by AE sensors is generated by breaking a pencil lead at the surface of a specimen. Using PLB, fairly reproducible AE can be generated. However, there are different sources of variability such as free lead length and lead angle [209]. Furthermore, in an industrial environment there are typically many AE sources, which are not necessarily related to the mechanism of interest. For example, AE events are likely to originate from hydraulic actuators due to valve noise, turbulent flow, and cavitation [193].

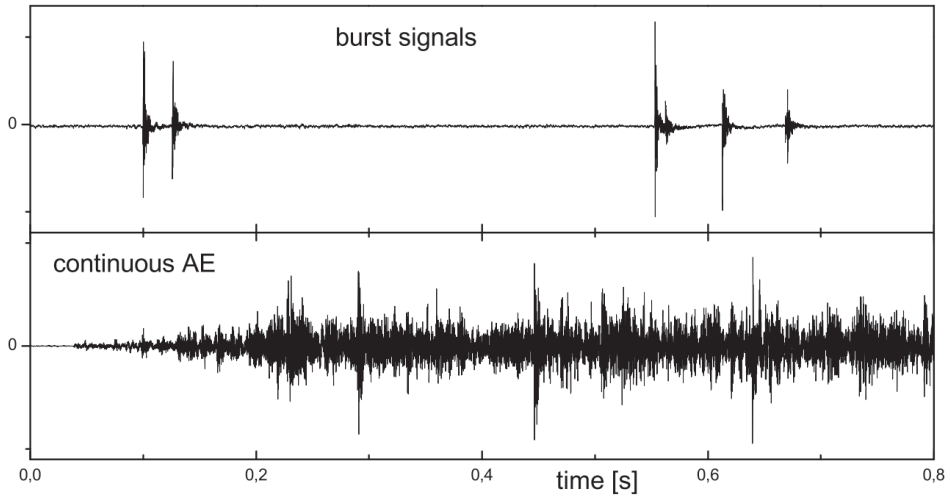

Figure 2.2: Example of burst type and continuous AE [98].

2.1.2 Acoustic Emission data analysis

Using suitable data analysis and interpretation, AE measurements can be related to different source mechanisms. According to Gutkin et al. [99] there are three different approaches: Characterization of to AE signals based on (i) a single parameter or (ii) using multiple parameters in conjunction with pattern recognition methods, and (iii) the characterization of AE based on modal analysis of the signal. The AE parameters are heuristically defined and can be extracted in time or frequency domain. Typical visualizations of AE data include time history plots, statistical distribution plots, and scatter plots [249]. However, while parameter extraction significantly simplifies storage and analyses of AE data, it can be expected that crucial information is not accessible after this data reduction process. In contrast, modal analysis of AE requires the continuous acquisition of the waveform data. Depending on the material and the geometry of the structure, different fundamental modes can be identified and used for interpretation of AE. Today, modern AE systems allow the continuous acquisition of AE waveform data (i.e. streaming mode) for continuous monitoring with high sample rates. However, due to the complexity of AE data, interpretation for diagnosis is difficult. Therefore, new approaches including advanced signal processing, such as time-frequency transformation and machine learning were suggested in literature, which are summarized in Sections 2.2 and 2.3.

Time domain

The classical approach to AE data analysis is realized in time domain. To separate individual AE bursts from background noise, the AE signal is compared to a threshold, which can be fixed or floating. Amplitudes below this threshold are neglected and amplitudes exceeding the threshold indicate AE activity. Typically, data acquisition of an AE system is triggered according to a predefined threshold. Furthermore, several parameters can be extracted to characterize a burst signal. In Figure 2.3, an annotated example of an AE burst is illustrated showing typical AE parameters.

According to ASTM E1316 [15], standard terminology for AE parameters is defined as

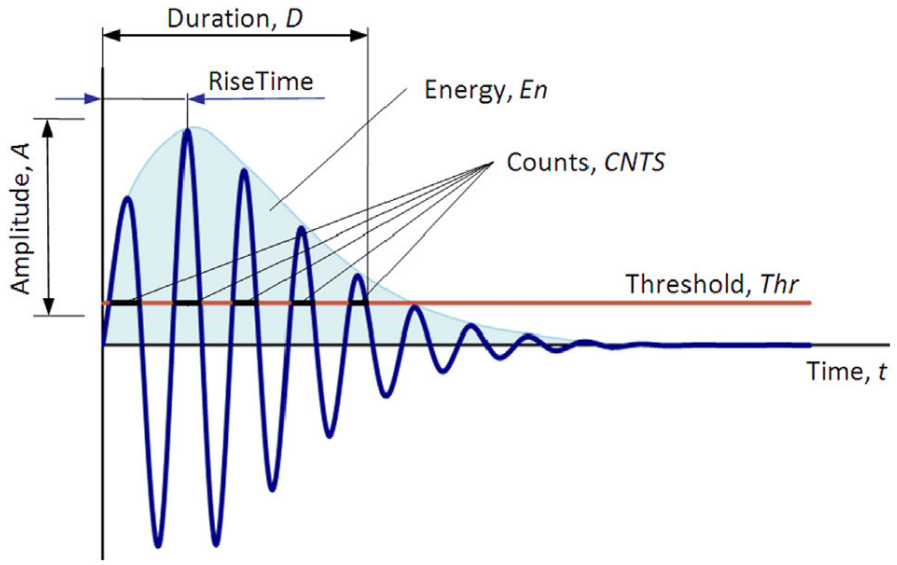

Figure 2.3: Illustration of parametric AE analyses [208].

- Amplitude—the peak voltage of the largest excursion attained by the signal waveform from an emission event,
- Duration—the time between AE signal start and AE signal end,
- Energy—the energy contained in a detected acoustic emission burst signal, with units usually reported in Joules and values which can be expressed in logarithmic form (dB, decibels),
- Rise time—the time between AE signal start and the peak amplitude of that AE signal, and
- Count—the number of times the AE signal exceeds a preset threshold during any selected portion of a test.

In practice, different definitions of AE energy are used. In Figure 2.3, energy En is indicated as measured area under the rectified signal envelope, which can be calculated as described in [125]

$$En = \sum_{t} |H(s(t))|, \tag{2.1}$$

where H is the envelope of the AE signal $s(t)$.

Using a set of different parameters, AE signatures can be established, which can be used to distinguish between different source mechanisms. Due to complexity of the related AE signatures, multivariate statistical analysis [19, 158] and pattern recognition [54, 102, 210] for AE source characterization were used in literature. However, the use of classical AE parameters is limited due to propagation related effects on AE waveforms.

Frequency domain

Besides parametric AE analysis, the frequency content can be used as a feature for damage characterization [19,43,68,99]. The frequency spectrum of an AE burst can be obtained e.g. using Fast Fourier Transform (FFT). According to Ni and Iwamoto [173] peak frequencies remain unchanged despite propagation. Therefore, features which are obtained in frequency domain are typically less sensitive to the propagation path. Similar to the time domain-based approach, different parameters can be used to characterize the spectrum of an AE burst. According to Grosse and Ohtsu [98], these are defined as

- Peak frequency—point in the power spectrum at which the peak magnitude is observed, and
- Frequency centroid—weighted average of frequency, as calculated in [155]

$$\frac{\sum_f A(f) \cdot f}{\sum_f A(f)}. \tag{2.2}$$

Modal analysis of AE

Besides heuristic approaches to AE data analysis, physical interpretation of AE waveforms was suggested. The use of modal AE analysis is specifically targeted at AE that propagates in thin structures. Typically, elastic waves propagate as guided waves in thin structures such as plates. However, according to Prosser [189], this concept can be extended to bulk wave propagation. The underlying idea is to exploit physical knowledge about wave propagation for comprehensive analysis of waveform data. In the frequency regime of interest, two distinct wave modes – flexural and extensional waves – exist, as explained in Section 2.1.4. The extensional wave mode is observed at higher frequencies and propagates at a higher velocity compared to flexural waves [189]. Therefore, the extensional mode is typically detected before the flexural mode. Examples of extensional and flexural wave modes are depicted in Figure 2.4.

Differences in AE waveforms are generally observed due to in-plane and out-of-plane source motion promoting either extensional or flexural wave mode, respectively [189]. Therefore, the goal of modal AE analyses is to establish a relationship between modal content of AE signals and different source mechanisms. For instance, several authors reported that in-plane motion may be associated with fiber breakage [43, 59, 68] or matrix crack [68, 164] in composite materials. These damage mechanisms promote high frequency extensional waves. In contrast, delamination is governed by out-of-plane motion and thus promotes the flexural waves in the material generating low-frequency signals [43, 59, 68, 164]. Surgeon et al. [232] demonstrated how the two plate modes can be detected and used to distinguish between different damage mechanisms. Furthermore, two examples of modal AE analysis were presented by Prosser [189] showing the application to the detection of matrix crack initiation in coupon specimens and delamination detection in rocket motor case rings.

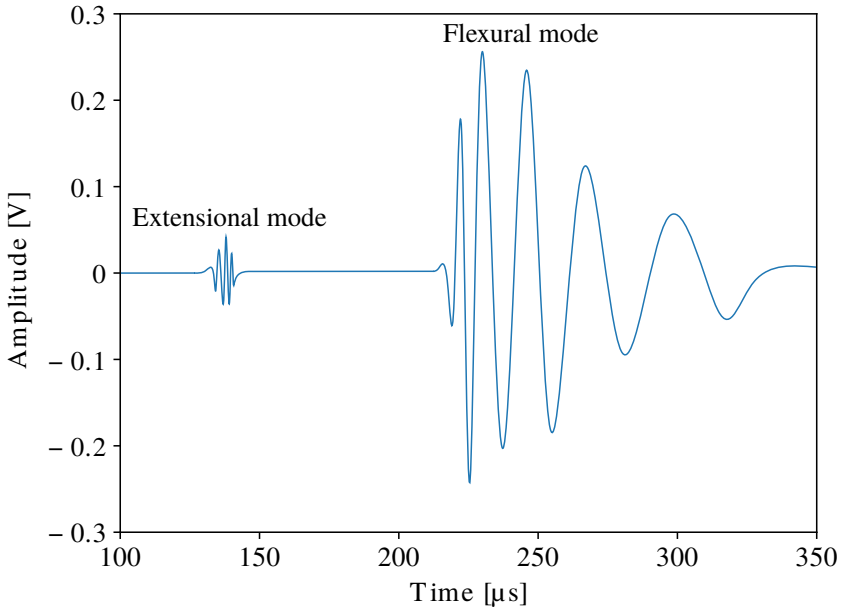

Figure 2.4: Illustration of flexural and extensional wave mode, adapted from [189].

2.1.3 Measurement technology

To record AE, small surface displacements need to be detected. Signals obtained from AE measurements are typically characterized by high frequency content and low amplitudes. Therefore, high sensitivity of the measuring system is required. Furthermore, high acquisition rates and adequate memory for data storage are crucial [189]. For instance, Al-Jumaili et al. [7] used a sample rate of 5 MHz for AE monitoring. Within the following sections, different AE sensing principles, sensor mounting procedures, and amplification and filtering are discussed. The topic of wave propagation is addressed in more detail in Section 2.1.4

Sensor technology

In literature, different sensing principles were suggested, which can be used for AE measurements. Besides piezoelectric sensing, these include the use of non-contact, laser-based techniques, fiber-optical sensors, and capacitive sensors. For instance, Ozevin et al. [178] suggested micro-electrical-mechanical sensors, because multiple resonant sensors can be integrated on a single chip providing high sensitivity at all frequencies of interest. Liang et al. [144] proposed fiber-optical AE sensors because they are not subject to chemical corrosion and insensitive to Electromagnetic Interference (EMI). Polymer-based, capacitive micromachined ultrasonic transducers for AE measurements, which can be produced lower cost compared to silicon-based transducers, were described by Hutchins et al. [116].

Today, piezoelectric transducers are most widely used. Due to electromechanical coupling of piezoelectric transducer and specimen, the mechanical stress waves are converted into an electrical signal using the well-known forward piezoelectric effect. Typically Lead Zirconate Titanate (PZT) is used as active material. Advantages include high sensitivity, ease of use,

and low cost [220]. In principle, two different types of piezoelectric AE sensors can be distinguished: broad-band and resonant sensors. Usually, higher sensitivity can be achieved using resonant sensors if the bandwidth of the AE signal is small compared to noise [220]. However, broad-band transducers are required for the purpose of waveform analysis [220], which are therefore widely used in scientific applications. Furthermore, Piezoelectric Wafer Active Sensor (PWAS), which are small, lightweight piezoelectric transducers, can be used instead of conventional AE sensors. Typically, PWAS are permanently bonded to the specimen and can be used in active and passive mode to excite and receive ultrasound stress waves. For instance, disc-shaped PWAS are frequently used in guided wave-based SHM to excite and receive different Lamb wave modes [265]. Recently, an overview of advances in using PWAS for SHM was presented by Mei et al. [166].

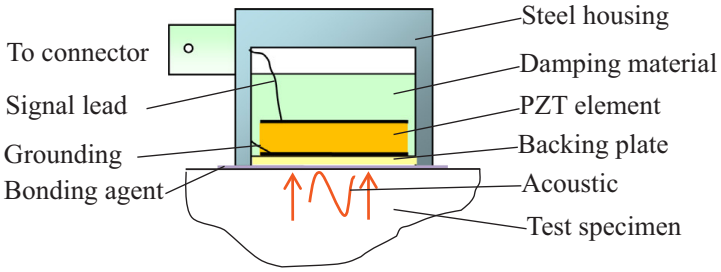

(a) Schematic cross section of conventional AE sensor [37].

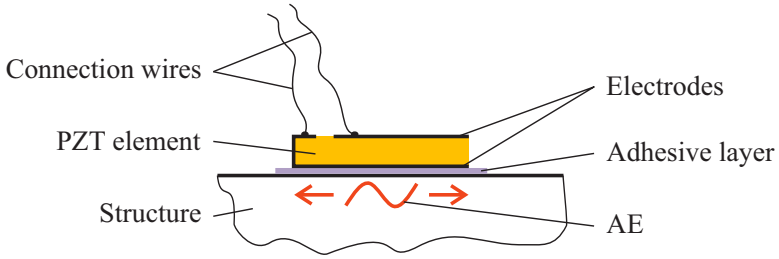

(b) Schematic cross section of PWAS.

Figure 2.5: Illustration of conventional AE sensor and PWAS mounted on a structure.

In Figure 2.5, the cross sections of a conventional AE sensor and PWAS, which are mounted to a structure, are illustrated. In case of conventional AE sensors, the active piezoelectric element is packaged inside a steel housing between a backing plate for protection and damping material. These sensors are usually mounted temporarily using e.g. wax or grease. However, it is well known that the frequency response has typically several resonances and waveform conversion of this complex dynamical system is difficult to understand. A numerical study of the conversion characteristics of different AE sensors is presented by Zhang et al. [267]. Different design parameters of the sensor including the active element and backing material are considered explicitly. However, larger errors in case of packaged sensors indicate that the measured waveforms are highly sensitive to the specific sensor design. The PWAS comprises a PZT element with electrodes at the surface to realize electrical connection. Therefore, resonances of PWAS depend only on the geometry of the PZT element. Usually, PWAS are permanently bonded to a structure using a suitable adhesive and connection wires are

soldered to the electrodes.

Bhuiyan et al. [37] compared measurement results using commercially available AE sensors to disc-shaped PWAS. Conventional AE sensors are mainly sensitive to the out-of-plane motion of the specimen surface [37]. In contrast to commercial AE sensors, PWAS are sensitive to out-of-plane and in-plane source motion [37]. Good agreement of the hit-based analysis is observed using each of the sensors. However, comparison of waveform data reveals notable differences in time and frequency domain. According to the results, higher sensitivity can be achieved at high frequencies using PWAS. However, while these sensors are widely used for research, industrial applications are rare. The reliability of PWAS is identified as an important topic and effects of different damages to PWAS on sensitivity or the generated wave field are addressed by Müller and Fritzen [169].

Sensor mounting

Using surface mounted AE sensors, which is usually the case for AE measurements, suitable coupling between the sensor and specimen surface is crucial. The transmission of acoustic energy and, hence, Signal-to-Noise Ratio (SNR) ratio may be improved by choosing a suitable couplant [85]. Standard procedures for mounting piezoelectric AE sensors are defined by ASTM International (E650) [16]. According to [16], the mounting methods (i) compression mount and (ii) bonding are distinguished. For compression mounts, the use of a coupling medium is advised to achieve optimal transmission of AE through the interface between sensor and structure. In case of bonding, an adhesive, which is suitable to attach sensors permanently to the structure and acts as a couplant, is used as bonding agent. Most frequently, either liquid couplants, gel, or grease are used in compression mounts. For permanent bonding, cyano-acrylic glue or epoxy adhesives are typically used in practice. However, the choice of the coupling medium has an effect on (i) the variability of the experimental results [85] and (ii) the response of the sensor to different wave modes [238].

The transmission behavior of different couplants was compared by Ono [175]. A face-to-face sensor/transducer arrangement was used. As couplants, liquids and gels (e.g. oil, silicone grease, and ultrasound gel) and a epoxy resin as adhesive for permanent bonding were considered. According to the experiments, transmission of epoxy is comparable to liquid couplants and is not affected by the curing process [175]. Furthermore it is important to note that an increase in couplant layer thickness has adverse effect on high frequency transmission [175]. Fasana and Gabribaldi [85] investigated the influence of different couplants on the variability of AE measurements. During their experiments, double sided adhesive tape, cyano-acrylic glue, wax, and grease were considered as couplants. It was confirmed by their experiments that – compared to dry coupling – increased reproducibility is achieved using each of these couplants [85]. Strong attenuation of the AE signal was observed using adhesive tape. Furthermore, it was pointed out that in contrast to grease, wax and cyano-acrylic glue provide bonding of the sensor to the structure so that no additional mounting fixture is required [85]. However, besides acoustic properties also the requirements resulting from the particular application, such as surface temperature of the structure or chemical compatibility, need to be considered when choosing a coupling medium. Furthermore, the effect of the couplant on the sensitivity of the sensor response was investigated by Theobald et al. [238]. Besides the acoustic impedance and acoustic absorption of the coupling medium, the layer thickness of the coupling reportedly has an effect on the performance of AE sensors. The best

sensitivity is achieved with minimum couplant thickness, especially at high frequencies [175].

Furthermore, it is important to note that the above mentioned publications focus on the transmission behavior for out-of-plane motion. However, AE is expected to comprise also in-plane motion in many applications, e.g. for detection of symmetric Lamb modes. Regarding the sensitivity to in-plane source motion, it was shown in [93] that a thin and stiff bonding layer is important for good transmission. Also, Theobald et al. [238] pointed out that high viscosity couplants or adhesives which provide stiff bonding between sensor and the structure improve the transmission of in-plane wave modes [238]. Therefore, it can be concluded that stiff coupling of AE sensors using a suitable adhesive is important to achieve high sensitivity to in-plane motion.

Filtering and acoustic emission detection

The challenge in AE measuring technology is to achieve high sensitivity of the measurement system while still providing low background noise levels. It is well known that AE equipment is highly sensitive to mechanical disturbances and EMI. For instance, background noise poses a severe problem to AE monitoring of wind turbine blades during operation reportedly leading to the detection of high AE activity in healthy wind turbine blades [218]. Also, Feng et al. [86] reported strong noise spikes, which made AE data analysis difficult. As most likely cause, EMI from a variable frequency drive and related control system, which was used during the experiments, was mentioned [86]. Furthermore, AE signals are only passively detected as they emerge from the material and the intensity cannot be increased to improve sensitivity [220]. Therefore, suitable filtering is of key importance for reliable AE data analysis.

In practice, pre-amplification and band-pass filtering of the signal are typically used. Low-pass filtering is employed to suppress electric noise whereas high-pass filtering is utilized to exclude low-frequency vibration from the mechanical domain [220]. For example, Loutas and Kostopoulos [150] reported bandpass filtering of 20 kHz – 1200 kHz. However, due to the broad-band character of AE, many conventional filtering methods are not applicable to reduce noise [220]. Furthermore, the accurate detection of AE, which is particularly important for fault localization, is difficult. The use of amplitude thresholding and additional timing parameters, which is widely used in practice, is of limited use in case of low SNR, variable noise levels due to different operating and environment conditions, or for the detection of overlapping AE events [183]. Therefore, advanced signal processing techniques are important for reliable and robust damage detection.

For improved analysis of AE, different approaches were suggested in literature, which include time-frequency domain transformations (e.g. using wavelet analysis) and machine learning. Pinal-Moctezuma et al. [183] compared different advanced methods for detection of AE in time domain. Based on the experimental results, Akaike Information Criterion (AIC) and Continuous Wavelet Transform (CWT)-based approaches provided the best performances for accurate detection of AE. Bai et al. [23] suggested alternative approaches for accurate detection of AE in time and time-frequency domain, which are independent of user-defined thresholds. These include time varying correlation method, which is based on surrogate significance test, CWT-based correlation, and a CWT-based binary map. Pomponi et al. [186] suggested wavelet block-thresholding for detection of AE and denoising of the signal. At the example of fatigue testing of welded joints, improved sensitivity was demon-

strated in comparison to conventional method [65]. Furthermore, Baccar and Söffker [19] suggested the use of CWT to characterize different AE sources in combination with a multivariate statistical approach to improve classification. Also, Hamdi et al. [102] suggested a pattern recognition approach using time-frequency transformation to identify different AE sources.

2.1.4 Wave propagation in solids

Guided waves are of particular importance in SHM, because structural elements in many applications can be considered as thin-walled structures (e.g. aircraft components, pipelines, pressure vessels, tanks). Subsequently, fundamentals of wave propagation are explained briefly with particular focus placed on Rayleigh and Lamb guided waves. From an analytical point of view, elastic wave propagation is well studied. For example, theoretical derivations of Rayleigh and Lamb wave propagation are presented in the work of Viktorov [244]. However, analytical solutions to the wave propagation problem are only valid under well-defined laboratory conditions. Most practical applications are significantly more complex (e.g. variable thickness, joints, multiple interfaces) so that analytical solutions are of limited practical use in context of AE. Therefore, detailed mathematical derivations are not given. Experimental techniques to address wave propagation are discussed. Finally, a brief overview of methods and tools for numerical simulation of wave propagation is presented at the end of this section.

Mechanical stress waves that propagate in elastic media carry energy in terms of particle motion, which can be described as a function of time and space. It is important to note that only certain types of elastic waves exist depending on the geometry of the medium. For instance, assuming an infinite medium, two fundamental wave modes namely longitudinal and transverse waves exist [94]. Additionally, different types of guided waves propagate in semi-infinite media such as half-space and plate. A summary of different elastic waves is presented in Table 2.2.

Table 2.2: Types of stress waves in elastic media [94].

Wave type	Particle motion, main assumption
Pressure (longitudinal; compressional; dilatational; P-; axial) waves	Parallel to the direction of wave propagation
Shear (transverse; distortional; S-) waves	Perpendicular to the direction of wave propagation
Flexural (bending) waves	Elliptical, plane sections remain plane
Rayleigh (surface acoustic) waves	Elliptical, amplitude decays quickly with depth
Lamb (guided plate) waves	Elliptical, free-surface conditions satisfied at the upper and lower plate surface

Besides interaction with interfaces, mechanical waves are subject to different propagation effects including attenuation and dispersion. However, the effects of wave propagation are usually not explicitly considered in context of AE. Nevertheless, propagation effects such as dispersion and attenuation remain a major challenge in AE data interpretation [2, 96].

For AE source localization using the time of arrival method, accurate knowledge of the wave speed is important. Furthermore, source-sensor distance is identified as major limiting factor for source characterization due to frequency-dependent energy attenuation [155].

Attenuation generally refers to a loss of amplitude due geometric spreading and energy dissipation. Amplitude attenuation can be described using attenuation coefficients. Asamene et al. [13] state the following relation between initial amplitude V_0 and signal amplitude V_m after propagation distance x

$$V_\mathrm{m} = \left(\frac{1}{\sqrt{x}}\right) V_0 \mathrm{e}^{-\alpha x} \tag{2.3}$$

of Lamb waves using attenuation coefficient α.

Dispersion describes the phenomenon of spatial divergence of a wave packet, which can be observed as it travels along the propagation path. In frequency domain, a single-frequency modulated burst can be represented by a spectrum with a main lobe and different side lobes [94]. In dispersive media, the wave packet travels at group velocity, whereas individual frequency components travel at different phase velocities depending on frequency. Therefore, the different propagation velocities lead to spatial separation of the frequency components. As a result, the wave packet is stretched increasingly with increasing distance from the source due to dispersion.

Rayleigh waves

Rayleigh waves describe a fundamental guided wave mode, which propagates at the free surface of a semi-finite medium, as illustrated in Figure 2.6. Therefore, Rayleigh waves propagate in heavy walled structures [176]. The amplitude of Rayleigh waves decreases rapidly with increasing distance from the surface [94]. The wave velocity of Rayleigh waves is proportional to the velocity of shear waves c_T and can be given as [244]

$$c_R = c_T \cdot \frac{0.87 + 1.12\nu}{1 + \nu}, \tag{2.4}$$

where ν denotes the Poisson's ratio.

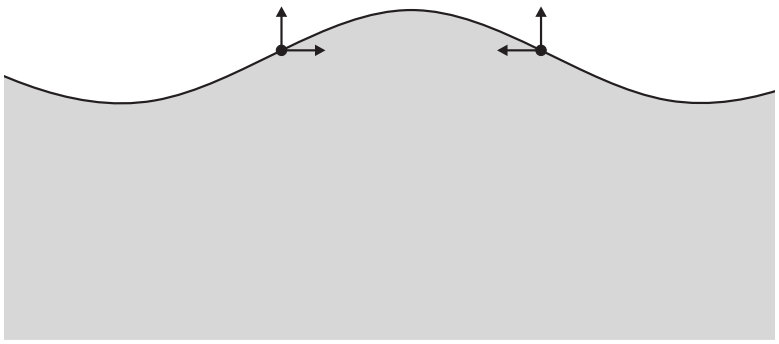

Figure 2.6: Visualization of Rayleigh wave particle motion.

In SHM, Rayleigh waves are particularly well suited for 2-D localization of AE sources

[220]. Regarding the use of Rayleigh waves in context of AE, Ono [176] calibrated different AE transducers using Rayleigh waves. Furthermore, the sensitivity of several AE sensors to different guided wave modes was compared. According to the results, sensitivity of AE sensors to Rayleigh waves is comparable to other guided wave modes [176]. Furthermore, it was mentioned that AE sensors with small aperture are more suitable for detection of Rayleigh waves [176].

Lamb waves

In thin plates, shear horizontal waves and Lamb waves exist. Lamb waves are frequently used in the field of active SHM for detection and localization of damage. As described by Giurgiutiu [94], two distinct modes of Lamb waves exist: the symmetrical and the anti-symmetrical mode, which are also referred to as extensional (S_0) and flexural mode (A_0), respectively. Fundamental S_0 and A_0 modes are illustrated in Figure 2.7. Additionally, higher order modes ($S_1, A_1, \ldots$) of these basic modes occur at increasing frequencies [94].

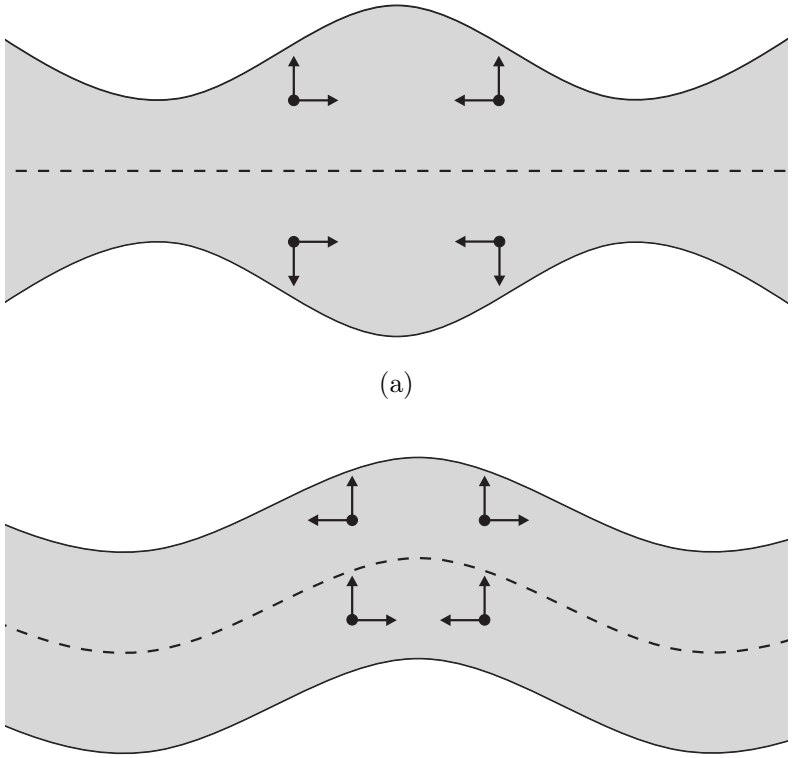

(a)

(b)

Figure 2.7: Visualization of Lamb wave particle motion: (a) extensional S_0 mode, (b) flexural A_0 mode, adapted from [137].

In contrast to Rayleigh waves, Lamb waves are dispersive, i.e. the phase and group velocities depend on the frequency and thickness of the plate [94]. Using classical plate theory, wave speeds c_L and c_F of longitudinal and flexural elastic waves in thin plates can

be obtained as described in [94]

$$c_L = \sqrt{\frac{E}{\rho(1-\nu^2)}} \quad \text{and} \tag{2.5}$$

$$c_F = \sqrt[4]{\frac{Eh^2}{12\rho(1-\nu^2)}}\sqrt{w}\,, \tag{2.6}$$

with Young's modulus (modulus of elasticity) E, mass density ρ, Poisson's ratio ν, plate thickness h, and angular frequency w. However, the analytical solution of c_L and c_F are only valid for low frequencies. At high frequencies, the phase and group velocities of Lamb waves can be obtained from dispersion curves. A database with dispersion characteristics of different composite laminates is provided by the Laboratory for Active Materials and Smart Structures, University of South Carolina. As an example, phase and group velocities of the fundamental Lamb wave modes for a cross-ply composite plate can be obtained at [138], which are shown in Figure 2.8.

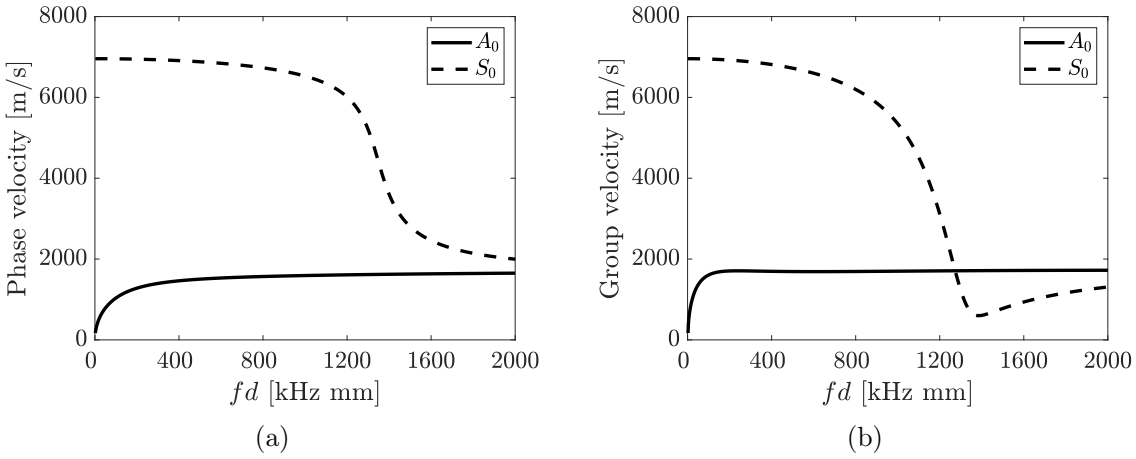

Figure 2.8: Dispersion curves showing group velocity and phase velocity of A_0 and S_0 modes of cross-ply CFRP material $[0/90/0/90]_s$ [138].

To address the challenges resulting from variable propagation paths experimentally, different mapping techniques have been proposed in literature. For source localization using the time of arrival method, accurate knowledge of the wave speed is required. However, in complex geometries and isotropic materials (e.g. composites) variable wave speeds lead to significant errors in source locations. An experimental approach to account for variable wave speed in source localization is referred to as delta-T mapping [29]. The error due to variable wave speed is compensated based on calibration of time differences between defined locations using artificial AE sources. Kundu et al. suggest an iterative optimization procedure to improve predicted source location [134]. Al Jumaili et al. [7] suggest parameter correction technique for classical AE parameters including amplitude, duration, count and energy. An empirical relation between source amplitudes and propagation paths is established by applying artificial sources. Different source locations are referenced on a grid within a defined area of interest. Based on the experimental results, a contour map can be

rendered for the structure, which relates measured parameter values to the source amplitude in different source locations. After the contour map is established, corrected parameters of a measured AE signal can be obtained. First, location of the source is determined. Then, the corrected source amplitude can be obtained from correction map using interpolation. The experimental results indicate that the corrected AE parameters lead to improved clustering of different source mechanisms. Similarly, Sause et al. [211] consider Probability of Detection (POD) as a function of propagation path. A reference dataset with known source locations is recorded. Using measurements from multiple sensors, a attenuation map is established. Under the assumption that POD is mainly affected by amplitude attenuation, the POD can be predicted for different source locations based on the attenuation map.

2.2 Advanced signal processing and filtering

Many advanced signal processing techniques are suggested to enhance AE measurements. In particular, the choice of a suitable data representation is important for interpretation of AE [230]. Empirical evidence in the field of machine learning supports the hypothesis that rich representations achieved by time-frequency transformation may be advantageous for classification of non-stationary signals [41]. Furthermore, alternatives to signal thresholds are explored by different researchers for reliable detection of AE waveforms. In the sequel, different methods for time-frequency domain analysis for AE signal classification and AIC for waveform picking are presented.

2.2.1 Time-frequency domain analysis

In general, AE measurements can be considered as non-stationary signals, which are composed of many signal bursts that are randomly distributed in time. Time-frequency transformations provide the mathematical foundation to represent non-stationary signals over both time and frequency simultaneously. Most commonly used time-frequency transformations are Short-Time Fourier Transform (STFT), wavelet transform, and Hilbert-Huang Transform (HHT). Regarding wavelet transform, CWT and DWT can be distinguished. Hamdi et al. [102] propose the use of HHT for AE-based damage classification because of (i) improved identification of frequency transitions and (ii) increased resolution in connection with the decomposition of non-stationary signals. According to [102], the comparison of the HHT to CWT and STFT yields that STFT is inferior due to the fixed time-frequency resolution. Both HHT and CWT suffer from information loss due to edge effects. The HHT lacks precision for instantaneous changes at high frequencies. The CWT is more flexible due to user-definable parameters. In general STFT and CWT are potentially suitable for real-time use. The implementation of HHT for real-time use is difficult due to high computational complexity [102, 269].

Short-Time Fourier Transform

The Fourier transform is a well known approach to calculate the frequency spectrum of stationary signals. The key idea is that any periodic signal can be represented as a superposition of sinusoids with different frequencies. However, the underlying stationarity assumption does typically not hold for experimental data. Therefore, STFT is frequently used in practice to

analyze non-stationary signals in time-frequency domain. Using a sliding window, multiple local Fourier spectra are calculated consecutively as the window moves along the time axis. The STFT of a signal $x(t)$ in time domain can be defined as [90]

$$X(\tau, \omega) = \int_{-\infty}^{\infty} x(t) g(t - \tau) e^{-jwt} dt. \tag{2.7}$$

The window function $g(t - \tau)$ is used to obtain the local Fourier spectrum at time τ. From the sequence of all local spectra $X(\tau, w)$ the spectrogram is composed. This idea was initially introduced using Gaussian function as window function. However, various window functions were proposed, such as Tukey, Hamming, or Blackman window [167]. For real-time use, the STFT algorithm can be implemented in FPGA logic [20].

However, for a given window size, the time and frequency resolution of the STFT is fixed as illustrated in Figure 2.9a. Furthermore, the time and frequency resolution of STFT is limited. The lower bound of time and frequency resolution can be given as [167]

$$\Delta\tau \cdot \Delta w \geq \frac{1}{2}, \tag{2.8}$$

where $\Delta\tau$ and Δw denote time- and frequency resolution, respectively. Therefore, the suitable window size is a trade-off between time and frequency resolution.

Wavelet transform

The wavelet transform is a time-frequency domain transformation, which can be used for non-stationary signals. The underlying concept is the representation of the original signal by a family of functions, which is derived from a base wavelet ψ by means of scaling and time shift. Commonly used wavelets are for instance Mexican-Hat wavelet, Morlet wavelet, Gaussian wavelet, Frequency-B-Spline wavelet, Shannon wavelet, and Harmonic wavelet.

For a continuous-time signal $x(t)$ the CWT can be defined as [90]

$$\mathcal{W}(s, \tau) = \frac{1}{\sqrt{s}} \int_{-\infty}^{\infty} x(t) \psi^*(\frac{t - \tau}{s}) dt, \tag{2.9}$$

where ψ^* denotes the conjugate complex of the base wavelet. The result of wavelet transformation is the scalogram, which is a time-scale representation of the original signal. In contrast to Fourier analysis, the base wavelet is localized in time and frequency. Therefore, the time-frequency resolution depends on the particular scale and – in contrast to fixed time-frequency resolution of STFT – is variable over the range of different frequencies.

The relationship of time-frequency resolution and scaling parameter s is illustrated in Figure 2.9b. Each point in the scalogram represents the original signal in terms of a scaled and shifted version of the base wavelet $\psi_{s,\tau}(t)$. On increasing scales, $x(t)$ is represented by dilated versions of the base wavelet. In general, lower frequencies correspond to increasing s. Improved frequency resolution and lower time resolution are obtained with increasing s.

In case of CWT, the range of possible values for s and τ is assumed as continuous. Therefore, highly detailed representation of the signal can be obtained, which leads to good interpretability. In contrast, wavelet coefficients are computed only for discrete values of s and τ

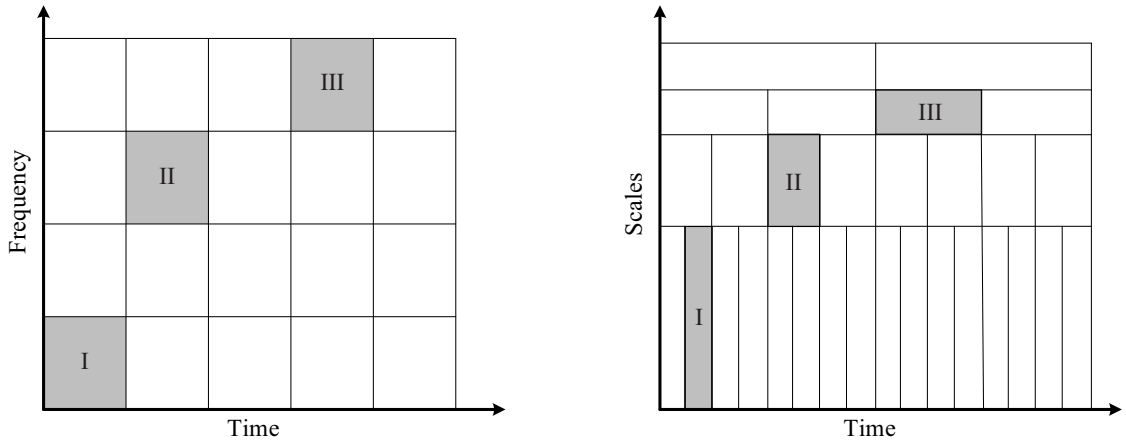

(a) Time-frequency resolution of STFT is fixed for a given window size.

(b) Time-frequency resolution of wavelet transform depends on scale.

Figure 2.9: Schematic illustration of time and frequency resolutions, adapted from [90].

using DWT. A logarithmic discretization scheme is typically used to avoid computation of redundant information [90]. Therefore, time complexity of DWT algorithm is substantially lower compared to CWT. This is of particular interest in context of real-time applications, where calculations are subject to time constraints. For instance, the minimum cycle time of 1 ms per 1024 samples at 32 scales was reported by Qassim et al. [190] using FPGA-based CWT implementation and Xilinx Spartan 3 computation core. Assuming a sample rate of 5 MHz, which is typical for AE measurements, this corresponds to measurement duration of approximately 0.2 ms. Implementation of DWT, which is suitable for real-time use, can be realized using cascaded multirate filter banks [22]. Each level of the decomposition is obtained by applying high- and lowpass filters. The output of the lowpass filter is used as input to the subsequent filter bank.

As a generalization of the DWT, the Wavelet Packet Transform (WPT) is obtained [111]. Similarly to DWT, the WPT can be implemented using multiple filter banks. In contrast to DWT, WPT decomposition can be implemented using the output of both high- and lowpass filter at each level. Hemmati et al. [111] described the use of WPT to extract signatures in AE signals from bearings. Bianchi et al. [38] suggested the use of WPT for detection of events in AE from tribological system.

2.2.2 Waveform picking

Besides suitable data representation, the identification of onset times of AE bursts is an important topic. Depending on SNR, large errors in time of arrival are obtained using simple threshold crossing. Therefore, different automatic picking algorithms are developed to improve time of arrival measurements. These include Short Term Average/Long Term Average (STA/LTA), wavelet thresholding [186], and surrogate significance test [23].

A well known and widely used alternative to threshold-based onset detection is derived from the AIC. The AIC originates from the field of system identification as a means for model

selection. The formulation of the AIC to calculate waveform onset times of seismic waves was initially given by Maeda in 1985. The application of an AIC picker to AE measurements is suggested in Kurz et al. [135] and good performance is achieved. The AIC function [135]

$$\mathrm{AIC}(i) = s_i \log(\mathrm{var}(S(1, s_i))) + (N - s_i - 1) \log(\mathrm{var}(S(s_i + 1, n))) \tag{2.10}$$

is calculated for each possible split point within a time window S around the approximate signal onset, which can be selected e.g. threshold-based. Under the assumption that the considered time window can be split into two sections containing either background noise or AE, the minimum of the AIC function is defined as optimal split point, which is considered as the signal onset. An example of AIC-based onset detection is presented in Figure 2.10.

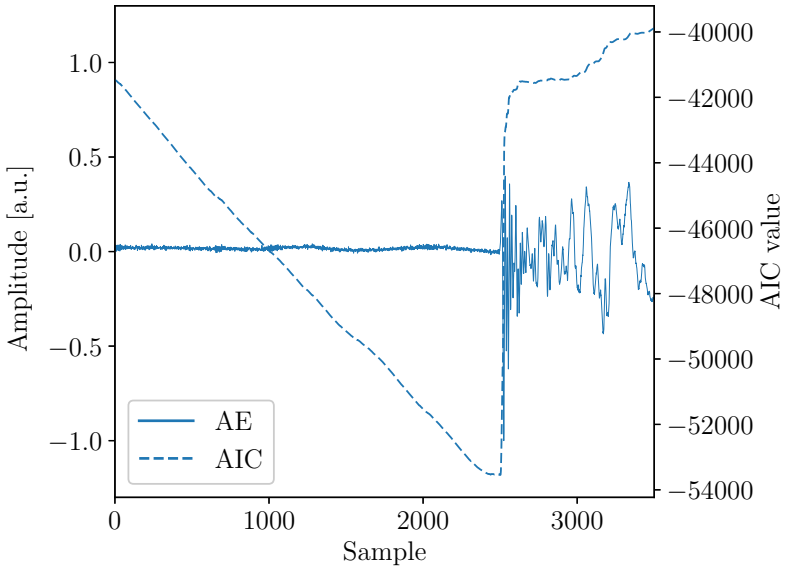

Figure 2.10: Example of AIC-based onset detection.

2.3 Machine learning for fault detection and diagnosis

In the last decade, machine learning has been ubiquitous in SHM literature for fault detection and diagnosis. For instance, Farrar et al. [84] defined the Statistical Pattern Recognition (SPR) paradigm, which provides the formal description of a four-step process to apply machine learning for SHM. Typical use cases of different data-driven approaches for SHM were illustrated in [260].

In general, the use of raw data is usually not suitable for machine learning and the extraction of sensitive features is crucial to apply machine learning approaches successfully [260]. Each data sample can be described by the feature vector $x = (x_1, x_3, \ldots, x_d)$, which can be interpreted geometrically as a point in a d-dimensional vector space $\mathcal{R}^d$. During exploratory data analysis, multi-dimensional plots of the feature space are useful for data visualization. Besides, many machine learning algorithms such as K-Nearest Neighbors (KNN) [133] or k-means algorithm rely on relative distances in the feature space. To improve the performance

of machine learning for high-dimensional feature spaces, dimensionality reduction techniques such as Principal Component Analysis (PCA) can be applied [49]. A summary of basic signal statistics such as mean, variance, or kurtosis, which are frequently used for vibration-based diagnosis was presented in [241]. In context of AE, the related hit parameters (e.g. [95]) as well as different frequency domain features such as peak frequencies or wavelet coefficients (e.g. [158]) can be used. However, the choice of a feature set is always application specific. Therefore, the identification of damage-sensitive features is considered as one of the key research topics in SHM literature [227].

Subsequently, machine learning methods that are relevant in context of this thesis are presented. This includes different supervised and unsupervised algorithms as well as the related evaluation schemes.

2.3.1 K-Nearest Neighbors classifier

The K-Nearest Neighbors (KNN) classifier is an instance-based supervised machine learning approach, which is well known for the simplicity of implementation. In principle, the classification approach is based on geometric interpretation of the feature space. Different distance measures, which can be used to define the relative distance between two samples a and b in the feature space $\mathcal{R}^d$ for KNN classification, are summarized in Table 2.3.

Table 2.3: Summary of distance measures, adapted from [133].

Measure	Mathematical definition
Euclidean distance	$d(a,b) = \left(\sum_{i=1}^{m} = \lvert a_i - b_i\rvert^2\right)^{\frac{1}{2}}$
Minkowsky distance	$d(a,b) = \left(\sum_{i=1}^{m} \lvert a_i - b_i\rvert^r\right)^{\frac{1}{r}}$
City block (Manhattan) distance	$d(a,b) = \sum_{i=1}^{m} \lvert a_i - b_i\rvert$
Chebychev distance	$d(a,b) = \max_{i=1}^{m} \lvert a_i - b_i\rvert$
Camberra distance	$d(a,b) = \sum_{i=1}^{m} \frac{\lvert a_i - b_i\rvert}{\lvert a_i + b_i\rvert}$

Given a set of training data, the relative distance between a test sample x and the training data is evaluated. Then, the k nearest neighbors of x are selected. Finally, a class label is assigned according to the majority class of the k nearest neighbors. Using Bayes theorem, the conditional probability of class C_i can be written as [39]

$$p(C_i|x) = \frac{p(x|C_i) \cdot p(C_i)}{p(x)} = \frac{k_i}{k}, \tag{2.11}$$

where k_i denotes the number of the k nearest neighbors that belong to C_i. Thus, $p(C_i|x) = 1$ if all k samples in the neighborhood of x belong to class i. According to Cover and Hart [58], the upper bound of error rate for 1-NN classification is determined as twice the Bayes error rate.

If data samples of the same class are located in close proximity to each other, high accuracy can be achieved. However, performance of KNN classifiers depends on the distance measure and appropriate choice of k. As an example, the classification results of KNN classification using different k are presented in Figure 2.11. It is notable that increasing k leads to homogeneous regions of the classification output compared to small values of k.

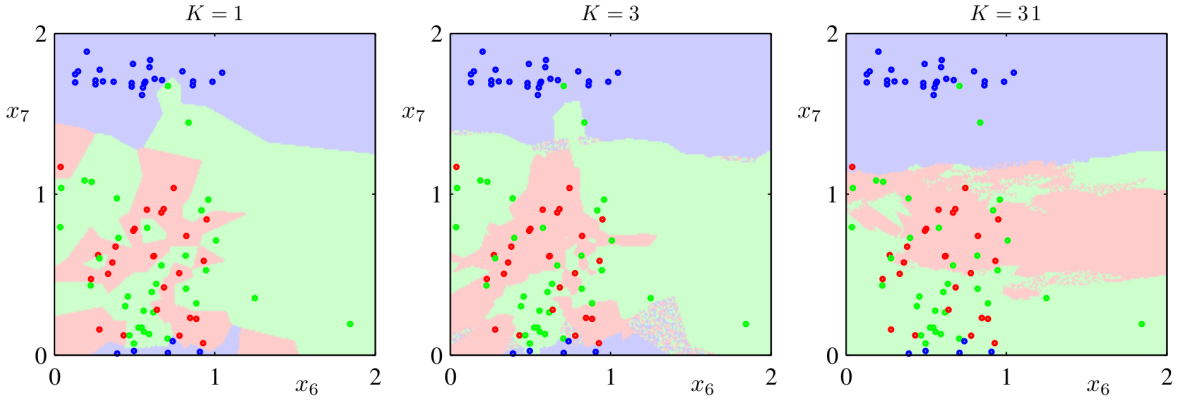

Figure 2.11: Illustration of KNN classification output depending on k [39].

From an application point of view it has to be stated that KNN does not scale well with increasing size of training data. Due to the lack of an internal data representation, the algorithm always operates on the whole training set, which leads to potentially long computational time during classification and large storage requirements [133]. However, KNN is considered as well suited to compare different feature sets. In particular, 1NN classifier is essentially parameter-free and therefore the performance depends only on the chosen feature set [247]. Despite the simplicity, exceptionally good performance is reported for nearest neighbor-based classification schemes [28].

2.3.2 Support Vector Machine

The Support Vector Machine (SVM) is a supervised machine learning algorithm, which can be used for classification and regression. Applications of SVM include fault diagnosis and process monitoring (e.g. [8, 207, 263]). A comprehensive summary of the fundamentals is given by Burges [47].

As illustrated in Figure 2.12, the key idea in SVM-based classification is to determine a hyperplane so that separation of the training data according to class labels is achieved. The corresponding decision function can be written as a plane equation using point-normal form $w \cdot x + b = 0$ [47]. Furthermore, support vectors (i.e. data points, which are located closest to the separating hyperplane) are of significant importance because they "contain all the information to design the classifier" [263]. As illustrated in Figure 2.12, the hyperplanes H_1 and H_2 are parallel to the separating hyperplane and pass through the support vectors [47]. The shortest distance between H_1 and H_2 is referred to as margin. During SVM training, the optimal separating hyperplane is determined by maximizing the margin.

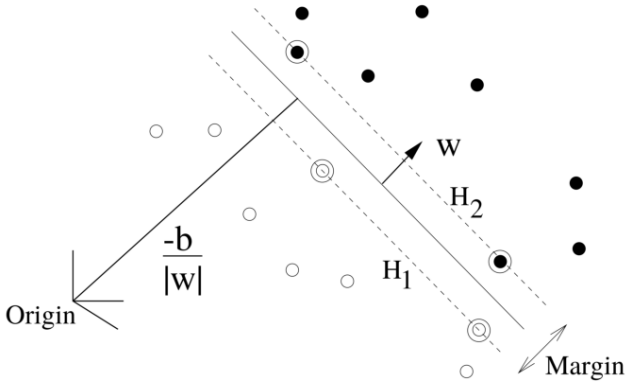

Figure 2.12: Illustration of feature space with separating hyper plane (support vectors are circled) [47].

The corresponding optimization problem can be written as [53]

$$\begin{aligned} \min_{w,b,\xi} \quad & \frac{1}{2} w^T w + C \sum_{i=1}^{l} \xi_i \\ \text{subject to} \quad & y_i \left(w^T \Phi(x_i) + b \right) \geq 1 - \xi_i,\ \xi_i \geq 0,\ i = 1, \ldots, l, \end{aligned} \tag{2.12}$$

with training dataset size l, regularization parameter C, slack variable ξ_i, which assigns additional cost to training errors [47], and function Φ that maps the feature vector x_i into a higher dimensional space. As a result, optimal values $w = w^*$ and $b = b^*$ are returned. Accordingly, unknown class labels of input data are computed according to the decision function [53]

$$\text{sgn} \left(w^{*T} \Phi(x) + b^* \right). \tag{2.13}$$

Instead of calculating the high-dimensional representation $\Phi(x)$ explicitly, a kernel function $K(x_i, x_j) \equiv \Phi(x_i)^T \Phi(x_j)$ is used to express the transformation implicitly. Any function K that satisfies mercers condition can be used as kernel function [47]. Many kernel functions are suggested in literature. The most frequently used kernel functions are listed below as [113]

- Linear: $K(x_i, x_j) = x_i^T x_j$
- Polynomial: $K(x_i, x_j) = (\gamma x_i^T x_j + r)^d,\ \gamma > 0$
- Radial Basis Function: $K(x_i, x_j) = \exp(-\gamma \|x_i - x_j\|^2), \gamma > 0$
- Sigmoid: $K(x_i, x_j) = \tanh(\gamma x_i^t x_j + r)$

From a practical point of view, Hsu et al. [113] give the advice to use a Radial Basis Function (RBF) kernel as a first choice due to numerical stability. In case of a large feature space the use of linear kernel is suggested.

2.3.3 K-means clustering

The k-means algorithms is an unsupervised machine learning algorithm which divides a dataset into k clusters, where k is a user-defined parameter. The following description of k-means clustering is based on Bishop et al. [39]. The idea is to divide the dataset into clusters so that the relative distance in the feature space $\mathcal{R}^d$ between all samples within a cluster and the respective cluster centroid is minimized, i.e. to find homogeneous groups within a dataset. Hence, the optimal clustering of a dataset with n samples $x_n \in \mathcal{R}^d$ can be defined as

$$\underset{r_{nk},\mu}{\arg\min}\ J = \sum_{i=1}^{k}\sum_{j=1}^{n} r_{ij}|x_j - \mu_i|^2, \tag{2.14}$$

with the cluster assignments r_{nk} using 1-of-k coding scheme and k cluster centroids μ, respectively. The cluster centers μ are initialized randomly at first. Then, the clustering is performed iteratively using a two-step procedure. First, class assignments r_{nk} for the given cluster centers μ are determined. Each sample x is assigned to one of the k clusters according to the minimal distance between μ and x as

$$r_{nk} = \begin{cases} 1 & \text{if } k = \underset{j}{\arg\min}\ |x_n - \mu_j| \\ 0 & \text{otherwise} \end{cases}. \tag{2.15}$$

Subsequently, the cluster centroids μ are updated using r_{nk} by calculating the mean of each cluster as

$$\mu_k = \frac{\sum_{i=1}^{n} r_{ik}\, x_n}{\sum_{i=1}^{n} r_{ik}}. \tag{2.16}$$

This procedure is repeated until convergence or maximum number of iterations is reached. The original formulation of the algorithm uses squared euclidean distance. However, different variations such as k-medoids or kernel k-means are proposed, which use different distance measures [117].

In literature, the k-means algorithm is used for clustering of AE data to identify damage mechanisms in composite material [202, 206, 270]. Furthermore, Diez et al. [71] suggest k-means clustering for SHM of bridges. Huang et al. [114] propose a framework for health monitoring of wind turbines using k-means clustering.

2.3.4 Hierarchical clustering

Hierarchical clustering algorithms can be used to determine clusters in a dataset unsupervised by the use of a hierarchical representation, i.e. a cluster tree, which is usually referred to as dendrogram. In general, agglomerative and divisive algorithms can be distinguished, which generate a hierarchical representation iteratively by either merging or splitting a dataset with k samples into $k-1$ clusters, respectively.

In agglomerative hierarchical clustering, the process of constructing the dendrogram is referred to as linkage. Prerequisite for linkage is the calculation of a distance matrix, which contains the pairwise distances between each sample in the dataset. In general, different linkage methods can be used. A summary is provided in [88]. Using single linkage, a link is established based on the minimum distance between any two samples in two different clusters [88]

$$d_s(C_a, C_b) = \min_{i \in C_a, j \in C_b} d(i, j). \tag{2.17}$$

In contrast, the maximum distance between any two samples in two clusters C_a, C_b

$$d_c(C_a, C_b) = \max_{i \in C_a, j \in C_b} d(i, j) \tag{2.18}$$

is considered in case of complete linkage.

An illustrative example showing the effect of different linkage methods is presented in Figure 2.13. It is notable that the dataset shown in Figure 2.13a can be split into two clusters as $C_1 = \{3, 4, 5\}$ and $C_2 = \{1, 2\}$. Using euclidean distance, the minimum distance of 5 between data points $\{1, 3\}$ and the maximum distance of 6.7 between data points $\{2, 5\}$ are obtained from the distance matrix. Therefore, the final link is placed at different heights in Figures 2.13b and Figure 2.13c, respectively.

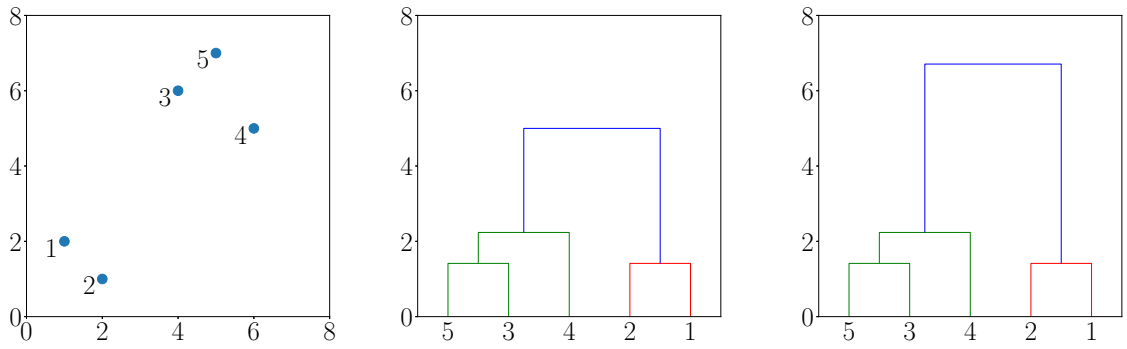

(a) Dataset. (b) Single linkage. (c) Complete linkage.

Figure 2.13: Example to illustrate the effect of different linkage.

Finally, clusters are obtained by cutting the dendrogram at suitable height. This can be a subjective decision. However, different tree cutting procedures exist to determine the optimal clusters with respect to certain criteria such as Calinski and Harabasz index, gap statistics, or dynamic tree cutting [221].

Zhou et al. [272] used hierarchical clustering and transmissibility estimates successfully to detect structural damage from the dynamic response of a 10-floor structure and free-free beam. Sevillano et al. [222] used hierarchical clustering and Electromagnetic Interference (EMI) method to detect debonding in a strengthened beam. According to the results, hierarchical clustering is not only suitable for unsupervised damage detection. It is also useful for visualization of complex datasets [222]. Furthermore, Saeedifar et al. [206] compared

different clustering algorithms to study the evolution of damage mechanisms in composites. Best performance with respect to repeatability is achieved with a hierarchical clustering approach [206].

2.3.5 Evaluation schemes

Performance evaluation is a key topic in machine learning. Different techniques can be used to assess the suitability of a model for a specific task or to compare different algorithms. Ultimately, the related performance measures can be used to drive the optimization of hyper parameters. However, depending on the learning approach (i.e. supervised or unsupervised) different methods are required. In the sequel, evaluation schemes for supervised and unsupervised machine learning and the related performance measures are presented.

Performance evaluation for supervised machine learning

The performance of a classifier can not be measured exactly because in general, the amount of available data is limited. Therefore, different empirical procedures are used to obtain an estimate of the performance. These include hold-out method as well as different resampling techniques such as cross validation. Using hold-out method, a dataset is split randomly into a training and a test set. Additionally, splitting the training set further into training and validation set is sometimes used for tuning the hyper parameters of a classifier [237].

However, quantifying the uncertainty of performance estimation is important to ensure robustness of the results. In general, hold-out methods are not suitable to obtain an estimate of the variance of performance [34]. Therefore, k-fold cross validation is typically used. The dataset is randomly split into k subsets and the classifier is trained k times. Each time the k-th fold is used as hold-out set. Leave-one-out cross validation denotes a special case, where each fold comprises only a single sample. Influencing factors on the estimate of the performance are (i) number of folds k, (ii) number of instances in a fold, (iii) the level of averaging, and (iv) repetitions of cross validation [259].

In the supervised case, the performance estimation involves always comparison of the classifier output with known class labels. Considering a binary classification problem, the output of a classifier is a label, which attributes the sample to one of two classes, i.e. positive class or negative class. The counts of correctly classified samples for each class are usually denoted as *true positive* (tp) and *true negative* (tn). Likewise, counts of incorrectly classified samples are denoted as *false positive* (fp) and *false negative* (fn) so that $tp+fp+tn+fn = |X|$. Subsequently, different methods that are widely used to assess the performance of a classifier are summarized. This includes confusion matrix, different performance measures, and Receiver Operator Curve (ROC)-based analysis.

Confusion matrix. The most direct way to illustrate the performance of a classifier is the confusion matrix. In a binary classification problem the confusion matrix is a 2×2 matrix showing the agreement of true labels and the classifier output in terms of frequency counts. Thus, elements on the main diagonal of the confusion matrix correspond to the count of correctly classified samples ($tp + tn$), whereas off-diagonal elements denote the count of classification errors ($fp + fn$). This concept can be readily extended to the problem of multi-class classification by defining the frequency counts of true and false classifications for

an individual class C_i as tp_i, tn_i, fp_i, fn_i. Examples of confusion matrices for the binary and multi-class cases are shown in Figure 2.14.

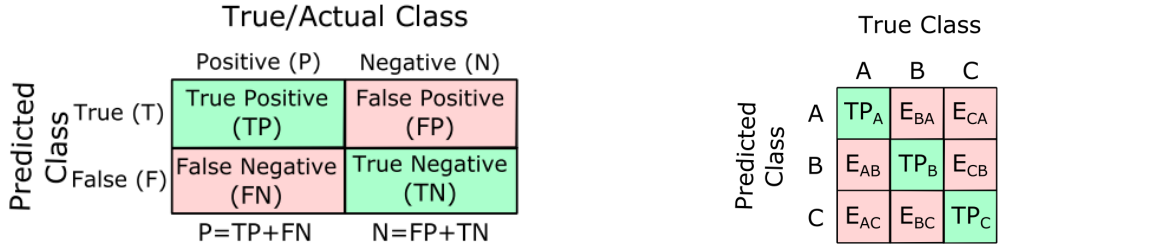

(a) Confusion matrix for binary problem.

(b) Confusion matrix for multi-class problem.

Figure 2.14: Illustration of confusion matrices [237].

Performance measures. Based on the confusion matrix different performance measures can be calculated, which are used to assess classification performance. A summary of performance measures that can be used to evaluate classifiers is given in Table 2.4. Most frequently, accuracy is reported, which denotes the fraction of correctly classified samples independent of their respective class and hence can be used to estimate the overall performance of a classifier. In contrast, recall and specificity, which denote the fraction of correctly classified positive and negative samples, provide a class-specific estimate of the performance. Recall provides as an estimate of detection rate. Specificity provides an estimate of true negative rate, which is the complement of false alarm rate. However, it is well known that improved detection rate can only be achieved at the cost of increased false alarm rate. This relationship is expressed by the ROC, which is discussed subsequently. Therefore, combined measures such as F score or Area Under Curve (AUC), which emphasize different types of classification errors are also used.

The performance measures for binary classification, which are presented in Table 2.4, can be extended to the multi-class case using two different averaging techniques [228]. Here, macro-averaging and micro-averaging have to be distinguished. Using macro-averaging, the performance estimate is calculated for each class individually and finally the performance estimate for the classifier is obtained as the mean of each intermediate result. In contrast, the tp, fp, tn, and fn counts are cumulated across multiple classes using micro-averaging. It has to be noted that the macro-averaging technique treats each class equal irrespective of the size, whereas large classes have a larger impact on the performance estimation using micro-averaging [228].

As discussed by Tharwat [237], the performance measures show different dependencies on class distribution. This is of particular importance in case of unbalanced datasets (i.e. datasets in which an individual class is significantly over- or underrepresented). Using a principled approach, Sokolova and Lapalme [228] define a total of eight invariance properties to assess the sensitivity of different performance measures to well-defined manipulations of the confusion matrix.

Receiver Operator Curve. In general, increased detection rate can only be achieved at the cost of increased false alarm rate. This general relationship between detection and false

Table 2.4: Summary of performance measures for binary classification [228].

Measure	Formula	Evaluation focus
Accuracy	$\frac{tp+tn}{tp+fn+fp+tn}$	Overall effectiveness of a classifier
Precision	$\frac{tp}{tp+fp}$	Class agreement of the data labels with the positive labels given by the classifier
Recall (Sensitivity)	$\frac{tp}{tp+fn}$	Effectiveness of a classifier to identify positive labels
F score[1]	$\frac{(\beta^2+1)tp}{(\beta^2+1)tp+\beta^2 fn+fp}$	Relations between true positive labels and those given by a classifier
Specificity	$\frac{tn}{fp+tn}$	How effectively a classifier identifies negative labels
AUC	$\frac{1}{2}\left(\frac{tp}{tp+fn}+\frac{tn}{tn+fp}\right)$	Ability of a classifier to avoid false classification

[1] β: weighting factor

alarm rate is expressed by ROC [156], which is obtained from plotting the detection rate (Sensitivity) against false alarm rate (1−Specificity). In Figure 2.15 an example of a ROC chart is given, showing the performance curves of several classifiers. Generally, high detection rate and low false alarm rate are considered as good performance. Accordingly, the optimal classifier is located at the point $(1, 1)$ in the ROC chart [156]. Comparing the classifiers A – D according to the corresponding ROC curves, classifier A performs best yielding highest detection rate with respect to false alarm rate in any case, whereas classifier D assigns class labels randomly providing equal detection and false alarm rates. Considering classifier B and C, however, the case is undecided because depending on the application each classifier might be superior.

The AUC value denotes the area under the ROC curve and is also used as performance measure of classifier algorithms. In general, large values for the AUC are obtained if the detection rate is large compared to false alarm rate. For an optimal classifier it holds $AUC = 1$. Otherwise, in case of $AUC = 0.5$ the classifier assigns class labels randomly. Therefore, useful classifiers are located in the range $[0.5, 1.0]$ of the AUC.

Performance evaluation for unsupervised machine learning

In contrast to supervised machine learning, a-priori knowledge about the data (e.g. label information) is generally not available in the unsupervised case. Using clustering algorithms, a solution that fits best to the structure/statistics of the data is determined automatically with respect to different criteria such as compactness, connectedness, or separation [106]. However, besides the trivial solutions, i.e. singleton clusters and one-cluster solution, many different solutions can be obtained and an objective evaluation of the results is difficult because the clusters to be defined are not known a-priori. Therefore, cluster validation

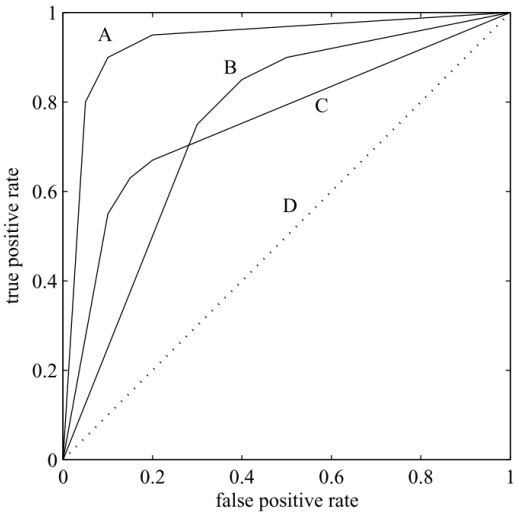

Figure 2.15: Comparison of different classifiers using ROC curve [156].

techniques are important to assure that the obtained results are appropriate in the problem domain.

Visualization techniques and visual inspection can be used in cluster validation to compare the results with domain specific knowledge. Additionally, different cluster validity indices are defined in literature, which can be used to assess the quality of a solution or to compare different partitions of the data. Comprehensive literature reviews of cluster evaluation are provided by Halkidi [100] and Handl et al. [106]. In general, cluster validity indices can be divided internal and external indices [106]. Internal indices take only the data into account, whereas external indices rely on additional (a-priori) information, e.g. known labels. Furthermore, an experimental study comparing different internal indices is presented by Hämäläinen et al. [101]. It is generally accepted that the choice of a suitable index is dependent on the application, i.e. the dataset. Subsequently, relevant cluster validity indices are presented.

Rand index. The Rand index R is computed as proportion of agreements between two different clustering solutions. Following the notation in [100], a set of cumulative counts to compare a clustering solution C and given partition of the dataset P can be defined as

- a: samples that belong to the same cluster in C and P,
- b: samples that belong to the same cluster in C and different clusters in P,
- c: samples that belong different clusters in C and to the same cluster in P, and
- d: samples that belong to different clusters in C and P,

so that $a + b + c + d = |X|$. Using this notation, the Rand index is defined as [100]

$$R = \frac{a + d}{a + b + c + d}\,. \tag{2.19}$$

The value $R = 1$ indicates that two solutions are identical. If a reference solution is given, R can be used as an external measure to compare the similarity between the obtained results and ground truth. In this case, R can be interpreted in analogy to accuracy, which is widely used in classification.

Davies-Bouldin index. The Davies-Bouldin index DB is an internal measure, which is defined as a linear combination of cluster homogeneity and cluster separation. The calculation fo DB is based on the pairwise evaluation of the different clusters in a given solution. Using a similarity measure R_{ij}, which relates the inter-cluster similarity (cluster size) to the intra-cluster separation (distance of cluster centroids), DB can be calculated as [100]

$$\begin{aligned} DB &= \frac{1}{N}\sum_{i=1}^{N} R_i, \quad \text{with} \\ R_i &= \max_{i=1,\ldots,N, i\neq j} R_{ij}. \end{aligned} \tag{2.20}$$

Thus, DB can be used to assess the quality of a clustering solution. In general, DB is minimized to obtain an optimal solution [100].

Cophenetic correlation coefficient. The cophenetic correlation coefficient CC is a measure of how well similarity relations in a dataset are preserved across different representations. Typically, CC is used as an internal measure to assess the quality of a dendrogram obtained from a hierarchical clustering algorithm. The dendrogram can be represented by a cophenetic matrix with the elements d^*_{ij} denoting the height at which two elements are merged into the same cluster. The correlation between the similarity matrix, which contains the pairwise distances d_{ij} of the original dataset, and the cophenetic matrix can be calculated as [112]

$$CC = \frac{\sum\limits_{i<j}\left(d_{ij} - \bar{d}\right)\cdot\left(d^*_{ij} - \bar{d}^*\right)}{\sqrt{\sum\limits_{i<j}\left(d_{ij} - \bar{d}\right)^2 \cdot \sum\limits_{i<j}\left(d^*_{ij} - \bar{d}^*\right)^2}}, \tag{2.21}$$

where $\bar{d}$ and $\bar{d}^*$ denote the average distances, respectively. Hence, CC indicates how well the pairwise distances between the samples in the original of applicationsdataset are represented by the dendrogram. Usually a dendrogram is considered as appropriate representation of the data if CC is close to 1.

2.4 State-of-the-art: Acoustic Emission for diagnosis and process monitoring

In the last decade, AE measurements received increasing attention for online monitoring in many applications. In context of this work, the fault detection in bearings and gear boxes, SHM of composites, and process monitoring are of particular relevance. Subsequently, an overview of the state-of-the-art is given by reviewing literature with a special focus placed on publications within the past 10 years.

2.4.1 Bearings and gear boxes

As an alternative to vibration analysis, which is considered as a classical approach, AE has received attention by many researchers for diagnosis of bearings and gear boxes. As a local technique, AE is expected to provide higher sensitivity to incipient faults compared to vibration analysis. A comprehensive review of AE monitoring of rotating machinery was given by Mba [163], which includes bearings, pumps, gear boxes, and rotating structures. As possible sources of AE impacting, cycling fatigue, friction, turbulence, material loss, cavitation, and leakage were mentioned [163]. Good correlation of AE parameters with machine condition is reported [75, 86, 151]. Subsequently, recent developments reported for bearing and gear box diagnosis are summarized.

In context of bearings and gear boxes, distributed faults (e.g. wear) and local faults (e.g. cracks) can be observed. Typically, local faults are associated with burst-type AE [142]. As an example, a typical AE signal related to a bearing fault on the outer race is presented in Figure 2.16. Periodic bursts, which are superimposed on continuous AE signal, can be detected. Furthermore, bearing faults are frequently masked by AE related to meshing gears [77].

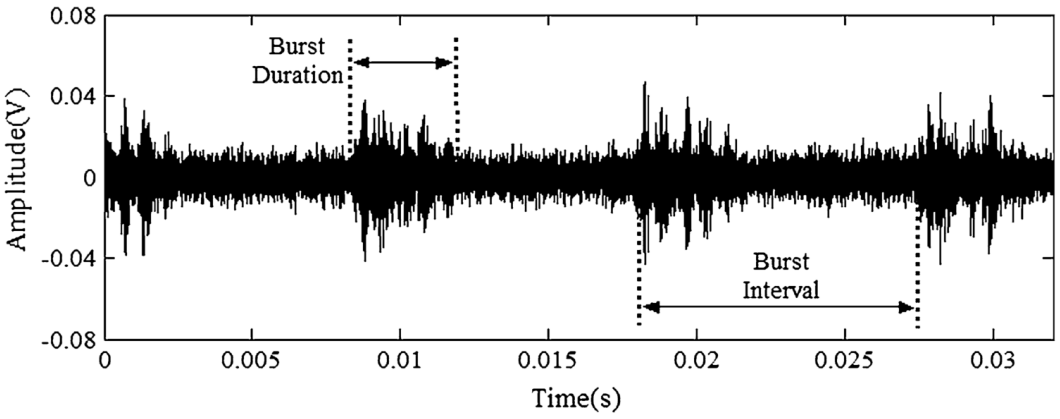

Figure 2.16: Example of AE from bearing with outer race fault [203].

The AE of bearings and gear boxes is typically characterized by strong periodic components, which are important for diagnosis. To extract diagnostic information from AE data, different signal processing techniques can be used. A typical approach to enhance damage signatures is band-pass filtering. Hemmati et al. [111] suggested the use of WPT to extract fault features from AE measurements and presented a new approach to choose an optimal wavelet filter using kurtosis to Shannon entropy ratio. The Shannon entropy is a measure which is used in information theory to characterize a random variable. It can be used as a measure of periodicity, where lower values indicate stronger periodicity of a signal [111]. Similarly, the Spectral Kurtosis (SK) is a statistical measure, which can be used to assess Gaussianity of a signal in different frequency bands [10]. High values of SK in a given frequency band indicate presence of transients. Based on SK, the kurtogram can be constructed [11], which is a graphical representation of SK as a function of filter bandwidth and spectral frequency. The kurtogram can be used to choose an optimal band-pass filter. For instance, Elasha et al. [78] used the kurtogram to extract suitable filter characteristics for

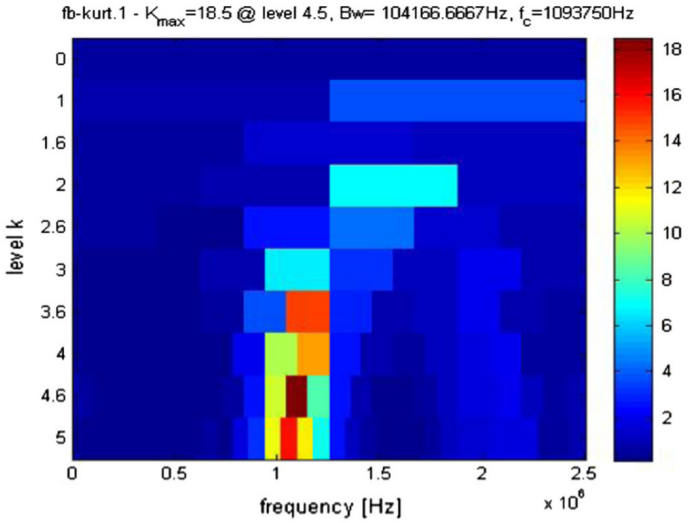

Figure 2.17: Kurtogram of AE signal associated with small bearing fault [78].

bearing diagnosis. As an example, the kurtogram of an AE signal associated with a small bearing defect is shown in Figure 2.17. Ruiz-Carcel et al. [203] showed that SK is an effective tool to choose a suitable frequency band for denoising of bearing AE signals using band-pass filtering. Eftekharnejad et al. [75] showed that the kurtogram can be used effectively for denoising of AE signals at the example of naturally damaged roller bearing. Li et al. [142] suggested the use of Empirical Mode Decomposition (EMD) and threshold based denoising of AE data. A condition indicator was defined using Malahanobis distance.

Another important property of AE signals from bearings and gears is cyclostationarity [12], i.e. statistics of AE follow a periodic pattern due to cyclic kinematics. Following the principle of cyclostationarity, Feng et al. [86] pointed out that explicit consideration of gear meshing kinematics can be useful for diagnosis. Based on cyclostationary AE analysis, two new condition indicators for gear diagnosis were defined, which are sensitive to pitting fault and variations in surface roughness [86]. Cyclostationary analysis of bearing faults was addressed by Kilundu et al. [128].

Besides denoising and extraction of fault signatures, different methods were developed to reduce the amount of data acquired during AE monitoring. To simplify AE-based bearing diagnosis, Liu et al. [146] suggested AE signal processing within a framework of compressive sensing [146], which allows reduction of acquired data and computation required. Also, Vicuna and Höweler [243] suggested a method for data reduction using an enveloping technique. The application for bearing diagnosis was demonstrated in two case studies [243]. Qu et al. suggested a demodulation technique, which allows to record AE at much lower sampling rates that are typically used for vibration monitoring [191].

To improve the reliability of AE-based diagnosis, the combined use of AE and vibration monitoring was proposed in literature. Li et al. [139] suggested the combination of AE and vibration-based diganosis using random forest for classifier fusion. Similarly, Khazaee et al. [127] achieved improved accuracy by fusing classification of acoustic and vibration measurements using Dampster-Schaefer rules. Loutas et al. [151] presented a methodology to integrate AE, vibration, and oil debris monitoring on the feature level.

Regarding bearing diagnosis, Martin-del-Campo et al. [159] used AE to detect lubricant contamination in rolling element bearings. Detection of contamination is difficult at high rotational speed. Compared to conventional analysis methods, stronger fault signatures are obtained at rotational speeds above 300 rpm. Schnabel et al. [217] investigated the detectability of plastic deformation in contaminated bearings by means of AE measurements. It was pointed out that the detectability of damage is strongly dependent on the operating conditions. At elevated speeds, AE signals, which are related to the plastic deformation, are masked by transient force signals [217]. In a different study, Schnabel et al. [216] used model experiments to address the influence of operating conditions on AE parameters. Based on the experimental results, functional relationships between contact time, event frequency, AE amplitude, and Root Mean Square (RMS) values were presented [216]. Hemmati et al. [111] presented an experimental study regarding the effect of fault size, speed, and load on conventional AE parameters. Different defects were artificially introduced on the outer race using an engraving tool. Using design of experiments approach, skewness and AE counts were identified as most suitable parameters under variable operating conditions. Eftekharnejad et al. [75] used AE and vibration measurements for diagnosis of naturally damaged bearing. Bearing failure was accelerated by increased contact force between rolling element and bearing race. After termination of the test, spalling on the bearing race could be observed. From the results it was concluded that AE is more sensitive to incipient faults compared to vibration measurements. Using similar experimental procedures, Elforjani and Mba [79] demonstrated the applicability of AE measurements for detection and quantification of natural faults in bearings. A new damage index was defined by Kilundu et al. [128] using spectral correlation in a narrow frequency band around the fault frequency. Al-Balushi et al. [5] suggested energy index to separate burst signals from noise in bearing condition monitoring.

Furthermore, the use of AE measurements for diagnosis of gear systems including spur gear, planetary gear, and worm gear was frequently addressed in literature. Feng et al. [86] used AE to monitor different wear phenomena in gear systems. According to the results, AE is sensitive to abrasive wear and pitting. The internal placement of the AE sensor was mentioned as main limitation for practical applications. Elasha et al. [78] placed a focus on the separation of bearing fault signals in planetary gear box using adaptive filter, spectral kurtosis, and envelope analysis. Comparison to a classical approach using vibration measurements showed that in this case, damages could be detected earlier using AE. Zhang et al. [268] suggested a methodology based on wavelet transform to obtain accurate time of arrival for localization of a faulty planet gear in a wind turbine planetary gear box. According to their results, fault localization could be improved in this complex structure. Vicuna and Molina [242] presented experimental results regarding the effect of different operation conditions including speed, load, and temperature on AE measurements taken from a planetary gear box. Rotational speed was identified as major influencing operational parameter. At lower rotational speed, an impact of load on AE signals was reported as well. However, the effect of load may be masked as rotational speed increases. Hamel et al. [103] investigated the effect of lubricating conditions on AE. To characterize the lubrication conditions, the specific oil film thickness was considered, which depends on different operating conditions such as load and temperature [103]. According to the experimental results, different lubricating conditions have an effect on AE in gears. Most importantly, it was stated that damage may be not detectable if surfaces are fully separated by the lubricant film. Elforjani et al. [80] used AE energy and RMS measurements for diagnosis of worm gear. Whereas spur and helical

gears are widely covered in literature, results from worm gear are less frequently reported. Experiments were conducted under different operating conditions. Parametric AE analyses were used and the results were compared to vibration measurements. It was concluded that AE measurements are more sensitive to damages in worm gear than vibration measurements. Soua et al. [229] presented measured data from a healthy wind turbine gear box under different operating conditions over a period of five days. Signatures of the healthy state were defined and an indicator to estimate the probability of a fault based on euclidean distance was suggested. In conclusion, the data presented in [229] can be considered as prerequisite to develop a monitoring system for wind turbine gear box. Eftekharnkejad et al. [74] presented experimental results of naturally damaged pinion shaft in a gear box. Different techniques are used for fault detection including AE, vibration, and motor current measurements. The AE signals are analyzed in time-frequency domain using wavelet transform. Wear of gear tooth surfaces and cracked pinion shaft could be detected. Finally, it was pointed out that the choice of a suitable data representation is crucial for successful fault detection.

In this section, a summary of recent literature regarding the use of AE for diagnosis of bearings and gear boxes is presented. Reportedly, AE is particularly suitable to detect incipient damages [75, 78, 80]. Furthermore, AE is sensitive to different mechanisms such as abrasive wear and pitting [86]. However, advanced signal processing is typically necessary to extract fault signatures. Different approaches were suggested in literature, which include wavelet transform [111], cyclostationary analysis [12], and SK [78]. The following challenges and limitations can be identified. It is important to note that AE measurements are susceptible to extraneous noise. In presence of noise, e.g. due to EMI [86], AE data analysis for diagnosis is difficult. Therefore, Feng et al. [86] used a selection of measurements, which were not affected by EMI, to show the relation between AE and surface degradation of gears more clearly. Furthermore, the influence of different operating conditions is identified as major limitation regarding the use of AE for diagnosis of bearings and gears [111, 216, 217, 243]. In particular, the detectability of damage in bearings using AE strongly depends on speed [159]. In gear boxes, the lubricating conditions have a strong impact on AE signatures [103]. Additionally, the AE sensors are most frequently mounted on moving parts, which may be a limiting factor in practical applications [86]. As a conclusion it can be stated that the use of AE measurements in combination with suitable signal processing can lead to improved diagnosis of bearings and gears. However, further developments are necessary to overcome the dependence on operating conditions. Furthermore, current sensor mounting techniques on moving parts inside the housing of gear box may be prohibitive for future applications. Therefore, the establishment of alternative sensor mounting strategies is also identified as a future research direction.

2.4.2 Composite materials

Composites are increasingly used as a replacement for metallic construction materials in many applications including aerospace and renewable energy. Key advantages are high specific strength and stiffness, corrosion resistance, and flexibility in design. Compared to metallic materials, composites are characterized by a lack of ductility. Furthermore, the sophisticated structure, which is composed of multiple constituents, gives rise to several micro-mechanical damage mechanisms including delamination, matrix crack, debonding, and fiber breakage. The damage accumulation process and related material degradation are

stochastic and depend on many influencing factors such as individual flaws present in the material, loading conditions, and interaction of the different mechanisms. For instance, it is known that impact load in transverse direction leads to Barely Visible Impact Damage (BVID), which is a complex damage pattern that is difficult to detect during visual inspection of the materials surface [205]. Therefore, reliable non-destructive evaluation of composites is important.

The use of AE measurements for in-situ inspection and SHM of composites is an active field of research. Examples of damage-related AE bursts that were recorded during fatigue testing of composite material are shown in Figure 2.18. Recent results indicate the utility of AE measurements as reliable method to assess BVID [205], which enables detection of damage initiation at an early stage compared to competing methods [174]. Similarly, Lissek et al. [145] reported high sensitivity of AE to cracking processes, which can not be detected by the use of load cell. Subsequently, the state-of-the-art regarding data analysis of AE and pattern recognition for diagnosis of composites and applications is presented. The focus is placed on continuous fiber materials with polymer matrix, i.e. Glass Fiber-Reinforced Polymer (GFRP) and Carbon Fiber-Reinforced Polymer (CFRP) material.

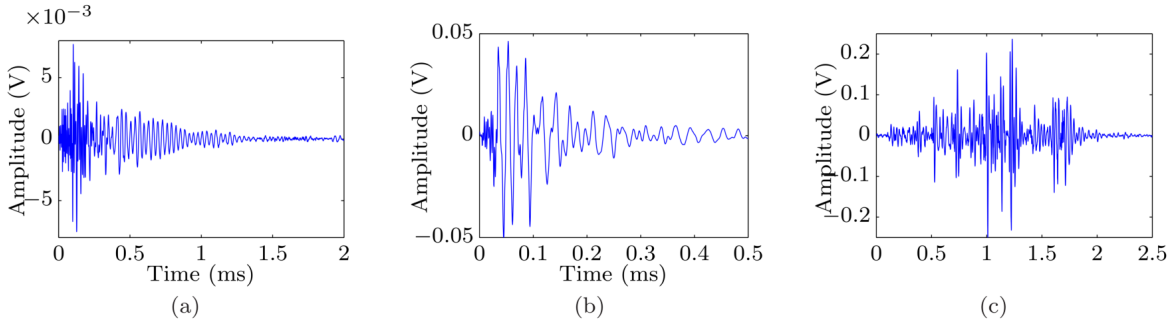

Figure 2.18: Examples of AE signals recorded during fatigue testing of composites [124].

Due to the complexity of AE data, analysis for diagnosis is difficult. Frequently, time behavior and cumulative plots of AE parameters are analyzed. This is a simple approach, which can be used to monitor damage accumulation and evolution qualitatively. McCrory et al. [164] used several AE parameters for classification of AE waveforms. Barile et al. [26] used AE parameters to monitor delamination in CFRP material. Three different stages of damage evolution could be distinguished based on AE activity. Roundi et al. [202] used classical AE parameters to monitor damage in GFRP material with different layup patterns during static and fatigue tensile tests. Using energy, amplitude, rise time, counts, and duration as input to a clustering algorithm, four different damage mechanisms were identified. Saeedifar et al. [204] established a relationship between cumulative AE energy and delamination growth experimentally. Nikbakht et al. [174] used cumulative AE energy and counts to highlight correlations between AE activity and the behavior of load-displacement curve of GFRP material, i.e. load drops due to initiation of damage mechanisms.

Despite promising results, AE parameters are strongly dependent on experimental conditions and reliable identification of different damage mechanisms is difficult. Therefore, advanced signal processing and pattern recognition are widely used. In literature, it was reported that different characteristic frequencies of AE bursts are related to each damage

mechanism. Furthermore, it is well known that the peak frequencies of an AE signal are less sensitive to different experimental conditions. Therefore, frequency and time-frequency domain analysis are frequently used to monitor damage accumulation in composites. Azadi et al. [17] used WPT to identify three different damage mechanisms (i.e. matrix cracking, fiber breakage, and debonding). Lissek et al. [145] used count rate, energy, and peak frequency analysis to monitor crack growth in three different aerospace CFRP laminates. Beheshtizadeh et al. [31] concluded that wavelet transform is superior for the analysis of AE signals because highly detailed representation is obtained – in particular regarding weak signal components. Using CWT, Baccar and Söffker [19] established a correlation between characteristic frequency ranges and corresponding damage mechanisms (delamination, matrix crack, debonding, and fiber breakage), which are observed during static indentation tests. Nazmdar Shahri et al. [172] suggested phase angle of Hilbert transform to identify dominant frequencies of different damage mechanisms. Yousefi et al. [264] used discrete wavelet packet decomposition and different clustering algorithms to identify different damage mechanisms in GFRP material. According to the results, different damages can be distinguished based on unique energy distributions across the frequency spectrum of the signal. Hamdi et al. [102] established a pattern recognition approach based on HHT. Oskouei et al. [198] used cluster analysis to identify characteristic frequencies of matrix crack, debonding, and fiber breakage. Gutkin et al. [99] carried out an extensive experimental program using different testing configurations and different types of CFRP material. A cluster analysis of the recorded AE signals was achieved, which indicates that in general the peak frequency distribution correlates well with the different clusters. Therefore, it was concluded that frequency content of AE is suitable for diagnosis and characteristic frequency ranges were assigned to different damage mechanisms.

A summary of characteristic frequencies reported in literature and related damage mechanisms is presented in Table 2.5. It is apparent that characteristic frequencies due to failure of composite material are located in a range between 10^1 kHz and 10^3 kHz. However, the specific frequency intervals vary among the publications. In this context, it has to be noted that a large variety different of materials, geometries, layup patterns and loading conditions were used. Typically, delamination is assigned to the lowest frequency range followed by matrix crack, debonding, and fiber breakage at increasing frequencies. Furthermore, assignment of damage mechanisms is not always unambiguous due to overlapping frequency intervals. In contrast to most reports, Oz et al. [177] claimed that high frequencies above 460 kHz can correspond to matrix cracks as well. Therefore, it can be concluded that characteristic frequencies are useful to distinguish different damage mechanisms. However, validation of the related damage mechanisms is important for reliable diagnosis.

To validate the results of source characterization, different in-situ and ex-situ techniques are available. A typical approach is to identify the different damage mechanisms after the experiment using e.g. scanning electron microscope [19, 172, 264] or ultrasonic C-scan [108, 164]. To reliably characterize the underlying source mechanisms, in-situ optical techniques can be used. Zhou et al. [270] and Oz et al. [177] used digital image correlation to complement AE measurements. Similarly, Munoz et al. [170] compared the results of AE monitoring and infrared thermography of composite specimens. Good correlation between AE and heat sources was observed for debonding and fiber breakage [170]. Li et al. [140] presented an experimental study in which transparent GFRP specimens were used to establish in-situ backlight imaging with a digital camera. Crack initiation and propagation were correlated

Table 2.5: Summary of frequency ranges that were reported for different micro-mechanical fracture mechanisms.

Matrix crack	Debonding	Delamination	Fiber breakage	Reference	Year
90-180 kHz	240-310 kHz	n.a.	> 300 kHz	de Groot et al. [67]	1995
100-350 kHz	n.a.	n.a.	350-700 kHz	Bohse [42]	2000
140 kHz	300 kHz	n.a.	405 kHz	Bussiba et al. [48]	2008
50-150 kHz	170-350 kHz	n.a.	n.a.	Marec et al. [158]	2008
< 50 kHz	200-300 kHz	50-150 kHz	400-500 kHz	Gutkin et al. [99]	2011
100-250 kHz	250-350 kHz	n.a.	400-500 kHz	Oskouei et al. [198]	2012
30-170 kHz	180-290 kHz	30-90 kHz	300-420 kHz	Hamdi et al. [102]	2013
100-190 kHz	250-310 kHz	n.a.	375-440 kHz	Yousefi [264]	2014
100-200 kHz	250-310 kHz	n.a.	375-440 kHz	Shahri [172]	2016
100-150 kHz	150-350 kHz	< 120 kHz	350-500 kHz	Baccar et al. [19]	2017
70-150 kHz	210-270 kHz	168-190 kHz	300-400 kHz	Chelliah [54]	2018
100-250 kHz	380-420 kHz	320-380 kHz	420-500 kHz	Sayar [214]	2018
100-250 kHz	250-420 kHz	n.a.	420-500 kHz	Azadi [17]	2019

with AE measurements. An alternative approach to validate AE, source characterization was presented in Brunner et al. [46]. The key idea is the use of special specimens which generate single dominant damage mechanism under defined loading conditions. In this case, dominant AE signatures can be identified in the measurements and assigned to the corresponding damage mechanism.

Due to the complexity of AE data, characterization of different AE source mechanisms is frequently treated as pattern recognition problem. Different machine learning algorithms are available, which can be used for data-driven characterization of different source mechanisms. Most frequently, unsupervised approaches are used because labeling of the data is difficult. For instance, k-means algorithm and derivatives were used for unsupervised clustering of AE data [141, 177, 202, 270]. Roundi et al. [202] and Zhou et al. [270] used classical AE parameters and the combination of k-means clustering and PCA for data reduction to distinguish between different damage mechanisms. According to Li et al. [141], the most relevant features are peak amplitude and peak frequency. Alternatively, Fuzzy C-Means (FCM) algorithm can be used [17, 198, 264]. In contrast to k-means, multiple cluster assignments with a different membership degree are possible using FCM. Oskouei et al. [198] used FCM with PCA to cluster of AE data [198]. Chelliah et al. [54] compared k-means, FCM, and Self Organizing Map (SOM) clustering [54]. Optimal combination of AE parameters as input to the clustering was determined with respect to Davies-Bouldin and silhouette index. According to the results, four clusters were identified and SOM approach appears as most appropriate technique [54]. Furthermore, comparison of k-means and FCM was provided by Yousefi et al. [264]. Similar clusters were obtained using k-means and FCM algorithm. However, k-means is less time consuming. Gutkin et al. [99] compared the three techniques k-means, SOM combined with k-means, and competitive neural networks. According to the results, combined SOM and k-means approach is most effective with respect to cluster quality and computational effort. However, the correlation of different clusters and related damage

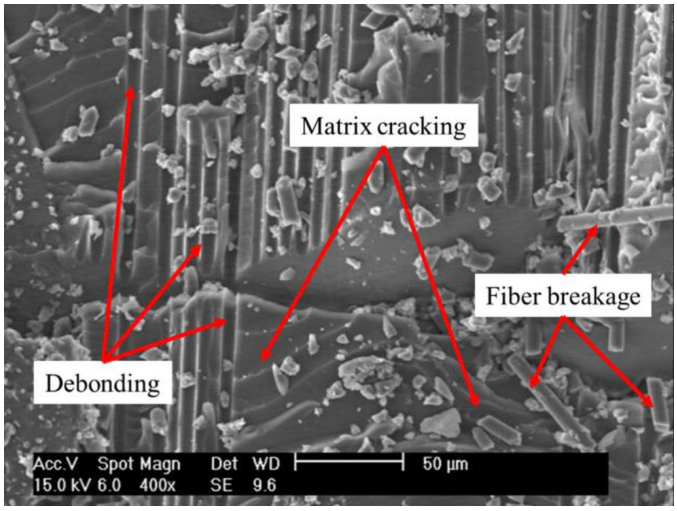

(a) Example of SEM micrograph showing typical damage modes of CFRP [17].

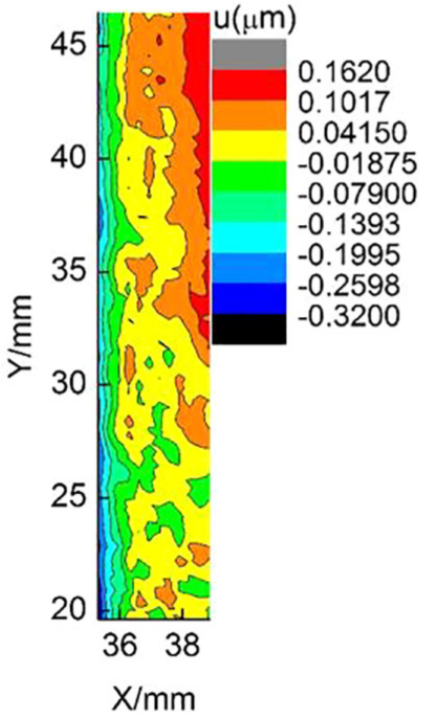

(b) Strain map obtained using DIC [270].

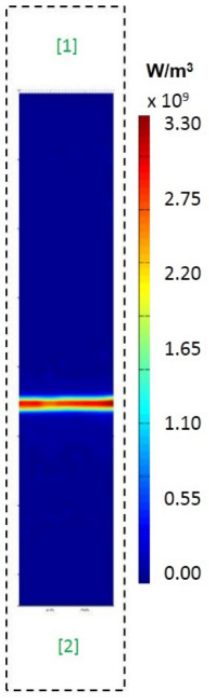

(c) Heat source field during failure of CFRP in tensile test [170].

Figure 2.19: Examples of damage verification techniques.

mechanisms is not obvious. Baccar and Söffker [19] presented a new pattern recognition approach using SVM for supervised classification of AE data.

As an alternative to pattern recognition, modal AE was considered in some publications to characterize different source mechanisms of AE signals. For modal AE analyses, effective

and reliable identification of the different modes in the measurements is of key importance. Barroso-Romero et al. [27] suggested mode identification based on phase and instantaneous frequency using Hilbert transform. Dahmene et al. [64] used narrow bandwidth filters to separate extensional (S_0) and flexural (A_0) Lamb modes prior to further signal processing. Frequency ranges of [25 kHz - 90 kHz] and [125 kHz - 300 kHz] were reported for S_0 and A_0 mode, respectively [64]. Subsequently, only features of the dominant mode were used to identify different damage mechanisms. Similarly, Martinez-Jequier et al. [160] suggested an algorithm for separation of S_0 and A_0 modes using hardware filters to monitor delamination in real-time. Two narrow frequency bands were defined to separate the two modes and a small time window was used to minimize propagation effects and reflections. Baker et al. [25] used modal AE principle to improve characterization of matrix crack compared to plain peak frequency analysis. Comparison of modal AE-based approach to methods that rely on advanced statistical analysis was presented by McCrory et al. [164]. To classify AE data according to modal content, Measured Amplitude Ratio (MAR) was suggested, which denotes the ratio between extensional and flexural wave mode amplitudes. This value serves as a measure of the modal content of a waveform. Values of MAR > 1 and MAR < 1 indicate a dominant extensional or flexural mode, respectively. According to the results [164], MAR-based classification was in accordance with artificial neural network classifier on a two-class problem.

In summary, it becomes clear that information, which is useful for AE data analysis and interpretation, can be obtained from the modal content of AE. It is worth mentioning that knowledge regarding the modal content of detected AE signals is of particular importance for accurate source localization because the propagation speed of S_0 and A_0 modes is different [27]. Furthermore, the use of modal ratios is suggested for diagnosis [160, 164]. Results of modal analysis may lead to a physical interpretation of AE (i.e. dominant in-plane or out-of-plane motion). However, it has to be noted that usually only two different modes can be observed in thin structures. Regarding diagnosis, this appears as a limiting factor. For instance, McCrory et al. used MAR to distinguish between two different classes. Similarly, Martinez-Jequier [160] used modal AE to identify delamination in composite material. To distinguish between the remaining damage mechanisms, additional analysis in frequency domain was necessary [160]. Therefore, it can be concluded that the interpretability of AE can be improved in specific cases using modal AE analysis. However, the use of pattern recognition for diagnosis is a more general approach.

The use of AE for monitoring of composite materials was suggested for different applications. However, it has to be noted that most studies were conducted using laboratory-scale specimens. Typical specimen geometries are coupons (e.g. [202, 213, 270]), double-cantilever beam (e.g. [26, 145, 204]), plates (e.g. [19, 164]), or end-notch flexure specimens (e.g. [172]). Few studies are related to real-world structures. For instance, Sause et al. [212] used a neural network model, which was trained on lab-scale experiments, to predict the burst pressure of small-scale and large-scale pressure vessels based on AE. Dahmene et al. [64] considered a full-scale specimen, which was extracted from a composite overwrapped pressure vessel. Han et al. [105] considered a full-scale wind turbine blade of a 100 kW unit under static loading. Also, Tang et al. [236] conducted fatigue testing of a wind turbine blade of 45.7 m in length. However, due to complex propagation behavior of AE waveforms, the distance between AE source and sensor is currently considered as major limiting factor for damage identification [155]. Additionally, the impact of accumulated damage within a material on

the wave propagation behavior has to be taken into account [96, 126]. Furthermore, Mouzakis et al. [168] suggested that material related AE signal attenuation is increased by aging. Experimental results of AE attenuation in composites were presented by Asamene et al. [13] and a parametric model of AE attenuation was proposed. To take the effects of wave propagation into account during parametric AE analyses, Maillet et al. [155] suggested the use of a calibration chart. Similarly, Aggelis and Matikas [2] suggested the use of correction curves to compensate the effect of wave propagation on classical AE parameters. The correction curves were determined using simulated AE data and a curve fitting procedure. However, obtaining the calibration curves for any possible propagation path could be difficult to realize. Furthermore, to ensure the reliability of AE-based SHM in real world applications, detailed understanding of the effect of wave propagation on detected AE signals is necessary. Therefore, it may be concluded that open research topics include the effect of wave propagation on AE and the development of alternative methods, which provide a practical solution to address the effects of wave propagation in experimental data.

To summarize, it can be stated that high sensitivity to different damages in composite structures can be achieved by AE measurements [145,174]. Regarding the characterization of different damage mechanisms, the use of pattern recognition, modal analysis, and validation of the results were covered in literature. However, the use of modal ratios for diagnosis as suggested in [160,164] is limited by the number of modes, which are typically observed in thin structures. Therefore, frequency domain features were most frequently used to distinguish between different damage mechanisms. A summary of characteristic frequencies that were reported in literature is provided in Table 2.5. However, while different damage mechanisms can be distinguished, different frequencies were reported in literature. Therefore it has to be concluded that the related frequencies are not universally applicable and have to be validated in each individual case. For advanced data analysis, different machine learning approaches can be used. Most frequently, unsupervised approaches are chosen to distinguish between different damage mechanisms. As a result, different clusters can be obtained. However, additional investigation and interpretation is usually required to relate the different clusters to underlying damage mechanisms. In contrast, using supervised approaches, a classification of the underlying damage mechanism is directly available. In context of diagnosis, this can be considered as an advantage. However, choosing a supervised approach, explicit knowledge regarding underlying damage mechanisms is required during training. Obtaining labeled data for training of supervised methods is usually difficult. Therefore, supervised approaches for classification of AE are used less frequently. Furthermore, the effect of wave propagation on AE signatures is currently not well understood. Therefore the distance between source and sensor is considered as a limiting factor for AE-based diagnosis of composites [155]. In particular, this poses a challenge in practical applications if variable propagation paths or complex geometries are considered. As a solution, different approaches, which are based on experimental calibration, were suggested in literature [2, 155]. However, labor intensive and time consuming experiments may be prohibitive in some practical applications. Furthermore, the dependence of AE on different operational and environmental factors is usually not considered in detail.

2.4.3 Process monitoring

Effective monitoring of industrial processes is important to improve product quality and process efficiency. In this field, AE received attention as passive, in-situ measurement technology. Subsequently, the fields of engineering process monitoring (i.e. chemical, food, biochemical, or pharmaceutical industries), and manufacturing process monitoring are distinguished.

Regarding chemical engineering processes, a comprehensive review of AE for in-situ monitoring was presented by Boyd and Varley [44]. Monitoring of bubble formation and collapse in gas-liquid dispersions, characterization of flow regimes in gas-liquid or solid-fluid dispersions, mixing processes, and monitoring of chemical reactions were mentioned as possible applications of AE. Applications in recent literature include characterization of flow conditions [115, 271], crystallization [92, 248], and mixing of solids [62].

Zhou et al. [271] proposed the integration of AE measurements to monitor flow conditions in gas-solid two-phase flow. Gas-solid two-phase flow systems are encountered different chemical processes and reactions such as cracking, combustion, and gasification. Different flow conditions affect gas-solid mixing, mass and heat transfer, and the reaction process and thus directly relate to productivity. Physical phenomena such as inter-particle and particle-wall collision, behavior of particle clusters, and gas phase are reflected in the AE measurements [270]. Husin et al. [115] demonstrated in an experimental study the feasibility of AE measurements to monitor flow conditions of two phase gas-liquid flow in a vertical pipeline. Such multiphase flow conditions are encountered e.g. in petrochemical or oil and gas industries. Using AE measurements, single bubble inception and collapse can be detected. Furthermore, a relation between AE and bubble activity as well as liquid viscosity was pointed out. Consequently, linear correlation between AE and gas-void fraction, which is an important design parameter, was established. Therefore, it is concluded that AE can be used as passive in-situ monitoring technology to characterize multiphase flow conditions.

Furthermore, Wang et al. [248] and Geherras et al. [92] showed by experiments that AE can be used to monitor crystallization, which is widely used for separation and purification in industrial processes. According to the experimental results, AE is sensitive to basic crystallization phenomena and early detection of nucleation events is possible [92]. Furthermore, it was suggested that AE could be used to characterize product quality, which opens new perspectives for AE-based process monitoring and control [92, 248].

Crouter and Briens [62] and Allen et al. [9] investigated the potential of AE to monitor solid powder mixing using V-blender [62] and convective mixer [9]. By experiments, it was shown that AE is sensitive to particle type and motion [62] as well as size, mass, and impeller speed [9]. Therefore, AE is considered as suitable technique to monitor powder mixing. However, it was also pointed out that AE does not provide chemical information and is only sensitive to physical properties AE.

In manufacturing, process monitoring can aid to reduce scrap parts, downtime due to failure, and to ensure quality. Relevant measures of product quality include surface roughness [179] and dimensional accuracy [130]. Besides improved process understanding, in-situ monitoring technology opens new opportunities for integration with closed-loop process control. As Everton et al. [83] pointed out, integration of in-situ monitoring and closed loop control in additive manufacturing processes is essential to overcome variability in product quality, which is currently a major limiting factor. Also the need for monitoring and control of conventional machining processes to improve efficiency and quality was stressed in a re-

view by Stavropoulos et al. [231]. For instance, Pahuja et al. [179] suggested the use of AE to monitor surface quality. However, direct measurements of relevant variables such as mass loss or surface profiles are difficult to establish online. Therefore, indirect measurements such as force, torque, AE, and acceleration are frequently used to characterize a process. A comprehensive review of the use of AE to monitor cutting processes is presented by Kishawy et al. [129]. Furthermore, the effect of lubrication conditions is important. A large variety of different MWFs is available, which can have an impact on the workpiece quality and efficiency of machining processes. Brinksmeier et al. [45] present an overview regarding the current understanding of related physical and chemical working mechanisms, which influence machining processes differently. Besides the basic functions of MWF, which include cooling and flushing of the contact zone during machining, their performance is highly sensitive to the composition [45]. Furthermore, it was pointed out that manufacturing processes can be understood as tribological systems [45]. The interaction of the lubricated sliding surfaces in the contact zone between tool and workpiece can be influenced by choosing different MWF. Typical parameters, which are used to characterize the condition of MWF in manufacturing are for instance the concentration of different additives, pH-value, or droplet size in emulsions. However, the related measurement techniques using e.g. refractometer, pH-meter, or dynamic light scattering are not suitable for online monitoring due to long measuring cycles and low accuracy [45]. Therefore, the development of alternative approaches, which are suitable for online monitoring of MWF, opens new perspectives to ensure optimal workpiece quality and efficiency of manufacturing processes.

Also, different examples of AE-based process monitoring in machining and additive manufacturing were presented in literature. An overview showing different monitoring and investigation variables, which are considered in literature to monitor machining and additive manufacturing, is presented in Table 2.6. In conventional machining operations, wear of the tool is of particular interest. Different wear mechanisms, such as adhesive and abrasive wear, can be distinguished [154]. Different conditions of the tools such as damage to the cutting edges [87] or blunt flutes [97] exist. In context of coated tools, differences in wear rates due to different coating can be detected is [196]. Furthermore, cutting conditions in a manufacturing process can be characterized according to different mechanisms of chip formation (e.g. continuous or discontinuous chip formation) using suitable monitoring techniques [110, 187]. Also, the formation of Build Up Edge (BUE) at the cutting edge, which can cause rapid tool wear, can be detected using AE measurements [4, 187]. In Figure 2.20 different sources of AE during cutting processes, which are typical for many machining operations such as drilling and turning, are illustrated. In additive manufacturing, relevant failure mechanisms including scratching and hitting between material and extruder, material peeling off, as well as material rubbing and sliding were considered by Wu et al. [261]. Liu et al. [147] distinguished different extruder states such as run-out-of-material, semi-blocked, and blocked extruder. Furthermore, pore concentration in the workpiece medium is an important measure to characterize the product quality in additive manufacturing [224].

In literature, the use of AE for online monitoring of machining operations was frequently suggested. Wang et al. [246] presented a tool wear monitoring approach in milling under minimum quantity lubrication conditions. Based on AE parameters, a cluster analysis was achieved to distinguish three different cutting conditions i.e. minimum quantity lubrication, fracture, and plastic deformation. Finally, linear correlation between AE energy and tool wear was established. Klocke et al. [130] used AE amplitudes in different frequency bands

Table 2.6: Summary of recent publications regarding AE-based monitoring of manufacturing processes.

Process	Signal analysis methods	Characterized variables	Reference	Year
Machining				
Milling	Energy	Tool condition	[246]	2019
Drilling	FFT, amplitude	Tool condition	[130]	2019
Turning	Parametric	BUE formation	[4]	2019
AWM*	WPT	Surface quality	[179]	2019
Cutting	FFT	Tool condition	[196]	2018
Turning, Grinding	Raw AE, frequency analysis	Tool wear, plastic deformation	[35]	2016
Milling	RMS, FFT, DWT	Surface quality, chip formation	[187]	2015
Turning	Power spectral density, auto-covariance	Tool condition	[154]	2015
Drilling	Parametric	Tool condition	[87]	2015
Turning	Amplitude, energy	Chip formation, tool wear, surface quality	[110]	2014
Turning	RMS	Tool condition	[132]	2013
Drilling	Mean power	Tool condition	[97]	2012
Additive manufacturing				
FFF*	Parametric	Process failure	[261]	2019
FDM*	Parametric	Extruder state	[147]	2018
DED*	RMS	Mass flow	[250]	2018
SLM*	WPT	Pore concentration	[224]	2018

*Abrasive Waterjet Machining (AWM), Fused Filament Fabrication (FFF), Fused Deposition Modeling (FDM), Direct Energy Deposition (DED), Selective Laser melting (SLM)

to characterize tool wear in drilling. Cluster analysis using k-means clustering was achieved to identify different wear conditions. Best results were obtained using AE amplitudes in a frequency range between 150 kHz and 250 kHz. Ahmed et al. [4] proposed a framework to monitor BUE phenomenon during turning using AE and force signals and machine learning. According to the results, AE RMS is most sensitive to BUE formation. Pahuja et al. [179] suggested the use of AE measurements and wavelet decomposition to monitor the surface roughness of abrasive waterjet machining. Ramasubramanian et al. [196] presented AE and vibration signals that were measured during cutting in FFT representation. Correlation of peak amplitudes with tool wear was observed. Bhuiyan et al. [35] investigated the contribution of tool wear and plastic deformation of the work material to AE measurements in turning. Prakash et al. [187] presented an experimental study regarding the effect of tool wear on chip formation mechanisms. Results indicate that characteristic frequencies from 125 kHz to 250 kHz and 62.5 kHz to 125 kHz are correlated with shearing and microfracture of chip formation, respectively. Maia et al. [154] established a correlation between AE, power spectral density, and tool wear. Ferrari et al. [87] used AE and thrust to distinguish

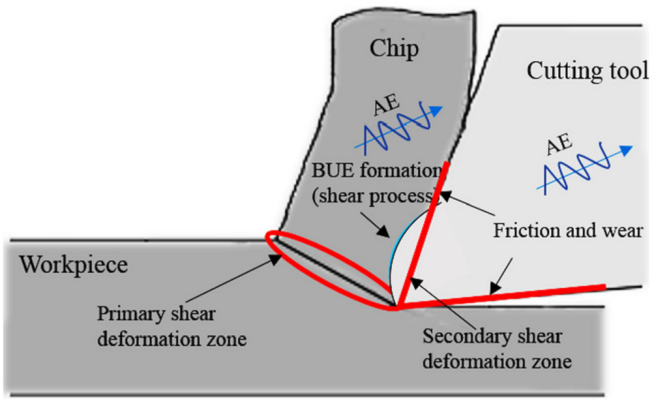

Figure 2.20: Schematic illustration of AE sources in cutting [4].

between different drill bit conditions. These include faults to cutting edge (craters) and flattened cutting edge. Specifically, mean power of AE was established as sensitive parameter to monitor drilling [87]. Hase et al. [110] used AE amplitude to characterize the cutting conditions. Larger AE amplitudes were observed in case of discontinuous chip formation compared to continuous chip formation. Kosaraju and Anne [132] used AE RMS to monitor flank wear and an empirical model of AE RMS in turning of titanium alloy was developed. Gomez et al. [97] used AE measurements to monitor tool condition of drill bits. Based on the experimental results, it was concluded that AE mean power is only sensitive to identify strongly worn tools whereas slight wear can not be detected.

Also, some recent publications addressed online monitoring of additive manufacturing using AE measurements. Wu et al. [261] used time and time-frequency domain features of AE to achieve a cluster analysis of different fault conditions in fused filament fabrication. Liu et al. [147] used multiple AE features extracted from time and time-frequency domain and an unsupervised clustering scheme to characterize the extruder state in fused deposition modeling. Whiting et al. [250] suggested the use of AE RMS to monitor the powder mass flow in directed energy deposition, which can be used for metal additive manufacturing. Powder mass flow is an important parameter to characterize the directed energy deposition process and related faults such as a clogged deposition head can be detected. Furthermore, Shevchik et al. [224] demonstrated the feasibility of monitoring pore concentration in the workpiece medium using AE measurements. The AE signals were processed in time-frequency domain using WPT and convolutional neural network was applied to classify three different qualities.

In summary, promising results were reported regarding the use of AE for in-situ process monitoring in a wide range of applications. In the field of process engineering, the sensitivity of AE to relevant physical phenomena opens the opportunity to obtain indirect measurements from processes, which are otherwise inaccessible. For instance, AE can be used to characterize flow conditions, crystallization phenomena, and particles in mixing processes. Finally, based on the literature review it can be concluded that besides online monitoring, AE measurements may be useful to establish closed loop control to ensure efficiency and product quality in chemical engineering processes. In manufacturing, AE was successfully used for online monitoring of tool wear in conventional machining processes and detection of process failure in additive manufacturing. Ultimately, the use of AE measurements for

closed loop control opens new perspectives to ensure efficiency and to reduce variability of quality in manufacturing. Regarding conventional machining processes, it has to be pointed out that according to literature, basic signal processing and statistical correlations were most frequently applied. However, only few publications considered advanced signal processing methods or machine learning approaches. Especially due to averaging during calculation of statistical measures, relevant information from the AE measurements might be inaccessible. Therefore, monitoring may be improved by advanced signal processing and data analysis techniques. Furthermore, suitable techniques for online monitoring of MWF condition, which is also important for high-quality and efficient machining, is still an open topic.

2.4.4 Summary and discussion

In the previous subsections, an overview of the state-of-the-art regarding the use of AE for diagnosis and process monitoring has been presented. Subsequently, the main conclusions are summarized and discussed in the light of open research topics.

Regarding the use of AE for diagnosis of bearings and gears, it was pointed out that AE is sensitive to different damage mechanisms including abrasive wear and pitting [86]. The comparison of AE to classical vibration measurements showed that AE is more sensitive to incipient damages [75]. In literature, the development of feature extraction techniques for AE from gears and bearings, which are based on advanced signal processing approaches, is a key topic. Different approaches including SK [78], cyclo-stationary analysis [12], and wavelet transform [111], were suggested. However, while promising results were reported under laboratory conditions, it is worth mentioning that AE measurements are susceptible to extraneous noise e.g. due to EMI as reported in [86]. Furthermore, some limitations can be identified, which may become relevant for the application of AE monitoring in practice. Usually, only a single fault or fault size is considered at a time during experiments. In practice, different faults, which have to be distinguished, may occur at the same time. Furthermore, the influence of variable operating conditions on AE in bearings and gear boxes is identified as limiting factor [111, 216, 217, 243]. In particular, it was reported that AE signatures are dependent on speed [159] and lubricating conditions [103]. It is important to note that even though high sensitivity can be achieved, damage related AE may be masked at certain operating conditions. Besides the effect of different operating conditions, the suitable placement of sensors is crucial. The sensitivity of AE depends on the propagation path between source and sensor [226]. Most frequently, sensors were mounted on moving parts of bearings or gear boxes to achieve highest sensitivity. However, it was also mentioned that such a strategy may not be a suitable solution in practice [86]. To improve the applicability of AE for diagnosis, the development of simple and non-invasive mounting procedures is important. To address this topic, alternative sensor mounting is explored in Section 4.2 of this thesis. Here, AE sensors are mounted stationary outside the housing of a gear box. The AE was measured continuously and characteristic signatures of different faults could be identified using CWT.

The use of AE to characterize different damage mechanisms in composites was also frequently suggested. Different approaches were used for analysis and interpretation of AE. These include parametric analyses, which usually rely on time-based qualitative analysis e.g. using cumulative plots (e.g. [174, 204]), advanced signal processing approaches using time-frequency transformations (e.g. [17,19,31]), and pattern recognition [141,177,202,270]. Additionally, modal analysis was suggested for damage characterization in composites [160, 164].

In contrast to pattern recognition, modal AE analysis can be used to achieve a classification of different damage mechanisms using a physical interpretation of AE. However, regarding the use for diagnosis, this approach is limited by the number of modes which are typically observed in thin specimens [164]. Therefore, pattern recognition can be considered as a more general approach. In contrast to supervised methods for pattern recognition, unsupervised methods usually require additional data analysis or interpretation to relate different classes of AE signals to specific damage mechanisms. Therefore, supervised methods may be more suitable for diagnosis. However, obtaining labeled AE data is difficult and time consuming. Therefore, approaches using unsupervised pattern recognition were most frequently suggested.

Furthermore, different in-situ and ex-situ techniques were suggested, which can be used to relate different clusters to distinct source mechanisms or to generate a dataset for training of supervised approaches. For instance, these include scanning electron microscope [19, 172, 264], digital image correlation [177, 270], or infrared thermography [170]. However, the evaluation of data-driven approaches, which is based on a test dataset, can only provide an estimate of the performance on future, unknown data. To date, detailed evaluation of the reliability of pattern recognition approaches under different operational and environmental conditions is an open topic. Finally, the effect of wave propagation on AE signatures is important to consider. Typically, the AE amplitudes are attenuated due to propagation in the material. In particular, this poses a challenge in practical applications if variable propagation paths or complex geometries are considered. As a solution, different approaches, which are based on experimental calibration, were suggested in literature [2, 155]. However, labor intensive and time consuming experiments may be prohibitive in some practical applications. Furthermore, the dependence of AE attenuation on different operational and environmental factors may have an impact, which is relevant for diagnosis.

Subsequently, some of the current challenges are addressed by contributions presented in this thesis as follows. In Section 4.4, experimental investigation of the reliability of AE-based damage classification under variable loading conditions is presented. As an example, a supervised classification scheme using STFT and SVM is suggested. Detectability of damage and probability estimates are used to assess the performance of the classifier. Finally, the results are discussed in the context of reliability assessment for SHM. Furthermore, detailed investigation of AE waveforms in time domain has not received much attention up to now. Recently, shape-based similarity measures were suggested as an alternative approach [55]. Key is the definition of a suitable similarity measure, which can be used to distinguish between different classes of waveform data. In Section 4.3, the performance of different shape-based similarity measures is evaluated at the example of AE in thin plates. Particular focus is placed on the robustness against waveform distortions due to misalignment and additive noise. Finally, an experimental investigation of AE signal attenuation in composite plates due to wave propagation is presented in Section 4.5. Full waveform data is analyzed in time and time-frequency domain using wavelet transform. Particular focus is placed on the dependence of AE attenuation on frequency and different loading conditions.

In the field of process monitoring, chemical engineering processes and manufacturing processes were distinguished. Regarding the use for monitoring of chemical engineering processes, it was mentioned that AE can be used to characterize different flow conditions [271], crystallization [92, 248], and mixing processes [9, 62]. Furthermore, conclusions regarding the process efficiency and product quality may be drawn based on AE measurements [92, 248].

Nevertheless, while the use of AE to monitor chemical engineering processes was suggested, it is important to note that AE is only sensitive to physical phenomena. Therefore, AE can not be used to characterize chemical properties directly [9]. However, the possibility to characterize chemical engineering processes, which are inaccessible for direct measurements, indirectly using AE opens new perspectives for online process control [92, 248]. By integrating AE into closed loop process control schemes to maintain efficient operation, productivity could be improved and optimal product quality could be achieved. The topic of AE-based process control is addressed in this thesis as follows. In Section 5.2, a proof of concept regarding the use of online AE measurements for closed loop process control is presented, which is a new approach. Using suitable online processing of AE, close to optimal operation of the process could be achieved and maintained.

Regarding manufacturing process monitoring, conventional machining and additive manufacturing were considered. For diagnosis of additive manufacturing processes, AE can be used to distinguish between different states of the process [147, 261]. Regarding conventional machining operations, such as drilling, turning, or grinding, monitoring of tool wear is of particular interest. Using AE, different wear mechanisms [154] and cutting conditions, i.e. chip formation and BUE formation [110, 187] can be distinguished. Furthermore, the application of AE to monitor the quality of the product directly was suggested [179, 224]. Besides tool condition, suitable lubrication conditions are also important for high-quality and efficient machining [45]. Therefore, the characterization of different MWF using AE, which is a new approach, is addressed in this thesis. In Section 5.1 an experimental investigation of AE during thread forming is presented. The AE measurements are compared to torque as a conventional process parameter. According to time-frequency domain analysis of AE using CWT, characteristic frequency bands are identified. Finally, AE is used to characterize different MWF compositions.

3 Development of Acoustic Emission measurement and control system

To obtain a timely statement regarding system condition or to realize control actions online, continuous acquisition and processing of AE is desirable. Therefore, a suitable AE measurement and control system is presented subsequently. The main contribution of this chapter is the development of a novel hardware architecture as low cost solution for AE measurements and control, which is based on an FPGA-based coprocessing platform. An FPGA-module is developed to obtain DWT coefficients in real-time. The use of the suggested hardware architecture for AE measurements and signal processing is demonstrated at the example of indentation testing of composite material. This chapter is based on the previously published works *High-speed data acquisition system for continuous acoustic emission monitoring and real-time signal processing using FPGA-based platform within a SHM framework* presented at the 9th European Workshop on Structural Health Monitoring [255] and the journal publication *Development of A Low-Cost FPGA-Based Measurement System for Real-Time Processing of Acoustic Emission Data: Proof of Concept Using Control of Pulsed Laser Ablation in Liquids* [254].

3.1 Materials and methods

Continuous acquisition and processing of full AE waveform data is still a challenging task due to limitations related to disk I/O and processing speed. Commercially available systems, which allow continuous sampling over long durations, are usually based on expansion cards for standard computers. However, besides high cost of these systems, bulky equipment might be prohibitive for field deployment. Shateri et al. [223] used a low-cost micro controller platform together with commercially available sensors to record AE waveforms. Intermittent data acquisition is triggered by a predefined threshold. Long term tests show that AE hits are detected reliably. However, only a limited sampling rate of 667 kHz is achieved [223]. For high-performance embedded implementations, hardware-software coprocessing architectures, i.e. an architecture where the CPU is complemented with hardware accelerators for specific tasks, are frequently proposed. Compared to fully hardware-based implementations, these architectures have the advantage of faster development of initial prototypes, increased flexibility for later changes, and ease of integration with peripheral components [56]. For instance, Cheng et al. [56] propose a hardware-software coprocessing architecture for automatic speech recognition. The system is implemented on FPGA fabric using soft processor and hardware accelerators. Also, Virupakshappa and Oruklu [245] develop a hardware architecture which is suitable for the embedded implementation of fault detection based on ultrasonic A-scans. In contrast to Cheng et al. [56], a SoC-based platform is chosen in [245], which comprises a CPU and FPGA fabric.

Furthermore, the focus of research was shifted towards advanced signal processing methods such as time-frequency domain transformations for reliable interpretation of AE measure-

ments. By leveraging data parallelism of FPGA-based hardware architectures, the related signal processing algorithms can be implemented efficiently. Therefore, a low-cost FPGA-based platform is chosen, which is illustrated in Figure 3.1. Key features are low cost, small form factor, and low power consumption, which makes this device ideally suited for field deployment and embedded applications. Furthermore, several widely used I/O interfaces including USB and Ethernet are available, which can be used to integrate the system with digital infrastructure or to realize control actions. Subsequently the hardware architecture and an FPGA-based implementation of the DWT, which is suitable for real-time use, are described in detail.

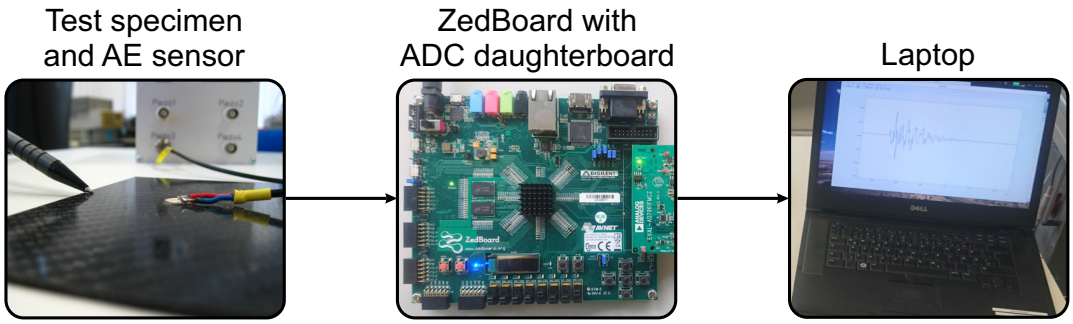

Figure 3.1: Illustration of the measurement system [255].

3.1.1 System overview

The design of the hardware architecture is inspired by the following principle ideas: i) leveraging data parallelism using FPGA-based hardware implementation to accelerate signal processing tasks such as filtering and feature extraction and ii) placing computing power, storage, and network capabilities close to data sources can lead to reduced latency for real-time analytics [91]. As a computational platform, the ZedBoard (xc7z020clg484-1) is chosen. This is an evaluation and development kit for Xilinx Zynq-7000 SoC, which provides periphery for interfacing with additional hardware and storage including USB, Ethernet, and a SD card slot. The dimensions of the board layout are 160 mm x 160 mm. The maximum power consumption is 60 W. The SoC comprises two subsystems namely Processing System (PS) with Cortex-A9 dual-core processor and Programmable Logic (PL) fabric running at clocks of 666 MHz and 100 MHz, respectively. Thus, this device allows efficient implementation of monitoring and control algorithms by leveraging both advantages of FPGAs for fast signal processing and flexibility of software programmable devices to implement higher level sequence control and communication interfaces. For data acquisition, Analog Devices AD7961 is used enabling analog-to-digital conversion at a sampling rate of 5 MHz with a resolution of 16 bit.

The overall system is illustrated in Figure 3.2. The PS runs a Linux operating system, which is used to implement general functionality of the device. This includes loading drivers and enabling Ethernet at boot time, configuration of the register bank, control of the data acquisition (start/stop), and storage. The measurement data are stored either on the SD Card or in external memory, i.e. USB drive in binary format.

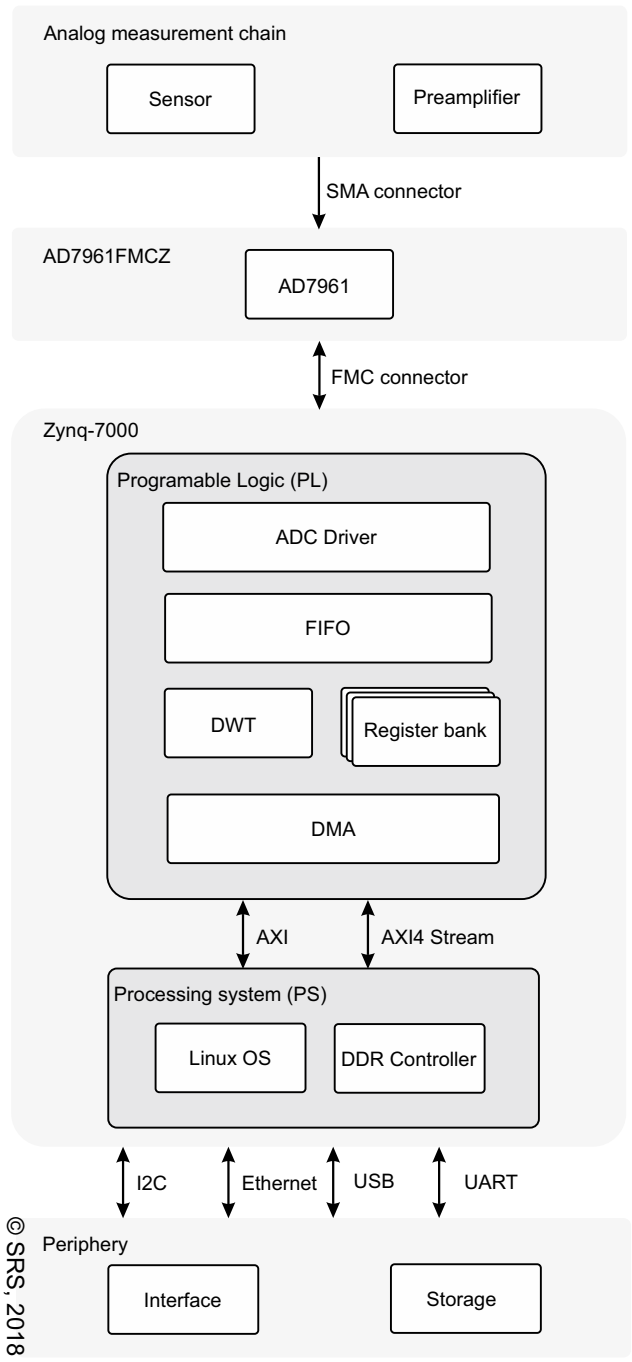

Figure 3.2: Illustration of the measurement system architecture [254].

3.1.2 Implementation of DWT module

The wavelet transform is a method for decomposition of non-stationary signals into joint time-frequency domain using a basis function, which is referred to as wavelet. In case of the DWT, decomposition of a signal can be achieved by using multirate filter banks, which are constructed from Finite Impulse Response (FIR) filters. Due to decimation of the input

signal by passing through each filter bank, the DWT provides a sparse representation of the input signal. Nevertheless, the original input signal can be reconstructed using DWT coefficients [22]. Furthermore, time complexity of the algorithm is $O(n)$. Therefore, DWT is well suited for denoising, data compression, and feature extraction in real-time applications.

Different architectures for hardware implementation of the DWT algorithm are proposed including pyramid and polyphase architectures [22]. Regarding sample-wise calculation of DWT coefficients it has to be noted that to ensure suitable reconstruction of the original signal, equalization of delays along all filter paths is required [21].

In equation 3.1 the well known implementation of DWT is given as

$$\begin{aligned} y_h[n] &= \sum_k x[n]h_0[k] \quad \text{and} \\ y_g[n] &= \sum_k x[n]g_0[k], \end{aligned} \tag{3.1}$$

where $y_h[n]$ and $y_g[n]$ are the outputs of the high- and low-pass filter, respectively. The related filter coefficients are denoted by $h_0[k]$ and $g_0[k]$. To obtain the DWT coefficients $y_h[2n]$ and $y_g[2n]$, the outputs are decimated by 2. For hardware efficient implementation of DWT, transformations including Noble entities are required to minimize the arithmetic workload and redundancies. Subsequently, polyphase realization using Quadrature Mirror Filter (QMF) pair as described in detail by Cunha et al. [63] is adopted. The main advantage of this approach compared to the classic implementation is the reduction of hardware resources required for synthesis of the algorithm (i.e. adders, multipliers, and number of clock cycles) by a factor of two.

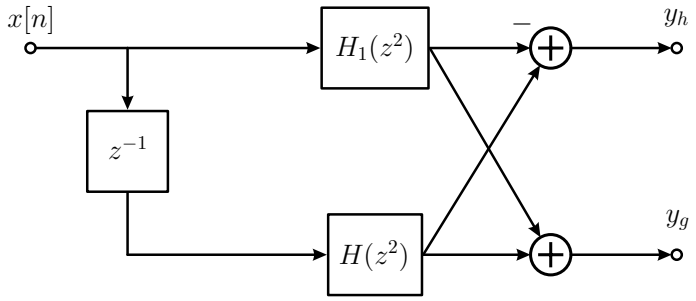

Figure 3.3: Block diagram of quadrature mirror filter, adapted from [254].

Implementation of 1-level DWT is illustrated in Figure 3.3. Here, $x[n]$ denotes a discrete-time input signal. By using QMF filter bank, the spectrum of $x[n]$ is divided into two sub-bands. Here, $H_1[z^2]$ and $H[z^2]$ denote the high- and low-pass FIR filters, which are defined by a finite set of coefficients referred to as taps. The number of taps is related to the filter order and the values are determined depending on the related wavelet basis and scaling function. The DWT coefficients are computed sample-wise as the corresponding output of

the high- and low-pass filter as

$$\begin{aligned} y_h[2n] &= \sum_{k/2} x[2n]h_0[2k] - \sum_{k/2} x[2n+1]h_0[2k+1] \quad \text{and} \\ y_g[2n] &= \sum_{k/2} x[2n]h_0[2k] + \sum_{k/2} x[2n+1]h_0[2k+1]. \end{aligned} \tag{3.2}$$

Here, $y_h[2n]$ and $y_g[2n]$ denote the details and approximation coefficients, respectively. Furthermore, $H(z^2)$ and $H_1(z^2)$ in frequency domain correspond to the time domain response $h_0[2k]$ and $h_0[2k+1]$ related to even and odd samples of $x[n]$. Multilevel DWT can be realized by cascading multiple QMF filter banks. In this case, approximate coefficients are used as input to the subsequent filter bank. In Figure 3.4 the implementation using cascading QMF filter banks is illustrated.

The DWT module is implemented using FIR filter with 12 taps and 12-bit quantization. The overall hardware utilization of single level DWT is shown in Table 3.1. It is worth mentioning that using QMF, only 12 taps are required as compared to 24 taps using the classic implementation. The raw data and DWT coefficients are stored temporarily in a FIFO queue and are transferred afterwards to the PS via direct memory access using AXI4-Stream interface. Additionally, maximum, minimum, mean, and energy of the DWT coefficients in each level are stored in the register bank, which is accessed via general purpose port.

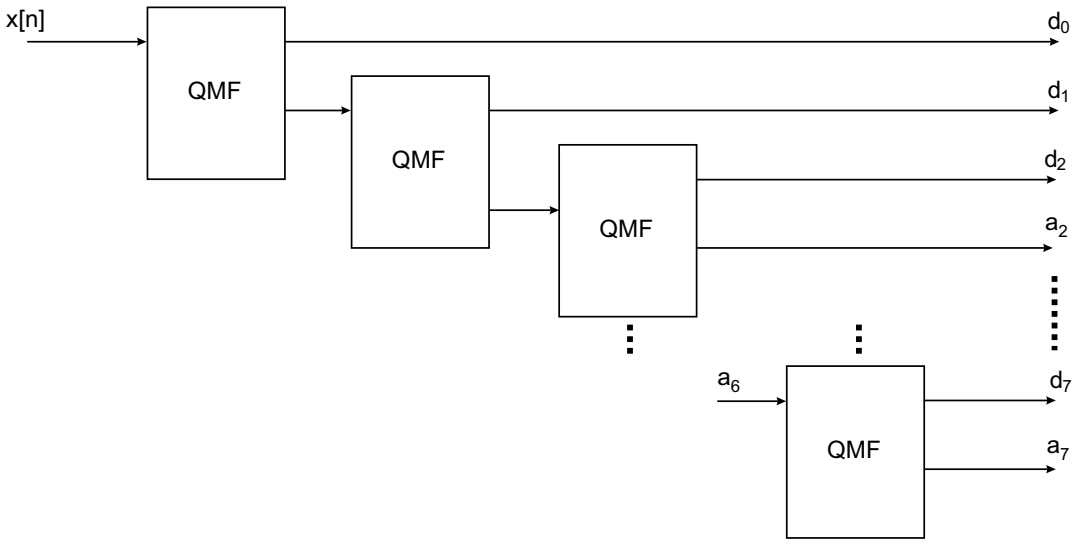

Figure 3.4: Illustration of cascaded filterbank [255].

Table 3.1: Hardware utilization of 1-level DWT module [254].

BRAM	DSP48E1	LUT	FF
116.5 (83.21 %)	12 (5.45 %)	7536 (14.17 %)	9274 (8.72 %)

3.2 Preliminary results

To demonstrate the use of the FPGA-based system for AE measurements, preliminary experiments are conducted. To record AE waveforms a disc-shaped piezoelectric element (0.55 mm in thickness, 10 mm in diameter, 3.6 MHz resonant frequency) is stiffly bonded to the surface of composite material by means of cyanoacrylic glue. Furthermore, a preamplifier is used for signal conditioning prior to digitalization. The raw waveforms are acquired with a sample rate of 5 MHz and 16 bit resolution. Additionally, DWT representation is calculated by the FPGA. Finally, both the raw waveform data and the corresponding DWT representation are stored. For further analysis and visualization, the data can be accessed via Ethernet. It is worth to mention that both the waveform data as well as the DWT coefficients are acquired in real time

3.2.1 Pencil lead break test

For initial tests of the measurement system, PLB tests were undertaken. Here, an AE source is simulated by breaking a pencil lead at the surface of a test specimen (Hsu-Nielsen source). As a result, a strong broad band acoustic signal is generated. This test is routinely used to check functionality of AE equipment. The results are presented in Figure 3.5 showing the raw measurement data and the DWT coefficients. The waveform is decomposed into the DWT coefficients d_0 – a_7 using 8 cascaded filter banks. Due to subsequent downsampling within each filter bank the bandwidth is reduced by a factor of 2. Thus, highest frequencies can be observed in level d_0 whereas lowest frequencies are located in level a_7.

3.2.2 Indentation testing of composite material

As previously reported by Baccar and Söffker [19], different micro-mechanical fracture mechanisms are expected to occur during indentation testing of composites. These include delamination, matrix crack, debonding, and fiber breakage, which can be distinguished based on peak frequencies of the AE signal [19]. During indentation testing, plate specimens of the dimension 425 mm x 425 mm x 1.8 mm are fixed using a clamping mechanism. Laminated cross ply material with woven fabric on the outer layers is used. During the test, the load is applied manually in transverse direction until fracture of the specimen. A sharp, cone-shaped indentation tool is used, which penetrates the surface of the material.

In Figure 3.6, the raw measurement data and cumulative energy at different levels of the DWT representation are shown. Here, several AE bursts are visible, which are related to the fracture of the material. In general the energy release rate (i.e. steps in cumulative energy) correlates well with the AE bursts observed in time domain. However, different distribution of energy among the frequency bands is evident. Furthermore, the bursts are unevenly distributed in time due to the stochastic nature of AE. Nevertheless, groups of successive bursts can be identified, which suggests a causal connection of their sequence.

For instance, a group of bursts, which follow each other closely in time, is visible after duration of 0.05 s. Considering the cumulative energy of each level, a rise of the red curve (level d_3) is detected during the first bursts, which indicates high peak frequencies. In contrast, the last burst in the group is related to a significant rise of the green curve (level d_6) and thus characterized by lower peak frequencies. Examples of the related signals are provided

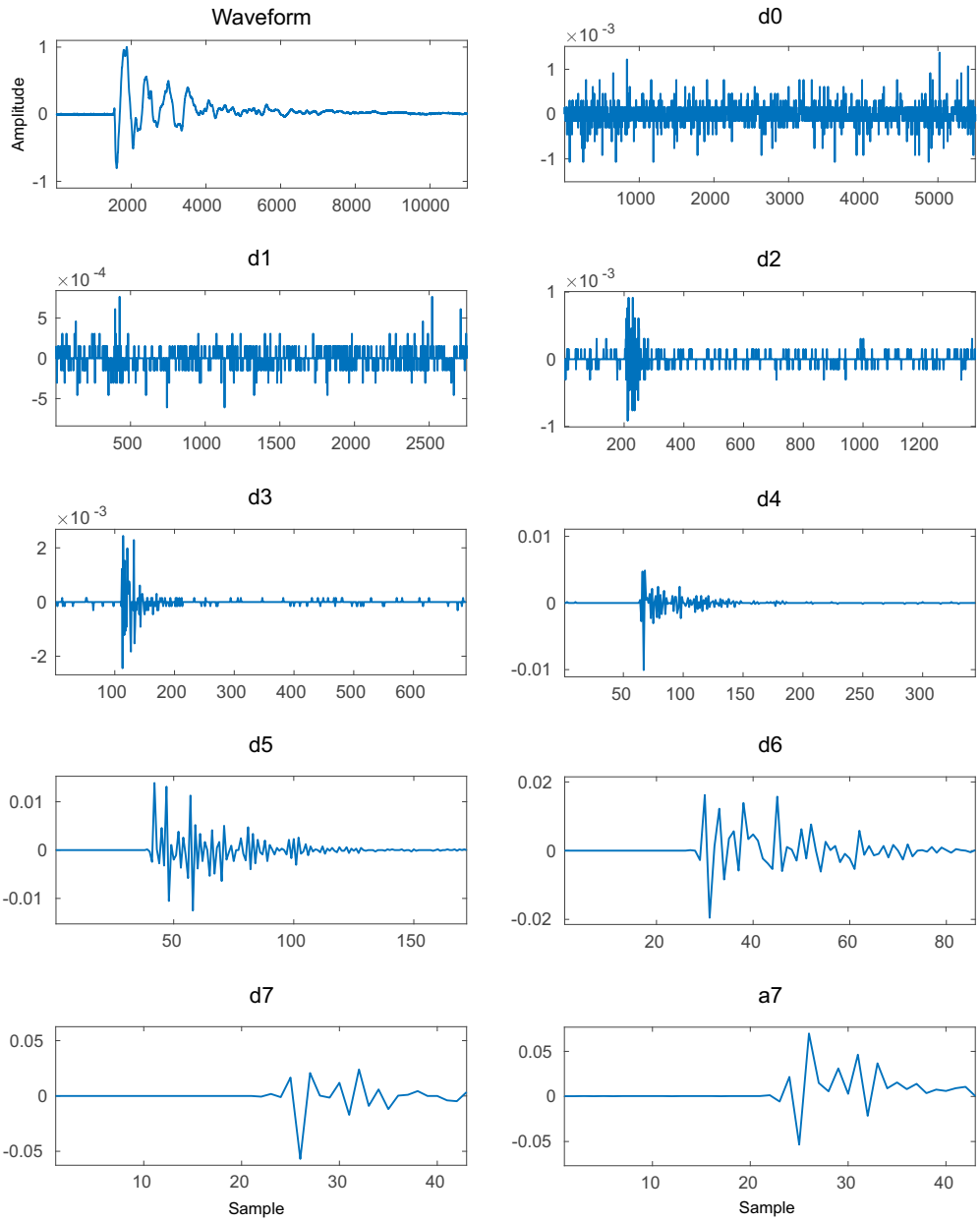

Figure 3.5: Decomposition of PLB into 8 DWT levels [255].

in the sequel. In Figure 3.7a, an example of high frequency AE burst is presented. Here, energy is primarily distributed in the scales d_3 and d_2 which corresponds to the frequency bands from 150 kHz to 312 kHz and from 312 kHz to 625 kHz, respectively. According to the literature, AE waveforms with peak frequencies above 350 kHz can be attributed to fiber breakage [19]. Similarly, the low frequency burst is shown in Figure 3.7b. Here, most of the energy is located in the level d_6 with the respective frequency band between 19 kHz and 39 kHz. The AE events with peak frequencies below 120 kHz are related to delamination of composites [19]. Thus it may be concluded that after fiber breakage subsequent delamination occurs due to stress redistribution.

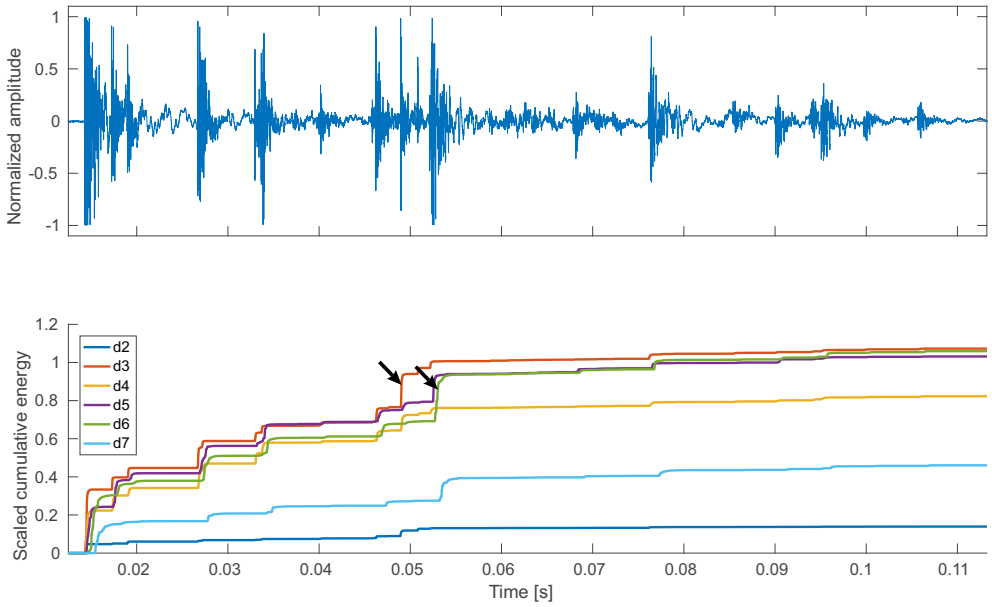

Figure 3.6: Raw data and cumulative sum of energy in different frequency bands [255].

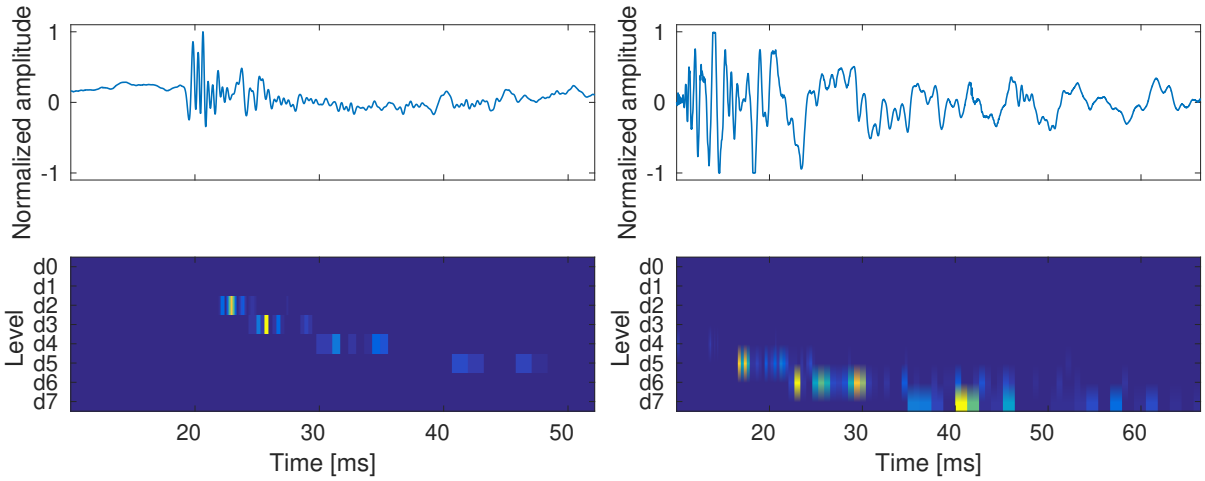

Figure 3.7: Time and time-frequency domain representation of AE bursts [255].

3.3 Summary

Regarding SHM, AE analysis is frequently used for highly sensitive in-situ inspection. Promising results have been reported in different applications such as process monitoring and control, where AE is suggested as highly sensitive in-situ measurement technique. However, most of the analyses are carried out offline due to the complexity of signal processing algo-

rithms (e.g. feature extraction and classification). To provide timely statements regarding the current system state or to realize related control actions, online processing of AE is required. In this chapter, a suitable low-cost solution is suggested. A hardware architecture is proposed, which is particularly suited for embedded implementations due to its small form factor and low power consumption. Waveforms are acquired with 16 bit resolution at a sample rate of 5 MHz. Furthermore, a FPGA-based implementation of DWT with 8 levels is used to calculate DWT coefficients in real time. The DWT coefficients can be stored along with the measurement data immediately. To demonstrate the use for AE measurements and signal processing, experimental results from PLB test and indentation testing are presented. In accordance with [19], different types of AE waveforms can be distinguished according to their frequency content. Furthermore, based on the cumulative sum of energy in different frequency bands, conclusions regarding the particular evolution of damage mechanisms can be drawn. In future work, a classification scheme can be implemented (in software and/or PL) to detect and distinguish different damage mechanisms automatically.

4 New results of Acoustic Emission for Structural Health Monitoring

Fault detection and classification are fundamental tasks in SHM. The detectability of damage is usually dependent on several factors including damage size or severity, sensitivity of the measurement equipment, environment, and experimental conditions. Furthermore, reliability of the damage classification, i.e. probability that a classification result is correct, has to be ensured. This chapter comprises several contributions regarding signal processing for damage detection, which were previously published as [251–253,257,258]. A new data-driven technique for detection of AE bursts is presented. Furthermore, new AE signal processing techniques to extract suitable features as input for classification algorithms are addressed. Reliability of SHM is discussed at the example of data-driven damage classification of composites. Finally, different effects on damage detectability due to wave propagation of AE are investigated experimentally.

4.1 Improved signal processing for acoustic emission using a data-driven approach

A key problem for processing AE measurements is to reliably identify relevant subsections of the measurement signal. Typically, a fixed threshold is used to distinguish between AE signals and noise. From an implementation point of view, this is approach is simple to realize and efficient. However, the choice of a suitable threshold is difficult. Therefore, a data-driven approach is suggested here, which takes preliminary measurements into account to determine a suitable threshold. This section is previously published as *Improved signal processing for acoustic emission using a data-driven approach*, which was presented at 9th European Workshop on Structural Health Monitoring [258]. The main contribution is the development of a method-oriented but practical methodology which can be used to determine a suitable threshold to distinguish between relevant subsections of AE measurements and noise.

4.1.1 Introduction

During continuous AE measurements, large amounts of data are acquired within a short amount of time. The ability to discard noise can reduce storage requirements and processing time. Therefore, extracting isolated signal patterns from continuously sampled data is important. This is of particular relevance with respect to waveform-based approaches, where increasingly complex algorithms for data analysis including time-frequency domain transformation and multivariate statistical methods are used. In contrast, many state-of-the-art AE systems use fixed thresholds to distinguish between relevant signals and noise. However, in practical applications this approach is inaccurate or even unfeasible due to low SNR.

In this section, a data driven approach to distinguish between relevant signals and noise is suggested. To identify a model from the AE data Platt calibration is used, which was developed to map the output of support vector machines to probabilities [184]. Here, implicit definition of the decision threshold allows taking into account data obtained from preliminary measurements such as PLB test. Furthermore, it has to be noted that in contrast to the related field of waveform picking, the focus is to determine a relevant subsection and not exact onset times.

In a first step, similarity of AE measurements to a baseline is computed. Furthermore, by determining the onset of the PLB signal manually or using a different method such as AIC, the measurement can be split in two disjoint sections containing the relevant signal and noise, respectively. Finally, a parametric model is derived from the obtained class-conditional distributions of distances using a curve fitting procedure. Based on this model a characteristic function which serves as a probabilistic measure indicating the presence of relevant signals can be computed. The feasibility of the approach is demonstrated using AE measurements from indentation tests of composite plates.

4.1.2 Background and related work

In general AE testing relies on passive monitoring of transient signals, which are related to elastic stress waves from different source mechanisms. The related signals are typically characterized by high frequency content and low amplitudes. Furthermore, relevant signals are transient and stochastically distributed in time. Therefore, large sections of noise are typically obtained in case of continuous monitoring. Research regarding signal processing of AE can be divided into (i) source characterization and (ii) waveform picking. In the following, a brief overview of the related works is presented.

To distinguish between different source mechanisms, features are used to emphasize characteristic properties of the related signals. By extracting suitable features, the interpretability of AE measurements can be enhanced. A detailed summary is given by Kaphle et al. [120]. In time domain, heuristic parameters are typically extracted from the measurements with respect to a fixed threshold. These include for instance maximum amplitude, rise-time, or energy. In contrast, waveform-based analysis refers to techniques, which consider the recorded waveforms as a whole. Here, signal features can be computed directly from raw data (e.g. higher order statistical moments) or using transformed representations in different domains (e.g. frequency- and time-frequency domain). Additionally, new parameters such as entropy and Chebychev moments were proposed for analysis of AE waveforms recently [52, 61].

In contrast, waveform picking focuses on finding the exact onset time of an AE waveform. Waveform picking is closely related to the task of AE source localization, where time-of-flight measurements are used to relate individual AE signals to their points of origin in a structure. A simple and in the field of AE testing widely adopted approach is amplitude thresholding. However, this approach is likely to provide inaccurate results leading to errors in the source location. Many advanced waveform picking approaches have their origins in the field of computational seismology [135]. Typically, a characteristic function is defined, which is used to emphasize the change of statistical properties of the measurements due to the presence of a signal. Then a user-defined threshold can be applied using the characteristic function instead of the raw data. For example, using the STA/LTA method, a characteristic function is defined using the ratio of average amplitudes within windows of different length

[135]. Thus, instantaneous changes in the amplitude distribution lead to peak values in the characteristic function. The onset of the AE signal can be detected by choosing a suitable threshold. Similarly, Rawles et al. [197] define a new characteristic function, which is based on the direct comparison between raw data and a reference set using a shape-based similarity measure. Furthermore, Pomponi et al. [186] propose a methodology based on wavelet block thresholding for onset detection. A thresholding rule is applied to individual subsections of each decomposition level leading to a binary mask that defines which coefficients are retained. The binary mask can be used to detect the onset of signals by finding the first non-zero element [186]. Using AIC [135], manual choice of thresholds is not required. The onset of the signal is determined as the global minimum of a characteristic function that can be computed sample-wise from raw data. Bai et al. [23] suggested an alternative approach based on surrogate significance test, which is independent of user-defined thresholds. The signal onset is determined as the intercept of different correlation functions.

4.1.3 Methodology

Subsequently, a new technique to extract relevant subsections from AE measurements is presented, which utilizes example data to determine a suitable detection threshold. As illustrated in Figure 4.1, the observed amplitudes of a continuously sampled AE signal belong to different probability distributions which are related to either relevant AE signals (i.e. transient waveforms referred to as hit) with superimposed noise or plain noise. However, the individual distributions are strongly dependent on the experimental conditions and the environment. Therefore, the choice of a suitable threshold is a trade-off between the sensitivity of the measurement system and rejection of noise and usually based on the experience of the operator. The underlying idea of the proposed approach is to estimate the probability that a given sample belongs to an AE signal using a parametric model. The parameters of the model can be identified from suitably chosen example data. Finally, the obtained model can be used to calculate a characteristic function to distinguish between relevant signals and noise by choosing a probability threshold. Thus, the related threshold in terms of the decision variable is defined implicitly, because it depends on the model parameters which are determined according to the example data.

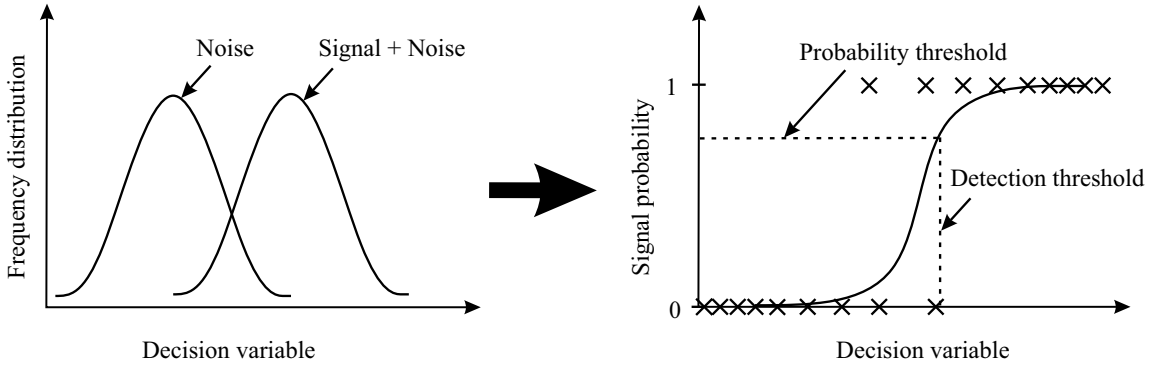

Figure 4.1: Illustration of the class-conditional amplitude distributions and mapping to signal probability [258].

To identify a model from the AE data, Platt calibration is used, which was developed to establish a mapping between numerical scores computed by SVM and probability estimates of the related classes [184]. As illustrated in Figure 4.1, two overlapping distributions of the decision variable are assumed. The sigmoid function

$$f(x) = \frac{1}{1 + \mathrm{e}^{Ax+B}} \tag{4.1}$$

is used as a model, where the parameters A and B are determined by a curve fitting procedure.

In the sequel, the AE measurement $S_{1:n}$ is assumed as a sequence of samples s_i in discrete-time

$$S_{1:n} = \{s_i,\, i = 1, 2, \ldots n\}\,, \tag{4.2}$$

where the duration between each sample is determined by a fixed sample rate. Each sample can belong to one of two classes i.e. noise ($y = 0$) or presence of AE signal ($y = 1$). Furthermore, signal probability refers to the likelihood that a given sample s_i belongs to an AE waveform. As decision variable the similarity of the measurement to a noise sample (baseline) is considered. For a given signal, the city block distance

$$d(S_{1:n}, N_{1:n}) = \sum_{i=1}^{n} |s_i - n_i| \tag{4.3}$$

is computed with respect to the noise sample using a sliding window.

To obtain an estimate of the class conditional probability $p(d|y)$, conditional densities $P(Y = \{0, 1\}|d)$ are determined after splitting the dataset into sections containing noise and relevant signals according to AIC using Maedas formula [135]

$$\mathrm{AIC}(i) = s_i\, \log(\mathrm{var}(S(1, s_i))) + (N - s_i - 1) \log(\mathrm{var}(S(s_i + 1, n))). \tag{4.4}$$

Finally, the parameters A and B of the sigmoid function are determined using least squares method. Given A and B, an estimate of the signal probability can be calculated as characteristic function by evaluating equation 4.1 sample-wise. Relevant subsections $S_{a:b}$ of AE measurements can be extracted by searching for contiguous blocks of samples exceeding a signal probability threshold T as

$$S_{a:b} = \{s_i \in S_{1:n} : s_i > \mathrm{T}\}\,. \tag{4.5}$$

In this case, the decision threshold is defined implicitly in terms of signal probability. The related threshold applied to the decision variable depends on the parameters A and B and thus is adjusted depending on the provided preliminary measurements.

4.1.4 Experimental evaluation

In this subsection, results of the experimental evaluation are presented. As an example, AE data from indentation testing of composite material are used. To detect relevant AE signals, the parameters of the related model are determined from PLB tests. The sensitivity of the

new approach is compared to an energy-based approach. Finally, examples of extracted waveforms are presented.

Experimental setup

The data which are used in the following are obtained from indentation testing experiments as described by Baccar and Söffker [19]. The mechanical test rig is illustrated in Figure 4.2. A plate with dimensions $425 \times 425 \times 1.8$ mm^3 of laminated cross-ply composite material with woven fabric on the outer layer is fixed horizontally below the indentation tool by using a custom clamping system. The AE sensor is stiffly bonded to the surface of the composite plate using cyanoacrylic glue. During the experiments, load is applied manually in transverse direction.

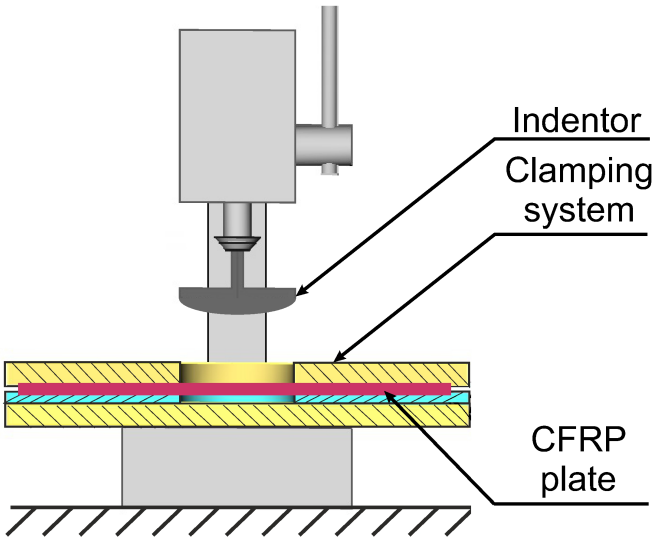

Figure 4.2: Illustration of the experimental setup [19].

A sharp, cone-shaped tool was used during the indentation test, which penetrates the material on increasing load. An example of a specimen after the test is shown in Figure 4.3. On the top side of the plate (Figure 4.3 (left)), typical indentation marks are visible at the surface. Apart from that, the surface remains undamaged. In contrast, extended damage can be observed on the bottom side (Figure 4.3 (right)). Here, buckling of the surface in a larger area indicates extensive delamination and damage to the matrix material. Furthermore, broken fibers of the woven fabric and a crack extending towards the top of the figure are visible.

Model fitting results

To determine the parametric model, measurements from three independent PLB tests are used. In Figure 4.4, results of fitting the model to the experimental data are illustrated. Figure 4.4a shows the obtained class conditional distributions of the decision variable after splitting the measurements into noise and relevant signals (hit) using AIC according to equation 4.4. Both distributions are skewed to the right and an overlap can be observed.

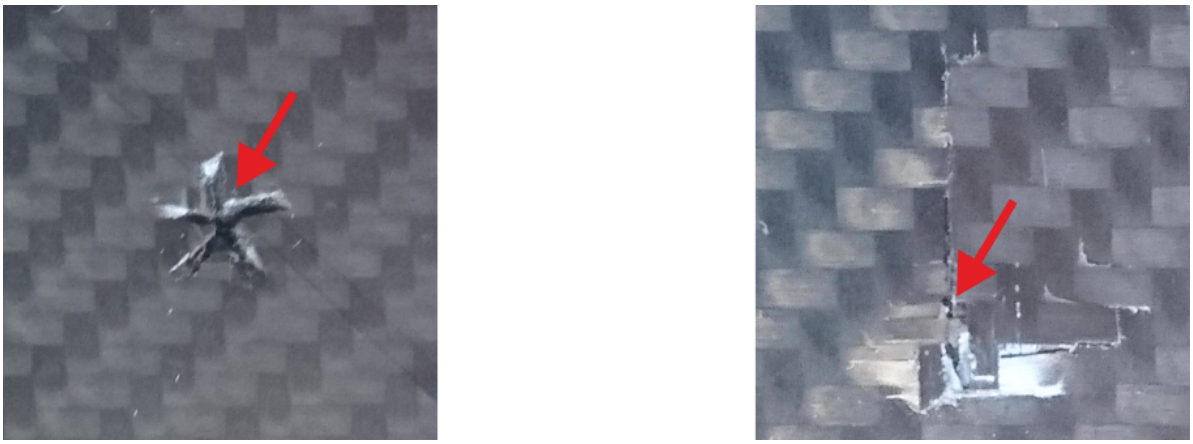

Figure 4.3: Close-up photograph of the composite plate (left: top, right: bottom) after indentation test [258].

However, the means are clearly separated. Compared to the amplitude distribution of relevant signals, the distribution related to plain noise is narrow and located at smaller values of the decision variable. The corresponding sigmoid function, which is used to model the mapping between the decision variable to signal probability is presented in Figure 4.4b.

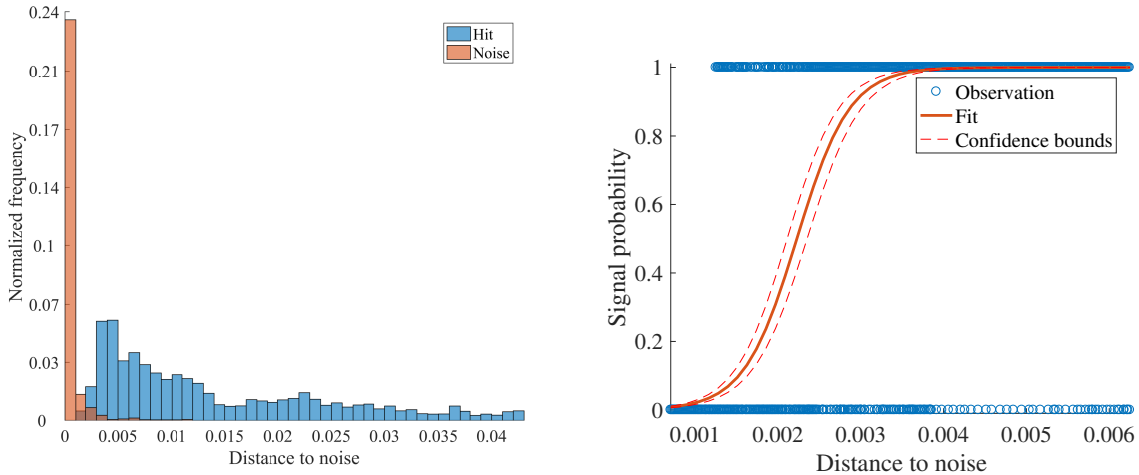

(a) (b)

Figure 4.4: Results of obtaining the model (a) histogram (b) curve fit [258].

Furthermore, results of several independent runs are summarized in Table 4.1. Here, additional artificial noise is added to the original measurements to investigate the effect of different SNR. It is noticeable that the absolute value of the parameter A, which controls the gradient of the sigmoid function, decreases due to lower SNR. Accordingly, the resulting sigmoid is stretched so that the corresponding signal probabilities are shifted towards larger values of the decision variable. Thus, sensitivity of the characteristic function is decreased in favor of improved noise rejection. Therefore it can be concluded that the adjustments of

the model parameters with respect to the example data are reasonable.

Table 4.1: Parameters determined for different SNR using three independent PLB [258].

SNR [dB]	A	B
60	-3191.80	7.13
30	-1512.82	9.69
25	-605.87	6.12

Sensitivity analysis

Given the model parameters, the signal probability can be estimated by evaluating the sigmoid function sample-wise. The result can be used as a characteristic function to detect relevant subsections of the AE measurement. In the sequel, the sensitivity of the signal probability as a characteristic function is compared to the energy envelope using ROC curves. For this type of analysis a ground truth is required. In Figure 4.5, a subsection of a measurement obtained during early stage of indentation test prior to the fracture of the specimen is shown. To obtain a ground truth for ROC analysis, this section has been labeled manually. Samples which were labeled as relevant AE signals are highlighted in green color.

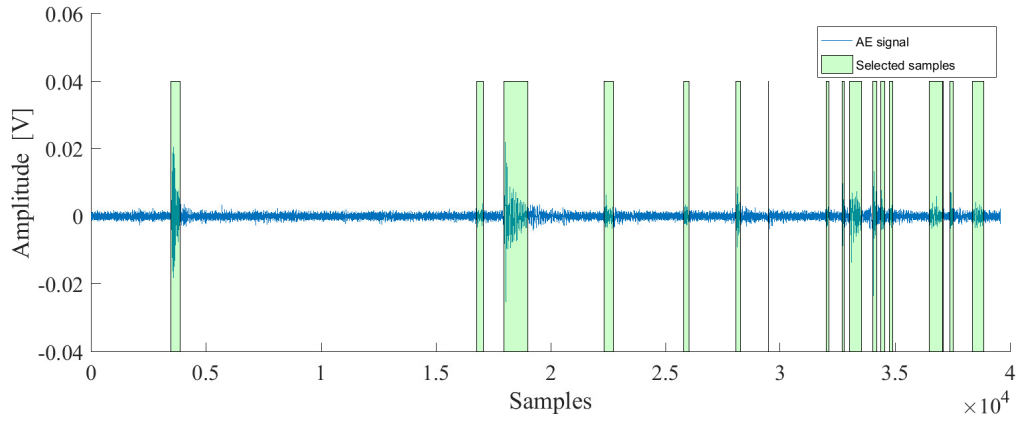

Figure 4.5: Ground truth for ROC evaluation [258].

In Figure 4.6 the results of the ROC analysis are presented for different values of SNR. The top right corner of the ROC corresponds to the lowest threshold, where each sample is detected as a relevant signal. Moving along the curve to the left, the ROC shows the behavior of true positive and false positive rates on increasing thresholds. Here, a decrease in false positive rate can only be achieved at the cost of a reduction in true positive rate. Improved performance of the detection algorithm is achieved as the ROC approaches the top left corner (i.e. high true positive rates are maintained while reducing the false positive rate). Therefore, the area under the ROC is frequently used to assess sensitivity of classification algorithms [156]. According to Figure 4.6, both estimated signal probability and energy envelope show decreasing areas under the ROC in case of lower SNR, thus indicating a

reduction in sensitivity due to the effect of noise. However, especially in the range of lower thresholds the ROC of the estimated signal probability as characteristic function (solid line) is clearly located above the ROC obtained using energy envelope (dashed line) indicating improved detection rate. Also, regarding the lowest SNR, the solid line indicates improved detection rate of the estimated probability over a wide range of possible thresholds. Thus, it can be concluded that in comparison to the energy envelope improved sensitivity can be achieved using the estimated signal probability.

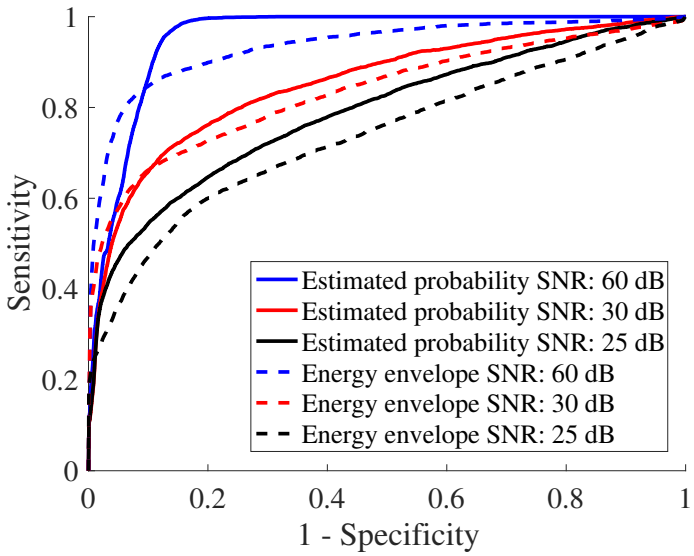

Figure 4.6: Comparison ROC curves using signal probability and energy envelope for different SNR [258].

Moreover, extraction of relevant waveforms from an AE measurement can be realized by searching for contiguous subsections of the signal exceeding a probability threshold. Using equation 4.5, relevant subsections were extracted from the subsection presented in Figure 4.5. Two examples of AE waveforms obtained at SNR of 30 dB and threshold of 0.1 are presented in Figure 4.7. In the first example (Figure 4.7a) the signal amplitude is large compared to the noise floor leading to a corresponding mean signal probability of 80.8 %. In contrast, the distance between the signal and the noise floor is smaller. Accordingly, lower mean signal probability of 36.27 % is obtained (Figure 4.7b).

4.1.5 Summary and conclusion

In this section, a new methodology to extract relevant waveforms from AE measurements using Platt calibration is presented. A parametric model of the data is determined using preliminary measurements. To distinguish between noise and relevant signals, the detection threshold is defined implicitly in terms of signal probability and adjusted according to the provided data. Experimental evaluation of the approach is presented at the example of AE measured during indentation test using laminated composite material. The results of multiple runs using different SNR indicate that the parameters of the fitted model are adjusted reasonably depending on the SNR. Furthermore, the sensitivity of the methodology

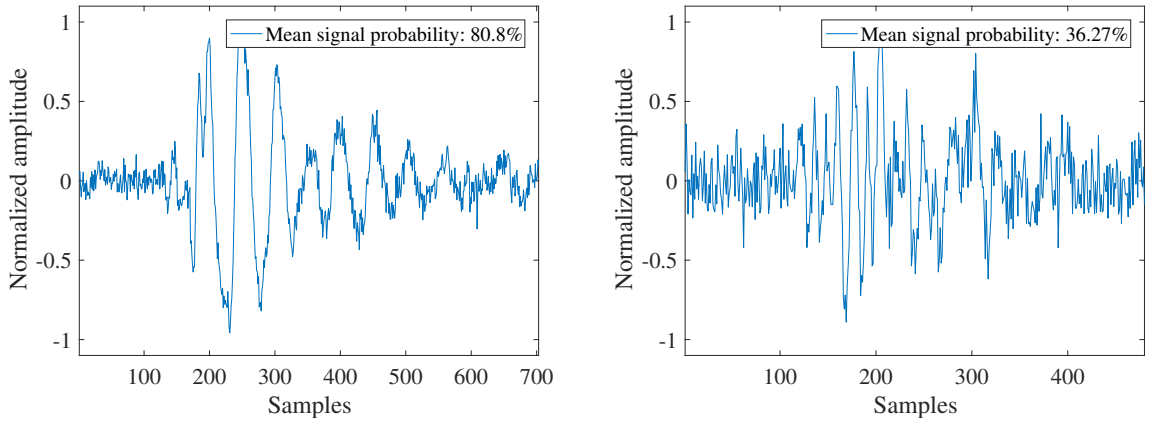

(a) (b)

Figure 4.7: Examples of extracted hits (a) high probability (b) low probability [258].

is compared to the energy envelope of the AE signal using ROC. From the results it can be concluded that improved sensitivity can be achieved for low thresholds.

4.2 Frequency-based damage detection of spur gear using wavelet analysis

The use of AE to monitor rotating machinery received considerable attention during the last decade. Key topic is suitable sensor placement. To achieve highest sensitivity, sensors are frequently, mounted on moving parts. Subsequently, mounting of AE sensors on the housing of a gear box is explored as an alternative approach. This is considered as relevant for the practical application of AE to gear box monitoring. An experimental investigation regarding AE signatures of different damage modes in a spur gear system is presented. As main contribution it can be stated that AE signatures related to different wear states of the gears can be detected using AE sensors mounted outside the housing of the gear box. The remainder of this section is based on the conference publication *Frequency-based damage detection of spur gear using wavelet analysis*, which was presented at 8th European Workshop on Structural Health Monitoring [253].

4.2.1 Introduction

Gear transmission systems are power transmitting elements, which are key components of modern drive trains. Due to cyclic loading patterns during operation, gear teeth are prone to fatigue failure. Depending on lubrication and loading conditions, also surface deterioration of the tooth flanks is observed. Besides wear, micro-pitting and pitting are typical damage modes in gear transmission systems. Pitting is known as surface fatigue, where subsurface cracks nucleate beneath the surface of the tooth flanks. Due to cyclic stresses, these cracks propagate through the material. Eventually, reaching the surface these subsurface cracks lead to extensive loss of material and formation of pits at the surface of the tooth flanks. In contrast to pitting, micro-pitting starts at the surface of the tooth flanks, where microscopic

pits can be observed. These are detected from visual inspection by gray appearance of the tooth flanks. Besides transmission errors due to resulting profile deviations, surface cracks possibly initiate at deteriorated surfaces and propagate into the body of the gear tooth, ultimately leading to gear tooth bending fatigue failure.

Recently, AE measurements received attention for monitoring of gear systems. Tan and Mba [234] as well as Hamel et. al. [103] identified asperity contact as major source of AE in meshing gears. During a meshing cycle, sliding and rolling contact of the mating surfaces occurs, where the teeth surfaces are subjected to normal and tangential forces, respectively. Continuous AE activity is presumably related to sliding contact of asperities, whereas burst type emissions are attributed to rolling contact of the gears [234]. Furthermore, bearing faults are masked by the meshing of the gears [77]. Therefore, the AE measurements are considered for detection of different damages in gear boxes, i.e. pitting [233] or tooth root crack [148].

However, monitoring of rotating machinery, such as gears, is challenging due to difficult sensor placement options. Singh et al. [226] conducted a transmissibility study on a gear test rig, where the attenuation of AE signals across different interfaces is investigated. The results indicate that AE attenuation is strongly dependent on the particular interfaces. Therefore, optimal propagation path, which provides the least attenuation, is not necessarily determined by the shortest propagation distance or the least amount of interfaces. To achieve low attenuation of the AE amplitudes, AE sensors are frequently mounted directly on the gears. To this end, a slip-ring is most frequently used to connect sensors attached to rotating parts to the acquisition hardware [76, 103, 194, 233–235, 239].

To avoid attaching sensors to moving parts, AE sensors are frequently mounted on fixed parts of gear box bearings (i.e. bearing races) [233, 239]. Moreover, Loutas et al. [149] developed a custom mounting fixture for AE sensors based on friction contact, where constant contact force between the fixed sensor and the rotating wheel is achieved by a spring element. Sensor location was verified using attenuation tests, where pencil-lead break tests were performed at different locations. The results show variable attenuation of the AE signal depending on the source location. Furthermore, the measurement noise inherent to the proposed mounting procedure was investigated by running the gear box without pinion and RMS levels of AE due to friction contact are determined. Comparing these RMS levels to normal operation (wheel and pinion) it is shown that noise RMS is considerably lower than RMS of AE due to meshing gears.

Typically time-domain features such as count rate, peak amplitude or rise time are considered to characterize burst type AE signals. In context of gears, RMS value of the signal is frequently used to extract diagnostic information from the continuous or mixed AE waveforms [76, 149, 194, 234]. Also higher order statistical moments of the signal, for instance kurtosis [148] or crest factor [103] are used to identify damage-specific features of different gear box damages. Furthermore, Al-Balushi et al. [6] suggest energy index, which is an time domain energy-based statistical feature, for extraction of diagnostic information from AE measurements. However, only few researchers consider the frequency content of AE measurements to assess the condition of gears. Toutounzakis et al. [240] identify the frequency range of AE associated with gear meshing as 25 kHz to 350 kHz. Scheer et al. [215] use wavelet analysis to extract damage specific frequency-domain features from AE measurements. In this context, tooth root crack and pitting faults are considered. By comparing AE measurements of each fault to a reference condition, short time pulses showing frequen-

cies between 200 kHz and 250 kHz are clearly identified and attributed to tooth root crack. In contrast to this, a broad band response of increased duration is observed in context of pitting, where different effects below 100 kHz and up to 400 kHz are observed. Therefore, similarly precise mapping of frequencies is not provided in this case.

Regarding the experimental procedures, damages are most frequently introduced artificially. For instance, Mazal et al. [162] use seeded gear damages by partially removing teeth by means of grinding. Also, Eftekharnedjad and Mba [76] investigate the detectability of seeded defects in a helical gear box using AE measurements. A drill is used to introduce seeded defects of different sizes, which are recognized from the time domain representation of the AE measurements. Loutas et al. [148] use a cut close to the dedendum of a tooth to simulate tooth root crack. In contrast, some researchers consider natural damages during their experiments. For instance Hamel et al. [103] consider natural pitting, which was introduced by prolonged running of the gear box. Also Tan et al. [233] consider natural pitting faults to compare the sensitivity of different diagnostic methods to natural faults.

Comparing the AE technique and vibration analysis, several authors conclude that AE is more sensitive to incipient damages than vibration analysis. Eftekharnedjad and Mba [76] state that in case of seeded defects, AE measurements are more sensitive to damage than vibration measurements. Also, Loutas et al. [148] compare the performance of vibration and AE technique for diagnosis of gears. In total, more than 40 signal features, containing conventional time domain as well as wavelet based features, are considered. The results indicate superiority of the AE technique over vibration technique for early detection of damage. Moreover, Tan et al. [233] compare three different condition monitoring techniques: AE, vibration analysis, and spectrometric oil analysis. According to the experimental results, the sensitivity of each method depends on applied torque during operation.

Furthermore, dependencies between gear box operating conditions and AE activity are investigated. According to Tan and Mba [235], rate of wear and therefore AE activity are related to oil film thickness. Raja Hamzah and Mba [194] state, that operating conditions which primarily effect specific oil film thickness are temperature, load, and speed. Experimental results indicate strong coupling between AE RMS levels and gear box speed [234, 235, 239]. Additionally, Toutountzakis and Mba [239] distinguish an instantaneous effect of changes in drive speed and a subsequent settling period. Furthermore, increase in AE RMS is also observed on increasing loads. Compared to the impact of speed the effect of load is less pronounced [194, 235]. In particular, Tan and Mba conducted experiments under different loads, where maximum temperature deviations are reported as 3.5°C. From the results, it is concluded that the effect of load on AE activity is negligible under isothermal conditions supporting the view that oil temperature is the dominant influencing factor on AE in gear boxes [235]. Moreover, Hamel et al. [103] investigate the effect of oil film thickness on the AE generation of defective gear teeth. In connection with natural pitting defects, the statistical parameters RMS, kurtosis and crest factor of the AE waveforms show decreasing values with increasing specific oil film thickness. Similarly, Toutountzakis and Mba [194] conclude that increased RMS values on increasing loads are related to a reduction in oil film thickness. These results indicate that AE is a suitable means to characterize friction contact of tooth flanks.

In this section, results of cooperative work between the Chair of Industrial and Automotive Drive Trains, Ruhr-Universität Bochum and the Chair of Dynamics and Control, Universität Duisburg-Essen are presented. Experiments were conducted to investigate the detectability

of different wear states of gears by means of AE measurements using sensors outside the housing of a gear box. To this end, a standard gear test rig located at the Chair of Industrial and Automotive Drivetrains, Ruhr-Universität Bochum is used and examined using the AE-equipment developed at the Chair of Dynamics and Control, University of Duisburg-Essen [18]. Besides normal operation, the damage modes micro- pitting and pitting are considered.

4.2.2 Experimental setup

To investigate the detectability of different damage modes in gear transmission systems, experiments were conducted. In the sequel, the experimental setup and signal processing are described. This includes the gear box test-rig, data acquisition, and signal processing. To relate the observations to actual machine states, a priori knowledge is used.

Gear box test-rig

The measurements were performed on a standard gear box test rig, which is usually used in connection with standardized procedures for wear-testing of lubricated gears. Originally, this test rig was developed at Forschungsstelle für Zahnräder und Getriebebau (FZG). A schematic drawing of the FZG test rig is shown in Figure 4.8. The test rig contains two cylindrical gear stages, namely testing and slave gears in a back-to-back arrangement. The slave gears are driven by an electric drive. Static torque loading of the gears is achieved via a torque clutch. Defined loads, which are specified in terms of Load Stage (LS), can be applied by means of calibrated weights and a lever arm. Thus, the electric drive only provides energy losses due to friction resulting from the gears and bearings according to the principal of circulating power. Lubrication of the gears is realized using immersion lubrication. During the experiments, similar pairs of gears in different condition, including normal operation, micro-pitting and pitting, were used. The pinion of each pair has 16 teeth which meshes with the wheel with 24 teeth providing a transmission ratio of $i = 1.5$. The wheel was driven at a speed of 1450 rpm providing rotational speed of 2175 rpm at the pinion shaft, which corresponds to a gear meshing frequency of approximately 580 Hz. Furthermore, the AE sensor was mounted outside the housing of the gear box in a horizontal orientation above the roller bearing of the pinion, as indicated in Figure 4.8. Besides the interface between the AE sensor and the housing, several interfaces are encountered along the propagation path including gear/shaft as well as shaft/bearing and bearing/housing interfaces. Because this bearing supports mainly radial loads, optimal transmission of AE is expected in this position.

Data acquisition

To record AE, detection of small surface displacements is necessary and therefore high sensitivity of the measuring system is required. During the experiments, a custom measurement chain was used that has been specifically designed for AE measurements and was successfully applied to characterize the wear state of metallic plates under sliding contact [18]. Disc-shaped piezoelectric elements of 0.55 mm thickness and diameter of 10 mm featuring a resonant frequency of 3.6 MHz were used. The AE waveform data was sampled continuously at a sample rate of 4 MHz. Time-frequency domain analysis of the measurement signal was

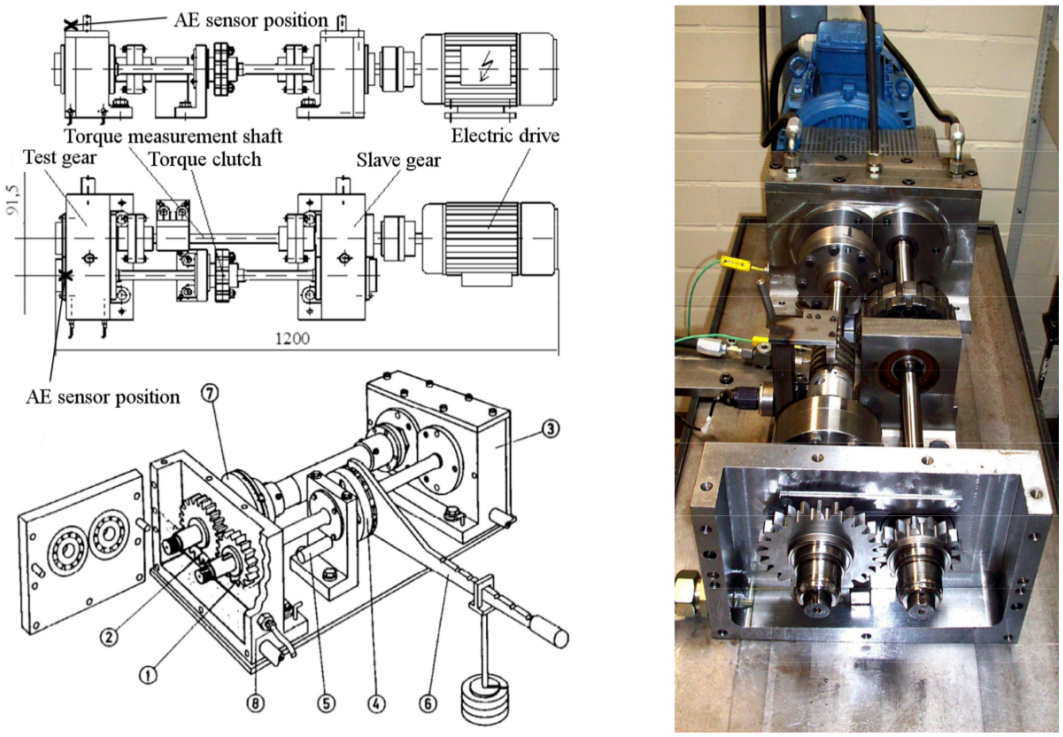

Figure 4.8: Illustration of FZG standard test rig, © Chair of Industrial and Automotive Drivetrains [253].

performed by means of continuous wavelet transform. Furthermore, rescaling of the obtained matrix of wavelet coefficients was performed for illustrative purposes. Due to increasingly low signal intensities on increasing frequencies, each row was normalized to a maximum value of 1. Thus, decoupling of the color scales at different frequencies is achieved. This procedure allows highlighting of low intensity effects at high frequencies.

4.2.3 Results

In the sequel, results of AE measurements from a FZG gear box test rig are presented. First, the sensitivity of the measurement chain to the meshing of the gears is verified by comparing the measurement results obtained under different operating conditions. Hereafter, joint time-frequency domain representation of measurement results obtained from different machine states is studied in detail. Here, different patterns are recognized depending on the wear state of the gear box and the causal relation to different damage modes is discussed. In Figure 4.9a, measurement results of the gear box under normal operation are shown in time-domain representation. In this case, the gears are fault free, which is considered the reference condition. The signal is characterized by transient waveforms, which show a periodic pattern of similar peak amplitudes. Furthermore, the period duration is approximately 1.7 ms, which corresponds to a frequency of 588 Hz. This matches the theoretical meshing frequency of the gears, indicating that the measurement signal is dominated by the meshing of the gears.

For comparison to the baseline pattern, measurement results from faulty gears are presented in Figure 4.9b. Visual inspection of the gears prior to the experiment revealed pitting

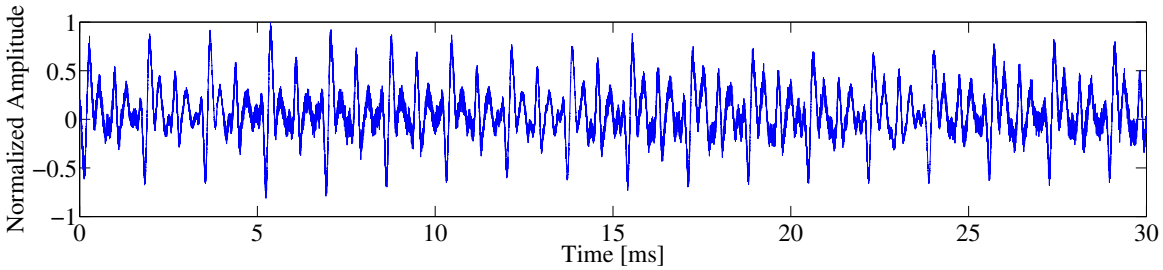

(a) Normal operation (fault free).

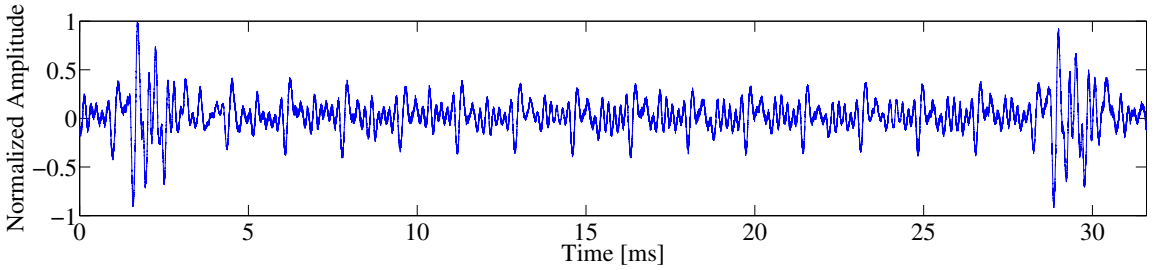

(b) Faulty condition (pitting).

Figure 4.9: Time-domain representation of measurement results [253].

at a single tooth of the pinion, while the wheel was classified as fault free. Here, the pitting defect acts as a marker indicating a full rotation of the pinion. From the measurements, a similar periodic pattern is observed. However, compared to the baseline pattern, additional discrete events are observed showing comparably large peak amplitudes. In between each peak amplitude event, 16 periods of the baseline pattern are observed. This is another strong indication of the causal relation between the observed periodic pattern and the gear mesh. Apparently, the observed baseline pattern is related to the meshing of the fault free pinion teeth and the wheel whereas peak amplitude events are observed each time the faulty tooth enters the mesh.

From the above considerations it can be concluded that the measurement chain is sensitive to the meshing of the gears. Furthermore, gear meshing seems to be dominant component of the measurement signal compared to possible additional sources of AE, i.e. roller bearings of the gear box, which is consistent with literature [77]. In the sequel, results of joint time-frequency decomposition of the AE measurements are presented. Different operating conditions are considered, including normal operation (fault free) under different loads as well as micro-pitting and pitting.

Load stages

In the following, normal operation is considered as reference condition. Using FZG test rig, defined loads (Load Stage (LS)) can be applied to the gears using calibrated weights and a lever arm. To investigate the effect of different loading conditions on the baseline pattern, measurements were performed with fault free gears under different loads. Examples of the measurements time-frequency decomposition obtained from the load stages LS 8 and LS 10 are presented in Figure 4.10. Besides a noise floor at approximately 400 kHz, peak

frequencies are observed in the spectrogram at frequencies between 50 kHz and 60 kHz.

These results are consistent with those obtained by literature. Toutountzakis et al. [240] reported the frequency content of gear mesh in the range of 25 kHz to 350 kHz. Furthermore, frequency content below 20 kHz is generally considered as measurement noise [233]. In contrast to this, similar effects were not apparent at loads below LS 8. Similarly, Hamzah et al. [194] reported increasing AE RMS levels on increasing loads, which is attributed to an increase of asperity contact due to a reduction of the oil film thickness. Therefore, increased energy of the AE signal at these frequencies is presumably related to an increase in asperity contacts and thus indicating increased wear rates.

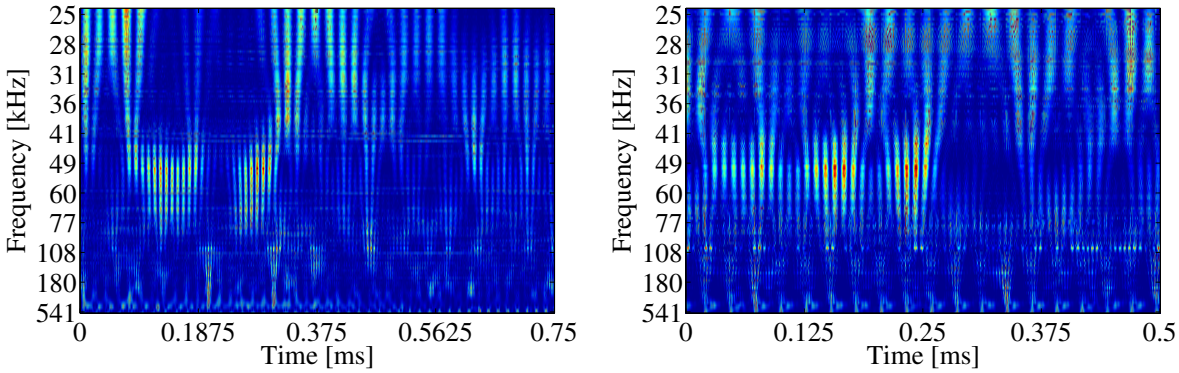

(a) LS 8 (b) LS 10

Figure 4.10: Time-frequency domain representation of measurement signal of normal operation under different loads [253].

Micro-pitting

In the following, the baseline pattern is used for comparison to identify characteristic, damage-related patterns from faulty gears. Here, a different set of gears is used. Prior to the experiments, visual inspection of the gears revealed matte gray surface appearance of several tooth flanks indicating micro-pitting as damage mode. The corresponding time-frequency decomposition of the measurement signal is presented in Figure 4.11. Compared to the baseline examples, additional patterns are observed in the ultrasound regime. Besides increased activity in the lower frequency range below 60 kHz, a downshift of the peak frequencies to approximately 30 kHz is observed. Furthermore, additional effects in the frequency range above 100 kHz are apparent. The increase in the energy content at the lower frequencies below 60 Hz is likely related to increased surface roughness of the tooth flanks. In principle, increase in surface roughness leads to a reduction in specific oil film thickness causing increase in asperity contacts [40]. Hence, energy in this frequency range is suspected to indicate deteriorated surfaces of the tooth flanks. Presumably, AE activity at increased frequencies above 100 kHz is attributed to wear related processes. Geometric stress concentration due to surface defects (i.e. tooling, debris dents, and disruption of the lubricating film in general) as well as the hydraulic-pressure-propagation mechanism are suspected as underlying mechanisms causing fatigue cracking of the material [81].

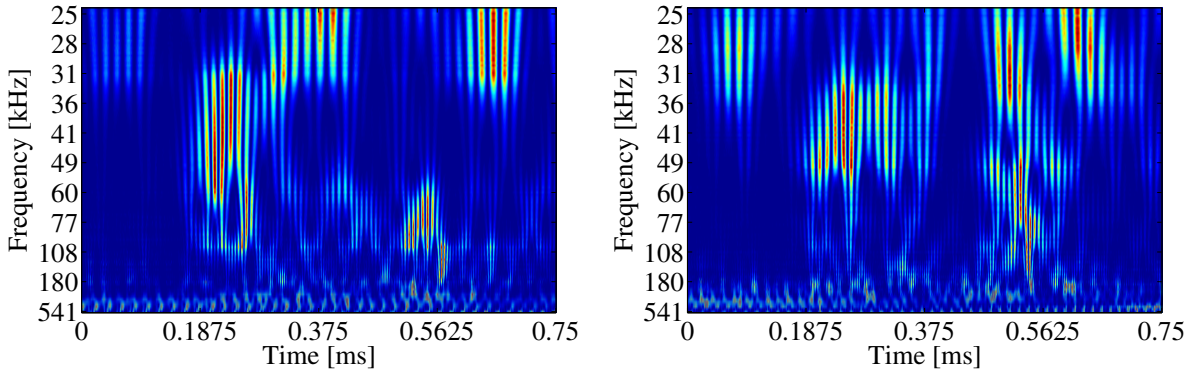

Figure 4.11: Time-frequency domain representation of micro-pitting [253].

Pitting

Finally, similar measurements were performed with a pair of gears containing pitting damage. During visual inspection of the gears, pitting was identified at a single tooth of the pinion whereas the wheel was fault free. Additional surface deterioration was not apparent. Results of the time-frequency decomposition of the signal obtained during meshing of the damaged tooth are presented in Figure 4.12. Here, a broad-band response between 30 kHz and 400 kHz is observed. Similar results were reported by Scheer et al. [215]. Compared to the frequency content associated with micro-pitting, an upshift of peak frequencies in the lower frequency band is observed. These are mainly located above 40 kHz. However, these results are matching the reference condition, indicating the absence of abnormal surface roughness. Furthermore, disruption of the elastohydrodynamic lubrication film at the pitting damage is expected. Therefore, peak frequencies below 60 kHz are suspected to result from asperity contacts between damaged gear surface and the mating gear. This is again a strong indication that peak frequencies below 60 kHz are related to the wear state of tooth flank surfaces. Additionally, during the experiments high frequency components are observed for the first time, which are suspected to be related to underlying mechanical fracture processes, e.g. crack initiation or propagation.

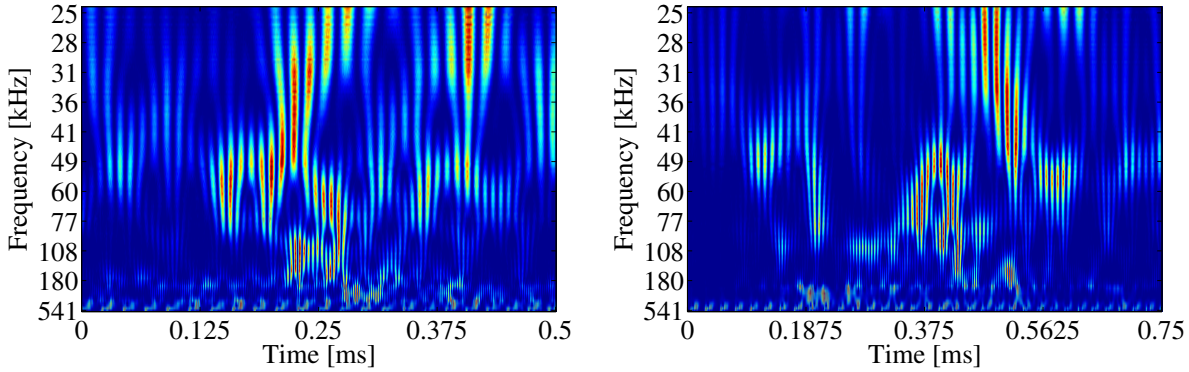

Figure 4.12: Time-frequency domain representation of pitting [253].

4.2.4 Summary and conclusion

Experiments were conducted on a spur gear test rig under different operating conditions including normal operation of fault free gears under different loads as well as different damage modes (i.e. micro-pitting and pitting). Despite attenuation due to multiple interfaces along the propagation path, the meshing frequency of the gears can be obtained directly from the time domain representation of the AE signal. Moreover, damage specific signatures in the joint time-frequency representation of the measurement signal could be identified depending on the condition of the gears. From these results the following can be concluded:

i) The gear meshing is recognized from static sensors mounted outside the housing of the gear box.

ii) Different damage modes can be recognized and distinguished from the time- frequency decomposition of the AE signals.

Furthermore, indication of deteriorated surface of the tooth flanks is suspected by peak frequencies in the lower ultrasound regime (i.e. 20 kHz to 60 kHz). Moreover, AE activity attributed to wear related processes (i.e. fatigue cracking of the material) is presumably located in the ultrasound regime at frequencies up to 400 kHz.

4.3 Shape-based similarity measures for classification of Acoustic Emission

Recently, the use of shape-based similarity measures has been suggested for waveform-based analysis of AE data [55]. For instance, Euclidean distance or Dynamic Time Warping (DTW) can be used to calculate the similarity between AE waveforms. The main contribution of this section is the comparison of different shape-based similarity measures at the example of clustering and classification of different AE source mechanisms. According to the results it can be stated that DTW can be used to mitigate the effects of waveform distortions including misalignment and additive noise to improve robustness of the classification. The following section is based on previous publication *Application of Shape-based Similarity Measures to Classification of Acoustic Emission Waveforms*, which was presented at the 11th International Workshop on Structural Health Monitoring [257].

4.3.1 Introduction

To develop an in-depth understanding of AE source mechanisms, detailed waveform analysis is required. Frequency- and time-frequency domain approaches are extensively used to deal with AE waveform data [121]. While competing methods use different statistics, cross-correlation, or autoregressive coefficients, detailed investigation of raw AE waveforms in time domain has not received much attention. In the data mining field, time series data receives particular attention. Shape-based approaches focus on distance calculation between time series as similarity measure. The idea also gained attention in related research fields, e.g. in computational seismology [197], to detect arrival times of seismic waves. Recently, the use of shape-based approach for the analysis of AE data was suggested [55].

In time series data mining, shape-based distance measures are frequently used to assess the similarity of time series objects. Considering each time series as a high dimensional feature vector, the distance of two time series can be computed using Lp-norms such as Euclidean distance. This approach is highly attractive, as it is parameter-free. Due to strict point-to-point comparison these measures are sensitive to scaling and time warping (i.e. non-linear shifting on the time axis causing local stretching or compression of the signal). While the former can be addressed by suitable normalization of the data, DTW is frequently used to achieve invariance of distance calculations to warping. Thus, DTW allows compensating for misalignment of individual time series elements.

In this section different similarity measures for shape-based classification are evaluated using hierarchical clustering, which is a typical approach. A reference dataset is constructed using pencil lead break tests in different orientations to simulate different physical AE sources (i.e. in-plane and out-of-plane source motion). Experiments are performed using thin plates of composite material. Subsequences of the AE signal in close proximity to a hit are considered. Hierarchical clustering as a typical approach is used to verify the suitability of different distance measures to assess the similarity of AE waveforms. Finally classification accuracy is assessed using different distance measures and one-nearest neighbor (1NN) classifier.

4.3.2 Related work

Regarding time series data, information is not only represented by values of variables, but also implicitly encoded in the particular sequence of occurrence. Therefore, defining a meaningful similarity measure for time series data is non-trivial. Esling and Agon [82] define similarity of time series informally as "recognition of perceptually similar objects even though they are not mathematically identical". According to a recent review, different approaches to assess the similarity of time series objects can be grouped into i) shape-based, ii) compression-based, iii) feature-based, and iv) model-based approaches [3]. Similarity can be estimated by comparing the compression ratio of different time series using standard compressor algorithms [122]. Shape-based similarity measures operate directly on the raw data, whereas feature-based or model-based approaches (i.e. statistics, autoregressive models) capture structural similarities of time series. Therefore, shape-based similarity is particularly suitable for detailed comparison of local patterns in time series data [3].

Time series data can be subject to several transformations, including uniform and time varying shift (additive) or scaling (multiplicative) in time and amplitude as well as additive noise or outliers [82]. Therefore, suitable normalization is crucial [195]. Most frequently, z-normalization (zero mean, unity standard deviation) is used [195]. Here, only amplitude scaling and shift are addressed. Depending on the application, additional invariances are required [28].

4.3.3 Methods

Subsequently, a brief description of shape-based similarity measures is provided. Furthermore, measures for performance evaluation are described.

Similarity measures

Formally, a time series can be defined in raw representation as an ordered series of elements $T_a = [a1, a2, \dots a_n]$ and $T_b = [b1, b2, \dots b_m]$, with $n, m \in N$ [72]. To assess the similarity of time series, a suitable distance function must be defined. As such, any general function $d(T_a, T_b)$ can be used, which provides meaningful output for pairwise comparison of T_a and T_b [72]. Following typical taxonomy, shape-based distance measures can be divided into lock-step and elastic measures [72]. Lock-step measures refer to a class of distance measures that compare the i-th elements of T_a and T_b. Thus, distance between two time series is computed using

$$d(T_a, T_b) = \left(\sum_{i=1}^{n} |a_i - b_i|^p \right)^{1/p}. \tag{4.6}$$

This approach requires equal length of both time series objects ($n = m$). Advantages are i) simplicity as it is parameter-free and ii) computational time, which is linear to the length of the time series ($\mathcal{O}(n)$) [247]. Due to the fixed mapping between samples, lock-step measures are sensitive to misalignment. In this paper, Euclidean Distance (ED) ($p = 2$), Cityblock Distance (CBD) ($p = 1$), and Chebyshev Distance (CHD) ($p = \infty$) are considered.

Using DTW, fixed mapping between the elements of T_a and T_b is relaxed. Also, time series of different length can be compared ($n \neq m$). A distance matrix can be calculated containing distances between each combination of elements a_i, b_j of T_a and T_b. Using optimization, alignment of T_a and T_b yielding minimal distance is computed. Boundary condition is used to limit start and end points of the warping path to (a_1, b_1) and (a_n, b_m). Furthermore, along the warping path only adjacent elements can be warped together (continuity) and warping is only allowed forward in time (monotonicity). For details see [123]. The DTW distance can be computed using

$$d_{\mathrm{DTW}} = \gamma(i, j) = d(a_i - b_i) + \min\{\gamma(i-1, j-1), \gamma(i-1, j), \gamma(i, j-1)\}, \tag{4.7}$$

with time complexity of $\mathcal{O}(nm)$ [123]. Additional computational burden of DTW can be addressed by optimized implementations including pruning strategies to abandon distance calculations early and by further constraining the warping path [195]. Also, constraining the warping path can lead to improved similarity assessment, because pathological matching of data points is avoided [72].

Performance assessment

The dendrogram is a binary tree illustrating the distance between different objects. Dendrograms are frequently used to assess the quality of similarity measures. The calculation of a distance matrix containing pairwise distances between each object in a dataset is fundamental. Hierarchical clustering algorithms operate on the distance matrix to construct the dendrogram by successively merging two most similar of k objects into $k - 1$ clusters. By appropriately cutting the dendrogram, branches of the tree provide a classification of objects into groups. A distance function is considered as good similarity measure if the obtained structure corresponds to the assumed similarity between objects in a dataset. Typically,

visual inspection of a dendrogram is sufficient in case of small datasets. On growing number of observations, comparison of different clusterings becomes increasingly difficult. Hence, different performance measures are also used in this paper.

In the following, the relevant performance measures are described briefly. For details the reader is referred to Handl et al. [106]. The Rand index R is computed as proportion of agreements between two different clusterings. Comparing a particular clustering result to a known ground truth, R can be interpreted in analogy to accuracy, which is well known from classification. The value $R = 1$ indicates that both clusterings are identical. Davies-Bouldin index DB is a measure describing the relation of cluster homogeneity and cluster separation. To compute the DB, cluster center must be determined. As averaging of time series data under DTW is non-trivial, the averaging technique developed in [182] is used. Small values of DB indicate good clustering results.

Finally, to motivate the use of shape-based distance measures for classification, cross-validation accuracy of 1NN classifier is used. This approach is proposed in [72] due to several advantages: despite its simplicity, 1NN classifier is highly competitive with many sophisticated approaches. According to [28] "all of the current empirical evidence suggests that simple nearest neighbor classification is exceptionally difficult to beat." Furthermore, 1NN classifier is parameter-free and thus allows objective evaluation of distance measures and reproducibility of results [72].

4.3.4 Experimental results

In thin plates two different wave modes can be excited using pencil lead break tests depending on the simulated source orientation [188]. Whereas AE sources at the surface of the specimen (out-of-plane source motion) give rise to dominant flexural mode, extensional wave mode is excited at the edge of the specimen (in-plane source motion). Accordingly, AE waveforms are recorded during pencil lead break tests in corresponding orientations.

To compare the performance of different similarity measures, a reference dataset is constructed. In total, 20 independent pencil lead break tests were recorded, 10 in each orientation. To construct the dataset, each waveform is z-normalized and aligned with respect to the onset of the AE burst. This can be calculated as local minimum of AIC [153], as indicated in Figure 4.13. The known class assignments are also given in Table 4.2.

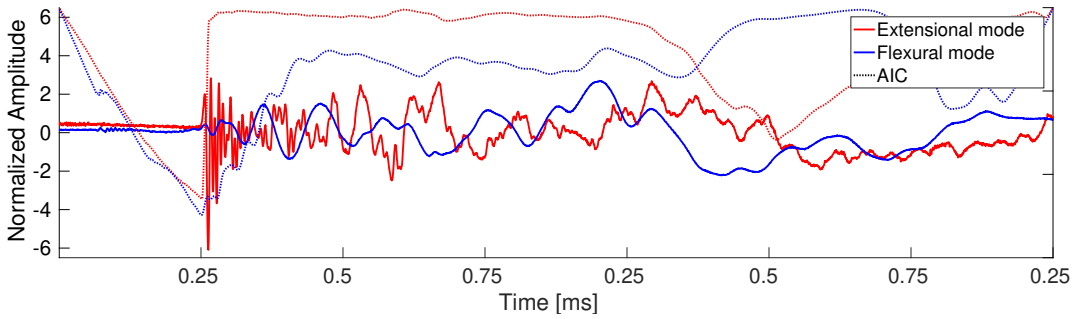

Figure 4.13: Examples of AE related to in-plane and out-of-plane source motion [257].

Specimens of carbonfiber/epoxy composite material with 1.8 mm in thickness are used. Resulting waveforms are detected using surface mounted piezoelectric broad-band sensor

of 0.55 mm in thickness and 10 mm in diameter. The corresponding cutoff frequency is 3.6 MHz. During the experiments, the signal is acquired continuously at a samplerate of 4 MHz using FPGA-based measurement system.

Subsequently, numerical experiments are performed using hierarchical clustering and 1NN classifier to investigate the effect of noise and misalignment.

Clustering performance Hierarchical agglomerative clustering is used to verify suitability of different distance functions as similarity measure. Clustering performance is assessed using the measures described in the previous section. First, an example is presented, where the waveform alignment is perturbed in time with random shift of 5 samples. Finally, clustering performance is evaluated under variable degree of noise and misalignment.

The dendrograms obtained using CBD and DTW are presented in Figure 4.14a and 4.14b, respectively. Additionally, cluster assignments obtained using different distance functions are stated in Table 4.2. According to the clustering, only CBD and DTW are able to recover the original groups from the data. Using DTW, a noticeable decrease of DB indicates more compact clusters in relation to cluster separation. This is also confirmed by comparing the dendrograms presented in Figure 4.14. Thus, it can be concluded that DTW provides improved representation of the distances between AE waveforms in the dataset.

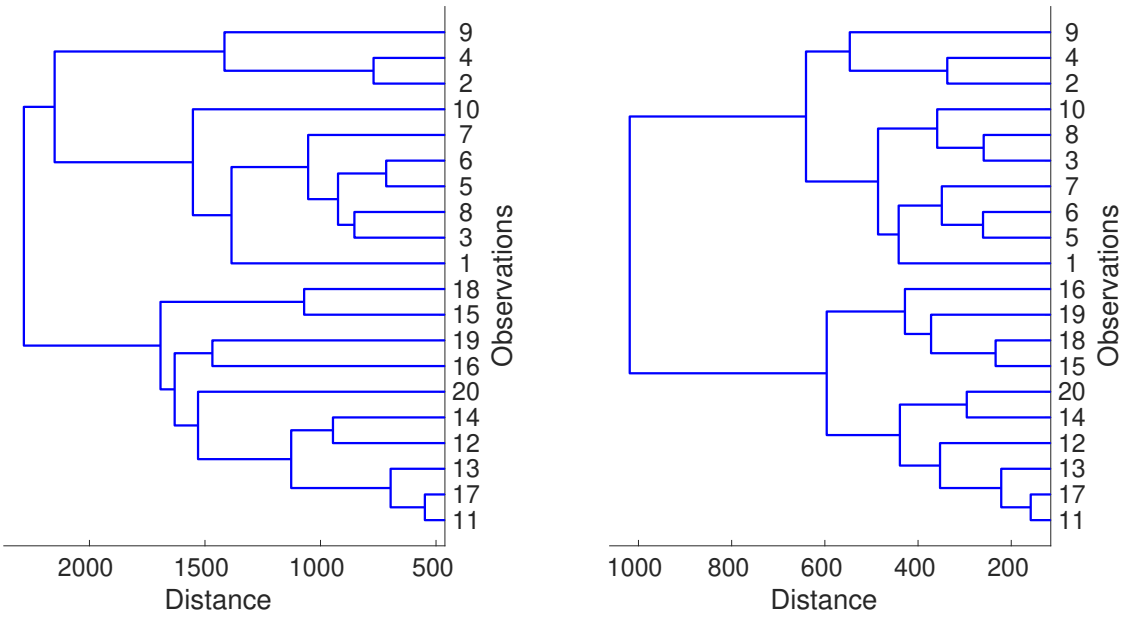

(a) City Block Distance (CBD).

(b) Dynamic Time Warping (DTW).

Figure 4.14: Dendrograms showing distances between waveforms related to PLB tests [257].

To investigate the effect of Gaussian noise, waveform alignment is maintained. The noise level is denoted by SNR. Additionally, the effect of signal misalignment is evaluated using random shift in time. The upper bound of shift with respect to burst onset is denoted. Each experiment is repeated 10 times. Mean values of the performance measures are shown.

Table 4.2: Clustering results using different similarity measures [257].

Method	Cluster assignment	R	DB
Known clustering	$\{1-10\}, \{11-20\}$		
Euclidean distance	$\{1,3,5-8,10-20\}, \{2,4,9\}$	0.52	1.15
City-block distance	$\{1-10\}, \{11-20\}$	1.00	1.29
Chebychev distance	$\{1,-6,8-20,\}, \{7\}$	0.48	0.40
Dynamic time warping	$\{1-10\}, \{11-20\}$	1.00	0.91

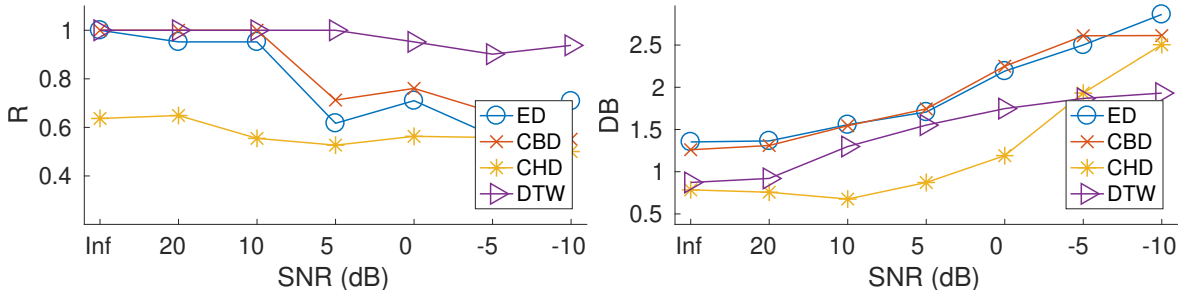

(a) Cluster performance with respect to SNR [257].

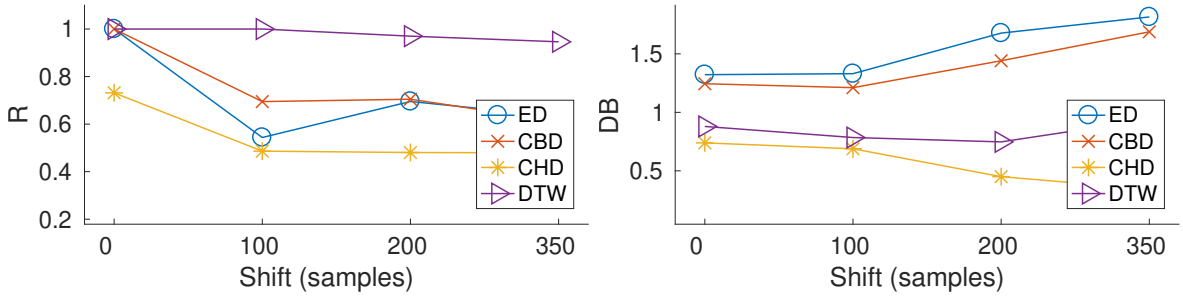

(b) Cluster performance with respect to misalignment.

Figure 4.15: Cluster performance (mean of 10 experiments) [257].

Regarding Gaussian noise, good performance with respect to R is observed over a wide range of different SNRs (Figure 4.15a). Compared to lock-step measures, DTW is more robust to noise. Degradation of ED and CBD in R occurs at SNR below 10 dB. Using DTW, slight decrease of R is observed at SNR below 5 dB. Also, DB indicates low cluster variance compared to cluster separation. Performance of CBD is better than ED. Furthermore, it has to be noted that CHD achieves minimum values with respect to DB indicating improved structure of the clustering. Taking into account R, which is close to 0.5, the obtained clustering is not useful with respect to the given problem. Essentially, using CBD it is not possible to recover the underlying structure of the dataset. Thus, in this case CBD is not a meaningful measure of similarity.

Whereas good performance with respect to R could be obtained under a wide range of SNRs, lock step measures are highly sensitive to misalignment of waveforms (Figure 4.15b). Detrimental degeneration of the clustering is already observed at shift of 100 samples, which

corresponds to an alignment error of 0.025 ms. In contrast, R indicates that clustering results using DTW are mostly in agreement with the ground truth.

Classification performance. The suitability of different distance measures for shape-based classification of AE waveforms is assessed. In Figure 4.16, accuracy of 10-fold cross-validation using 1NN classifier is shown. Compared to hierarchical clustering it is noticeable that CHD, which performed poorly using hierarchical clustering, provides useful results in 1NN classification. However, CHD performance degenerates quickly in presence of distortions. Also, CHD is outperformed by ED and CBD. In contrast, ED and CBD yield classification accuracy which is similar to DTW over a wide range of SNRs. Above SNR of -5 dB, DTW is superior to lock-step distance measures. In this case, ED leads to an improvement compared to CBD. The misalignment of AE waveforms has only a small effect on 1NN classification using DTW. Lock-step measures degrade with increasing alignment errors. Here, CBD performs best in each case.

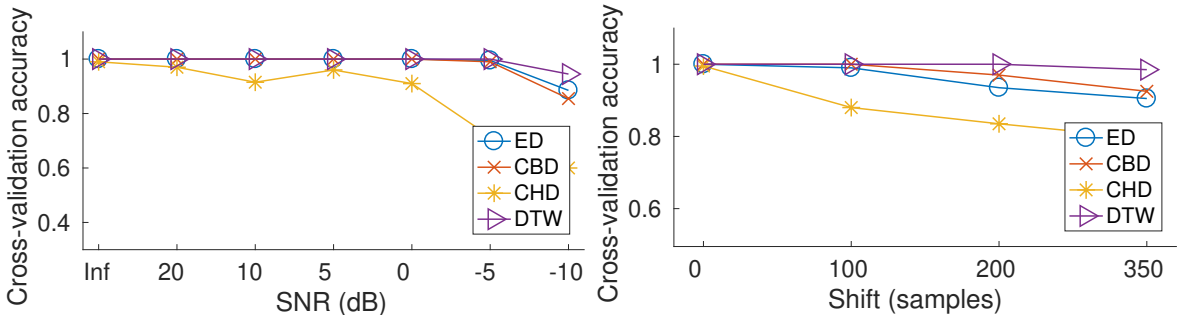

Figure 4.16: Classification performance (mean of 10 experiments) [257].

4.3.5 Summary and conclusions

In this section, the use of shape-based approaches for classification of AE waveforms is discussed. Different similarity measures are evaluated using hierarchical clustering, which is a typical approach. Finally, classification results using 1NN classifier are presented. According to the results, DTW is superior to lock-step measures. Frequently, CBD outperforms ED and CHD. High classification accuracy is achieved over a range of distortions. Therefore, it can be concluded that lock-step measures suffice for classification of AE waveforms if the onset of AE bursts can be detected accurately. Elastic measures (i.e. DTW) are required for robustness against misalignment.

4.4 Reliability analysis of frequency-based Acoustic Emission classification

Currently, the systematic reliability assessment of SHM systems is an open issue. Using data-driven approaches, the performance on future unknown data can only be estimated. Therefore, reliability of SHM is investigated in this section at the example of damage detection in composites. A supervised approach is used to classify different damage mechanisms.

Detectability of damage and probability estimates are used to assess the reliability of the results. Finally the results are discussed within the context of reliability assessment for SHM. The main contribution in this section is an explicit consideration of different loading conditions in the reliability estimation of the SHM system. According to the results, large scattering of classification reliability is identified as new scientific challenge. The following section is based on the previously published journal paper *Investigation of damage detectability in composites using frequency-based classification of Acoustic Emission measurements* [252].

4.4.1 Introduction

The recent rise of composites is owed to their beneficial properties, such as fatigue strength, impact resistance, and lightweight, resulting from their sophisticated structure. Today, the more widespread use of composites is restricted for several reasons. In contrast to metallic materials, which are generally assumed to exhibit homogeneous mechanical properties, composites form a complex system defined by the constituent materials properties, geometry, and distribution [1]. Furthermore, composites lack a pronounced ductile behavior [181]. During failure of composites, several micro-mechanical fracture mechanisms are observed [181]. In literature, SHM systems are proposed to overcome these challenges and to ensure equal safety and reliability of composite structures [59]. This includes that a SHM system has to provide reliable measurements and conclusions regarding the actual system state.

In composites, distinct types of damage are observed as the result of underlying micro-mechanical fracture mechanisms. These include delamination, matrix crack, fiber breakage, and debonding [158]. Whereas debonding merely describes the loss of adhesion between fiber and matrix material, delamination denotes the separation of layers in laminated materials [59]. The resulting AE waveforms are characteristic to the particular source mechanism. Hence, AE measurements can be utilized to identify the corresponding fracture mechanism, which has already been shown in several case studies [59, 60, 68, 102, 164]. To identify characteristic frequencies of distinct AE source mechanisms, peak frequency analysis was applied by several researchers [48, 67, 102]. De Groot et al. [67] identified damage-specific signatures of four different micro-mechanical damage modes namely matrix crack [90 kHz, 100 kHz], debonding [240 kHz, 310 kHz], fiber breakage [$>$ 300 kHz], and fiber pull-out [180 kHz, 240 kHz] in CFRP material in terms of peak frequencies. Similarly, Hamdi et al. [102] identified delamination [30 kHz 90 kHz], matrix crack [30 kHz 170 kHz], debonding [180 kHz 290 kHz], and fiber breakage [300 kHz 420 kHz] as distinct classes of micro-mechanical damage in composites using HHT.

To identify characteristic peak frequencies and to track damage accumulation under different experimental conditions Bussiba et al. [48] used STFT. Based on their experimental results, three characteristic frequencies were identified, which correspond to the damage mechanisms matrix crack (140 kHz), debonding (300 kHz), and fiber-breakage (405 kHz) [48]. Moreover, mechanical thresholds for the onset of AE activity were determined, indicating that no damage occurs below these threshold values [48].

The damage characterization task is most frequently considered as classification problem. Pattern recognition algorithms are a suitable method to address this type of problem [230]. In the supervised case, a representative set of training data is used to generate the statistical model. Most frequently used classifier algorithms are KNN, neural networks, and SVM. Das et al. [66] state that SVM is suitable to identify damage modes in composites. Joint time-

frequency transformation is performed prior to the classification to extract damage specific features [66].

To realize SHM systems in practice, a suitable and therefore well defined reliability of the classification must be achieved. This includes high detection rates as well as low false-alarm rates, so that the system can be accepted. Furthermore, the classification should be robust against external disturbances. The reliability of conventional Non-Destructive Testing (NDT) methods is frequently assessed using POD, which is a probabilistic approach [136]. The POD curve describes the likelihood that a certain flaw is detected as a function of flaw characteristic a such as size or depth. These POD curves can be computed directly from experimental data, where two approaches are distinguished. In case of binary response of the inspection system hit/miss analysis is employed, whereas $\hat{a}$ vs. a approach can be used if continuous output $\hat{a}$ of the inspection system is available [136]. Commonly the $a_{90|95}$ value is determined from the POD curve as performance measure of the inspection system [219].

Due to conceptual differences between SHM and NDT, reliability of SHM systems is usually not quantified. To determine the POD curve of a NDT inspection technique, fixed decision threshold of the sensor response $\hat{a}$ is determined using model (calibration) specimens under controlled laboratory conditions [157]. Due to the in-service application of SHM, damages evolve over time and exclusion of disturbances is generally not possible [57]. Consequently, the sensor output is compared to a baseline signal for damage detection, where deviations cannot be readily attributed to damage due to in-situ effects and hence require appropriate interpretation [157]. Influencing factors of NDT systems are for instance reported as testing equipment and procedures, material and geometry of test specimens, and individual properties of the particular defect [136]. In contrast to this, SHM systems are reportedly affected by loading conditions [57], temperature [157], and sensor degradation [157]. Gagar et al. [89] report strong dependence of AE activity on the particular loading conditions using aluminum specimens under cyclic loading patterns. Furthermore, Schubert Kabban et al. [219] mention that the assumption of independent observations is not feasible in case of SHM systems, because measurements are performed at high acquisition rates to determine the current state-of-health in real-time leading to several dependent observations.

Subsequently, an experimental study regarding the impact of different loading conditions on the reliability of supervised classifiers is presented. Due to practical relevance, diagnosis of a composite structure is chosen to showcase SHM implementation. A mechanical test rig is used to simulate a load bearing structure of composite material while AE measurements are performed. Furthermore, a statistical pattern recognition approach using STFT-based feature extraction and SVM-based classification of the measurement results is proposed as example. The performance of the classifier is evaluated using 10-fold cross validation, which is a widely accepted approach in the field of machine learning for evaluating classifiers. Finally, the reliability of the classification results obtained from the deployed model is evaluated with respect to damage evolution and variable loading conditions using probability estimation. This result is new and could not be detected from previous publications. In the following sections, the experimental procedure is introduced, the measuring chain as well as the employed signal processing techniques are described. Hereafter experimental results of the proposed procedure are presented and discussed with respect to reliability considerations of SHM applications. Finally, the main conclusions from the experimental results are summarized.

4.4.2 Experiments

The experiments are performed to investigate the effect of loading conditions and damage evolution on the reliability of automatic damage classification. To this end, a test rig is used to subject specimens of composite material to cyclic loading patterns while AE measurements are performed for diagnostic purposes. In this section, the mechanical test rig, data acquisition hardware, and methods used for signal processing are briefly described.

Mechanical test rig

To simulate an in-service, load-bearing structure, a mechanical test rig is used. Specimens of composite material are subjected to cyclic loading patterns. The major components of the test-rig are presented in Figure 4.17. The frame construction of the test rig consists of aluminum profiles having a vise attached to fixate the specimen during testing. Furthermore, a slider-crank mechanism is used to apply bending load by deflecting the specimens tip.

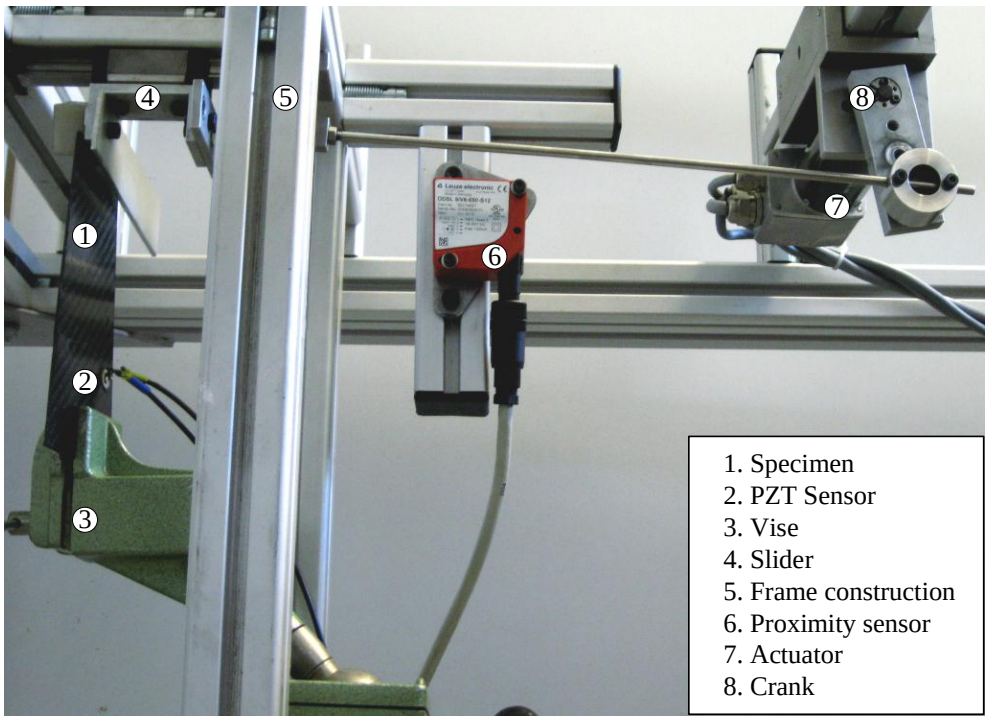

Figure 4.17: Components of the mechanical test rig, SRS U DuE [252].

For actuation of the test rig, a servo-controlled direct current motor is mounted on the aluminum frame. Setpoint values for the motor current are read from analog input in the range of $0 - 5$ V. Moreover, a laser proximity sensor is used for contactless displacement measurement. The sensor provides a maximum resolution of 0.1 mm in the maximum measuring range of $50 - 650$ mm of distance. Here, the measuring range was configured to an interval of 65 mm.

Data acquisition

To record AE, a surface-mounted piezoelectric acceleration sensor is used. It consists of a disk-shaped piezoceramic element of 0.55 mm in thickness and 10 mm in diameter. As bonding agent, cyanoacrylic glue was used to attach the sensor to the specimen. This couplant provides good reproducibility compared with other couplants [85]. Furthermore, the stiff bonding improves transmission properties of in-plane wave modes and provides permanent bonding of the sensor to the structure [238]. For data acquisition a FPGA A/D-board offering 16 bit resolution at a maximum sample rate of 25 MHz is used. A sample rate of 4 MHz is chosen as suitable trade-off between resolution and technical requirements. The waveforms are acquired continuously.

Subsequently, examples of acquired waveforms are presented in Figure 4.18 and Figure 4.19, respectively. Time-series data and time-frequency domain representation using CWT are presented. The event shown in Figure 4.18 is considered as representative of delamination. The source motion of this fracture mechanism is mainly characterized by out-of-plane displacement. According to literature, AE events of high amplitude exhibiting a dominant flexural wave mode are presumably associated with delamination [59,68,164]. Furthermore, these waveforms are highly dispersive and show long durations [189]. In general agreement, the frequency content of delamination is reported in the lower frequency band of the ultrasonic regime at frequencies of [50 kHz, 150 kHz] according to Gutkin et al. [99], whereas Hamdi et al. [102] reported lower frequencies of delamination events in the range of [30 kHz, 90 kHz].

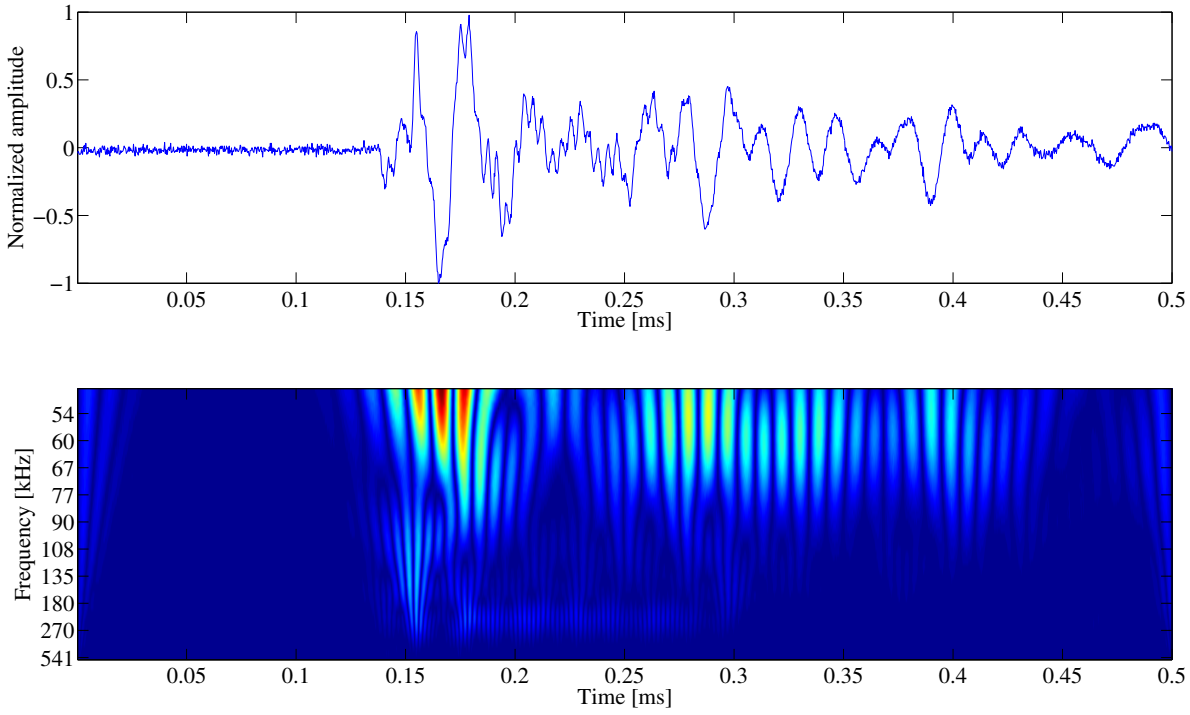

Figure 4.18: Time and time-frequency representation of delamination events [252].

In contrast, the AE waveform presented in Figure 4.19 is attributed to the class of fiber

breakage. This type of damage occurs, if the maximum strain of the fiber is exceeded due to excessive deformation of the matrix material. The rapid redistribution of stress due to the reinforcement failure primarily activates in-plane source motion. Therefore, high frequency extensional modes featuring short rise time and duration are associated with fiber breakage [59,68]. According to literature, the peak frequency is localized at frequencies above 300 kHz. Maximum frequency range of fiber-breakage was reported by Bohse et al. [42] at frequencies in the range of [350 kHz, 700 kHz], whereas the lowest frequencies were reported as larger than 300 kHz by De Groot et al. [67].

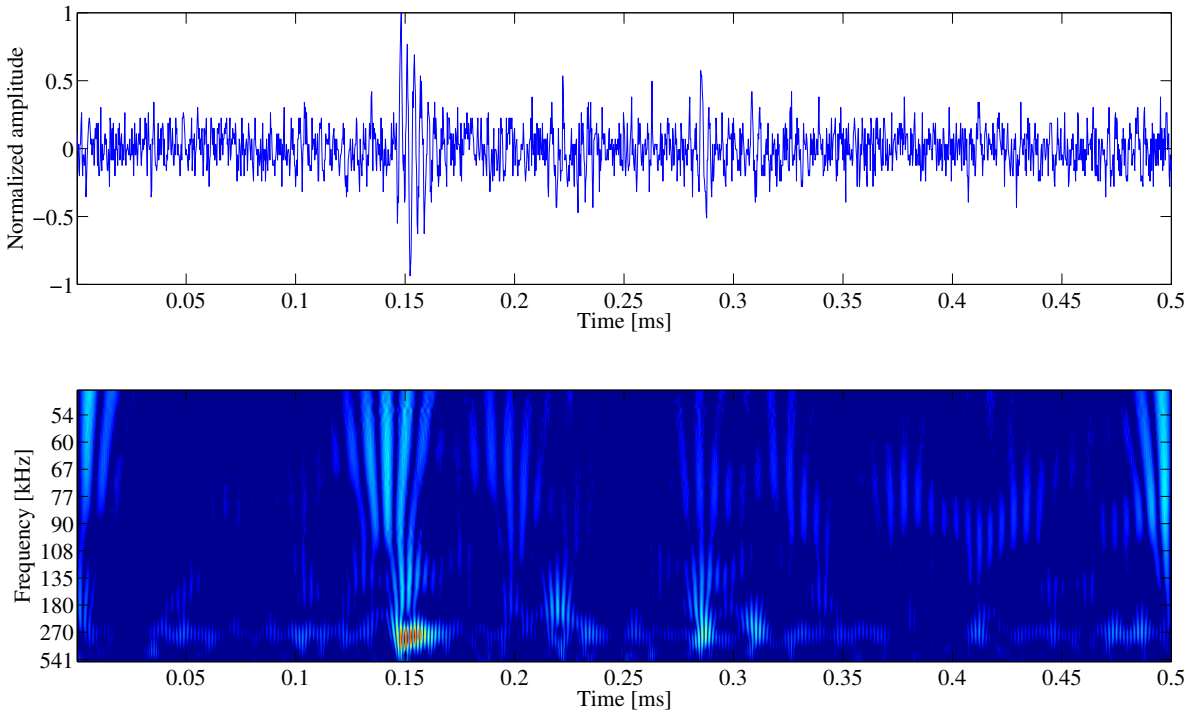

Figure 4.19: Time and time-frequency representation of fiber breakage events [252].

Pattern recognition

To implement a classifier for AE data, LIBSVM library is used [53]. A RBF kernel is chosen and the related parameters are optimized using grid search. As input to the classifier, STFT coefficients are calculated. In addition to class predictions, probability estimates are computed to assess the reliability of the results obtained from the deployed model using the implementation described by Chang and Lin [53].

By default the SVM provides only predictions of the class label based on the decision value $\hat{f}$ computed from the feature vector x. To obtain class conditional probabilities $p_i = P(y = i \,|\, x)$, $i = 1, \ldots, k$ in a classification problem with k classes, pairwise class probabilities $P(y = i \,|\, y = i \text{ or } j,\, x)$ are estimated as

$$r_{ij} \approx \frac{1}{1 + e^{A\hat{f}+B}}, \tag{4.8}$$

where A and B are determined according to training data [53]. Finally, by solving the optimization problem

$$\begin{aligned} \min_{p} \quad & \frac{1}{2}\sum_{i=1}^{k}\sum_{j:j\neq i}(r_{ji}p_i - r_{ij}p_j)^2 \\ \text{subject to} \quad & p_i \geq 0,\ \forall i,\ \sum_{i=1}^{k} p_i = 1 \end{aligned} \tag{4.9}$$

class conditional probabilities p_i are obtained [53].

4.4.3 Results

Subsequently, the performance of SVM-based classification of AE data and related dependencies with respect to the load applied are investigated. The AE measurements are taken from multiple specimens while they were subjected to cyclic loading patterns. Because AE is an in-situ inspection technique, damage detection is possible on initiation or propagation of damage and is therefore non-deterministic [185]. Moreover, variability of the classification results may be related to the evolution of individual defects. Reportedly, loading conditions affect the activation of AE source mechanisms in aluminum specimens [89]. Therefore, measurements are performed at different points in time, while keeping the excitation motion constant to study the spread of classification performance over time due to statistical scattering and damage evolution. Finally, measurements are performed using different loading conditions to investigate the impact on classification performance.

A labeled dataset containing true class labels is constructed based on the results from several fracture tests. In particular, three-points bending as well as indentation flexure tests were used. During each experiment, a large number of different AE signals can be detected, which are related to the fracture of the specimen. Reportedly, each of the damage modes can be identified in connection with three points bending [102], whereas indentation flexure tests promote primarily delamination [7]. From these experiments, several characteristic peak frequencies could be identified. The lowest characteristic frequency was assigned to delamination exhibiting peak frequencies in the spectrogram at approximately 45 kHz, which is in accordance with the findings of several authors [99, 102]. Furthermore, matrix crack is attributed to peak frequencies of 95 kHz, which is in line with multiple reports from literature [24, 67, 102, 158]. Moreover, debonding is presumably associated to frequencies of approximately 245 kHz, which is in accordance with literature [67, 99, 102, 158]. Finally, the maximum frequency of 300 kHz is assigned to fiber breakage, which is located at the lower end of frequencies being reportedly related to fiber breakage [24, 67, 102]. From each of the four classes (i) delamination, (ii) matrix crack, (iii) debonding, and (iv) fiber breakage, 60 representative samples of AE are selected from a set of 13 fracture tests to construct a dataset for SVM training. Using a window size of 1024 data points, STFT coefficients between 40 kHz and 500 kHz are obtained as input to the classifier. The corresponding dataset is illustrated in Figure 4.20.

The classification performance of the SVM algorithm is evaluated using 10-fold cross validation. A RBF kernel is used as proposed by Hsu et al. [113], where optimal classifier parameters C and γ were determined with respect to cross validation accuracy using grid-search.

The SVM testing performance is summarized in Table 4.3. In general, good classification performance is achieved using this dataset.

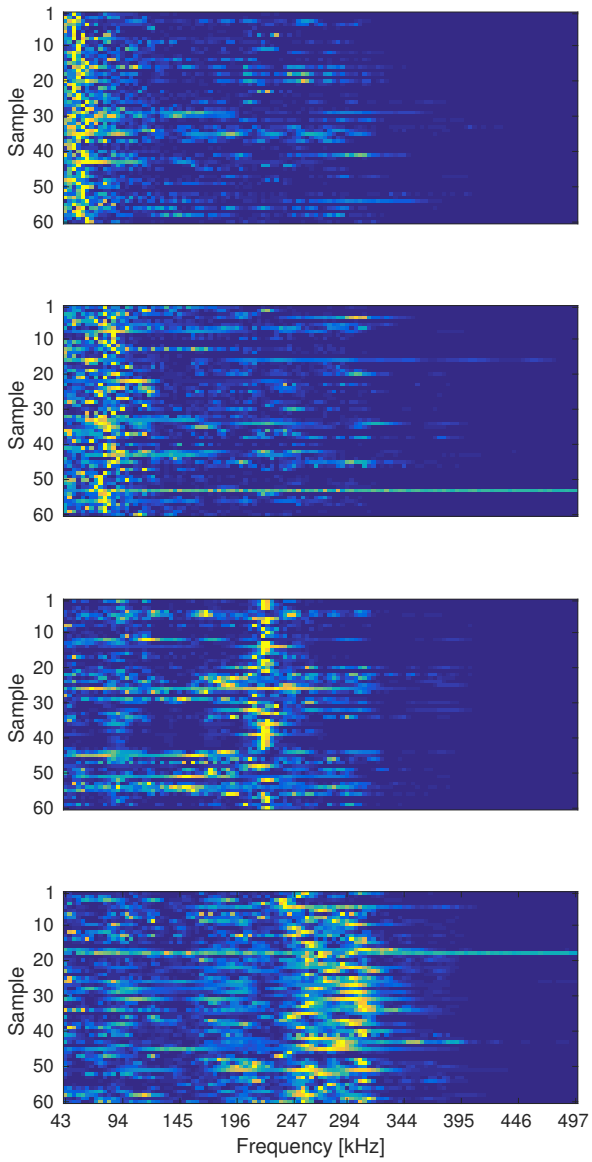

Figure 4.20: Visualization of the dataset used to build the classifier [252].

During the cyclic loading experiments, coupon shaped specimens of the dimension 75 × 175 × 1.8 mm^3 are used. The specimens were manufactured from carbon fiber/epoxy composite material consisting of three layers of [90°/0°/90°] unidirectional layup patterns and two woven carbon/epoxy prepregs. Furthermore, similar initial damage was introduced to each specimen by means of three points bending, because a strain-threshold must be exerted to initiate AE activity in bending tests [48]. Using carbon fiber/polymer composites, a significant fraction of the breaking load needs to be applied to give rise to micro-mechanical fracture due to the high bending elasticity of the material. According to Hamstad [104], only low AE activity is detected at 90 % of breaking load if undamaged composite material

Table 4.3: Cross validation performance [252].

Class	Accuracy	Specificity	Sensitivity
Delamination	0.94	0.85	0.96
Matrix crack	0.95	0.90	0.96
Debonding	0.94	0.87	0.96
Fiber breakage	0.97	0.93	0.98

is subjected to cyclic bending load. Therefore, split crack is introduced as initial damage prior to cyclic bending experiments.

Constant excitation

To investigate the spread of the classification results over time, the excitation motion is kept constant and several measurements are performed at different points in time. Each measurement series covers 20 min of time and data acquisition is initiated every 5 min for a duration of 2 s. Accordingly, five datasets are obtained per test series. Subsequently, the results of two measurement series using single specimen and two different excitation motions of (a) [8mm, 4 Hz] and (b) [18 mm, 5 Hz] are presented. To assess the reliability of the classification results, mean values of the probability estimation are used.

In Figure 4.21a, results of the probability estimation, which are related to excitation motion (a), are presented. This loading pattern is characterized by small amplitudes and intermediate frequency of cyclic load. In this example, probability estimates between 80 % and 90 % are achieved in most of the cases. Lowest probability estimates are obtained for matrix crack. Highest values of the probability estimation are frequently related to debonding. Furthermore, no significant changes in the probability estimates are apparent over the duration of the experiment.

Similar results were obtained using controlled excitation motion (b), which provides increased load intensity. The results are presented in Figure 4.21b. Again, significant changes in the probability estimation could not be detected during the experiment. However, compared to the results of excitation (a), the overall classification performance could be improved by using increased intensity of the loading pattern. This is especially noticeable in case of matrix crack. Furthermore, highest probability estimation is now obtained for delamination in most of the cases, whereas best results were usually obtained for debonding using lower load intensity (see Figure 4.21a).

The main conclusion to be drawn from these experiments is that results obtained remain constant over time. Only low scattering of the classification performance is observed among different points in time indicating that fundamental changes to the initial damage pattern due to i.e. crack development are not observed during operation and test time. This is important because it excludes related effects for the further experiment series to be reported in the sequel. However, an effect of the load intensity on probability estimates is apparent. Generally, slight improvement in the probability estimation of the classification results using higher load amplitude and frequency is evident. Also, the class with highest probability estimation is different depending on the load intensity indicating the dependence of classification reliability on loading conditions. Therefore, detailed investigation of the effect of

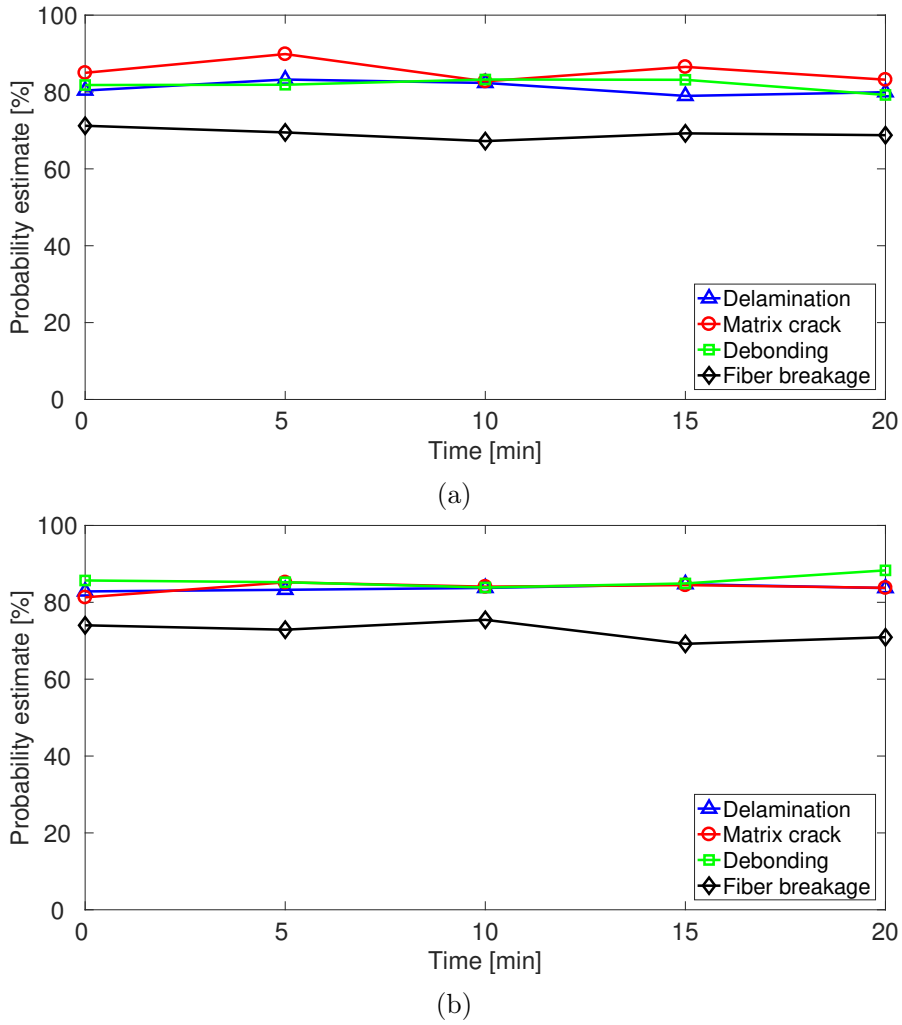

Figure 4.21: Mean values of probability estimation over time [252].

loading conditions on the classification performance are presented in the sequel.

Variable excitations

The evaluation of the classification performance presented in Table 4.3 is agnostic of environmental influences such as loading conditions because it is based on a finite set of example data. To investigate the dependence of the classification reliability on the loading conditions from a principle point of view, several specimens of composite material were subjected to different cyclic loading patterns. Each of the specimens is treated identically. Prior to the experiments, a split crack is introduced so that mode I crack opening occurs as a result of bending load. To show that the reliability of the classification results typically vary depending on the loading conditions, three specimens S-I – S-III are selected.

During the experiments, AE measurements are taken while subjecting each of the specimens to any pair of the frequencies [2 Hz 3 Hz 4 Hz 5 Hz 6 Hz] and amplitudes [6 mm 9 mm 12 mm 15 mm 18 mm]. Hence, 25 datasets are acquired per specimen. During each

measurement, data is acquired for 1.25 s. Furthermore, each series of measurements follows the identical sequence. The first measurement is carried out using the lowest excitation amplitude and frequency of [6 mm 2 Hz]. Hereafter, the frequency of the excitation motion was increased stepwise up to 6 Hz prior to increasing the excitation amplitude.

The classification results obtained for each measurement series using the specimens S-I – S-III are summarized in Table 4.4. Similar to the previous experiments, mean values of the probability estimation are computed for each dataset. From these results contour plots are rendered to illustrate the dependence of probability estimation on the excitation motion. Here, the probability estimation is plotted on a color scale while the x- and y-axis denote the amplitude and frequency of the excitation motion, respectively. Damage detection with a high probability estimate is denoted by a red shade. In case that no damage was detected, the probability estimation was set to 0, which corresponds to a dark blue shade.

Table 4.4: Probability estimation with respect to excitation motion [252].

Delamination	Matrix crack	Debonding	Fiber breakage
Specimen S-I			
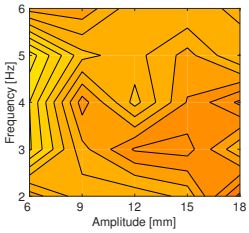	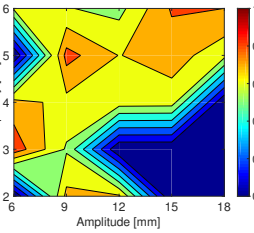	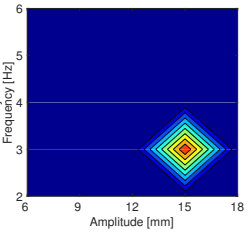	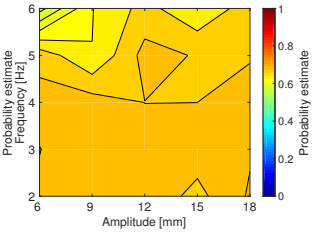
Specimen S-II			
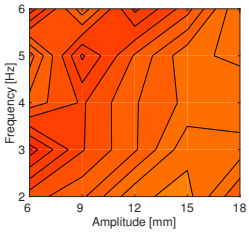	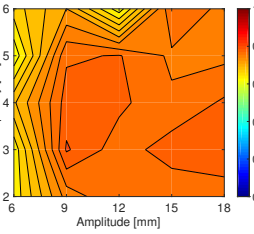	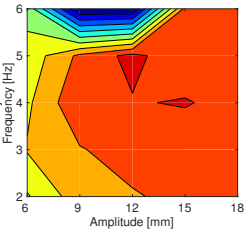	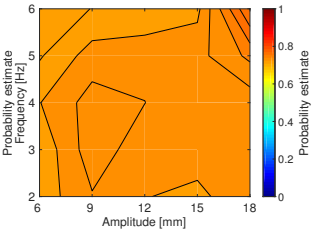
Specimen S-III			
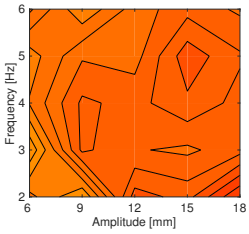	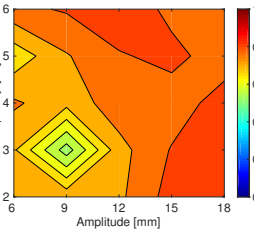	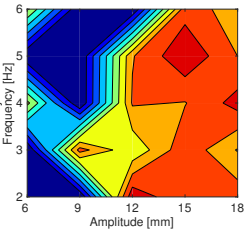	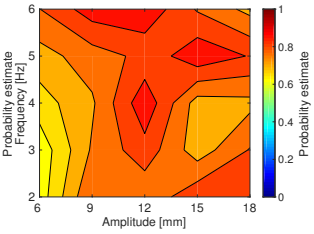

Good results are generally achieved in connection with delamination. This damage mode is detected at any of the excitations. In many cases, high probability estimation is achieved. However, regions of excitation conditions (frequency, amplitude) leading to best probability estimates differ among the specimens.

Regarding matrix crack, a strong dependency between loading patterns and classification results is apparent. Especially regarding specimen S-I, matrix crack could not be detected in several cases depending on the excitation. Considering specimens S-II and S-III, improvement of the probability estimates related to the classification results is observed on increasing load amplitudes. In contrast, matrix crack is most frequently detected at small load amplitudes using specimen S-I.

Considering debonding, the effect of excitation motion on classification performance is more pronounced. Using each of the specimens, damage is not detected depending on the loading pattern. Especially in case of S-I, debonding could only be detected during a single measurement. Similarly, improved damage detectability is observed on increasing load amplitudes. Considering specimens S-II and S-III, it is noticeable that regions related to best classification results are different among the specimens.

Fiber breakage could also be detected throughout each loading pattern. Analyzing the related probability estimations, improved results are frequently obtained for larger load amplitudes. However, improved results are achieved for high frequency loading pattern using specimen S-III. In contrast, improved probability estimation is obtained at low excitation frequencies in case of S-I.

According to the experimental results presented in this section, strong dependencies of (i) damage detectability and (ii) the reliability of classification results on excitation motion become evident. Whereas delamination and fiber breakage appear to be less sensitive to variable excitations, the classification results of matrix crack and debonding strongly vary with excitation motion. Due to a high degree of variability among specimens and classes, a direct relationship between excitation motion and classification reliability could not be established. Nevertheless, cumulative trends are apparent. Frequently, increased load amplitudes lead to improvements in the detectability of damage and the corresponding probability estimate of the classification result. Also, an increase in the frequency of the cyclic loading pattern leads to improved probability estimates in several cases. Similar findings are reported by Gagar et al. [89], where influences on the activation of AE source mechanisms are investigated using different aluminum specimens under cyclic loading conditions. Here, large scattering of the AE waveform features under identical test conditions was observed. Furthermore, these results indicate cumulative trends in AE source activation with respect to loading conditions.

4.4.4 Discussion

Viewing the results in the light of SHM reliability the question rises, which method can be used to evaluate the reliability of SHM systems. In the past, several ideas have been reported, which address different aspects to adopt POD philosophy to SHM applications. For instance, in contrast to conventional NDT, the results of SHM systems are statistically not independent due to high acquisition rates [219]. In this context, Schubert Kabban et al. [219] propose a new methodology to adopt POD procedures to provide compatibility with dependent measurement data, which is obtained from SHM systems. Furthermore, multiple approaches developed to assess the reliability of SHM systems are summarized by Mandache et al. [157]. In particular, time-based POD is proposed to address the effect of damage evolution [157]. It is suggested to find a formulation of the POD, which enables stating the probability of detecting specific defect growth within a given time interval. Multi-dimensional POD is proposed to take the effect of several in-situ effects, i.e. load-

ing conditions, on SHM reliability into account [157]. This includes the computation of POD with respect to each influencing factor to determine the actual reliability of the SHM system in particular situations. However, the approach requires availability of quantitative information on each influencing factor. Furthermore, quantitative knowledge regarding the impact of in-situ effects on the reliability is necessary. To minimize the experimental effort required to determine POD, model-assisted approaches can be used [136]. Cobb et al. [57] propose a model-assisted approach for determining POD of crack detection in aluminum specimens using in-situ ultrasonic inspection technique. Moreover, Eckstein et al. [73] suggest a methodology to quantify SHM performance by using cumulative distribution functions to establish a probabilistic relationship between the detected and real damage size. From this representation, multiple metrics of SHM performance, such as minimum detectable damage size to define a lower bound of POD as accuracy of the inspection method, and probability of false alarm are derived. However, identification of the underlying distribution functions is – particularly in context of in-situ inspection techniques, where a posteriori verification of real damage size is usually not possible – still an open issue.

From the aforementioned approaches to SHM reliability assessment it is noticeable, that the common weak point is characterized by missing detailed knowledge about the impact of different factors on SHM related reliability properties. In this context, especially the experimentally shown results from the previous section states that the loading (which is unknown in practice) strongly effects the detectability of defects as well as the distinguishability of different damages. However, large scattering of the results prevents the establishment of a direct relationship, which strongly aggravates the online monitoring as well as the verification of healthy states.

4.4.5 Summary and outlook

Reliability assessment of supervised SHM systems is an open issue which has to be solved before SHM comes into practice, especially regarding composite materials, which provide several advantages in many engineering applications. Currently, the more extensive use of composite material is restricted because safety and reliability requirements can not be met due to complex damage modes. Due to its practical relevance, diagnosis regarding detection and discrimination of four different fracture mechanisms leading to failure composite material was chosen in this work as a showcase of SHM. The experimental results using a damage classification scheme were discussed with respect to their reliability.

To investigate influences on the classification reliability of deployed models, a mechanical test rig is used to subject specimens of composite material to various cyclic loading patterns. During loading of the specimens AE measurements are performed. Furthermore, STFT and SVM are chosen as an example for extraction of time-frequency domain features from time-series data and classification of the measurement results. Two different types of experiments are performed. At first, constant excitations are used to assess the reproducibility of the classification results. Significant effects of damage evolution could not be detected, leading to the assumption that test conditions are constant for the duration of the following experiments. Hereafter, a second series of experiments is performed using variable excitation motions. From the experimental results it becomes evident, that the performance of the classifier strongly depends on the excitation motion. However, a direct relation could not be established due to large spreading of the classification results among multiple specimens

of identical structure, partly leading to contradicting observations. Based on the chosen example related to fault detection and damage discrimination in CFRP material, the large scattering of the classification reliability under identical testing conditions is identified as a new scientific challenge in the context of reliability assessment of SHM systems.

4.5 Attenuation of Acoustic Emission due to wave propagation in composites

In the previous section, reliability of diagnosis using AE and data-driven classification schemes under different operating and environment conditions is discussed. Another important influencing factor is related to the propagation of AE in the material. Due to viscoelastic behavior of polymer matrix used in many composite materials, dispersion of AE waveforms is observed and the signals are strongly attenuated. Subsequently, an experimental study regarding the propagation behavior of AE is presented. This section is based on the previously published conference paper *Experimental Results of Acoustic Emission Attenuation Due to Wave Propagation in Composites*, which was presented at the 11th Annual Conference of the Prognostics and Health Management Society (PHM 2019) [251]. Particular focus is placed on the frequency dependence of acoustic emission attenuation and the effect of different loading conditions. As main contribution it can be stated that depending on source frequency and external load, different attenuation is observed, which can have an impact on the detectability of AE.

4.5.1 Introduction

Today, composites are widely used in different applications due to their good mechanical properties. However, their use is currently limited by a lack of ductility and several micro-mechanical damage mechanisms, which adversely effect the fatigue behavior of these materials. Therefore, the reliable detection and characterization of damage is crucial for health monitoring of composite structures. In this context, AE measurements are widely used. The passive acquisition of ultrasound stress waves, which propagate in a structure due to damage, allows in-situ detection and localization of damage in large structures with only few sensors using suitable signal processing techniques.

In composite material, characteristic AE waveforms are observed, which can be attributed to different micro-mechanical damage mechanisms. For instance, delamination is characterized by dominant out-of-plane motion in a composite plate, whereas fiber breakage excites primarily in-plane source motion [59]. In plate specimens, these waveforms propagate usually as fundamental symmetric and asymmetric Lamb wave modes S_0 and A_0. Different AE waveform features can be exploited to characterize the underlying micro-mechanical damage mechanism. However, according to Johnson et al. [119], classification of AE measurements in time domain using classical waveform parameters is considered as difficult due to propagation effects such as amplitude attenuation. According to Ni and Iwamoto [173], peak frequencies are less sensitive to the propagation path and hence more effective for monitoring of composite materials. Therefore, frequency and time-frequency domain analyses are excessively used for characterization of AE waveforms.

As reported in literature, different data-driven classification schemes can be implemented

for automated characterization of AE waveforms. Wavelet transform is used by Marec et al. [158] to define new features which can be used to distinguish between matrix cracking and debonding. Furthermore, Gutkin et al. [99] studied AE obtained from tensile tests with different specimens using unsupervised techniques. According to the results, clusters agree with patterns in the peak frequency distribution. In contrast, Hamdi et al. [102] used HHT to extract AE features in time-frequency domain. Effectiveness of the approach is demonstrated using k-means clustering. Similarly, Nazmdar Shahri et al. [172] developed a signal processing technique based on HHT to characterize different damage mechanisms. A methodology based on multivariable analysis of wavelet coefficients is developed by Baccar and Söffker [19] to improve the classification and distinguishability of four different damage mechanisms. Similarly, time-frequency domain transforms including wavelet transform and Choi-Williams transform are used by Beheshtizadeh et al. [32] to identify characteristic frequencies of different damage mechanisms in composite materials. Scattering of the classification reliability among different loading conditions using a supervised data-driven method is reported in [252].

Another approach, which exploits theoretical knowledge about wave propagation, is modal AE. Amplitude ratios of the two fundamental Lamb wave modes are evaluated to characterize the underlying source mechanism. Two examples of modal AE analysis are presented by Prosser [189]. The application to the detection of matrix crack initiation in coupon specimens and delamination detection in rocket motor case rings is demonstrated. According to McCrory et al. [164], MAR provides improved clarity in the AE data interpretation compared to unsupervised data-driven approaches. Based on this idea, hardware filters for real-time monitoring of delamination in composite plates are suggested by Martinez-Jequier et al. [160]. Similarly, Dahmene et al. [64] used narrow-band filters for mode separation to extract the dominant mode from AE measurements. Recently, Barroso-Romero et al. [27] suggested mode identification based on phase and instantaneous frequency using Hilbert transform.

However, despite promising results, the source-sensor distance is identified as major limiting factor for AE-based damage characterization due to frequency dependent attenuation of AE [155]. In contrast to surface waves (i.e. Rayleigh waves), Lamb waves show frequency dependent amplitude attenuation due to dispersion. Regarding the effect on classical AE parameters, a location-based correction scheme of waveform parameters is implemented by Aggelis et al. [2] using a numerical technique. In an experimental study of AE due to mechanical loading of composite coupon specimens, Maillet et al. [155] reported decrease of frequency centroid with propagation distance. As a solution, a calibration chart for parameter correction depending on propagation distance is suggested. Furthermore, experimental results of AE attenuation in composite plates are presented by Asamene et al. [13]. A parametric attenuation model is presented taking geometric spreading and material damping into account. According to the results, strong attenuation of the A_0 mode is observed compared to S_0 mode. An experimental study regarding the complex propagation behavior of AE in a rotor system is presented by Li et al. [143]. Through the literature review it becomes clear that empirical correlations between micro-mechanical damage mechanisms and AE waveform parameters are useful to characterize different source mechanisms. Promising results are reported using different techniques. However, the application to composite materials is currently limited by the source-sensor distance due to frequency dependent attenuation of AE waveforms. In this section, new experimental results of acoustic emission attenuation

in composite plates are presented. Particular focus is placed on the frequency dependence of acoustic emission attenuation and the effect of different loading conditions. Furthermore, full waveform data are analyzed in time and time-frequency domain using wavelet transform.

The remainder of this section is structured as follows. In Section 4.5.2 experimental procedures are described. New experimental results are presented in Section 4.5.3 and implications for AE-based health monitoring are discussed. Finally, summary and conclusions are given in Section 4.5.4.

4.5.2 Experiments

As typical specimens, thin CFRP plates with the dimensions $440 \times 440 \times 2$ mm^3 are used. The specimens are manufactured from CFRP material, which is provided by a major aerospace company as example specimen. Wide specimen dimensions are chosen to enable reflection free measurements of AE waveforms. The experimental setup is illustrated in Figure 4.22. For artificial source generation and signal acquisition, four disc-shaped PWAS with 0.55 mm in thickness and diameter of 10 mm are used. The PWAS are bonded to the surface of the specimen using cyanoacrylic adhesive. Sensor locations are chosen in the center of the plate at uniform distances of 40 mm.

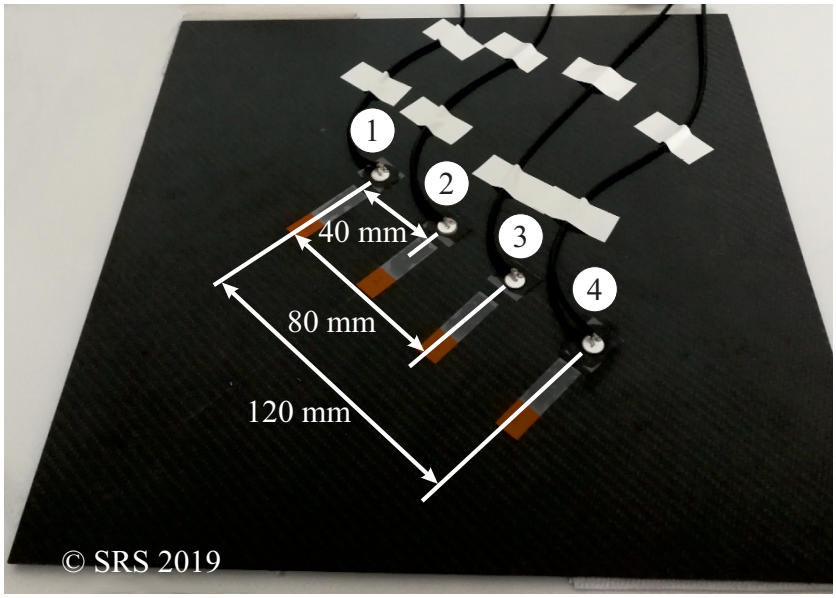

Figure 4.22: Experimental setup: CFRP plate with four PWAS bonded to the surface [251].

Artificial source generation

For testing purposes, artificial AE sources are typically used e.g. to verify suitable sensor coupling or to calibrate source localization systems. In literature, the PLB test, which refers to the excitation of stress waves by manually breaking a pencil lead at the surface of the specimen, is typically used. Even though PLB signals are fairly reproducible, there are different sources of variability due to handling such as free lead length or angle of the

lead [209]. Alternatively, according to Kharrat et al. [124], repeatable artificial AE sources can be generated using a surface bonded PWAS transmitter as well.

For the intended measurements of AE attenuation, highly reproducible excitations are required to obtain comparable results from multiple experiments. Therefore, artificial AE sources are generated using a surface-bonded PWAS as transmitter to achieve reproducible results. This approach allows well defined excitation. The source characteristics can be easily modified. To simulate AE, the PWAS in location 1 is driven by a signal generator using sine bursts of three cycles at different frequencies.

Data acquisition

The remaining three PWAS transducers at locations 2-4 are used as sensors to record AE waveforms at different distances from the source. For data acquisition, a custom three-channel AE system is used. An impedance transformer is used for signal conditioning before digitization. Measurements are triggered externally and taken in streaming mode to ensure that full waveform data are acquired over the relevant measurement period. The waveform data are sampled continuously at 4 MHz with 16 bit resolution using a dedicated FPGA-based data acquisition system and stored to a hard drive for subsequent analyses.

4.5.3 Results and discussion

Subsequently, experimental results regarding the attenuation of simulated AE in CFRP material are presented. First, the attenuation effect is studied qualitatively in time- and time-frequency domain. Furthermore, attenuation coefficients are determined for different frequencies. Finally, the impact of external load is addressed.

Effect of attenuation on AE waveforms

To illustrate the effect of attenuation due to wave propagation qualitatively, measurements of AE waveforms at distances of $d = 40$ mm, $d = 80$ mm, and $d = 120$ mm from the source are presented. As an example, a sine burst comprising three cycles at 100 kHz is chosen as artificial source. In Figure 4.23a, the related AE waveforms recorded at each sensor location are shown in time domain. The time delay between the measurements is attributed to the time-of-flight of the wave packet. From the results, a decrease in amplitude as well as the spreading of the wave packet in time is clearly visible. The cycle number of the wave packet increases with propagation distance, which is related to the dispersion effect. Furthermore, separation of modes due to the different propagation velocities can be observed after a distance of 120 mm.

Similarly, time-frequency domain representation of the AE waveforms is shown in Figure 4.23b. Here, different frequencies are excited by the source which can be detected at sensor 1 after 40 mm of propagation distance. The peak frequency of the sensor response is detected at 100 kHz, which corresponds to the simulated AE source. A second peak is observed above 200 kHz. The effect of waveform dispersion is also apparent in this representation. Due to different propagation velocities, the peak amplitude of the higher frequency mode is observed earlier in time than the 100 kHz peak. This effect is more pronounced after a propagation distance of 80 mm. However, whereas the peak frequency of 100 kHz can still

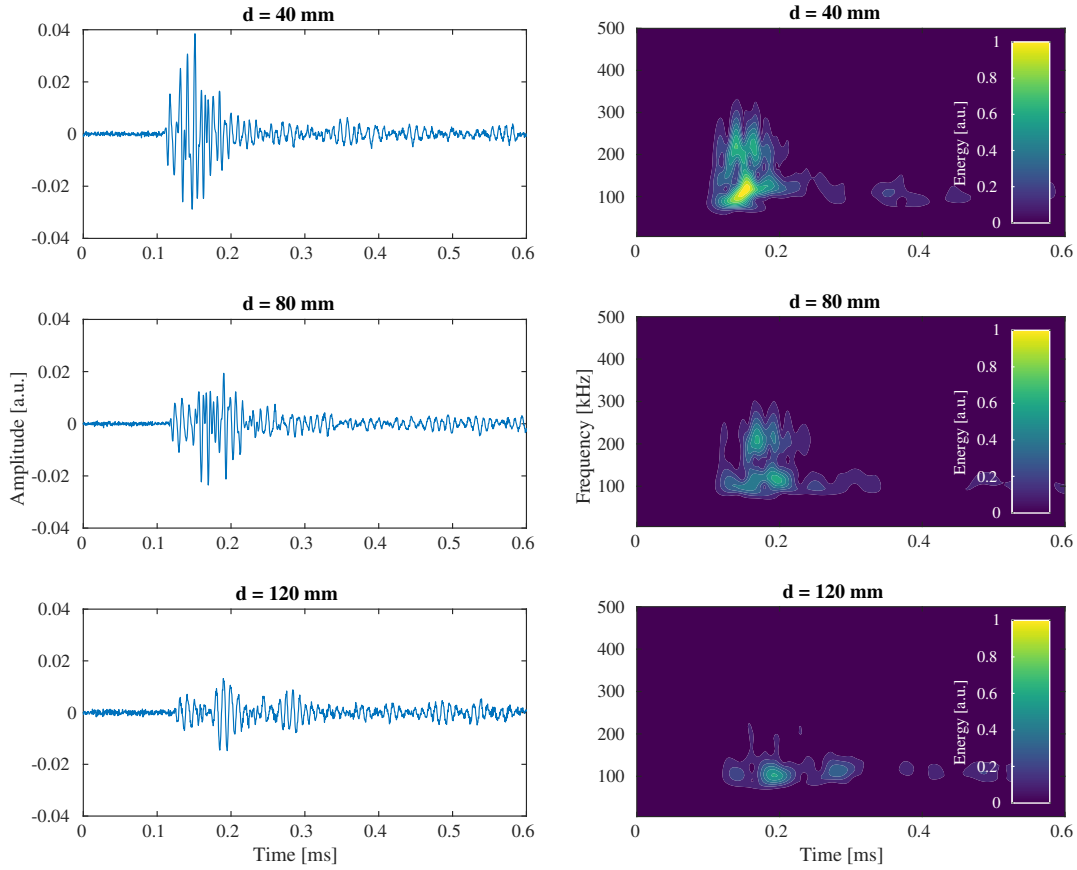

(a) (b)

Figure 4.23: Representative measurements of simulated AE at different distances from source in (a) time domain and (b) time-frequency domain [251].

be detected after 120 mm propagation distance, higher frequencies are strongly attenuated and can hardly be detected.

Effect of frequency and loading conditions

Subsequently, the dependence of the AE attenuation on frequency and loading conditions is investigated. To this end, attenuation coefficients are determined experimentally. In a plate, the relation between initial amplitude of a stress wave V_0 and the amplitude of a signal V_i measured in a propagation distance x_i from the source can be assumed as [13]

$$V_i = \frac{1}{\sqrt{x_i}} V_0 \, \mathrm{e}^{-\alpha x_i}, \tag{4.10}$$

where $\frac{1}{\sqrt{x_i}}$ describes the reduction in amplitude due to geometric spreading and exponential decay using attenuation coefficient α describing attenuation due to material damping. Hence,

the damping coefficient α can be calculated as described in [13]

$$\alpha = \frac{1}{x_3 - x_1} \ln\left(\frac{V_1\sqrt{x_1}}{V_3\sqrt{x_3}}\right) \tag{4.11}$$

using the peak amplitudes V_1 and V_3 measured at the locations x_1 and x_3, which correspond to the propagation distance of 40 mm and 120 mm, respectively.

In Figure 4.24, measured peak amplitudes and the theoretical damping behavior are compared at different frequencies of the simulated AE. Here, the theoretical attenuation (solid line) is calculated using damping coefficient α, which is determined according to equation 4.11. Good agreement between the measurements and theoretical attenuation is observed. Furthermore, it is apparent that attenuation due to material damping is stronger at higher frequency of 280 kHz.

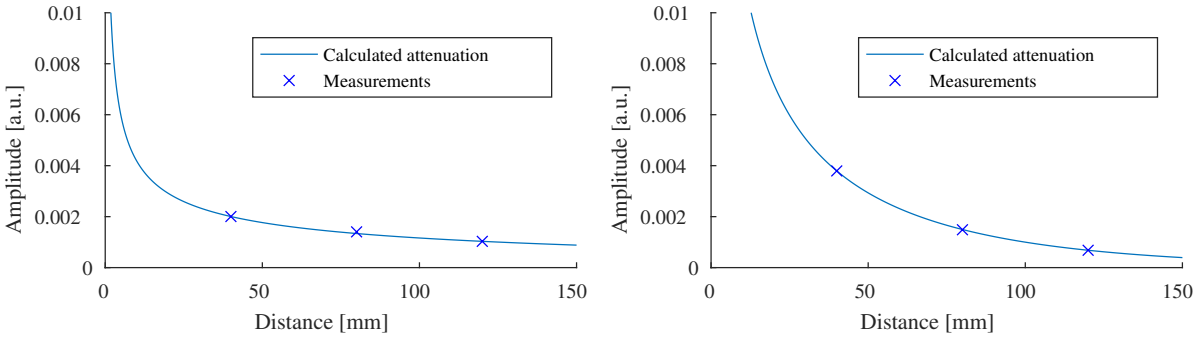

(a) 60 kHz. (b) 280 kHz.

Figure 4.24: Comparison of theoretical AE attenuation and measured peak amplitudes [251].

To investigate the frequency dependence of attenuation, the frequency of the simulated AE source is increased from 30 kHz up to 300 kHz in 10 kHz steps and the corresponding attenuation coefficient is determined according to equation (4.11). Each experiment is repeated 100 times. The signals are averaged in time domain to increase signal to noise ratio. Damping coefficients are determined using the root mean square of the related wavelet coefficients. External bending load is applied using two different setups as illustrated in Figure 4.25. In Figure 4.25a, a three-points bending setup is illustrated, which represents a typical configuration for material testing experiments. The load is applied in normal direction to the plate surface by clamps attached to the free edges and a support placed at the center of the plate. In contrast, a different clamping device, which allows to achieve bending of the plate without the use of a support, is shown in Figure 4.25b. The load is applied in parallel to the plate surface and the position of the plate edges in normal direction to the plate surface is fixed by the clamping device. Thus, bending of the plate is achieved without external forces acting on the plate surface within the propagation path. A total of five different loads is considered by increasing the height of the curvature in 10 mm steps.

From the results presented in Figure 4.26, it can be detected that AE attenuation varies notably with the frequency of the simulated source. In the unloaded case, maximum attenuation of simulated AE waveforms is obtained at a frequency of 150 kHz. Increasing

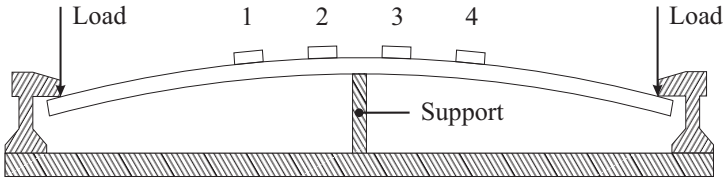

(a) Schematic illustration of three-points bending setup [251].

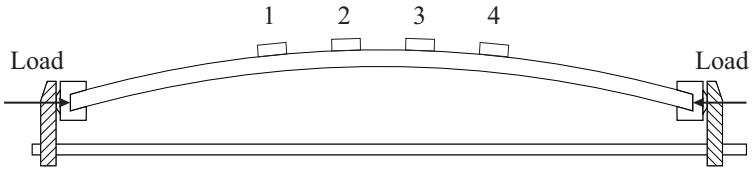

(b) Schematic illustration of the clamping device.

Figure 4.25: Clamping devices to apply bending load (1-4: PWAS 1-4, PWAS 1 active).

attenuation coefficients are obtained at frequencies from 50 kHz up to 150 kHz. Above 150 kHz attenuation decreases at first leading to lower attenuation between 200 kHz and 250 kHz. However, above 250 kHz increasing attenuation of simulated AE is observed again.

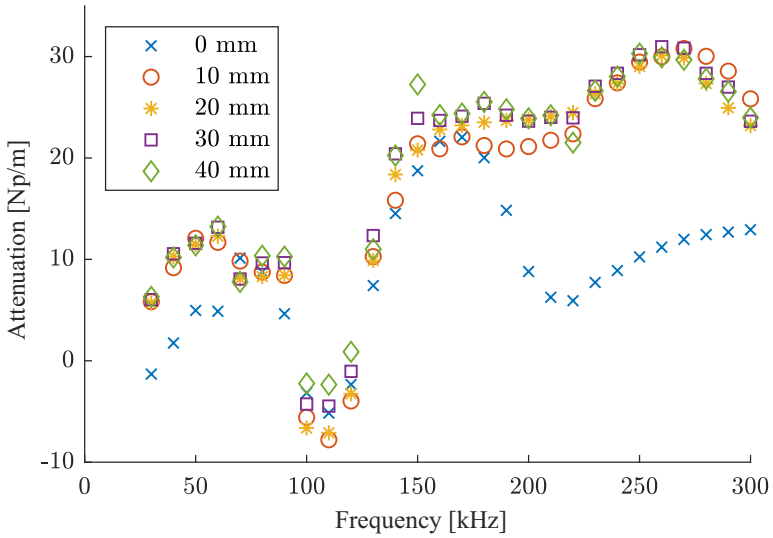

Figure 4.26: Comparison between attenuation coefficients of free and clamped plate [251].

In the loaded case is notable that in this experiment slight changes in external loading conditions have already a strong impact on the attenuation characteristics of the specimen. Compared to the unloaded case, stronger attenuation of the AE waveforms is observed over a wide range of excitation frequencies if external load is applied. This effect is particularly

pronounced below 100 kHz and above 150 kHz. In contrast to the unloaded case, where the attenuation coefficients decrease at frequencies from 150 kHz to 200 kHz, increasing attenuation coefficients are obtained in this frequency range. Furthermore, maximum attenuation is shifted to approximately 250 kHz in case of the loaded specimen. Above 250 kHz, AE attenuation shows a decreasing trend.

In Figure 4.27, attenuation coefficients, which were obtained using the clamping device shown in Figure 4.25b are presented. In contrast to the previous results, bending of the plate is achieved without external force acting on the plate surface within the propagation path. In the unloaded case, similar behavior of the attenuation is observed over frequency. However, the impact of load is less pronounced compared to the three-points bending setup. For low small bending loads, a clear trend can not be identified in the attenuation behavior. For maximum bending load, an increase of AE attenuation can be detected in the high frquency range between 250 kHz and 300 kHz.

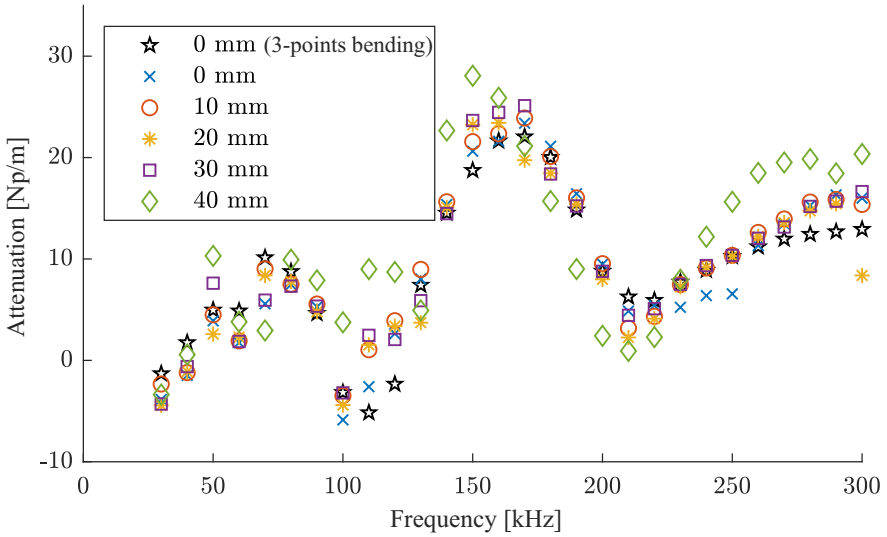

Figure 4.27: Comparison between attenuation coefficients of free and clamped plate [251].

From the experimental results, it can be concluded that for a specific transfer path between source and sensor, detectability of an AE source depends also on the frequency spectrum of the corresponding source mechanism. Furthermore, it can be expected that due to dispersion and attenuation, AE signatures of different source mechanisms in frequency domain are not invariant to the propagation path. In particular, regarding data-driven approaches based on statistical pattern recognition, which are widely studied for source characterization of AE, it has to be noted that dispersion and frequency dependent attenuation could have an impact on the distinguishability of different source mechanisms. Additionally, it can be concluded that to achieve robust detection and classification of AE, loading conditions have to be taken into consideration. In particular, it is notable that the support placed within the propagation path has strong impact on attenuation behavior of the material, which may be relevant for the use of AE during material testing experiments e.g. using a three-points bending setup.

4.5.4 Summary and conclusion

In this section, new experimental results regarding the AE attenuation characteristics of CFRP material due to wave propagation are presented. As typical specimens, thin plates manufactured from aerospace material are used. From the results it becomes clear that attenuation of AE due to propagation depends on the source frequency. Additionally, increased attenuation of the simulated AE waveforms is observed in a wide range of frequencies due to external bending load. A particularly high increase in attenuation can be observed due to a support placed within the propagation path. Therefore, it can be concluded that source frequency and external load may have an impact on the detectability of AE. To improve AE data analyses and interpretation, the impact of wave propagation and different loading conditions on the detectability of different source mechanisms has to be considered. Consequently, this includes the impact of attenuation on the performance of data-driven classification approaches. In future work, the optimization of sensor location based on detailed investigation of the propagation path may be considered. Furthermore, wave propagation related effects on AE signatures could be taken into account during training of a machine learning model to increase classification reliability.

5 New results of Acoustic Emission for process monitoring

As pointed out in [231], there is a need for innovative monitoring and control approaches to achieve efficient and sustainable manufacturing processes. Accurate sensing techniques, which allow to take in-situ measurements non-destructively or non-invasively over extended periods of time, can be considered as key enabling technology. Therefore, this chapter is focused on the use of AE as passive sensing technique for process monitoring and control. In the first section, an experimental study regarding AE signatures of different process conditions during thread forming is presented [256]. Subsequently, the use of AE to monitor PLAL nanoparticle production is explored. Finally, a proof of concept regarding the online use of AE data for control of the PLAL process is presented [254].

5.1 Experimental investigation of Acoustic Emission during thread forming

In manufacturing, the use of different Metal Working Fluid (MWF) has strong impact on tool wear. To identify wear mechanisms in friction contact, AE measurements can be used. In this section, AE signatures during thread forming using different MWF are investigated. As main contribution it is shown that AE is a suitable means to identify different MWF in thread forming. Based on AE signatures, different qualities of MWF can be distinguished. The following section is based on the previously published conference paper *In-situ wear monitoring: An experimental investigation of acoustic emission during thread forming*, which was presented at at the 11th International Workshop on Structural Health Monitoring [256].

5.1.1 Introduction

Estimation of tool wear is considered a difficult task due to complex interactions between tool and workpiece as well as noise originating from the environment. Besides different process parameters such as torque, thrust, or temperature, AE has emerged as a promising technique for indirect assessment of tool wear in different machining operations such as drilling or turning. The AE source mechanisms can be related to plastic deformation, chipping, or elastic interaction of surfaces.

Thread forming is a transformative manufacturing process for generating threads in ductile materials. As the thread geometry is manufactured by cold forming of the material, lubricating properties of the MWF strongly effect tool wear and workpiece quality. In this section, a tribometer is used to carry out thread forming trials under well-controlled experimental conditions. Different MWFs are considered, including lubricating oils as well as water-based MWFs. Time-frequency domain analysis of the AE signal is applied using CWT. Different process phases, forward and reverse, can be distinguished according to peak frequencies of

the AE signal. Furthermore, k-means clustering is used to identify different MWFs based on AE measurements. Energy in different frequency bands is used as a feature.

During the elastic-plastic interaction of surfaces under sliding motion structural alterations at the surface of the material can be observed, which ultimately cause surface fatigue and loss of material. Different principal mechanisms, namely adhesive and abrasive wear, can be distinguished. Since the contact zone is difficult to access, AE has recently been used to study wear in friction contact. It is generally accepted, that wear mechanisms can be distinguished based on the frequency content of the related AE. However, the relation to corresponding physical mechanisms is not unambiguous.

Asamene et al. [14] investigate the effect of different parameters in reciprocating contact of flat steel surfaces on the corresponding AE. Frequencies of 100 kHz and above, up to 700 kHz are considered. Hase et al. [109] study the AE during pin-on-block experiments to relate properties of the AE signal to distinct wear mechanisms. Frequencies between 250 kHz and 1 MHz are attributed to abrasive wear, whereas frequencies of up to 1.1 MHz can be related to adhesive wear. However, mild adhesive wear also excites frequencies in a lower regime between 10 kHz and 100 kHz [154]. Baccar and Söffker [18] suggest a novel health-monitoring approach for tribological system using frequency-selective analysis of AE. Three distinct wear phases of metallic plates in sliding contact can be distinguished according to the frequency content of AE signal.

In TCM, AE is frequently used as a means for indirect wear estimation in different machining operations. To develop indicators describing tool wear states, correlations between AE signal features and process parameters (i.e. power consumption, torque, or cutting forces) are exploited [200]. For instance, Gomez et al. [97] investigate the correlation between AE and torque in drilling operations. Mean power of the AE signal envelope and average spectral power in different frequency bands are considered. According to the results, burst type events could be related to chip breakage, whereas continuous AE is attributed to plastic deformation and friction, respectively. Statistical analysis shows that different types of worn drill bits (i.e. cutting edge and flute edge) can be distinguished. Also, increased wear of the tool leads to a shift of the signal power spectrum to increased frequencies. Using this approach, severely worn tools are identified reliably. Similarly, Ferrari and Gomez [87] address the relationship between thrust and AE in drilling. Compared to torque, thrust is considered to be particularly well suited to assess time behavior of the drilling process. Sensitivity of AE to tool wear is confirmed. However, correlation between thrust and tool wear could not be established.

Similarly, AE has been considered to assess the tool condition in turning. Bhuiyan et al. [36] investigate the effect of tool wear on AE and vibration measurements during turning in dry conditions. In particular, RMS of AE and vibration measurements is used as a feature. As a conclusion from this study, AE is sensitive to wear rates of the tool whereas vibrations are related to the surface roughness. Hase et al. [110] identified chip generation (continuous or discontinuous) as major influencing factor on AE. Furthermore, special emphasis is placed on the complex interaction between flank wear, cutting conditions (shear angle), and roughness of the machined surface during generation of chips. Moreover, Maia et al. [154] use the frequency content of AE signals to distinguish between different source mechanisms (i.e. adhesive and abrasive wear, plastic deformation).

From the summary above it is apparent that most frequently the condition of the tool is subject of investigation. However, machining operations are usually not performed under dry

conditions. To achieve improved performance MWF are typically used, which have major impact on the tribological conditions during friction contact [45]. To date, the underlying mechanisms are not well understood. Subsequently, an experimental study regarding the relationship between AE and wear at the example of thread forming is presented. The goal is to investigate, if changes in the interaction of surfaces during friction contact can be detected by means of AE.

5.1.2 Experimental procedure

To investigate the relationship between AE and different MWF in friction contact, thread forming is chosen as an example. As thread forming is a non-cutting machining operation, AE signal from the contact area is mostly free from superimposed AE due to chip formation or breakage. Furthermore, AE bursts due to cracking are avoided by ductility of workpiece material. Therefore, it can be assumed that in principle AE detected during thread forming is mainly related to friction and material deformation. The process itself runs discontinuously. During forward operation, the tap advances into the workpiece and threads are generated due to plastic deformation. Subsequently, the machine stops and the tool is extracted from the workpiece during reverse cycle. While material deformation is completed after forward cycle, interactions of tool- and workpiece surfaces also occurs during reverse.

Thread forming trials are carried out on a tribometer of type *Tauro 120*, providing closed-loop control of process parameters. In total, 112 M6 threads of 28 mm in depth are formed at a speed of 1000 rpm using different MWF. In between each trial, the tool is cleaned with brushes. As workpiece, a Ck45 (1.1191) steel plate with drilled pilot holes of 5.6H7 mm is used. Throughout the experiments, single thread forming tool of the type *Emuge M6-6HX InnoForm1-Z HSSE-TiN-T1* is used. The active tool length is 8 mm with a cutting lead of approximately 2-3 mm. The thread pitch is 1 mm. The experimental setup is illustrated in Figure 5.1.

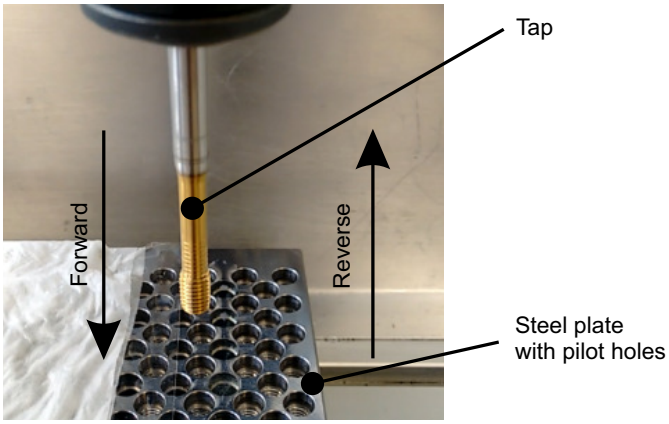

Figure 5.1: Illustration of experimental setup showing thread forming tool and workpiece [256].

Torque is directly measured by the tribometer. For AE measurements, a custom FPGA-based AE measurement system is used. To this end, a disc-shaped broadband piezoelectric transducer of diameter 10 mm and 0.55 mm in thickness is mounted on the work piece

using cyanoacrylic glue. The AE waveforms are acquired continuously at a sampling rate of 4 MHz. The AE signal is decomposed in time-frequency domain using CWT. To distinguish between different conditions k-means algorithm is used where energy of the AE signal in distinct frequency bands is used as a feature. Besides reference lubricating oil, two different emulsions and two different performance lubricating oils are used. The composition of MWF differs in the concentration of phosphorus, which is considered as anti-wear additive. Detailed information is given in Table 5.1. The particular sequence of trial series is stated in Table 5.2. First, 32 trials are performed using the reference oil (run in).

Table 5.1: Phosphorus concentration in MWF [256].

MWF	Emulsion 1	Emulsion 2	Oil 1	Oil 2
w [1e-3 %]	316,3	4,8	8	160

Table 5.2: Sequence of thread forming trials [256].

Trial series	MWF	Trial #
1	Reference	1-32
2	Emulsion 1	33-40
3	Emulsion 2	41-48
4	Oil 1	49-56
5	Oil 2	57-64
6	Reference	65-72
7	Oil 2	73-80
8	Oil 1	81-88
9	Emulsion 2	89-96
10	Emulsion 1	97-104
11	Reference	105-112

5.1.3 Results and discussion

Subsequently, results of the experimental study are presented. To investigate the relationship of friction and AE, comparison of AE energy and torque measurements is provided. Finally, cluster analysis using k-means algorithm is performed to distinguish between different MWF based on AE energy features.

Visual inspection of spectrograms

In the sequel, the time behavior of thread forming process is considered in time and time-frequency domain. Figure 5.2 shows examples of AE waveforms measured during thread forming using lubricating oil and water-based emulsion. In time domain representation, continuous AE signal with uniform amplitudes is observed. On large time scales, these measurements do not permit conclusions regarding underlying source mechanisms. In contrast,

two distinct process phases – forward operation and reverse – can be distinguished in time-frequency domain. During forward operation (0.1 s - 1.8 s), dominant frequency band in the range between 80 kHz and 150 kHz is detected. In contrast to this, lower frequencies between 50 kHz and 60 kHz are observed during reverse (2 s - 3.6 s).

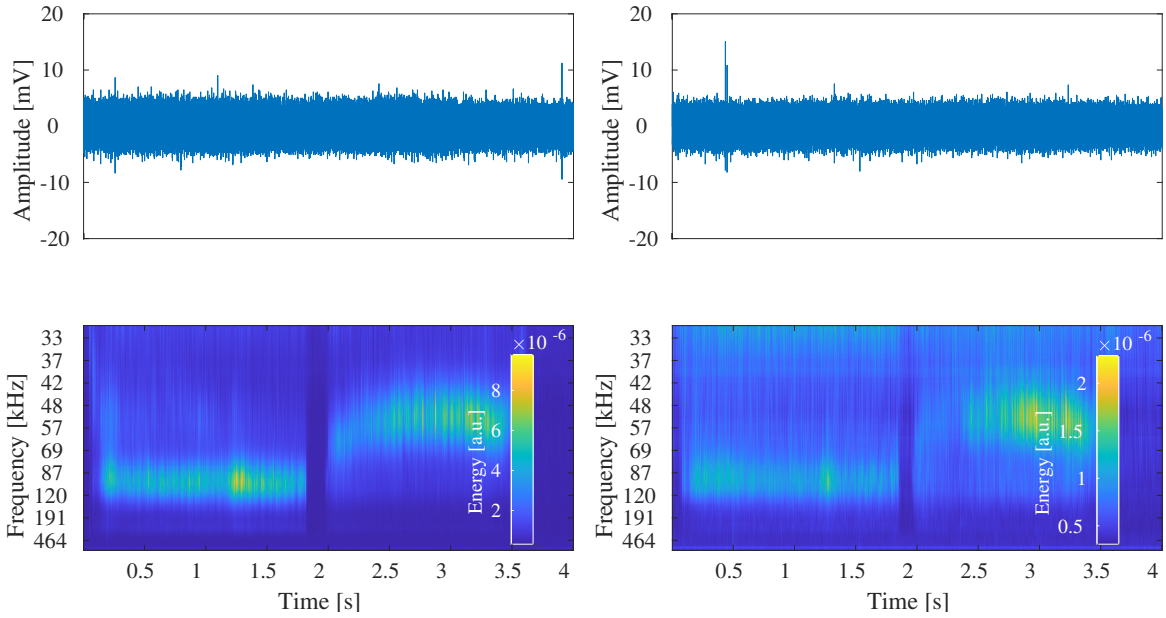

(a) Emulsion 2.

(b) Oil.

Figure 5.2: Examples of AE measurements during thread forming, adapted from [256].

These frequency ranges can be attributed to mild adhesive wear [154]. Also, plastic deformation has been characterized as a weak signal which is close to white noise [131]. Hence, this observations may also be explained by plastic deformation during forward operation and elastic relaxation of workpiece material during reverse.

Furthermore, a transient effect is evident during the forward cycle after 1.3 seconds. This effect is invariant in time and particularly pronounced in connection with emulsions. Using speed and tap geometry, a corresponding depth of approximately 20 mm can be calculated.

According to these results, temporal analysis of the AE measurements provides additional information to characterize the process. In this case, it is possible to relate dominant frequencies to distinct process phases by resolving the measurements in time and frequency domain. Furthermore, transient effects can be located in time. Ultimately, this allows establishment of a chronological sequence of events. These are essential aspects to develop a deeper understanding of the underlying physical mechanisms.

Comparison of AE energy and torque

Both, torque and AE are frequently used as indicators of tool wear. In Figure 5.3, comparison between mean torque and AE energy during each thread forming trial is provided. Mean values of CWT coefficients from consecutive time windows are used. The AE energy released during each trial is computed as the sum of all CWT coefficient means. Key features of AE energy and torque behavior (step like transition at changepoints between trial

series) are similar. However, AE energy shows additional features which are not observed in torque. In particular, a decreasing trend of AE energy is observed in trial series 1, which can be attributed to running in of the tool. In contrast, torque remains constant within a certain range or variability. Also, several peaks of AE energy are not reflected in torque measurements.

The use of different MWF clearly effects torque and AE energy. Lowest values are achieved for oil 1 and 2, whereas increased torque and AE energy can be detected using the emulsions 1 and 2. Also, whereas both lubricating oils show similar results, emulsion 2 can be related to increased values of torque and AE energy. Moreover it is noticeable that the reduction in torque and AE energy after the use of lubricating oils is permanent. In trial series 9 and 10 a reduction in AE energy and torque is detected compared to trial series 2 and 3.

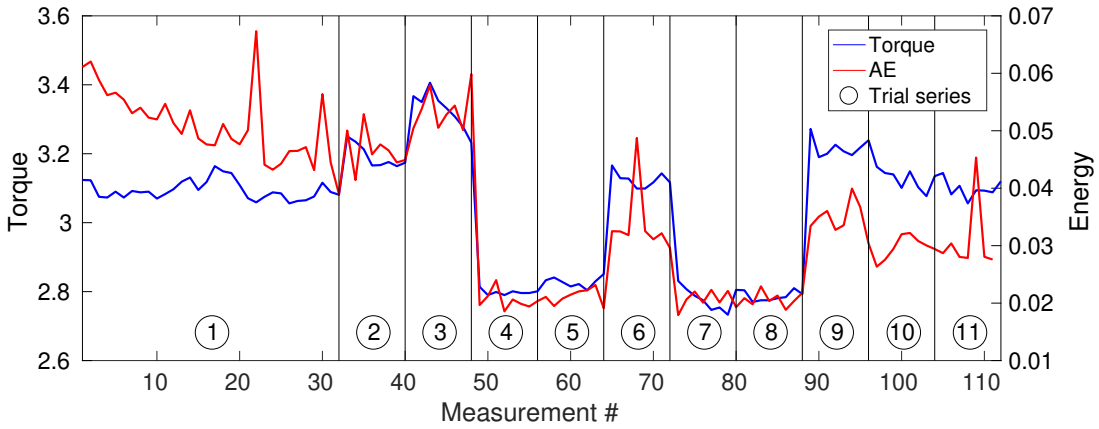

Figure 5.3: Comparison of AE energy and torque measurements [256].

These results lead to the conclusion that both AE energy and torque are related to the interaction between tool and workpiece surfaces during thread forming. As AE energy reflects differences between individual trials to a greater extent it is possible to reveal trends, which are not apparent in torque measurements. Permanent reduction in AE energy could be and indicator of changes in the tool surface properties (i.e. tribological conditioning).

Cluster analysis

In the previous sections, dependence of AE energy on the MWF is investigated. Furthermore, different process phases of thread forming (forward, reverse) can be related to dominant frequency bands. In this section, cluster analysis is conducted to investigate if thread forming trials with different MWFs can be distinguished using AE and k-means algorithm. The energy of AE signal in two frequency bands, which are denoted by central frequencies $f_2 = 115$ kHz and $f_1 = 57$ kHz, is used as a feature.

In Figure 5.4, clustering results and known ground truth are compared. The clustering results obtained for the two emulsions with different concentration are presented in Figure 5.4a and Figure 5.4b. The clusters are in good agreement with the known ground truth. Also, good cluster separation is achieved. Moreover, the MWF composition effects AE energy in each process phase to different degree. In Figure 5.4a and Figure 5.4b, clusters are clearly

separated in f_2. Lower AE energy during forward operation using emulsion 1 is indicated. In contrast, clusters are overlapping with respect to f_1 (reverse). This is in accordance with the composition of the MWF. Emulsion 1 contains an increased concentration of phosphorus leading to improved lubrication. In contrast, separation of trials using lubricating oils is not possible (Figure 5.4c). Comparison between different MWF types (emulsion 2, oil 1, and the reference) is provided in Figure 5.4d. The clusters are well separated in the feature space indicating dependence of AE on the quality of the MWF. The lowest energy is detected using high performance lubricating oil, whereas maximum AE energy is related to emulsion. The reference MWF is located in between.

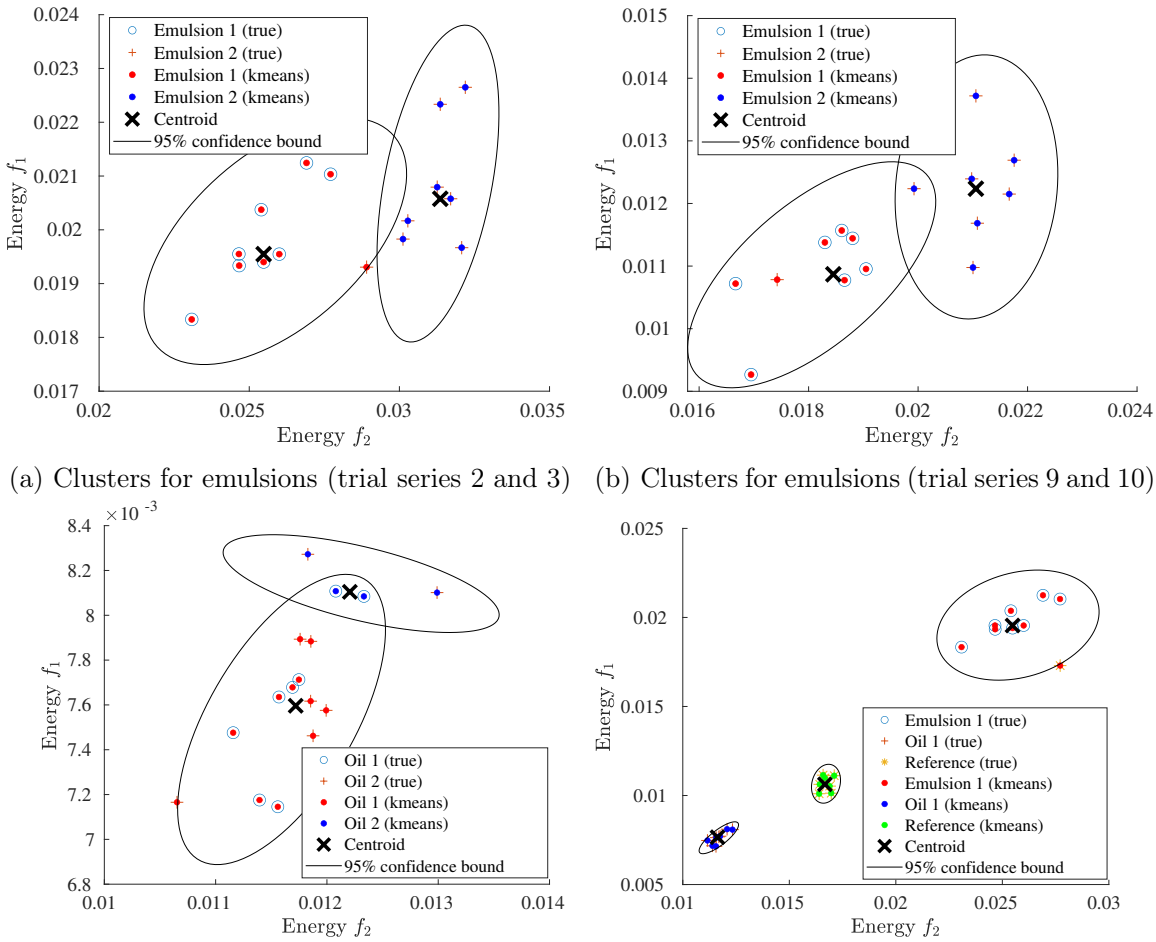

(a) Clusters for emulsions (trial series 2 and 3)

(b) Clusters for emulsions (trial series 9 and 10).

(c) Clusters for oils (trial series 4 and 5).

(d) Clusters for different MWF types (trial series 2,4, and 11).

Figure 5.4: Clustering results obtained using AE energy in two frequency bands, adapted from [256].

5.1.4 Summary and conclusions

In this contribution, experimental investigation of AE at the example of thread forming is presented. The goal is to investigate, whether changes in the interaction between tool

and workpiece surfaces (wear) can be detected by means of AE measurements. According to the results, both AE energy and torque are closely related to changes of the MWF. Lower energy levels of the AE signal using high performance lubricating oils indicate a dependency between wear rates and quality of the MWF. Compared to torque, AE provides a more accurate representation of the process. According to cluster analysis using k-means algorithm, the MWF of different quality could be distinguished indicating a dependence between AE and different MWF. Additionally, detailed investigation of AE signal in the time-frequency domain gives rise to enhanced insight into the temporal behavior of the machining operation. Therefore, AE is considered as a valuable tool for in-situ monitoring of wear to be used in future investigations to develop an in depth understanding of the fundamental mechanisms in surface interactions governing wear phenomena.

5.2 Application of Acoustic Emission to control of pulsed laser ablation in liquids

Besides manufacturing, AE is also gaining interest for in-situ monitoring in the process industry. Typically, chemical processes are performed in a confined environment and direct measurements of important process variables can be difficult to obtain due to physical or technological limitations. The sensitivity of AE to different physical phenomena can be exploited to obtain indirect measurements online, which can be used for monitoring and control. As main contribution, a proof of concept for the online use of AE in process control is demonstrated at the example of Pulsed Laser Ablation in Liquids (PLAL). The remainder of this section is based on the journal publication *Development of A Low-Cost FPGA-Based Measurement System for Real-Time Processing of Acoustic Emission Data: Proof of Concept Using Control of Pulsed Laser Ablation in Liquids* [254].

5.2.1 Introduction

The PLAL is a process for synthesis of nanoparticles from different materials using high energy laser. High energy laser pulses with a duration on the order of several nano seconds are used during PLAL to ignite a plasma on the surface of the target material. Furthermore, the high energy laser pulses cause formation of a cavitation bubble at the interface between the target material and the liquid. Nanoparticles are formed due to condensation in the gas phase of the cavitation bubble and are dispersed in the liquid after collapse [266]. Compared to chemical synthesis of nanoparticles, this process leads to a particularly clean product due to confinement in liquid environment e.g. water.

The placement of the target material at a suitable Working Distance (WD) is crucial to achieve high productivity of PLAL. The ablated mass per unit time depends strongly on the position of the target with respect to the focal point of the laser [201]. However, adjusting the WD manually is difficult and time consuming because direct measurement of the ablated mass requires disassembly of the test rig. Therefore, automatic adjustment of the WD based on in-situ measurements of the productivity is desirable.

A typical method to measure the productivity in-situ is Ultraviolet/Visible (UV/VIS) spectroscopy. However, the use of this method for process monitoring and control is limited to a small concentration range. Furthermore, there is a dependence on the material, the

particle size, and the particle shape. Therefore the use of AE measurements for automatic adjustment of the WD is suggested in [254]. Zhu et al. [273] established a correlation between material ablation rate and audible acoustic waves (sound) using wideband microphone. This idea is used to implement an automatic positioning algorithm to improve productivity of PLAL. Different to [273], a surface mounted piezoelectric sensor is used to record AE.

5.2.2 Laser ablation test rig

Subsequently, the PLAL test rig used during the experimental study is described. The ablation chamber is constructed so that the target can be placed in a fixed position on a translatory precision stage, which is driven by a stepper motor to adjust the WD. As target material, gold and copper sheet metal (purity: 99.99 %) of 0.5 mm and 1 mm thickness are used, respectively. Furthermore, Milli-Q ultra pure water is used as liquid. Continuous water flow through the ablation chamber at a fixed flow rate of 50 ml/min is realized using plunger pump Ismatec RHP 100994.

The AE related to the PLAL is recorded by a piezoelectric element, which is permanently mounted on the back side of the ablation chamber. A preamplifier is used for signal conditioning before the AE signal is digitized and processed on the ZedBoard (Figure 5.5). Here, control input of the stepper motor is calculated based on the AE measurements. Additionally, as a reference UV/VIS spectroscopy is used to monitor the nanoparticle concentration in the liquid by conducting the output flow of the ablation chamber through a cuvette (1 cm path length). According to Rehbock et al. [199], extinction in the UV/VIS spectrum at a wavelength of 380 nm is proportional to the nanoparticle concentration. A detailed summary of the equipment used during the experiments is provided in Table 5.3.

Table 5.3: Equipment of PLAL test rig [254].

Equipment	Specification
Laser: Rofin Sinar RS-Marker 100D	Wavelength: 1064 nm Power: 32.5 W Repetition rate: 5 kHz Pulse duration: 40 ns Scan speed: 600 mm/s
Plunger pump: Ismatec RHP 100994	Flow rate: 50 ml/min
UV/VIS	Lamp: Ocean Optics DH-Mini Detector: Red-Tide USB 650

5.2.3 Results

In this section, the results of different experiments to show sensitivity of AE to PLAL and to demonstrate the online use of AE for process control are presented. First, correlation between AE energy, WD, and PLAL productivity is established by choosing different WD manually.

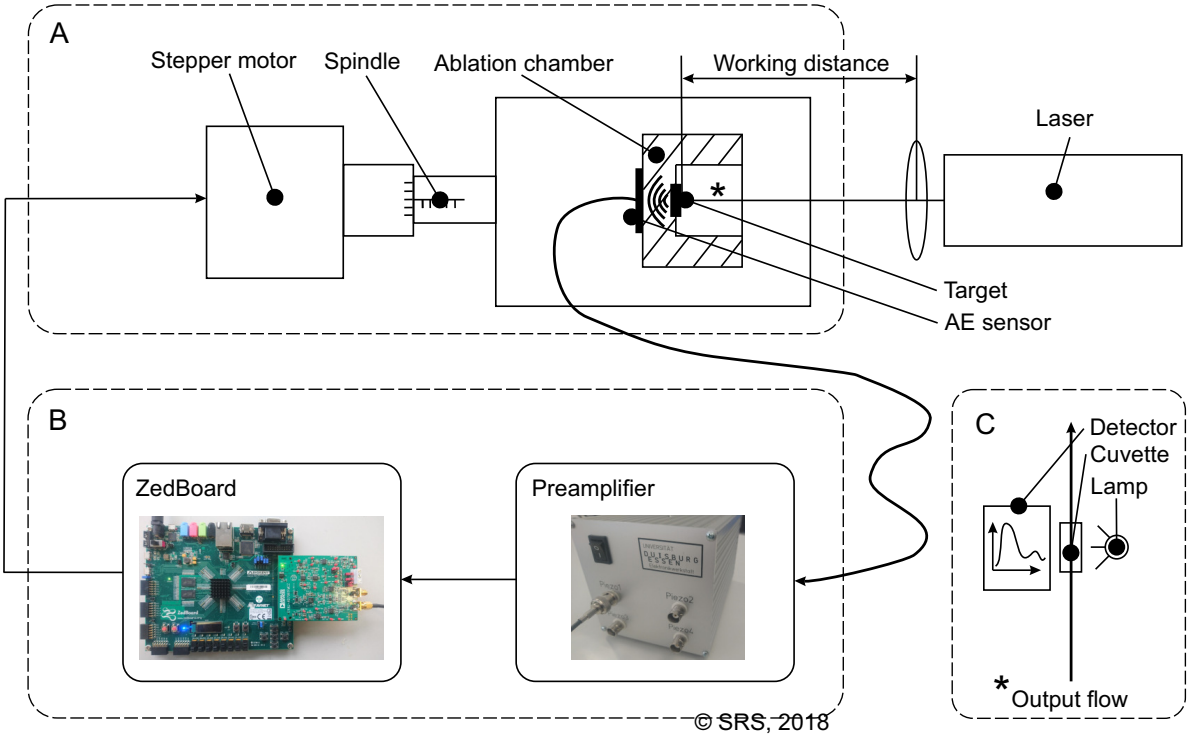

Figure 5.5: Illustration of the experimental setup: A: Process plant, B: Signal processing and control, C: UV/VIS measurement [254].

Finally, results of automatic WD adjustment are used to demonstrate the capabilities of the newly developed system described in Chapter 3 for AE measurements and signal processing.

Preliminary investigation of AE energy

During PLAL, ablation productivity strongly depends on the WD. To realize an automatic adjustment of the WD, a correlation between the AE energy and the productivity of the ablation is established in the sequel. In-situ UV/VIS spectroscopy and AE measurements are conducted simultaneously at different WD in proximity of the optimal WD using gold targets. Results of the AE measurements are compared to the nanoparticle concentration in the liquid as a reference. During each AE measurement, data are acquired for a duration of 7 s with a sample rate of 4 MHz. Averaged results using a total of 16 individual measurements are reported.

In Figure 5.6a the frequency spectrum of the AE signal is shown for different WD. At frequencies of 5 kHz and 10 kHz, AE energy peaks are evident. Furthermore, considering peak values of the frequency spectra, dependence of AE intensity on the WD is clear. Maximum energy is obtained for the working distance of 74 mm. In Figure 5.6b, comparison to in-situ UV/VIS measurements is presented. The maximum concentration of nanoparticles in the liquid is also obtained at a WD of 74 mm. As already reported in [273], a correlation between AE energy and productivity of PLAL can be observed. In difference to the work of Zhu et al. [273], a piezoelectric, mechanically coupled sensor is used, which has higher frequency bandwidth compared to a microphone. However, strong scatter of the AE energy

values is evident as it can be seen in Figure 5.6. Thus, approximate coefficients of DWT are used to reduce noise.

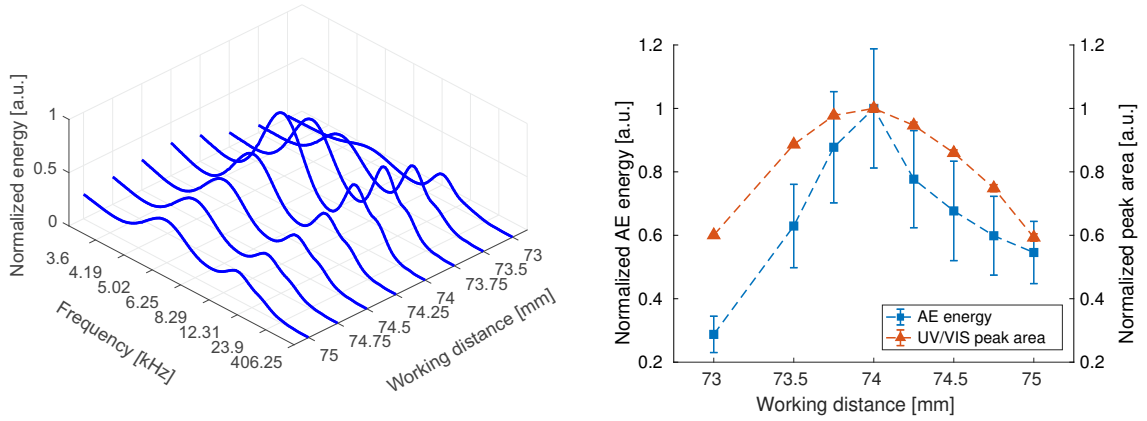

(a) Frequency spectra of AE during ablation (average of 16 measurements).

(b) Comparison of AE and UV/VIS.

Figure 5.6: Results for PLAL at different working distances [254].

Automatic adjustment of working distance

During PLAL, maximum productivity is achieved if the WD is adjusted so that the target surface is placed close to the focal point of the laser. However, the exact position leading to the best possible productivity is not known [201]. Furthermore, the corresponding spindle position is subject to variability, which is related to the mounting of the ablation chamber on the translatory stage and the placement of the target in the ablation chamber. Therefore, tuning of the optimal WD is difficult and time consuming so that due to the physical nature of the process, PLAL is frequently performed at possibly suboptimal WD.

To find and maintain a suitable WD, an iterative search algorithm for automatic positioning of the ablation chamber, which uses AE energy as objective, is realized. Here, a gradient-based search heuristic, which does not require a mathematical model, is used. The raw measurement data is processed by the DWT module in real-time using the PL core. The search algorithm is implemented on the PS running within the Linux operating system. To reduce noise, AE energy is obtained from the approximate coefficients of the DWT. As it is shown in the previous section, the AE energy is a convex function of the position so the optimal WD is expected at the maximum AE energy. Within each step, the position is changed in search direction with a fixed step size and measurement of the related AE is conducted. However, due to scatter of the AE energy, direct calculation of the gradient from two consecutive measurements is not feasible. Therefore, AE energy obtained at each step is stored in a buffer of fixed size holding the past N values. The gradient is estimated by an averaging procedure. Additionally, after each change of the search direction, a minimum number of measurements must be acquired. Moving towards the desired position, a positive gradient of the AE energy is obtained. If the estimated gradient is negative, the search

direction is reversed. Parameters of the search algorithm such as step size and the buffer size can be determined empirically.

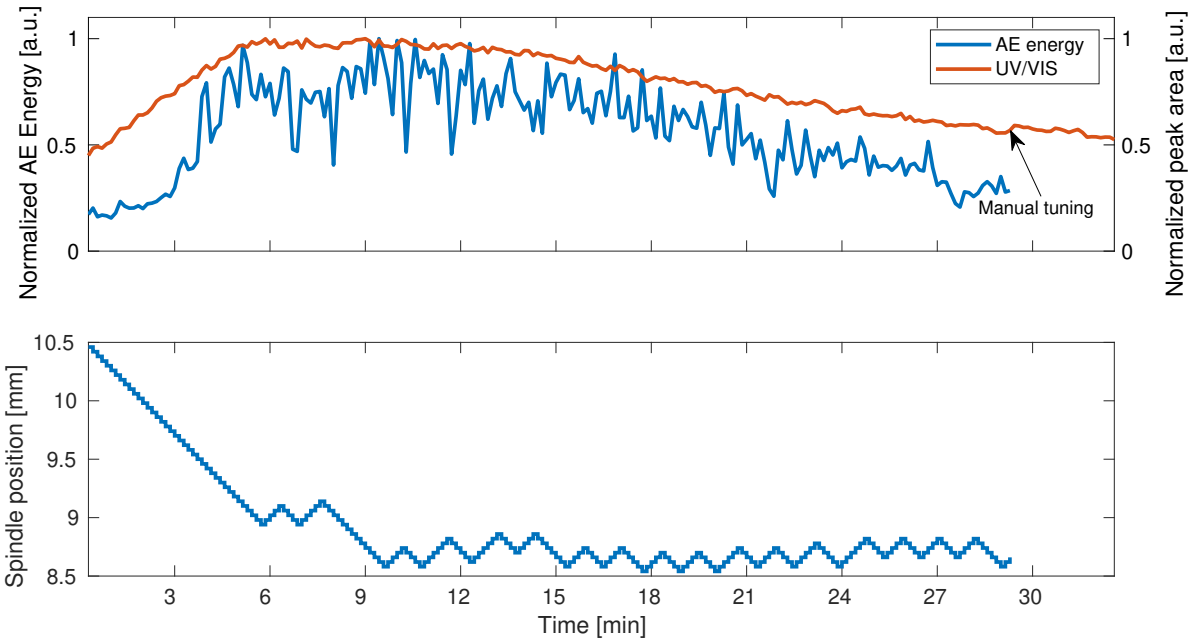

(a) Experimental run I.

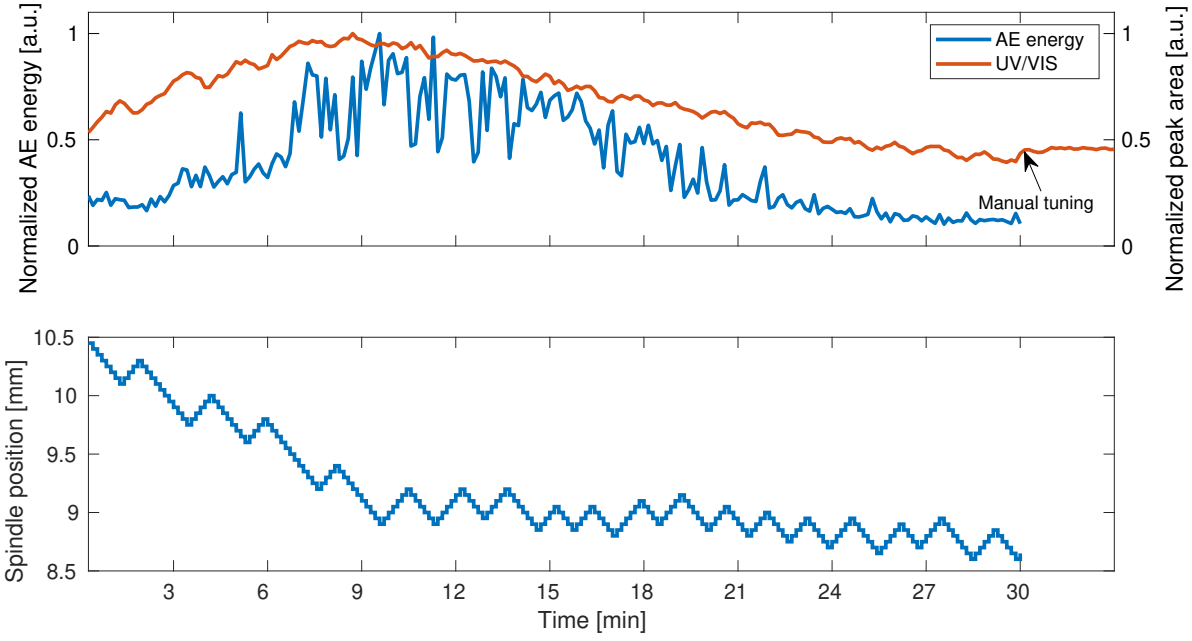

(b) Experimental run II.

Figure 5.7: Automatic positioning results [254].

The experimental results of the automatic positioning algorithm on the PLAL test rig are presented in Figure 5.7. Each experiment was run for approximately 30 min. Different

parameters for step size and buffer size were tested. During each iteration, full AE waveform data are acquired for 1.5 s at a sample rate of 5 MHz. The real-time DWT module is used to filter the AE signal. After 30 min, the automatic positioning was stopped to verify the determined position by manual tuning. Because the WD is dependent on the mounting of the ablation chamber on the translational stage and the placement of the target, WD can not be determined accurately and hence spindle position is reported, which is directly related to the WD.

The AE energy and UV/VIS measurements are in good agreement. Furthermore, the related spindle position is shown. The initial position was 10.5 mm in both cases. In the beginning of the experiment, the spindle position is adjusted towards the optimal WD by the algorithm. At the same time, the rise in AE energy and UV/VIS measurements indicates increased productivity. After 10 minutes, the spindle position settles in a range between 8.5 mm and 9 mm. After a period of constant productivity, decay of the AE energy is observed while the optimal WD does not change.

5.2.4 Summary and conclusion

Promising results have been reported, where AE is suggested as highly sensitive in-situ measurement technique for process monitoring and control. However, most of the analyses are carried out offline due to the complexity of signal processing algorithms (e.g., feature extraction and classification). To provide timely statements regarding the current system state or to realize related control actions, online processing of AE is required. At the example of PLAL nanoparticle production, it is shown that full waveform data from the AE sensor can be acquired and processed at a sample rate of 5 MHz. A novel hardware architecture, which is described in Chapter 3 of this thesis, is used.

As a proof of concept, automatic adjustment of the WD during PLAL for nanoparticle production is used. In the field of PLAL, the adjustment of a suitable WD is important but difficult and time consuming. Therefore, in-situ measurement techniques are necessary to assess the productivity and to implement automatic adjustment of the WD. Typically, UV/VIS spectroscopy is used to determine the concentration of nanoparticles in liquids. However, this technique can not be applied in general due to the dependence of the signal on the material, the particle size, and the particle shape. In addition, online UV/VIS spectroscopy is limited to a small concentration range. The use of AE measurements is a new approach to in-situ characterization of PLAL productivity. Generally, a good correlation between UV/VIS and AE energy is observed using copper and gold targets. It can be concluded that AE measurements provide a suitable means to assess the productivity of PLAL.

However, compared to UV/VIS measurements, large scatter of the AE energy is observed, which makes automatic positioning difficult. This is possibly related to the nonstationary character of the process, which until now is not perfectly understood. Possible explanations are absorption and scattering of the laser energy by cavitation bubbles and evaporated liquid inside of the ablation chamber as well as effects related to pulsating liquid flow (plunger pump) and the scan pattern. Also, at a given WD the productivity of PLAL in a flow setup is expected to be constant due to the continuous removal of the nanoparticles from the ablation zone. The decay of UV/VIS and AE energy (and thus productivity), which is observed during the experiments, could be attributed to changed process dynamics due

to thermal effects i.e. heating of the target and the ablation chamber. The experimental results show that using AE measurements, close to optimal WD with an accuracy between 0.25 mm and 0.75 mm can be achieved by applying a typical search algorithm.

6 Summary, conclusion, and outlook

Recently, AE was frequently suggested to obtain in-situ measurements for SHM and for process monitoring and control. Several advantages, such as high sensitivity to incipient damages, detectability of damages in a distance from the source, and characterization and localization of source mechanisms using advanced signal processing techniques, are inherent to the measurement principle. Current challenges are related to the continuous data-acquisition and online signal processing, data analysis and interpretation, and reliability under variable experimental and operating conditions. Subsequently, the related contributions presented in this thesis are summarized and conclusions are drawn. Finally, an outlook on future work is given.

6.1 Summary and conclusion

Regarding the use of AE for SHM and for process monitoring and control, the following main research questions are established in this thesis:

- Which alternative sensor mounting strategy can be used to simplify the application of AE in practice?
- How does the reliability of an individual classification result depend on environmental and operational factors?
- How can the effect of variable operational and environmental conditions on AE signatures be characterized?
- How can AE be processed effectively to characterize the productivity or product quality of a process?
- Which hardware platform is suitable to implement AE monitoring such that control actions can be realized online?

These are addressed by the contributions, which are presented in this thesis. In Chapter 2, AE is explained from a phenomenological point of view and conventional approaches to AE signal processing are summarized. Furthermore, the topics of measurement equipment, sensor technology, and wave propagation are addressed. Finally, the state-of-the-art is presented in Section 2.4.

In Chapter 3, a measurement system, which is suitable for continuous acquisition of AE waveform data is presented. The main contribution of this chapter is the development of a new hardware architecture as low cost solution for AE measurements. Key features are small form factor and low power consumption, which makes this device ideally suited for field deployment and embedded applications. A hardware-software coprocessing architecture is chosen. An implementation of DWT with 8 levels is realized using FPGA to calculate DWT coefficients in real time. Furthermore, several widely used I/O interfaces can be used to

integrate the system with digital infrastructure or to realize control actions. Therefore, this hardware platform is considered as well suited to implement online AE-based monitoring and control.

In Chapter 4, new results regarding the use of AE for SHM are presented. The reliability assessment of AE-based damage classification is addressed and the effect of operational and environmental factors on AE signatures is investigated. Furthermore, an alternative mounting strategy to simplify AE-based SHM is explored. Subsequently, the individual contributions are summarized.

- A data-driven approach is suggested as method-oriented but practical procedure, which can be used to determine a suitable threshold to distinguish between relevant subsections of AE measurements and noise. The main advantage is that a threshold for burst detection can be defined implicitly by the use of preliminary measurements.

- An experimental study is presented regarding AE sensor placement for gear box monitoring. In research, AE sensors are frequently mounted on moving parts of laboratory test rigs for highest sensitivity. However, such an approach might not be possible in practical applications. Therefore, the mounting of AE sensors outside the housing of a gear box is explored as a simple alternative, which is considered as relevant for the practical use of AE for gear box monitoring. According to the results, AE signatures related to different wear states of the gears can be detected using AE sensors mounted outside the housing of the gear box.

- The performance of different shape-based similarity measures is compared at the example of clustering and classification of different AE source mechanisms. In literature, shape-based similarity measures are suggested for waveform-based analysis of AE. According to the results, high classification accuracy could be achieved. In particular, elastic measures show robustness against waveform distortions including misalignment and additive noise.

- The reliability of data-driven fault detection is investigated. Key is the explicit consideration of different loading conditions. The results show a dependence on load. However, establishment of a direct relation is difficult due to scatter of the reliability estimation among different specimens. Therefore, assessment of classification reliability is raised as new scientific challenge.

- Finally, the effect of wave propagation on AE signatures is investigated. Special focus is placed on the frequency dependence of material related AE attenuation. Depending on source frequency and external load, different attenuation is observed, which may have an impact on the detectability of AE.

In Chapter 5, new results for process monitoring are presented. In particular, characterization of process productivity and product quality are addressed. Subsequently, the individual contributions are summarized.

- At the example of thread forming process, the use of AE for the characterization of different Metal Working Fluid (MWF) is investigated. Regarding thread forming, wear mechanisms in friction contact are of particular interest, which can be detected using

AE measurements. The use of different MWF, has a strong impact on tool wear. According to the results, AE is a suitable means to identify different MWF in thread forming. Based on AE signatures, different qualities of MWF can be distinguished.

- In the process industry, in-situ measurements are necessary for process monitoring and to ensure an optimal working point. The online use of AE in process control is demonstrated at the example of Pulsed Laser Ablation in Liquids (PLAL). In PLAL, the choice of Working Distance (WD) is crucial to achieve high productivity. However, direct measurements are difficult to obtain and the use of competing methods is limited. Therefore, AE is suggested as an indirect measurement for monitoring purposes. Finally, automatic WD adjustment to ensure high productivity is implemented using online AE measurements.

6.2 Outlook

Based on the contributions presented in this thesis, the following directions for future work are suggested. Regarding the development of AE measurement equipment for research, a low-cost hardware platform, which can be used in different applications for AE measurements and process control is suggested. In future work, the deployment of a classifier on the suggested hardware architecture may be attempted for automated classification of AE. Furthermore, a simple algorithm is used to demonstrate the proof of concept for process control at the example of PLAL. For future applications, versatile I/O-interfaces allow the integration with more powerful hardware to implement advanced control algorithms.

For the use of AE in SHM, different data-driven approaches for automated AE data analysis are explored. To improve damage detectability and distinguishability, the optimization of sensor location based on detailed investigation of the propagation path may be considered in the future. Furthermore, wave propagation related effects on AE signatures could be taken into account during training of a machine learning model to increase classification reliability.

Finally, at the example of thread forming the usefulness of AE for process monitoring is pointed out. Different MWF can be distinguished using AE measurements. This correlation may be useful in the future to establish AE-based qualification scheme for MWF.

References

[1] B. D. Agarwal, L. J. Broutman, and K. Chandrashekhara. *Analysis and performance of fiber composites*. John Wiley & Sons, 2006.

[2] D. G. Aggelis and T. E. Matikas. Effect of plate wave dispersion on the acoustic emission parameters in metals. *Computers and Structures*, 98-99:17–22, 2012.

[3] S. Aghabozorgi, A. Seyed Shirkhorshidi, and T. Ying Wah. Time-series clustering - A decade review. *Information Systems*, 53:16–38, 2015.

[4] Y. S. Ahmed, M. S. Alam, A. F. Arif, and S. C. Veldhuis. Use of acoustic emission and cutting force signals to monitor built-up edge formation in stainless steel turning. *International Journal of Advanced Manufacturing Technology*, 103:2257–2276, 2019.

[5] K. R. Al-Balushi, A. Addali, B. Charnley, and D. Mba. Energy index technique for detection of acoustic emissions associated with incipient bearing failures. *Applied Acoustics*, 71(9):812–821, 2010.

[6] K. R. Al-Balushi and B. Samanta. Gear fault diagnosis using energy-based features of acoustic emission signals. *Proceedings of the Institution of Mechanical Engineers, Part I: Journal of Systems and Control Engineering*, 216(3):249–263, 2002.

[7] S. K. Al-Jumaili, K. M. Holford, M. J. Eaton, and R. Pullin. Parameter Correction Technique (PCT): A novel method for acoustic emission characterisation in large-scale composites. *Composites Part B: Engineering*, 75:336–344, 2015.

[8] L. Al-Shrouf, M.-S. Saadawia, and D. Söffker. Improved process monitoring and supervision based on a reliable multi-stage feature-based pattern recognition technique. *Information Sciences*, 259:282–294, 2014.

[9] P. Allan, L. J. Bellamy, A. Nordon, and D. Littlejohn. Non-invasive monitoring of the mixing of pharmaceutical powders by broadband acoustic emission. *Analyst*, 135(3):518–524, 2010.

[10] J. Antoni. The spectral kurtosis: a useful tool for characterising non-stationary signals. *Mechanical Systems and Signal Processing*, 20(2):282–307, 2006.

[11] J. Antoni. Fast computation of the kurtogram for the detection of transient faults. *Mechanical Systems and Signal Processing*, 21(1):108–124, 2007.

[12] J. Antoni. Cyclostationarity by examples. *Mechanical Systems and Signal Processing*, 23(4):987–1036, 2009.

[13] K. Asamene, L. Hudson, and M. Sundaresan. Influence of attenuation on acoustic emission signals in carbon fiber reinforced polymer panels. *Ultrasonics*, 59:86–93, 2015.

[14] K. Asamene and M. Sundaresan. Analysis of experimentally generated friction related acoustic emission signals. *Wear*, 296:607–618, 2012.

[15] ASTM International. ASTM E 1316-02a: Standard terminology for nondestructive examinations. ASTM International, West Conshohocken, PA, USA, 2003.

[16] ASTM International. ASTM E 650-97: Standard guide for mounting piezoelectric Acoustic Emission sensors. ASTM International, West Conshohocken, PA, USA, 1997.

[17] M. Azadi, H. Sayar, A. Ghasemi-Ghalebahman, and S. M. Jafari. Tensile loading rate effect on mechanical properties and failure mechanisms in open-hole carbon fiber reinforced polymer composites by acoustic emission approach. *Composites Part B: Engineering*, 158:448–458, 2019.

[18] D. Baccar and D. Söffker. Wear detection by means of wavelet-based acoustic emission analysis. *Mechanical Systems and Signal Processing*, 60-61:198–207, 2015.

[19] D. Baccar and D. Söffker. Identification and classification of failure modes in laminated composites by using a multivariate statistical analysis of wavelet coefficients. *Mechanical Systems and Signal Processing*, 96:77–87, 2017.

[20] M. Bahoura. FPGA implementation of a feature extraction technique based on fourier transform. In *2012 24th International Conference on Microelectronics (ICM)*, Algiers, Algeria, December 16-20, 2012.

[21] M. Bahoura and H. Ezzaidi. Real-time implementation of discrete wavelet transform on FPGA. In *IEEE 10th International Conference on Signal Processing Proceedings*, Beijing, China, October 24-28, 2010.

[22] M. Bahoura and H. Ezzaidi. FPGA-implementation of discrete wavelet transform with application to signal denoising. *Circuits, Systems, and Signal Processing*, 31(3):987–1015, 2012.

[23] F. Bai, D. Gagar, P. Foote, and Y. Zhao. Comparison of alternatives to amplitude thresholding for onset detection of acoustic emission signals. *Mechanical Systems and Signal Processing*, 84:717–730, 2017.

[24] K. M. Bak, K. KalaiChelvan, G. Vijayaraghavan, and B. Sridhar. Acoustic emission wavelet transform on adhesively bonded single-lap joints of composite laminate during tensile test. *Journal of Reinforced Plastics and Composites*, 32(2):87–95, 2013.

[25] C. Baker, G. N. Morscher, V. V. Pujar, and J. R. Lemanski. Transverse cracking in carbon fiber reinforced polymer composites: Modal acoustic emission and peak frequency analysis. *Composites Science and Technology*, 116:26–32, 2015.

[26] C. Barile, C. Casavola, and G. Pappalettera. Acoustic emission waveform analysis in CFRP under mode I test. *Engineering Fracture Mechanics*, 210:408–413, 2019.

[27] M. Barroso-Romero, D. Gagar, S. Pant, and M. Martinez. Wave mode identification of acoustic emission signals using phase analysis. *Acoustics*, 1:450–472, 2019.

[28] G. E. Batista, X. Wang, and E. J. Keogh. A complexity-invariant distance measure for time series. In *SIAM International Conference on Data Mining*, 2011.

[29] M. G. Baxter, R. Pullin, K. M. Holford, and S. L. Evans. Delta T source location for acoustic emission. *Mechanical Systems and Signal Processing*, 21:1512–1520, 2007.

[30] N. Beganovic and D. Söffker. Structural health management utilization for lifetime prognosis and advanced control strategy deployment of wind turbines: An overview and outlook concerning actual methods, tools, and obtained results. *Renewable and Sustainable Energy Reviews*, 64:68–83, 2016.

[31] N. Beheshtizadeh and A. Mostafapour. Processing of acoustic signals via wavelet & Choi - Williams analysis in three-point bending load of carbon/epoxy and glass/epoxy composites. *Ultrasonics*, 79:1–8, 2017.

[32] N. Beheshtizadeh, A. Mostafapour, and S. Davoodi. Three point bending test of glass/epoxy composite health monitoring by acoustic emission. *Alexandria Engineering Journal*, 58(2):567–578, 2019.

[33] A. Behnia, H. K. Chai, and T. Shiotani. Advanced structural health monitoring of concrete structures with the aid of acoustic emission. *Construction and Building Materials*, 65:282–302, 2014.

[34] Y. Bengio and Y. Grandvalet. No unbiased estimator of the variance of k-fold cross-validation. *Journal of Machine Learning Research*, 5:1089–1105, 2004.

[35] M. S. H. Bhuiyan, I. A. Choudhury, M. Dahari, Y. Nukman, and S. Z. Dawal. Application of acoustic emission sensor to investigate the frequency of tool wear and plastic deformation in tool condition monitoring. *Measurement*, 92:208–217, 2016.

[36] M. S. H. Bhuiyan, I. A. Choudhury, and Y. Nukman. Tool condition monitoring using acoustic emission and vibration signature in turning. In *Proceedings of the world congress on engineering*, London, UK, July 4-6, 2012.

[37] Y. Bhuiyan, B. Lin, and V. Giurgiutiu. Characterization of piezoelectric wafer active sensor for acoustic emission sensing. *Ultrasonics*, 92:35–49, 2019.

[38] D. Bianchi, E. Mayrhofer, M. Gröschl, G. Betz, and A. Vernes. Wavelet packet transform for detection of single events in acoustic emission signals. *Mechanical Systems and Signal Processing*, 64-65:441–451, 2015.

[39] C. M. Bishop. *Pattern recognition and machine learning*. Springer, 2006.

[40] G. Blake and J. Reynolds. Case study involving surface durability and improved surface finish. *Gear Technology*, pages 66–75, 2012.

[41] B. Boashash and S. Ouelha. Automatic signal abnormality detection using time-frequency features and machine learning: A newborn EEG seizure case study. *Knowledge-Based Systems*, 106:38–50, 2016.

[42] J. Bohse. Acoustic emission characteristics of micro-failure processes in polymer blends and composites. *Composites Science and Technology*, 60:1213–1226, 2000.

[43] J. Bohse. Damage analysis of polymer matrix composites by acoustic emission testing. In *Proceedings of European WG on AE*, Berlin, Germany, 2004.

[44] J. W. R. Boyd and J. Varley. The uses of passive measurement of acoustic emissions from chemical engineering processes. *Chemical Engineering Science*, 56(5):1749–1767, 2001.

[45] E. Brinksmeier, D. Meyer, A. G. Huesmann-Cordes, and C. Herrmann. Metalworking fluids - Mechanisms and performance. *CIRP Annals - Manufacturing Technology*, 64(2):605–628, 2015.

[46] A. J. Brunner. Identification of damage mechanisms in fiber-reinforced polymer-matrix composites with acoustic emission and the challenge of assessing structural integrity and service-life. *Construction and Building Materials*, 173:629–637, 2018.

[47] C. Burges. A tutorial on support vector machines for pattern recognition. *Data Mining and Knowledge Discovery*, 2(2):121–167, 1998.

[48] A. Bussiba, M. Kupiec, S. Ifergane, R. Piat, and T. Böhlke. Damage evolution and fracture events sequence in various composites by acoustic emission technique. *Composites Science and Technology*, 68(5):1144–1155, 2008.

[49] L. Cao, K. Chua, W. Chong, H. Lee, and Q. Gu. A comparison of PCA, KPCA and ICA for dimensionality reduction in support vector machine. *Neurocomputing*, 55:321–336, 2003.

[50] P. Cawley. Structural health monitoring: Closing the gap between research and industrial deployment. *Structural Health Monitoring*, 17(5):1225–1244, 2018.

[51] M. Cerrada, R. V. Sánchez, C. Li, F. Pacheco, D. Cabrera, J. Valente de Oliveira, and R. E. Vásquez. A review on data-driven fault severity assessment in rolling bearings. *Mechanical Systems and Signal Processing*, 99:169–196, 2018.

[52] M. Chai, Z. Zhang, and Q. Duan. A new qualitative acoustic emission parameter based on Shannon's entropy for damage monitoring. *Mechanical Systems and Signal Processing*, 100:617–629, 2018.

[53] C.-C. Chang and C.-J. Lin. LIBSVM: A library for support vector machines. *ACM Transactions on Intelligent Systems and Technology*, 2:27:1–27:27, 2011. Software available at `http://www.csie.ntu.edu.tw/~cjlin/libsvm`.

[54] S. K. Chelliah, P. Parameswaran, S. Ramasamy, A. Vellayaraj, and S. Subramanian. Optimization of acoustic emission parameters to discriminate failure modes in glass–epoxy composite laminates using pattern recognition. *Structural Health Monitoring*, 18(4):1253–1267, 2019.

[55] S. Chen, C. Yang, G. Wang, and W. Liu. Similarity assessment of acoustic emission signals and its application in source localization. *Ultrasonics*, 75:36–45, 2017.

[56] O. Cheng, W. Abdulla, and Z. Salcic. Hardware-software codesign of automatic speech recognition system for embedded real-time applications. *IEEE Transactions on Industrial Electronics*, 58(3):850–859, 2011.

[57] A. C. Cobb, J. Fisher, and J. Michaels. Model-assisted probability of detection for ultrasonic structural health monitoring. In *4th European-American Workshop on Reliability of NDE*, Berlin, Germany, 2009.

[58] T. Cover and P. Hart. Nearest Neighbor Pattern Classification. *IEEE Transactions on Information Theory*, 13(1):21–27, 1967.

[59] D. Crivelli, M. Guagliano, M. Eaton, M. Pearson, S. Al-Jumaili, K. Holford, and R. Pullin. Localisation and identification of fatigue matrix cracking and delamination in a carbon fibre panel by acoustic emission. *Composites Part B: Engineering*, 74:1–12, 2015.

[60] D. Crivelli, M. Guagliano, and A. Monici. Development of an artificial neural network processing technique for the analysis of damage evolution in pultruded composites with acoustic emission. *Composites Part B: Engineering*, 56:948–959, 2014.

[61] D. Crivelli, J. McCrory, S. Miccoli, R. Pullin, and A. Clarke. Gear tooth root fatigue test monitoring with continuous acoustic emission: Advanced signal processing techniques for detection of incipient failure. *Structural Health Monitoring*, 17(3):423–433, 2018.

[62] A. Crouter and L. Briens. Passive acoustic emissions from particulates in a V-blender. *Drug Development and Industrial Pharmacy*, 41(11):1809–1818, 2015.

[63] A. P. A. Cunha, S. F. Wirtz, D. Söffker, and N. Beganovic. Implementation of frequency-based classification of damages in composites using real-time FPGA-based hardware framework. In *ASME 2017 International Design Engineering Technical Conferences & Computers and Information in Engineering Conference*, Cleveland, OH, USA, August 6-9, 2017.

[64] F. Dahmene, S. Yaacoubi, M. El Mountassir, N. Bendaoud, C. Langlois, and O. Bardoux. On the modal acoustic emission testing of composite structure. *Composite Structures*, 140:446–452, 2016.

[65] A. Danyuk, I. Rastegaev, E. Pomponi, M. Linderov, D. Merson, and A. Vinogradov. Improving of acoustic emission signal detection for fatigue fracture monitoring. *Procedia Engineering*, 176:284–290, 2017.

[66] S. Das, A. N. Srivastava, and A. Chattopadhyay. Classification of damage signatures in composite plates using one-class SVMs. In *2007 IEEE Aerospace Conference*, Big Sky, MT, USA, March 3-10, 2007.

[67] P. J. de Groot, P. A. M. Wijnen, and R. B. Janssen. Real-time frequency determination of acoustic emission for different fracture mechanisms in carbon/epoxy composites. *Composites Science and Technology*, 55(4):405–412, 1995.

[68] R. de Oliveira and A. Marques. Health monitoring of FRP using acoustic emission and artificial neural networks. *Computers & Structures*, 86:367–373, 2008.

[69] A. Dia, L. Dieng, L. Gaillet, and P. B. Gning. Damage detection of a hybrid composite laminate aluminum/glass under quasi-static and fatigue loadings by acoustic emission technique. *Heliyon*, 5(3):e01414, 2019.

[70] K. Diamanti and C. Soutis. Structural health monitoring techniques for aircraft composite structures. *Progress in Aerospace Sciences*, 46(8):342–352, 2010.

[71] A. Diez, N. L. D. Khoa, M. Makki Alamdari, Y. Wang, F. Chen, and P. Runcie. A clustering approach for structural health monitoring on bridges. *Journal of Civil Structural Health Monitoring*, 6(3):429–445, 2016.

[72] H. Ding, G. Trajcevski, P. Scheuermann, X. Wang, and E. J. Keogh. Querying and mining of time series data: Experimental comparison of representations and distance measures. *Proceedings of the VLDB Endowment*, 1(2):1542–1552, 2008.

[73] B. Eckstein, C. Fritzen, and M. Bach. Considerations on the reliability of guided ultrasonic wave-based SHM systems for CFRP aerospace structures. *Proceedings of the 6th European Workshop on Structural Health Monitoring*, pages 1–8, 2012.

[74] B. Eftekharnejad, A. Addali, and D. Mba. Shaft crack diagnostics in a gearbox. *Applied Acoustics*, 73(8):723–733, 2012.

[75] B. Eftekharnejad, M. R. Carrasco, B. Charnley, and D. Mba. The application of spectral kurtosis on acoustic emission and vibrations from a defective bearing. *Mechanical Systems and Signal Processing*, 25(1):266–284, 2011.

[76] B. Eftekharnejad and D. Mba. Seeded fault detection on helical gears with acoustic emission. *Applied Acoustics*, 70:547–555, 2009.

[77] F. Elasha, M. Greaves, D. Mba, and A. Addali. Application of acoustic emission in diagnostic of bearing faults within a helicopter gearbox. *Procedia CIRP*, 38:30–36, 2015.

[78] F. Elasha, M. Greaves, D. Mba, and D. Fang. A comparative study of the effectiveness of vibration and acoustic emission in diagnosing a defective bearing in a planetry gearbox. *Applied Acoustics*, 115:181–195, 2017.

[79] M. Elforjani and D. Mba. Accelerated natural fault diagnosis in slow speed bearings with acoustic emission. *Engineering Fracture Mechanics*, 77:112–127, 2010.

[80] M. Elforjani, D. Mba, A. Muhammad, and A. Sire. Condition monitoring of worm gears. *Applied Acoustics*, 73:859–863, 2012.

[81] R. Errichello. Morphology of micropitting. *Gear Technology*, pages 74–81, 2012.

[82] P. Esling and C. Agon. Time-series data mining. *ACM Computing Surveys*, 45(1):1–34, 2012.

[83] S. K. Everton, M. Hirsch, P. I. Stavroulakis, R. K. Leach, and A. T. Clare. Review of in-situ process monitoring and in-situ metrology for metal additive manufacturing. *Materials and Design*, 95:431–445, 2016.

[84] C. R. Farrar and K. Worden. An introduction to structural health monitoring. *Philosophical Transactions of the Royal Society A: Mathematical, Physical and Engineering Sciences*, 365(1851):303–15, 2006.

[85] A. Fasana and L. Garibaldi. Measurement of acoustic emission signals: influence of the couplant. *Key Engineering Materials*, 347:375–380, 2007.

[86] P. Feng, P. Borghesani, H. Chang, W. A. Smith, R. B. Randall, and Z. Peng. Monitoring gear surface degradation using cyclostationarity of acoustic emission. *Mechanical Systems and Signal Processing*, 131:199–221, 2019.

[87] G. Ferrari and M. P. Gómez. Correlation between acoustic emission, thrust and tool wear in drilling. *Procedia Materials Science*, 8:693–701, 2015.

[88] L. Ferreira and D. B. Hitchcock. A comparison of hierarchical methods for clustering functional data. *Communications in Statistics—Simulation and Computation*, 38(9):1925–1949, 2009.

[89] D. Gagar, P. Foote, and P. Irving. Effects of loading and sample geometry on acoustic emission generation during fatigue crack growth: Implications for structural health monitoring. *International Journal of Fatigue*, 81:117–127, 2015.

[90] R. X. Gao and R. Yan. *Wavelets: Theory and applications for manufacturing*. Springer, 2011.

[91] G. Georgakoudis, C. Gillan, A. Hassan, U. I. Minhas, I. Spence, G. Tzenakis, H. Vandierendonck, R. Woods, D. S. Nikolopoulos, M. Shyamsundar, P. Barber, M. Russell, A. Bilas, S. Kaloutsakis, H. Giefers, P. Staar, C. Bekas, N. Horlock, R. Faloon, and C. Pattison. NanoStreams: Codesigned microservers for edge analytics in real time. In *Proceedings of 2016 International Conference on Embedded Computer Systems: Architectures, Modeling and Simulation (SAMOS)*, Konstantinos, Greece, July 17-21, 2016.

[92] N. Gherras, E. Serris, and G. Fevotte. Monitoring industrial pharmaceutical crystallization processes using acoustic emission in pure and impure media. *International Journal of Pharmaceutics*, 439:109–119, 2012.

[93] V. Giurgiutiu. Tuned Lamb wave excitation and detection with piezoelectric wafer active sensors for structural health monitoring. *Journal of Intelligent Material Systems and Structures*, 16(4):291–305, 2005.

[94] V. Giurgiutiu. *Structural Health Monitoring with Piezoelectric Wafer Active Sensors (2nd Edition)*. Academic Press, 2014.

[95] N. Godin, S. Huguet, and R. Gaertner. Integration of the Kohonen's self-organising map and k-means algorithm for the segmentation of the AE data collected during tensile tests on cross-ply composites. *NDT and E International*, 38:299–309, 2005.

[96] N. Godin, P. Reynaud, and G. Fantozzi. Challenges and limitations in the identification of acoustic emission signature of damage mechanisms in composites materials. *Applied Sciences*, 8(8):1267, 2018.

[97] M. P. Gómez and A. M. Hey. Assessment of cutting tool condition by acoustic emission. *Procedia Materials Science*, 1:321–328, 2012.

[98] C. U. Grosse and M. Ohtsu. *Acoustic Emission Testing*. Springer, 2008.

[99] R. Gutkin, C. Green, S. Vangrattanachai, S. Pinho, P. Robinson, and P. Curtis. On acoustic emission for failure investigation in CFRP: Pattern recognition and peak frequency analyses. *Mechanical Systems and Signal Processing*, 25(4):1393–1407, 2011.

[100] M. Halkidi. On Clustering Validation Techniques. *Journal of Intelligent Information Systems*, 17:107–145, 2001.

[101] J. Hämäläinen, S. Jauhiainen, and T. Kärkkäinen. Comparison of internal clustering validation indices for prototype-based clustering. *Algorithms*, 10(3):105, 2017.

[102] S. E. Hamdi, A. Le Duff, L. Simon, G. Plantier, A. Sourice, and M. Feuilloy. Acoustic emission pattern recognition approach based on Hilbert-Huang transform for structural health monitoring in polymer-composite materials. *Applied Acoustics*, 74(5):746–757, 2013.

[103] M. Hamel, A. Addali, and D. Mba. Investigation of the influence of oil film thickness on helical gear defect detection using acoustic emission. *Applied Acoustics*, 79:42–46, 2014.

[104] M. A. Hamstad. A review: Acoustic emission, a tool for composite-materials studies. *Experimental Mechanics*, 26:7–13, 1986.

[105] B. H. Han, D. J. Yoon, Y. H. Huh, and Y. S. Lee. Damage assessment of wind turbine blade under static loading test using acoustic emission. *Journal of Intelligent Material Systems and Structures*, 25(5):621–630, 2014.

[106] J. Handl, J. Knowles, and D. B. Kell. Computational cluster validation in post-genomic data analysis. *Bioinformatics*, 21(15):3201–3212, 2005.

[107] Q. Hao, X. Zhang, K. Wang, Y. Shen, and Y. Wang. A signal-adapted wavelet design method for acoustic emission signals of rail cracks. *Applied Acoustics*, 139:251–258, 2018.

[108] W. Harizi, S. Chaki, G. Bourse, and M. Ourak. Mechanical damage characterization of glass fiber-reinforced polymer laminates by ultrasonic maps. *Composites Part B: Engineering*, 70:131–137, 2015.

[109] A. Hase, H. Mishina, and M. Wada. Correlation between features of acoustic emission signals and mechanical wear mechanisms. *Wear*, 292-293:144–150, 2012.

[110] A. Hase, M. Wada, T. Koga, and H. Mishina. The relationship between acoustic emission signals and cutting phenomena in turning process. *International Journal of Advanced Manufacturing Technology*, 70(5-8):947–955, 2014.

[111] F. Hemmati, W. Orfali, and M. S. Gadala. Roller bearing acoustic signature extraction by wavelet packet transform, applications in fault detection and size estimation. *Applied Acoustics*, 104:101–118, 2016.

[112] M. Holgersson. The limited value of cophenetic correlation as a clustering criterion. *Pattern Recognition*, 10:287–295, 1978.

[113] C.-W. Hsu, C.-C. Chang, and C.-J. Lin. A practical guide to support vector classification. Technical report, Department of Computer Science, National Taiwan University, 2003.

[114] Q. Huang, Y. Cui, L. B. Tjernberg, and G. Ab. Wind turbine health assessment framework based on power analysis using machine learning method. *2019 IEEE PES Innovative Smart Grid Technologies Europe (ISGT-Europe)*, 2019.

[115] S. Husin, A. Addali, and D. Mba. Feasibility study on the use of the acoustic emission technology for monitoring flow patterns in two phase flow. *Flow Measurement and Instrumentation*, 33:251–256, 2013.

[116] D. A. Hutchins, D. R. Billson, R. J. Bradley, and K. S. Ho. Structural health monitoring using polymer-based capacitive micromachined ultrasonic transducers (CMUTs). *Ultrasonics*, 51(8):870–877, 2011.

[117] A. K. Jain. Data clustering: 50 years beyond k-means. *Pattern Recognition Letters*, 31(8):651–666, 2010.

[118] A. K. S. Jardine, D. Lin, and D. Banjevic. A review on machinery diagnostics and prognostics implementing condition-based maintenance. *Mechanical Systems and Signal Processing*, 20(7):1483–1510, 2006.

[119] M. Johnson and P. Gudmundson. Broad-band transient recording and characterization of acoustic emission events in composite laminates. *Composites Science and Technology*, 60(15):2803–2818, 2000.

[120] M. Kaphle, A. C. C. Tan, D. P. Thambiratnam, and T. H. T. Chan. Effective discrimination of acoustic emission source signals for structural health monitoring. *Advances in Structural Engineering*, 15(5):706–716, 2012.

[121] M. R. Kaphle, A. C. C. Tan, D. P. Thambiratnam, and T. H. T. Chan. Study of acoustic emission data analysis tools for structural health monitoring applications. *Journal of Acoustic Emission*, 29:243–250, 2011.

[122] E. Keogh, S. Lonardi, C. A. Ratanamahatana, L. Wei, S. H. Lee, and J. Handley. Compression-based data mining of sequential data. *Data Mining and Knowledge Discovery*, 14:99–129, 2007.

[123] E. Keogh and C. A. Ratanamahatana. Exact indexing of dynamic time warping. *Knowledge and Information Systems*, 7:358–386, 2005.

[124] M. Kharrat, V. Placet, E. Ramasso, and M. L. Boubakar. Influence of damage accumulation under fatigue loading on the AE-based health assessment of composite materials: Wave distortion and AE-features evolution as a function of damage level. *Composites Part A: Applied Science and Manufacturing*, 109:615–627, 2018.

[125] M. Kharrat, E. Ramasso, V. Placet, and M. L. Boubakar. A signal processing approach for enhanced Acoustic Emission data analysis in high activity systems: Application to organic matrix composites. *Mechanical Systems and Signal Processing*, 70-71:1038–1055, 2016.

[126] M. Kharrat, E. Ramasso, V. Placet, and M. L. Boubakar. A signal processing approach for enhanced acoustic emission data analysis in high activity systems: Application to organic matrix composites. *Mechanical Systems and Signal Processing*, 70-71:1038–1055, 2016.

[127] M. Khazaee, H. Ahmadi, M. Omid, A. Moosavian, and M. Khazaee. Classifier fusion of vibration and acoustic signals for fault diagnosis and classification of planetary gears based on Dempster-Shafer evidence theory. *Proceedings of the Institution of Mechanical Engineers, Part E: Journal of Process Mechanical Engineering*, 228(1):21–32, 2014.

[128] B. Kilundu, X. Chiementin, J. Duez, and D. Mba. Cyclostationarity of Acoustic Emissions (AE) for monitoring bearing defects. *Mechanical Systems and Signal Processing*, 25(6):2061–2072, 2011.

[129] H. A. Kishawy, H. Hegab, U. Umer, and A. Mohany. Application of acoustic emissions in machining processes: analysis and critical review. *International Journal of Advanced Manufacturing Technology*, 98:1391–1407, 2018.

[130] F. Klocke, B. Döbbeler, T. Pullen, and T. Bergs. Acoustic emission signal source separation for a flank wear estimation of drilling tools. *Procedia CIRP*, 79:57–62, 2019.

[131] R. Kocich, M. Cagala, J. Crha, and P. Kozelsky. Character of Acoustic Emission signal generated during plastic deformation. In *30th European Conference on Acoustic Emission Testing & 7th International Conference on Acoustic Emission*, Granada, Spain, September 12-15, 2012.

[132] S. Kosaraju and V. G. Anne. Online tool condition monitoring in turning titanium (grade 5) using acoustic emission: modeling. *International Journal of Advanced Manufacturing Technology*, 67:1947–1954, 2013.

[133] S. Kotsiantis, I. Zaharakis, and P. Pintelas. Supervised machine learning: A review of classification techniques. *Informatica*, 31:249–268, 2007.

[134] T. Kundu, X. Yang, H. Nakatani, and N. Takeda. A two-step hybrid technique for accurately localizing acoustic source in anisotropic structures without knowing their material properties. *Ultrasonics*, 56:271–278, 2015.

[135] J. H. Kurz, C. U. Grosse, and H. W. Reinhardt. Strategies for reliable automatic onset time picking of acoustic emissions and of ultrasound signals in concrete. *Ultrasonics*, 43(7):538–546, 2005.

[136] J. H. Kurz, A. Jüngert, S. Dugan, G. Dobmann, and C. Boller. Reliability considerations of NDT by Probability of Detection (POD) determination using ultrasound phased array. *Engineering Failure Analysis*, 35:609–617, 2013.

[137] R. Lammering, U. Gabbert, M. Sinapius, T. Schuster, and P. Wierach. *Lamb-Wave Based Structural Health Monitoring in Polymer Comoposites*. Springer, 2017.

[138] LAMSS. Lamss database, 2019. http://www.me.sc.edu/research/lamss/Download/Softwares/LAMSS-COMPOSITES_V1.zip (accessed 05.04.2019).

[139] C. Li, R. V. Sanchez, G. Zurita, M. Cerrada, D. Cabrera, and R. E. Vásquez. Gearbox fault diagnosis based on deep random forest fusion of acoustic and vibratory signals. *Mechanical Systems and Signal Processing*, 76-77:283–293, 2016.

[140] L. Li, S. V. Lomov, and X. Yan. Correlation of acoustic emission with optically observed damage in a glass/epoxy woven laminate under tensile loading. *Composite Structures*, 123:45–53, 2015.

[141] L. Li, S. V. Lomov, X. Yan, and V. Carvelli. Cluster analysis of acoustic emission signals for 2D and 3D woven glass/epoxy composites. *Composite Structures*, 116:286–299, 2014.

[142] R. Li and D. He. Rotational machine health monitoring and fault detection using EMD-based acoustic emission feature quantification. *IEEE Transactions on Instrumentation and Measurement*, 61(4):990–1001, 2012.

[143] Z. Li, W. Lu, and Y. Xiao. Propagation characteristics of acoustic emission signal in rotor system. *Advances in Engineering Reseach*, 184:189–193, 2019.

[144] S. Liang, C. Zhang, W. Lin, L. Li, C. Li, X. Feng, and B. Lin. Fiber-optic intrinsic distributed acoustic emission sensor for large structure health monitoring. *Optics Letters*, 34(12):1858–60, 2009.

[145] F. Lissek, A. Haeger, V. Knoblauch, S. Hloch, F. Pude, and M. Kaufeld. Acoustic emission for interlaminar toughness testing of CFRP: Evaluation of the crack growth due to burst analysis. *Composites Part B: Engineering*, 136:55–62, 2018.

[146] C. Liu, X. Wu, J. Mao, and X. Liu. Acoustic emission signal processing for rolling bearing running state assessment using compressive sensing. *Mechanical Systems and Signal Processing*, 91:395–406, 2017.

[147] J. Liu, Y. Hu, B. Wu, and Y. Wang. An improved fault diagnosis approach for FDM process with acoustic emission. *Journal of Manufacturing Processes*, 35:570–579, 2018.

[148] T. Loutas, G. Sotiriades, I. Kalaitzoglou, and V. Kostopoulos. Condition monitoring of a single-stage gearbox with artificially induced gear cracks utilizing on-line vibration and acoustic emission measurements. *Applied Acoustics*, 70(9):1148–1159, 2009.

[149] T. H. Loutas, J. Kalaitzoglou, G. Sotiriades, and V. Kostopoulos. A novel approach for continuous acoustic emission monitoring on rotating machinery without the use of slip ring. *Journal of Vibration and Acoustics*, 130(6):064502, 2008.

[150] T. H. Loutas and V. Kostopoulos. Health monitoring of carbon/carbon, woven reinforced composites. Damage assessment by using advanced signal processing techniques. Part I: Acoustic emission monitoring and damage mechanisms evolution. *Composites Science and Technology*, 69(2):265–272, 2009.

[151] T. H. Loutas, D. Roulias, E. Pauly, and V. Kostopoulos. The combined use of vibration, acoustic emission and oil debris on-line monitoring towards a more effective condition monitoring of rotating machinery. *Mechanical Systems and Signal Processing*, 25(4):1339–1352, 2011.

[152] B. Lu, Y. Li, X. Wu, and Z. Yang. A review of recent advances in wind turbine condition monitoring and fault diagnosis. In *2009 IEEE Power Electronics and Machines in Wind Applications*, Lincoln, NE, USA, 2009.

[153] N. Maeda. A method for reading and checking phase times in autoprocessing system of seismic wave data. *Zisin*, 38(3):365–379, 1985.

[154] L. H. A. Maia, A. M. Abrao, W. L. Vasconcelos, W. F. Sales, and A. R. Machado. A new approach for detection of wear mechanisms and determination of tool life in turning using acoustic emission. *Tribology International*, 92:519–532, 2015.

[155] E. Maillet, C. Baker, G. N. Morscher, V. V. Pujar, and J. R. Lemanski. Feasibility and limitations of damage identification in composite materials using acoustic emission. *Composites Part A: Applied Science and Manufacturing*, 75:77–83, 2015.

[156] M. Majnik and Z. Bosnić. ROC analysis of classifiers in machine learning: A survey. *Intelligent Data Analysis*, 17(3):531–558, 2013.

[157] C. Mandache, M. Genest, M. Khan, and N. Mrad. Considerations on structural health monitoring reliability. In *International Workshop Smart Materials, Structures & NDT in Aerospace*, Montreal, Quebec, Canada, 2011.

[158] A. Marec, J. H. Thomas, and R. El Guerjouma. Damage characterization of polymer-based composite materials: Multivariable analysis and wavelet transform for clustering acoustic emission data. *Mechanical Systems and Signal Processing*, 22(6):1441–1464, 2008.

[159] S. Martin-del Campo, S. Schnabel, F. Sandin, and P. Marklund. Detection of particle contaminants in rolling element bearings with unsupervised acoustic emission feature learning. *Tribology International*, 132:30–38, 2019.

[160] J. Martínez-Jequier, A. Gallego, E. Suárez, F. J. Juanes, and Á. Valea. Real-time damage mechanisms assessment in CFRP samples via acoustic emission Lamb wave modal analysis. *Composites Part B: Engineering*, 68:317–326, 2015.

[161] M. Martinez-Luengo, A. Kolios, and L. Wang. Structural health monitoring of offshore wind turbines: A review through the statistical pattern recognition paradigm. *Renewable and Sustainable Energy Reviews*, 64:91–105, 2016.

[162] P. Mazal, L. Nohal, F. Hort, and V. Koula. Possibilities of the damage diagnostics of gearboxes and bearings with acoustic emissions method. In *Proceedings of the 18th World Conference on Nondestructive Testing*, Durban, South Africa, April 16-20, 2012.

[163] D. Mba and R. B. Rao. Development of acoustic emission technology for condition monitoring and diagnosis of rotating machines: bearings, pumps, gearboxes, engines, and rotating structures. *The Shock and Vibration Digest*, 38(1):3–17, 2006.

[164] J. P. McCrory, S. K. Al-Jumaili, D. Crivelli, M. R. Pearson, M. J. Eaton, C. A. Featherston, M. Guagliano, K. M. Holford, and R. Pullin. Damage classification in carbon fibre composites using acoustic emission: A comparison of three techniques. *Composites Part B: Engineering*, 68:424–430, 2015.

[165] N. Md Nor, C. R. Che Hassan, and M. A. Hussain. A review of data-driven fault detection and diagnosis methods: applications in chemical process systems. *Reviews in Chemical Engineering*, 2019.

[166] H. Mei, M. F. Haider, R. Joseph, A. Migot, and V. Giurgiutiu. Recent advances in piezoelectric wafer active sensors for structural health monitoring applications. *Sensors*, 19(2), 2019.

[167] A. Mertins. *Signaltheorie*. Springer-Verlag, 2013.

[168] D. E. Mouzakisa and D. G. Dimogianopoulos. Acoustic emission detection of damage induced by simulated environmental conditioning in carbon fiber reinforced composites. *Engineering Fracture Mechanics*, 210:422–428, 2019.

[169] I. Mueller and C. P. Fritzen. Inspection of piezoceramic transducers used for structural health monitoring. *Materials*, 10(1):71, 2017.

[170] V. Munoz, B. Valès, M. Perrin, M. L. Pastor, H. Welemane, A. Cantarel, and M. Karama. Damage detection in CFRP by coupling acoustic emission and infrared thermography. *Composites Part B: Engineering*, 85:68–75, 2016.

[171] A. Nair and C. Cai. Acoustic emission monitoring of bridges: Review and case studies. *Engineering Structures*, 32(6):1704–1714, 2010.

[172] M. Nazmdar Shahri, J. Yousefi, M. Fotouhi, and M. Ahmadi Najfabadi. Damage evaluation of composite materials using acoustic emission features and Hilbert transform. *Journal of Composite Materials*, 50(14):1897–1907, 2016.

[173] Q. Q. Ni and M. Iwamoto. Wavelet transform of acoustic emission signals in failure of model composites. *Engineering Fracture Mechanics*, 69(6):717–728, 2002.

[174] M. Nikbakht, J. Yousefi, H. Hosseini-Toudeshky, and G. Minak. Delamination evaluation of composite laminates with different interface fiber orientations using acoustic emission features and micro visualization. *Composites Part B: Engineering*, 113:185–196, 2017.

[175] K. Ono. Through-transmission characteristics of AE sensor couplants. *Journal of Acoustic Emission*, 34:1–11, 2017.

[176] K. Ono. Rayleigh wave calibration of acoustic emission sensors and ultrasonic transducers. *Sensors*, 19(14):3129, 2019.

[177] F. E. Oz, N. Ersoy, and S. V. Lomov. Do high frequency acoustic emission events always represent fibre failure in CFRP laminates? *Composites Part A: Applied Science and Manufacturing*, 103:230–235, 2017.

[178] D. Ozevin, D. W. Greve, I. J. Oppenheim, and S. P. Pessiki. Resonant capacitive MEMS acoustic emission transducers. *Smart Materials and Structures*, 15(6):1863–1871, 2006.

[179] R. Pahuja and M. Ramulu. Surface quality monitoring in abrasive water jet machining of Ti6Al4V–CFRP stacks through wavelet packet analysis of acoustic emission signals. *The International Journal of Advanced Manufacturing Technology*, 104:4091–4104, 2019.

[180] M. R. Pearson, M. Eaton, C. Featherston, R. Pullin, and K. Holford. Improved acoustic emission source location during fatigue and impact events in metallic and composite structures. *Structural Health Monitoring*, 16(4):382–399, 2017.

[181] M. A. Pérez, L. Gil, and S. Oller. Impact damage identification in composite laminates using vibration testing. *Composite Structures*, 108(1):267–276, 2014.

[182] F. Petitjean, A. Ketterlin, and P. Gançarski. A global averaging method for dynamic time warping, with applications to clustering. *Pattern Recognition*, 44(3):678–693, 2011.

[183] F. Pinal Moctezuma, M. Delgado Prieto, and L. Romeral Martinez. Performance analysis of acoustic emission hit detection methods using time features. *IEEE Access*, 7:71119–71130, 2019.

[184] J. Platt. Probabilistic outputs for support vector machines and comparisons to regularized likelihood methods. *Advances in large margin classifiers*, 10(3):61–74, 1999.

[185] A. Pollock. Probability of detection for acoustic emission. *Journal of Acoustic Emission*, 25:231–237, 2007.

[186] E. Pomponi, A. Vinogradov, and A. Danyuk. Wavelet based approach to signal activity detection and phase picking: Application to acoustic emission. *Signal Processing*, 115:110–119, 2015.

[187] M. Prakash, M. Kanthababu, and K. P. Rajurkar. Investigations on the effects of tool wear on chip formation mechanism and chip morphology using acoustic emission signal in the microendmilling of aluminum alloy. *International Journal of Advanced Manufacturing Technology*, 77:1499–1511, 2015.

[188] W. Prosser, K. Jackson, S. Kellas, B. Smith, J. Mckeon, and A. Friedman. Advanced, waveform based acoustic emission detection of matrix cracking in composites. *Materials Evaluation*, 53(9):1052–1058, 1995.

[189] W. H. Prosser. Waveform analysis of AE in composites. In *International Symposium on Acoustic Emission From Composite Materials*, San Antonio, 1998.

[190] Y. T. Qassim, T. Cutmore, D. James, and D. Rowlands. FPGA implementation of morlet continuous wavelet transform for EEG analysis. In *International Conference on Computer and Communication Engineering (ICCCE 2012)*, Kuala Lumpur, Malaysia, July 3-5, 2012.

[191] Y. Qu, E. Bechhoefer, D. He, and J. Zhu. A new acoustic emission sensor based gear fault detection approach. *International Journal of Prognostics and Health Management*, 3:32–45, 2013.

[192] T. B. Quy, S. Muhammad, and J.-M. Kim. A reliable acoustic emission based technique for the detection of a amall leak in a pipeline system. *Energies*, 12(8):1472, 2019.

[193] M. Rabiei and M. Modarres. Quantitative methods for structural health management using in situ acoustic emission monitoring. *International Journal of Fatigue*, 49:81–89, 2013.

[194] R. Raja Hamzah and D. Mba. The influence of operating condition on acoustic emission (AE) generation during meshing of helical and spur gear. *Tribology International*, 42(1):3–14, 2009.

[195] T. Rakthanmanon, B. Campana, A. Mueen, G. Batista, B. Westover, Q. Zhu, J. Zakaria, and E. Keogh. Addressing big data time series: Mining trillions of time series subsequences under dynamic time warping. *ACM Transactions on Knowledge Discovery from Data*, 7(3):3047–3051, 2013.

[196] K. Ramasubramanian, N. Arunachalam, and M. S. Rao. A study on CVD diamond coated cutting tools wear performance using vibration and acoustic emission signals. *Procedia CIRP*, 72:1415–1420, 2018.

[197] C. Rawles and C. Thurber. A non-parametric method for automatic determination of P-wave and S-wave arrival times: application to local micro earthquakes. *Geophysical Journal International*, 202(2):1164–1179, 2015.

[198] A. Refahi Oskouei, H. Heidary, M. Ahmadi, and M. Farajpur. Unsupervised acoustic emission data clustering for the analysis of damage mechanisms in glass/polyester composites. *Materials & Design*, 37:416–422, 2012.

[199] C. Rehbock, V. Merk, L. Gamrad, R. Streubel, and S. Barcikowski. Size control of laser-fabricated surfactant-free gold nanoparticles with highly diluted electrolytes and their subsequent bioconjugation. *Physical Chemistry Chemical Physics*, 15(9):3057–3067, 2013.

[200] A. G. Rehorn, J. Jiang, and P. E. Orban. State-of-the-art methods and results in tool condition monitoring: A review. *International Journal of Advanced Manufacturing Technology*, 26:693–710, 2005.

[201] S. Reich, P. Schönfeld, A. Letzel, S. Kohsakowski, M. Olbinado, B. Gökce, S. Barcikowski, and A. Plech. Fluence threshold behaviour on ablation and bubble formation in pulsed laser ablation in liquids. *Chemical Ph*, 18(9):1084–1090, 2017.

[202] W. Roundi, A. El Mahi, A. El Gharad, and J. L. Rebiere. Acoustic emission monitoring of damage progression in Glass/Epoxy composites during static and fatigue tensile tests. *Applied Acoustics*, 132:124–134, 2018.

[203] C. Ruiz-Cárcel, E. Hernani-Ros, Y. Cao, and D. Mba. Use of spectral kurtosis for improving signal to noise ratio of acoustic emission signal from defective bearings. *Journal of Failure Analysis and Prevention*, 14(3):363–371, 2014.

[204] M. Saeedifar, M. Fotouhi, M. Ahmadi Najafabadi, H. Hosseini Toudeshky, and G. Minak. Prediction of quasi-static delamination onset and growth in laminated composites by acoustic emission. *Composites Part B: Engineering*, 85:113–122, 2016.

[205] M. Saeedifar, M. A. Najafabadi, D. Zarouchas, H. H. Toudeshky, and M. Jalalvand. Barely visible impact damage assessment in laminated composites using acoustic emission. *Composites Part B: Engineering*, 152:180–192, 2018.

[206] M. Saeedifar, M. A. Najafabadi, D. Zarouchas, H. H. Toudeshky, and M. Jalalvand. Clustering of interlaminar and intralaminar damages in laminated composites under indentation loading using acoustic emission. *Composites Part B: Engineering*, 144:206–219, 2018.

[207] B. Samanta and C. Nataraj. Use of particle swarm optimization for machinery fault detection. *Engineering Applications of Artificial Intelligence*, 22:308–316, 2009.

[208] D. Sánchez-Molina, E. Martínez-González, J. Velázquez-Ameijide, J. Llumà, M. C. R. Soria, and C. Arregui-Dalmases. A stochastic model for soft tissue failure using acoustic emission data. *Journal of the mechanical behavior of biomedical materials*, 51:328–36, 2015.

[209] M. G. R. Sause. Investigation of pencil-lead breaks as acoustic emission sources. *Journal of Acoustic Emission*, 29:184–196, 2011.

[210] M. G. R. Sause, A. Gribov, A. R. Unwin, and S. Horn. Pattern recognition approach to identify natural clusters of acoustic emission signals. *Pattern Recognition Letters*, 33(1):17–23, 2012.

[211] M. G. R. Sause, F. F. Linscheid, and M. Wiehler. An experimentally accessible probability of detection model for acoustic emission measurements. *Journal of Nondestructive Evaluation*, 37(2):1–12, 2018.

[212] M. G. R. Sause, S. Schmitt, B. Hoeck, and A. Monden. Acoustic emission based prediction of local stress exposure. *Composites Science and Technology*, 173:90–98, 2019.

[213] M. G. R. Sause, S. Schmitt, and S. Kalafat. Failure load prediction for fiber-reinforced composites based on acoustic emission. *Composites Science and Technology*, 164:24–33, 2018.

[214] H. Sayar, M. Azadi, A. Ghasemi-Ghalebahman, and S. M. Jafari. Clustering effect on damage mechanisms in open-hole laminated carbon/epoxy composite under constant tensile loading rate, using acoustic emission. *Composite Structures*, 204:1–11, 2018.

[215] C. Scheer, W. Reimche, and F. Bach. Early fault detection at gear units by acoustic emission and wavelet analysis. *Journal of Acoustic Emission*, 25:331–340, 2007.

[216] S. Schnabel, S. Golling, P. Marklund, and R. Larsson. The influence of contact time and event frequency on acoustic emission signals. *Proceedings of the Institution of Mechanical Engineers, Part J: Journal of Engineering Tribology*, 231(10):1341–1349, 2017.

[217] S. Schnabel, P. Marklund, R. Larsson, and S. Golling. The detection of plastic deformation in rolling element bearings by acoustic emission. *Tribology International*, 110:209–215, 2017.

[218] P. J. Schubel, R. J. Crossley, E. K. G. Boateng, and J. R. Hutchinson. Review of structural health and cure monitoring techniques for large wind turbine blades. *Renewable Energy*, 51:113–123, 2013.

[219] C. M. Schubert Kabban, B. M. Greenwell, M. P. DeSimio, and M. M. Derriso. The probability of detection for structural health monitoring systems: Repeated measures data. *Structural Health Monitoring*, 14(3):252–264, 2015.

[220] C. B. Scruby. An introduction to acoustic emission. *Journal of Physics E: Scientific Instruments*, 20(8):946–953, 2000.

[221] P. Sebastiani and T. T. Perls. Detection of significant groups in hierarchical clustering by resampling. *Frontiers in Genetics*, 7:144, 2016.

[222] E. Sevillano, R. Sun, A. Gil, and R. Perera. Interfacial crack-induced debonding identification in FRP-strengthened RC beams from PZT signatures using hierarchical clustering analysis. *Composites Part B: Engineering*, 87:322–335, 2016.

[223] M. Shateri, D. Thomson, M. Ghaib, and D. Svecova. System for logging acoustic emission signals from FRP reinforcing rods that is suitable for field and long term laboratory testing. In *Structural Health Monitoring 2017, Stanford, USA, September 12-14*, 2017.

[224] S. A. Shevchik, C. Kenel, C. Leinenbach, and K. Wasmer. Acoustic emission for in situ quality monitoring in additive manufacturing using spectral convolutional neural networks. *Additive Manufacturing*, 21:598–604, 2018.

[225] B. Sick. On-line and indirect tool wear monitoring in turning with artificial neural networks: a review of more than a decade of research. *Mechanical Systems and Signal Processing*, 16(4):487–546, 2002.

[226] A. Singh, D. R. Houser, and S. Vijayakar. Detecting gear tooth breakage using acoustic emission: a feasibility and sensor placement study. *Journal of Mechanical Design*, 121(4):587, 1999.

[227] H. Sohn, C. R. Farrar, F. M. Hemez, and J. J. Czarnecki. A review of structural health monitoring literature: 1996-2001. *Los Alamos National Laboratory, USA*, 2003.

[228] M. Sokolova and G. Lapalme. A systematic analysis of performance measures for classification tasks. *Information Processing and Management*, 45(4):427–437, 2009.

[229] S. Soua, P. Van Lieshout, A. Perera, T. H. Gan, and B. Bridge. Determination of the combined vibrational and acoustic emission signature of a wind turbine gearbox and generator shaft in service as a pre-requisite for effective condition monitoring. *Renewable Energy*, 51:175–181, 2013.

[230] W. Staszewski. Intelligent signal processing for damage detection in composite materials. *Composites Science and Technology*, 62(7-8):941–950, 2002.

[231] P. Stavropoulos, D. Chantzis, C. Doukas, A. Papacharalampopoulos, and G. Chryssolouris. Monitoring and control of manufacturing processes: a review. *Procedia CIRP*, 8:421–425, 2013.

[232] M. Surgeon and C. Buelens. Waveform based analysis techniques for the reliable acoustic emission testing of composite structures. *Journal of Acoustic Emission*, 18:34–40, 2000.

[233] C. K. Tan, P. Irving, and D. Mba. A comparative experimental study on the diagnostic and prognostic capabilities of acoustics emission, vibration and spectrometric oil analysis for spur gears. *Mechanical Systems and Signal Processing*, 21(1):208–233, 2007.

[234] C. K. Tan and D. Mba. Experimentally established correlation between acoustic emission activity, load, speed, and asperity contact of spur gears under partial elastohydrodynamic lubrication. *Proceedings of the Institution of Mechanical Engineers, Part J: Journal of Engineering Tribology*, 219(6):401–409, 2005.

[235] C. K. Tan and D. Mba. Identification of the acoustic emission source during a comparative study on diagnosis of a spur gearbox. *Tribology International*, 38(5):469–480, 2005.

[236] J. Tang, S. Soua, C. Mares, and T. H. Gan. A pattern recognition approach to acoustic emission data originating from fatigue of wind turbine blades. *Sensors*, 17(11):1–12, 2017.

[237] A. Tharwat. Classification assessment methods. *Applied Computing and Informatics*, 2018.

[238] P. Theobald, B. Zeqiri, and J. Avison. Couplants and their influence on AE sensor sensitivity. *Journal of Acoustic Emission*, 26:91–97, 2008.

[239] T. Toutountzakis and D. Mba. Observations of acoustic emission activity during gear defect diagnosis. *NDT and E International*, 36(7):471–477, 2003.

[240] T. Toutountzakis, C. K. Tan, and D. Mba. Application of acoustic emission to seeded gear fault detection. *NDT & E International*, 38(1):27–36, 2005.

[241] P. Večeř, M. Kreidl, and R. Šmíd. Condition indicators for gearbox condition monitoring systems. *Acta Polytechnica*, 45(6):35–43, 2005.

[242] C. M. Vicuña. Effects of operating conditions on the Acoustic Emissions (AE) from planetary gearboxes. *Applied Acoustics*, 77:150–158, 2014.

[243] C. M. Vicuña and C. Höweler. A method for reduction of Acoustic Emission (AE) data with application in machine failure detection and diagnosis. *Mechanical Systems and Signal Processing*, 97:44–58, 2017.

[244] I. A. Viktorov. *Rayleigh and Lamb waves physical theory and applications*. Plenum Press, 1967.

[245] K. Virupakshappa and E. Oruklu. A hardware/software co-design architecture for ultrasonic flaw detection with hidden Markov model and wavelet transform. In *2017 IEEE International Ultrasonics Symposium (IUS)*, Washington, DC, USA, September 6-9, 2017.

[246] C. Wang, Z. Bao, P. Zhang, W. Ming, and M. Chen. Tool wear evaluation under minimum quantity lubrication by clustering energy of acoustic emission burst signals. *Measurement*, 138:256–265, 2019.

[247] X. Wang, A. Mueen, H. Ding, G. Trajcevski, P. Scheuermann, and E. Keogh. Experimental comparison of representation methods and distance measures for time series data. *Data Mining and Knowledge Discovery*, 26(2):275–309, 2012.

[248] X. J. Wang and Y. Huang. An investigation of the acoustic emission generated during crystallization process of salicylic acid. *Powder Technology*, 311:350–355, 2017.

[249] M. Wevers and K. Lambrighs. Applications of acoustic emission for SHM: a review. In *Encyclopedia of Structural Health Monitoring*. John Wiley & Sons, 2009.

[250] J. Whiting, A. Springer, and F. Sciammarella. Real-time acoustic emission monitoring of powder mass flow rate for directed energy deposition. *Additive Manufacturing*, 23:312–318, 2018.

[251] S. F. Wirtz, S. Bach, and D. Söffker. Experimental results of acoustic emission attenuation due to wave propagation in composites. In *Proceedings of the Annual Conference of the PHM Society*, Scottsdale, AZ, USA, September 21-26, 2019.

[252] S. F. Wirtz, N. Beganovic, and D. Söffker. Investigation of damage detectability in composites using frequency-based classification of Acoustic Emission measurements. *Structural Health Monitoring*, 18(4):1207–1218, 2019.

[253] S. F. Wirtz, N. Beganovic, P. Tenberge, and D. Söffker. Frequency-based damage detection of spur gear using wavelet analysis. In *8th European Workshop On Structural Health Monitoring (EWSHM 2016)*, Bilbao, Spain, July 5-8, 2016.

[254] S. F. Wirtz, A. P. Cunha, M. Labusch, G. Marzun, S. Barcikowski, and D. Söffker. Development of a low-cost FPGA-based measurement system for real-time processing of acoustic emission data: Proof of concept using control of pulsed laser ablation in liquids. *Sensors*, 18(6):1775, 2018.

[255] S. F. Wirtz, A. P. A. Cunha, N. Beganovic, and D. Söffker. High-speed data acquisition system for continuous acoustic emission monitoring and real-time signal processing using FPGA-based platform within a SHM framework. In *9th European Workshop on Structural Health Monitoring*, Manchester, UK, July 10-13, 2018.

[256] S. F. Wirtz, A. Demmerling, and D. Söffker. In-situ wear monitoring: An experimental investigation of acoustic emission during thread forming. In *Structural Health Monitoring 2017*, Stanford, CA, USA, September 12-14, 2017.

[257] S. F. Wirtz and D. Söffker. Application of shape-based similarity measures to classification of acoustic emission waveforms. In *Structural Health Monitoring 2017*, Stanford, USA, September 12-14, 2017.

[258] S. F. Wirtz and D. Söffker. Improved signal processing of acoustic emission for structural health monitoring using a data-driven approach. In *9th European Workshop on Structural Health Monitoring*, Manchester, UK, July 10-13, 2018.

[259] T. T. Wong. Performance evaluation of classification algorithms by k-fold and leave-one-out cross validation. *Pattern Recognition*, 48(9):2839–2846, 2015.

[260] K. Worden and G. Manson. The application of machine learning to structural health monitoring. *Philosophical Transactions of the Royal Society A: Mathematical, Physical and Engineering Sciences*, 365(1851):515–537, 2006.

[261] H. Wu, Z. Yu, and Y. Wang. Experimental study of the process failure diagnosis in additive manufacturing based on acoustic emission. *Measurement*, 136:445–453, 2019.

[262] B. Yang and D. Sun. Testing, inspecting and monitoring technologies for wind turbine blades: a survey. *Renewable and Sustainable Energy Reviews*, 22:515–526, 2013.

[263] Z. Yin and J. Hou. Recent advances on SVM based fault diagnosis and process monitoring in complicated industrial processes. *Neurocomputing*, 174:643–650, 2016.

[264] J. Yousefi, M. Ahmadi, M. N. Shahri, A. R. Oskouei, and F. J. Moghadas. Damage categorization of glass/epoxy composite material under mode II delamination using acoustic emission data: A clustering approach to elucidate wavelet transformation analysis. *Arabian Journal for Science and Engineering*, 39(2):1325–1335, 2014.

[265] L. Yu, G. Santoni-Bottai, B. Xu, W. Liu, and V. Giurgiutiu. Piezoelectric wafer active sensors for in situ ultrasonic-guided wave SHM. *Fatigue and Fracture of Engineering Materials and Structures*, 31(8):611–628, 2008.

[266] D. Zhang, B. Gökce, and S. Barcikowski. Laser Synthesis and Processing of Colloids: Fundamentals and Applications. *Chemical Reviews*, 117(5):3990–4103, 2017.

[267] L. Zhang, H. Yalcinkaya, and D. Ozevin. Numerical approach to absolute calibration of piezoelectric acoustic emission sensors using multiphysics simulations. *Sensors and Actuators, A: Physical*, 256:12–23, 2017.

[268] Y. Zhang, W. Lu, and F. Chu. Planet gear fault localization for wind turbine gearbox using acoustic emission signals. *Renewable Energy*, 109:449–460, 2017.

[269] Z. Zheng, Y. L. Wang, and C. Ping. Real-time implementation of vector Hilbert-Huang transform. In *2010 Third International Conference on Intelligent Networks and Intelligent Systems*, Shenyang, China, November 1-3, 2010.

[270] W. Zhou, W.-Z. Zhao, Y.-N. Zhang, and Z.-J. Ding. Cluster analysis of acoustic emission signals and deformation measurement for delaminated glass fiber epoxy composites. *Composite Structures*, 195:349–358, 2018.

[271] Y. Zhou, L. Yang, Y. Lu, X. Hu, X. Luo, and H. Chen. Flow regime identification in gas-solid two-phase fluidization via acoustic emission technique. *Chemical Engineering Journal*, 334:1484–1492, 2018.

[272] Y.-L. Zhou, N. M. M. Maia, R. P. C. Sampaio, and M. A. Wahab. Structural damage detection using transmissibility together with hierarchical clustering analysis and similarity measure. *Structural Health Monitoring*, 16(6):711–731, 2017.

[273] S. Zhu, Y. F. Lu, and M. H. Hong. Laser ablation of solid substrates in a water-confined environment. *Applied Physics Letters*, 79(9):1396–1398, 2001.

List of publications

Intermediate results presented/published in the following conferences/journals or prepared for submission to following journals are stated as an integral part of this thesis:

1. S.F. Wirtz, S. Bach, D. Söffker. Experimental results of acoustic emission attenuation due to wave propagation in composites. 11th Annual Conference of the Prognostics and Health Management Society, Scottsdale, AZ, USA, September 21-26, 2019.

2. M. Labsuch, A.P.A. Cunha, S.F. Wirtz, S. Reichenberger, E. Cleve, D. Söffker, S. Barcikowski. Acoustic emission control avoids fluence shifts caused by target runaway during laser synthesis of colloids. *Applied Surface Science*, 479:887-895, 2019.

3. S.F. Wirtz, N. Beganovic, D. Söffker. Investigation of damage detectability in composites using frequency-based classification of Acoustic Emission measurements. *Structural Health Monitoring*, 18(4):1207–1218, 2019.

4. S.F. Wirtz, D. Söffker. Improved signal processing of Acoustic Emission for Structural Health Monitoring using a data-driven approach. 9th European Workshop On Structural Health Monitoring (EWSHM 2018), UK, Manchester, July 10-13, 2018.

5. S.F, Wirtz, A.P.A. Cunha, N. Beganovic, D. Söffker. High-speed data acquisition system for continuous Acoustic Emission monitoring and real-time signal processing using FPGA-based platform. 9th European Workshop On Structural Health Monitoring (EWSHM 2018), UK, Manchester, July 10-13, 2018.

6. W. Sheng, S.F. Wirtz, D. Söffker. Wavelet Packet Transform-Based Feature Extraction for Acoustic Emission Pattern Recognition. 9th European Workshop On Structural Health Monitoring (EWSHM 2018), UK, Manchester, July 10-13, 2018.

7. S.F. Wirtz, A.P.A. Cunha, M. Labusch, G. Marzun, S. Barcikowski, D. Söffker. Development of A Low-Cost FPGA-Based Measurement System for Real-Time Processing of Acoustic Emission Data: Proof of Concept Using Control of Pulsed Laser Ablation in Liquids. *Sensors*, 18(6):1775, 2018.

8. S.F. Wirtz, D. Söffker. Application of shape-based similarity measures to classification of Acoustic Emission waveforms. In: Chang, F.K.; Kopsaftopoulos (Ed.): Structural Health Monitoring 2017, USA, Stanford, September 12-14, 2017, pp. 1177-1184.

9. S.F. Wirtz, A.L. Demmerling, D. Söffker, D. In-situ wear monitoring: An experimental investigation of Acoustic Emission during thread forming. In: Chang, F.K.; Kopsaftopoulos (Ed.): Structural Health Monitoring 2017, USA, Stanford, September 12-14, 2017, pp. 1198-1205.

10. S. Rothe, S.F. Wirtz, G. Kampmann, O. Nelles, D. Söffker. Ensure the reliability of damage detection in composites by fusion of differently classified Acoustic Emission measurements. In: Chang, F.K.; Kopsaftopoulos (Ed.): Structural Health Monitoring 2017, Stanford, USA, September 12-14, 2017, pp. 1380-1387.

11. A.P.A. Cunha, S.F. Wirtz, D. Söffker, N. Beganovic. Implementation of frequency-based classification of damages in composites using real-time FPGA-based hardware framework. ASME 2017 International Design Engineering Technical Conferences & Computers and Information in Engineering Conference, Cleveland, Ohio, USA, August 6-9, 2017, pp. 1-8.

12. S.F. Wirtz, N. Beganovic, P. Tenberge, D. Söffker. Gear transmission monitoring 4.0: What can be expected from upcoming diagnostic and prognostic systems. 11. Aachener Kolloquium für Instandhaltung, Diagnose und Anlagenüberwachung (AKIDA), Aachen, November 15-16, 2016.

13. S. Rothe, S.F. Wirtz, D. Söffker. About the reliability of diagnostic statements: fundamentals about detection rates, false alarms, and technical requirements. 11. Aachener Kolloquium für Instandhaltung, Diagnose und Anlagenüberwachung, Aachen, Germany, November 15-16, 2016.

14. S.F. Wirtz, N. Beganovic, P. Tenberge, D. Söffker. Frequency-based damage detection of spur gear using wavelet analysis. European Workshop on Structural Health Monitoring, Bilbao, Spain, July 5-8, 2016.

15. S.F. Wirtz, N. Beganovic, D. Söffker. Experimental results of frequency-based classification of damages in composites. European Workshop on Structural Health Monitoring, Bilbao, Spain, July 5-8, 2016.

Supervised theses

In the context of research projects at the Chair of Dynamics and Control, the following student thesis has been supervised by Sebastian Felix Wirtz and Univ.-Prof. Dr.-Ing. Dirk Söffker. Development steps and results of the research work and the student theses are included in this thesis.

1. S. Bach. Experimentelle Charakterisierung des Ausbreitungsverhaltens von Ultraschallwellen, Master Thesis, October 2019.

The following student theses, which are not included in this thesis, were supervised by Sebastian Felix Wirtz and Univ.-Prof. Dr.-Ing. Dirk Söffker.

2. I. Aldallah. Optimization and test of a demonstrator for the practical implementation of control loops with Matlab/Simulink, LabView, CoDeSys, and Arduino, Master Thesis, June 2020.

3. S. O. Doruk. Acoustic Emission-based diagnosis of composites using Convolutional Neural Networks: How wave propagation affects classification performance, Master Thesis, May 2020.

4. W. Boschmann. Convolutional Neural Network (CNN) for classification-based gear monitoring, Master Thesis, January 2020.

5. Z. Ma. Aufbau, Inbetriebnahme und Einbindung eines Batterieversuchsstandes für individualisierte Lade- und Entladecharakteristiken in einen HiL Antriebsstrang, Master Thesis, June 2019.

6. P. Brauer. Entwicklung und Aktualisierung einer Vorgehensweise zur arbeitssicherheitstechnischen Bewertung von Versuchsständen, Bachelor Thesis, May 2019.

7. A. Al Nassan. Evaluierung von Hardware Plattformen zur Implementierung von Regelkreisen. Master Thesis, December 2018.

8. M. Schielke. Deep learning zur Datenanalyse für Structural Health Monitoring, Master Thesis, March 2018.

9. Y. Su. Entwicklung und Aktualisierung einer Vorgehensweise zur Sicherheitstechnischen Bewertung von Versuchsständen, Bachelor Thesis, October 2017.

10. Y. El-Bahrawy. Application of statistical pattern recognition to data-based damage detection in bearings using benchmark data, Bachelor Thesis, July 2017.

11. Y. M. Wang. Literature research on lifetime models for composite material, Bachelor Thesis, September 2016.

DOI: 10.17185/duepublico/72136
URN: urn:nbn:de:hbz:464-20200720-151815-2